Ceramic Nanostructured Catalysts

Gilbank, Alexander

Award date:
2015

Awarding institution:
University of Bath

Ceramic Nanostructured Catalysts

Alexander Gilbank

A thesis submitted for the degree of Doctor of Philosophy

University of Bath
Department of Chemical Engineering

January 2015

Table of Contents

List of Figures

List of Tables

Acknowledgements

First and foremost I would like to thank my supervisor, Laura Torrente Murciano, for her continual aid and guidance. Especially for the time and work she gave to helping me become a more proficient scientific author. I believe that your help has made me more capable of planning and structuring practical and literary pursuits, as well as improving my presentation skills. Thank you.

I would like to thank all those of our research group, 'Catalysis and Process Integration' (CaPI). Specific thanks goes to Simon Bishopp and Rebecca Bamford for their help with overcoming issues during my PhD, especially in the early stages. Their help and assistance in the setting up of our research laboratory also can not go unnoted, and also leads me to thank Pawel Plucinski for the share of space and equipment during the transitional period of being without a laboratory.

Alfred Hill, another member of our group (CaPI) also greatly deserves my gratitude, for his help and aid, most notably with my absence of a Chemical Engineering background. His advice and guidance were invaluable and our 'Tour de Lyon' during our confrence trip to EuropaCat-XI will not be forgotten.

My thanks also extends to the technicians at the University of Bath, for their help in setting up and using equipment, the access to which, gives me the chance to offer my thanks to those who provided it. Specific appreciation should be given to Fernando Acosta for his help in teaching me to use much of the analytical equipement utilised in this work, to John Bishop, whose skills in the field of electronics made the catalytic rig possible and John Mitchels whose ability and knowledge of microscopy continues to astound.

For their use of TEM and facilities I thank the Research Complex at Harwell and the UK Catalysis Hub. For the funding and opportunity to undertake this work I thank the University of Bath. My thanks also extends to our collaborators who allowed my work to extend to an international level.

For their help, advice and aid in solving many issues and concerns that arise during a PhD, and also for their attempts to keep me sane, I give my appreciation to Ben Firth, Daniel Minet, William Lewis, Jenny Crabtree and again to Rebecca Bamford and Simon Bishopp. Many lunches and coffee breaks were spent together and cryptic crosswords solved. *Star of 'Cast Away' with first initiallised gives appreciations (6).*

For all those unnamed, as I will doubtlessly have forgotten some, whose guidance I've received and support I've been given to get to this stage, thank you.

Personal appreciation also goes to my loved ones, my family, my mum, dad and sister who have put up with having a son/brother in education for so long and always supported me. Also special thanks is given to my girlfriend, Grace Childs, whose love and support have helped to keep me going for these past few years, and in spite of any problem, can always make me smile.

Finally I would like to thank those who venture to read this work and hope that it can provide useful information for the progress in the field of ceramic based nanostructured catalysts and their use as supports for metal nanoparticles.

Abstract

Catalysis has an effect on almost every aspect of our lives. They are used to help grow the food we eat, clean the water we drink and produce the fuels our civilisation is so dependent upon. Homogeneous catalysts, those in the same phase as the reaction medium, are highly selective as a result of their tuneable nature, for example through changes to ligands in a metal complex. However, their separation from the reaction medium can become a problematic, costly, non-green issue, overcome through the use of heterogeneous catalysts which can be removed and recycled by simple separation techniques such as filtering and sedimentation.

A major limitation on understanding the behaviour of heterogeneous catalysts is the presence of different active sites due to different exposed crystal surface, concentration of defects and morphological variations. With such considerations, the first section of this thesis focuses on the synthesis of discrete and well-defined nanostructured materials (ceria and titanate) using a single-step hydrothermal method.

Nanostructured ceria with different morphologies (particles, rods and cubes), present a high oxygen storage capacity and thermal stability. Their oxidation catalytic activity was assessed using CO oxidation as a model reaction as a function of their physical and chemical properties, tuned by morphological control at the nanoscale. An inverse relationship is observed between crystallite size and rates of reaction normalised per surface area. Smaller crystallites present a constrained geometry resulting in a higher concentration of defects, highly active catalytically due to their unsatisfied coordination and high surface energy. The surface to bulk oxygen ratio generally increased as the surface area increased, however, ceria nanorods present a higher surface oxygen content than that which would be predicted according to their surface area, likely due to the selective exposure of the (110) and (100) dominating crystal surfaces presenting more facile oxygen atoms in their surface. Additionally a relationship between surface to bulk oxygen ratios and activation energies was also ascribed to the more facile nature

of oxygen atoms on these surfaces and their more readily formed oxygen vacancies as a result. This activity is as a result of the formation of oxygen vacancies being the rate-controlling step.

The thermal stability of nanostructured ceria (particles, rods and cubes) was also studied to investigate their performance under cyclic high temperature applications. For this, the materials were pre-treated at 1000 °C under different atmospheres (inert, oxidative and reducing). In all cases, the materials sinter, consequently resulting in a dramatic decrease in surface area. Interestingly, their catalytic activity per surface area towards CO oxidation, seems to be maintained, although those materials pre-treated under inert and oxidising atmospheres became inactive in consecutive catalytic runs. However, nanostructured ceria pre-treated at 1000 °C under hydrogen appeared to maintain its activity per surface area. The presence of hydrogen during thermal treatment does not only facilitate the removal of surface oxygen, but also the bulk oxygen, resulting in a rearrangement of the structure that facilitates its catalytic stability.

Titanate nanotubes were shown to be inactive for CO oxidation and thus were used in the second part of this thesis as a support for platinum nanoparticles to study the effect of the structure and metal-support interaction on the resulting catalytic activity. The study focuses on the effect of different loading methods (ion exchange and incipient wetness impregnation) of platinum nanoparticles on the resulting metal particle size, dispersion, metal-support interaction and consequently their resulting catalytic activity.

Ion exchange consistently resulted in smaller nanoparticles with a lower dispersion of sizes and more active catalyst, both in terms of turnover frequency values and activation energy, compared with incipient wetness impregnation. The catalytic activity of the platinum supported on titanate nanotubes increases as the metal particle size decreases to a size value (between 1 and 2.5 nm) below which a dramatic decrease in activity is observed. Despite initial differences in catalytic activity between the different catalysts, it was observed that after initial reactions to 400 °C, the activation energy was independent of metal loading weight and was instead inherent of the loading method, suggesting the presence of similar active sites.

Abbreviations

Notation	Meaning
AAS	Atomic absorption spectroscopy
BET	Brunauer, Emmett, Teller
BDDT	Brunauer, Deming, Denting, Teller
CeNP	Ceria nanoparticles (synthesised at 70 ºC, 5M NaOH)
$CeNR_A$	Ceria nanorods (synthesised at 100 ºC, 15M NaOH)
$CeNR_B$	Ceria nanorods (synthesised at 70 ºC, 15M NaOH)
$CeNR_C$	Ceria nanorods (synthesised at 100 ºC, 10M NaOH)
$CeNC_A$	Ceria nanocubes (synthesised at 180 ºC, 15M NaOH)
$CeNC_B$	Ceria nanocubes (synthesised at 180 ºC, 10M NaOH)
GHSV	Gas hourly space velocity
IE	Ion exchange
IWI	Incipient wetness impregnation
MFC	Mass flow controller
OSC	Oxygen storage capacity
Pre-NP	Pre-synthesised nanoparticles loaded via IWI
TCD	Thermal conductivity detector
TEM	Transmission electron microscopy
TGA	Thermal gravimetric analysis
TiNT	Titanate nanotubes
TOF	Turnover frequency
TiPt	Pt nanoparticles supported on titanate nanotubes
TPIT	Temperature programmed inert treatment
TPO	Temperature programmed oxidation
TPR	Temperature programmed reduction
WHM	Width at half maximum
wt.%	Weight percentage of total mass
XPS	X-ray photoelectron spectroscopy
XRD	X-ray diffraction

Dissemination

Torrente-Murciano, L., Gilbank, A., Puertolas, B., Garcia, T., Solsona, B., Chadwick, D., *Shape-dependency activity of nanostructured CeO_2 in the total oxidation of polycyclic aromatic hydrocarbons*. App. Cat. B, **2013**, 132-133, p116-122.

Gilbank, A., Torrente-Murciano, L., *Thermal Stability of Nanostructured Ceria as an Oxidation Catalyst.* EuropaCat-XI, Lyon, France, **2013**, Sept. 1st-6th, Oral Presentation.

Gilbank, A., Torrente-Murciano, L., *Thermal Stability and Catalytic Activity of Ceria Nanostructures*. Sustainable and Environmental Catalysis, IChemE event, University of Bath, UK, **2013**, Sept. 25th-26th, Poster Presentation.

Chapter 1

Introduction

Around 90% of all commercial chemicals are obtained through a catalytic process[1, 2]. Globally, catalysis is responsible for the production of hundreds of billions of pounds worth of materials annually[1, 2], having applications in numerous industries, including but not limited to, pharmaceuticals[3], foods[4], fuels[5], water treatment[6], agriculture[7] and polymers[8]. Their ability to increase reaction rates, selectivity and yields, reduces costs, labour and waste production making them essential in practically every aspect of modern life.

Impressive progress in the field of catalysis has been achieved over the last century, the most noteworthy accomplishment being the Haber process for synthesising ammonia from nitrogen and hydrogen for its use in agricultural fertilizers. This one catalytic process is said to be principally responsible for the current explosion in human population[9]. However, we are currently facing new challenges associated with a continually increasing population, depletion of resources and global climate change threatening our current way of life. The development of novel catalysts is essential to tackle these issues in a sustainable manner and has already been highlighted as one of the twelve principles of Green Chemistry[10].

There are two main types of catalysts: heterogeneous and homogeneous. Homogeneous catalysts have the advantage of easier control over selectivity and activity, for example, through the modification of ligands of a metal complex. Small changes to these ligands can have a substantial effect on rate, yield and selectivity through electron donation and steric bulk effects. Heterogeneous catalysts however, have a more complex structure, with many potential reaction sites of different activity that can be difficult to quantify. By existing in the same phase, homogeneous catalysts have the advantage of very fast diffusion rates. The transfer of reagents to and from the catalytic site will much more rarely limit the rate of reaction in homogeneous catalysts compared to heterogeneous. The understanding and study of heterogeneous catalysts becomes more laborious due to the possibility of mass transfer limiting the rate associated to internal and external diffusion of reactants and products.

Despite the high reaction rates and selectivity characteristics of homogeneous systems, their separation from the reaction medium can be energy intensive and in some cases, problematic. Catalysts are typically expensive due to the use of precious metals and recyclability is required for the economic feasibility of the process, additionally, they can often be toxic. Even without such concerns, full separation from the products is normally a necessity, and can require expensive steps and the production of waste after the reaction. However, heterogeneous catalysts can overcome these issues through simple separation processes, such as filtration or sedimentation.

Metal nanoparticles can be classified between heterogeneous and homogeneous catalysts due to their sizes (normally below 10 nm). They present interesting properties, not only having a higher concentrations of highly active atomic configurations and defects but also due to their potential non-metallic nature at sizes approaching their de Broglie wavelength[11]. These properties have shown metals usually considered inert, such as gold, active at the nanoscale.

While metal nanoparticles are still most definitely a solid nanoparticle, they can be smaller than bulky homogeneous catalysts, re-emerging the issue of separation. Immobilisation of metal nanoparticles on a support has been shown to counter this issue[12], whilst the support itself affords properties to the metal nanoparticles that can tune their catalytic behaviour.

1.1. Metal Nanoparticles

Metal nanoparticles are typically defined as particles with a diameter between 1 and 100 nm. However, from a catalytic perspective and for the purpose of this thesis metal nanoparticles will be considered as those that are below ~15nm due to the higher fraction of surface atoms, shown in Figure 1.1.

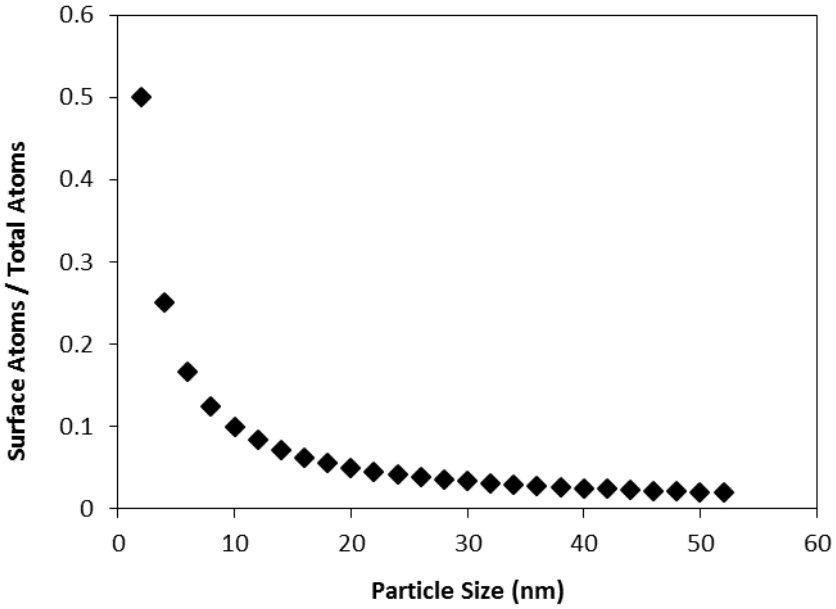

Figure 1.1 – Fraction of atoms at the surface of spherical nanoparticles[13].

The higher fraction of surface atoms is not the only property that makes < 15 nm metal nanoparticles of interest. There are further properties that are only applicable to smaller metal nanoparticles, specifically higher concentrations of defects and a shift to non-metallic like properties[14]. Surface atoms have a higher energy than bulk atoms due to the absence of surrounding atoms. Atoms in defect sites are of higher unsatisfied coordination and thus, higher energy. The concentration of defects increases with decreasing particle size due to the constrained geometry. The unsatisfied coordination makes such atoms highly favour the adsorption of surrounding molecules in order to minimise their surface energy. Non-metallic

metal nanoparticles exhibit a band gap that can potentially afford alternative redox routes for reaction pathways[11].

Metal nanoparticles have applications in many areas, such as anti-microbial[15], medicine[16], materials[17] and catalysis[11]. The high unsatisfied coordination and resulting surface energy, high concentration of defects and non-metallic nature of metal nanoparticles are principally what make them of specific interest with regards to catalysis.

One of the very properties that makes metal nanoparticles of interest catalytically, high surface energy due to unsatisfied coordination, also results in the challenge of preventing agglomerations into more stable but inactive particles. The smaller the nanoparticle the higher the ratio of surface to bulk atoms, therefore the higher the favourability that the particles will agglomerate to reduce the energy associated with this[18]. Stabilisation of metal nanoparticles can be achieved through the use of capping agents reducing their surface energy and preventing their agglomerations[19]. However, whilst this stabilises the surface it usually reduces the activity of the metal nanoparticle, leading to a competitive adsorption and/or steric hindrance for the transfer of reactants and products to and from the reaction sites. For catalysis, a more advantageous method of preventing agglomeration is to immobilise the metal nanoparticles on a support, so called, heterogenisation. This approach additionally facilitates the separation of the metal nanoparticles from the reaction media and products, allowing for easier recyclability.

There is a vast amount of research studying heterogeneous catalysts that comprise of immobilised metal nanoparticles. A high number of metal-support combinations have been studied for their catalytic activity. Supports such as cellulose[20], ceramics[21], zeolites[22] and carbon[23] have all been studied with a variety of metals. Though there are still challenges to be overcome in this field, specifically regarding thermal stability and mass transfer limitations.

As the temperature is increased during reaction conditions there is a tendency for metal nanoparticles to become mobile upon the surface of the support due to the correlation between particle size and melting point[18]. This leads to agglomerations into larger, often less catalytically active nanoparticles. There is also the possibility of the support denaturing during reaction conditions, which make it self-evidently unsuitable for nanoparticle stabilisations.

Highly porous structures, such as zeolites, can often result in a higher surface area, making agglomeration less of an issue due to higher dispersion. Additionally, the nanoparticles can be encapsulated inside pores avoiding their agglomeration and in some specific cases providing stereoselectivity. However, porous supports may also result in longer diffusion pathways or reactants to the metal nanoparticle surface which can become rate limiting. There is also the potential for blocking of pores that can result in significant portions of the catalyst becoming unavailable.

To overcome these limitations, nanostructured materials, defined as materials with at least one dimension within the nanometre scale offer an alternative for the immobilisation of metal nanoparticles on their external surfaces. Their high surface areas, tuneable chemical compositions and exposed crystal surfaces, facilitate the dispersion of the metal and control of the interaction between the metal and support. Currently, much of the research in this area has been devoted to the use of carbon nanotubes as catalytic support due to their unique chemical and physical properties[24]. Despite the large pool of studies of ceramics as supports for metal nanoparticles, the effect of the control of their morphology at the nanoscale has still to be fully exploited.

1.2. Nanostructured Materials

Nanostructured materials can be classified according to the dimensions of nanoscale control. This system of classification places nanoparticles in their own category, as zero dimensional (0D) nanostructures. One dimensional (1D) nanostructures are those with one dimension substantially larger than the others, including rods, wires and tubes, where axial growth is controlled anisotropically. Two dimensional (2D) nanostructures include sheets and belts. While three dimensional (3D) nanostructures can be as simple as cubes of have increased morphological complexity such as flowers. Figure 1.2 shows a collection of some nanostructured morphologies in the literature with different dimensions of control.

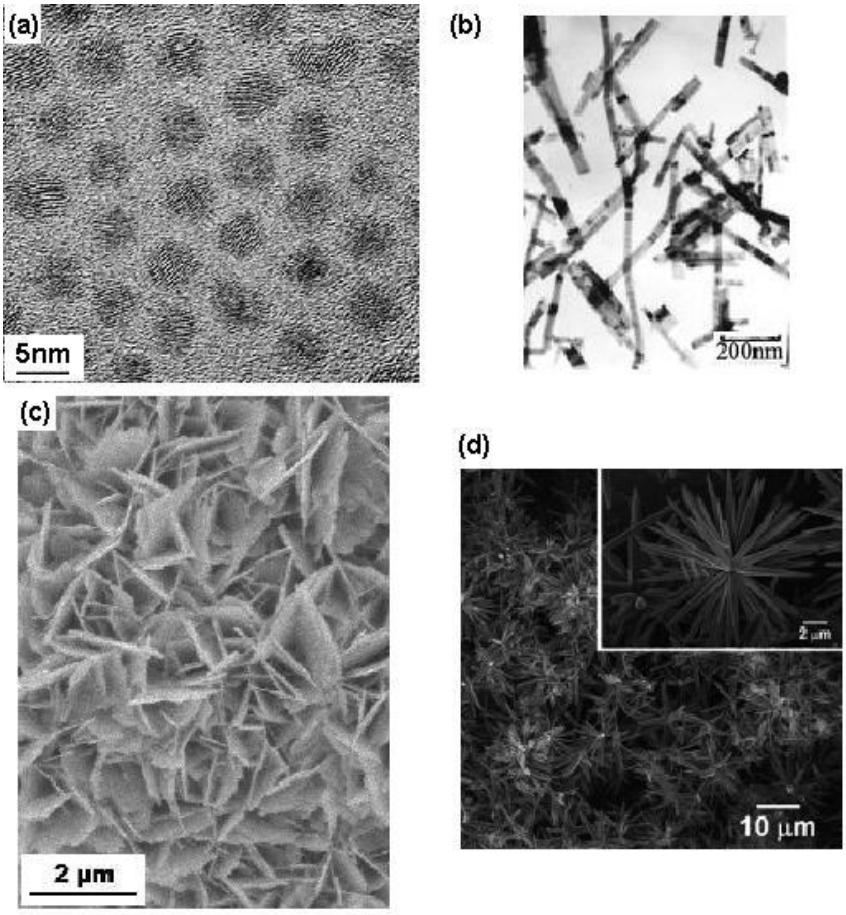

Figure 1.2 – Transmission electron microscopy images of (a) 0D nanoparticles, quantum dots, of CdS[25], (b) 1D nanostructures, CdS nanorods[26], (c) 2D nanostructures, Ag nanosheets[27] and (d) 3D nanostructures, ZnO nanoflowers[28].

Ceramic materials (such as titania, ceria, silica and alumina) are widely used in industry as catalytic supports due to their high mechanical[29], thermal[30] and chemical stability[31]. This thesis focuses on the investigation of the relationship between the morphology at the nanoscale and the physical and surface properties of different ceramic nanostructured materials, specifically in their use as catalysts and as metal nanoparticles supports.

The surface of the crystal structure is defined by the plane through which the crystal lattice is cleaved. The Miller index, is the commonly used notation, which gives the lowest discrete reciprocal lattice vectors. Changing the morphology at the nanoscale can selectively change the exposed crystal plane and thus the chemical and physical properties of the surface. This is of specific interest to catalysis, where active sites are at the surface of the material.

Ceria is a ceramic, which as well as displaying high thermal, mechanical and chemical stability, also offers a high oxygen storage capacity[32, 33]. By changing the exposed crystal surface a higher concentration of oxygen vacancies can be exposed that consequently changes the oxygen storage capacity of the material. One of the main catalytic uses of ceria is in catalytic convertors as a three-way catalyst, due to its high oxygen storage capacity. As the oxygen storage capacity can be varied by changing the exposed crystal plane and that these crystal planes can be selectively exposed in specific nanostructured morphologies, means that through controlling nanostructure growth, different catalytic activities can be achieved.

1.3. Aims and Objectives

The overall aim of this thesis is to investigate the effect of the morphology at the nanoscale on the physical and surface properties of different ceramic nanostructured materials, specifically in their use as a catalysts and as metal nanoparticle supports. For this purpose a series of objectives are identified.

Investigate the relationship between ceria nanostructured morphology and its catalytic activity.

Ceria nanostructures of different morphologies (particles, rods and cubes) will be synthesised through an alkali hydrothermal method. Through controlled changes to the temperature and alkali concentration, different morphologies will be synthesised with well-defined and distinct structures. All morphologies will be fully characterised through various techniques including N_2 adsorption, XPS, TEM, TPR, XRD and Raman spectroscopy. Surface area, crystal structure, aspect ratios, crystallite size, surface oxygen content and the oxidation states of ceria will all be analysed.

The catalytic activity of the different nanostructured ceria will be assessed using carbon monoxide oxidation as a model reaction. Studies will be carried out to relate their activity to their physical and chemical properties including crystallite size, surface area, surface to oxygen content and cerium oxidation state.

Investigate the relationship between atmosphere and thermal stability of ceria nanostructured catalysts.

The stability of nanostructured ceria at high temperature under different atmospheres will be studied. The different nanostructures will be exposed to reducing, oxidising and inert atmospheres up to 1000 °C. Their physical characteristics and oxidative catalytic activity will be evaluated after said thermal treatments in repeat catalytic cycles.

Investigate the effect of different methods of supporting metal nanoparticles on nanostructured materials.

Metal nanoparticles will be immobilised on a nanostructured support (titanate nanotubes) through different methods. The selected methods are ion exchange and incipient wetness impregnation.

The effect of synthesise methods and the metal loading on the resulting particle size and dispersion will be investigated through complimentary characterisation techniques including transmission election microscopy imaging and carbon monoxide chemisorption.

Investigate the catalytic activity of different metal nanoparticles supported on ceramics.

The oxidative catalytic activity of platinum nanoparticles supported on titanate nanotubes using different loading methods will be assessed using carbon monoxide oxidation

as a model reaction. A relationship between the metal nanoparticle size, metal loading and loading method with the resulting catalytic activity will be investigated. The same immobilised metal nanoparticle catalysts will be used in consecutive catalytic cycles (heated and cooled) to study the stability of the catalytic activity.

1.4. Thesis Structure

The thesis is divided into two major sections. The first section, Chapters 3 to 5, focuses on the study of the effects of the morphology at the nanoscale of ceria on the stability and catalytic activity. The second section, Chapters 6 and 7, focuses on the titanate nanotubes as supports for immobilising metal nanoparticles. An emphasis is made on the effect of metal loading methods and metal loading content on the resulting nanoparticle size and dispersion and how these characteristics effect catalytic activity and catalytic stability.

Chapter 2 describes in detail the experimental procedures, including synthesis methods for all nanostructured materials and metal nanoparticles. The analytical techniques used and the equipment employed to carry out these analyses are described. The chapter also includes the design of the carbon monoxide oxidation rig and its experimental validation.

Chapter 3 contains a literature review of the current state of the art of the synthesis of ceramic nanostructured materials, with a focus on ceria nanostructures and titania/titanate nanotubes. The mechanisms of nanostructure growth and synthetic routes are reviewed in detailed. Fundamental concepts regarding the crystal structure of such materials are also included.

Chapter 4 investigates the hydrothermal synthesis of different nanostructured ceria morphologies and titanate nanotubes. Full characterisation of the materials is used to study the effect of the synthesis conditions on their physical and chemical properties. Their catalytic activity for oxidation reactions is assessed using carbon monoxide oxidation as model reaction.

The relationship between the catalytic activity and their physical and chemical properties is presented.

Chapter 5 studies the effect of thermal treatment under different atmospheres, reducing, oxidising and inert on ceria morphologies as oxidative catalysts. The catalytic activity, after these thermal pre-treatments is evaluated using carbon monoxide oxidation as a model reaction in consecutive catalytic cycles.

Chapter 6 contains a review of the state of the art literature related to the synthesis and properties of metal nanoparticles and their use as catalysts for oxidation reactions, with an emphasis on carbon monoxide oxidation. Special focus is given to supported platinum nanoparticles and titania and titanate as supports.

Chapter 7 investigates the effect of the loading methods of platinum nanoparticles on nanostructured titanate nanotubes and the resulting metal particle size and dispersion by means of physical characterisation. Furthermore, oxidative catalytic activity of these materials is studied for the CO oxidation reaction in consecutive catalytic heating and cooling cycles. The results of these studies are correlated to the particle size, loading method, metal loading and the role of metal-support interaction.

Chapter 8 presents a conclusion of the results and findings of this thesis and makes suggestions for possible future work as a result of the work undertaken here.

Chapter 2

Experimental and Catalyst Testing Validity

One aim of this thesis is to investigate the variations in catalytic activity and thermal stability of nanostructured materials and how these properties can be benefitted through variations in the nanoscale morphology. This chapter provides information on all the methods and procedures followed for the synthesis, characterisation and catalytic tests used in this thesis. It also provides a validation study of the kinetic regime governing the catalytic studies.

Nanostructured ceria and titanate materials were synthesised through alkali hydrothermal methods. Platinum and gold nanoparticles were synthesised on titanate nanotubes (TiNT) via ion exchange (IE) and incipient wetness impregnation (IWI) methods. Platinum nanoparticles were also pre-synthesised prior to their loading on titanate nanotubes via the wetness impregnation procedure.

The nanostructured materials were characterised using transmission electron microscopy (TEM) imaging, X-ray diffraction (XRD), X-ray photoelectron spectroscopy (XPS), Raman spectroscopy, temperature programmed reduction/oxidation/inert treatment (TPR/TPO/TPIT)

and low temperature nitrogen adsorption. The platinum loadings were determined by atomic absorption spectroscopy (AAS) where appropriate and metal particle sizing was performed through TEM and CO chemisorption.

2.1. Synthesis of Nanostructured Ceramic Materials

All nanostructured materials used in this work were synthesised via alkali hydrothermal methods using stainless steel Parr acid digestion vessels equipped with PTFE liners (50 mL and 300mL volume), busting discs and pressure relief discs. Separate PTFE liners were used for each material to prevent cross-contamination. The synthesis conditions for each of the nanostructured materials are summarised in Table 2.1. In a typical synthesis method, the material precursor was added to a solution of sodium hydroxide (Fisher Scientific) with the desired concentration prepared using ultra high conductive water (18.2 MΩ cm). Titanium dioxide (Fisher Scientific) and cerium nitrate hexahydrate (Sigma Aldrich) were used as precursors for the titanate and ceria materials respectively. The solution was then sealed in the acid digestion vessel and heated to the synthesis temperature, unstirred, in an air-circulating oven to favour a homogeneous temperature profile across the vessel. The synthesis temperature was controlled by a thermopar inside the oven. The PTFE liners were filled up to no more than 75% of their total volume for safety reasons.

Table 2.1 – Conditions used for the synthesis of ceria and titania based nanostructures in the 300 mL acid digestion vessel.

Precursor / g	Concentration of NaOH / M	Temperature / ºC	Time / hours	Structure
TiO_2, 10.0	200 mL, 10M	130	24	Nanotubes
$Ce(NO_3)_3$ $6H_2O$, 3.0	200 mL, 5M	70	10	Nanoparticles
$Ce(NO_3)_3$ $6H_2O$, 3.0	200 mL, 10M	100	10	Nanorods
$Ce(NO_3)_3$ $6H_2O$, 3.0	200 mL, 10M	180	10	Nanocubes
$Ce(NO_3)_3$ $6H_2O$, 3.0	200 mL, 15M	70	10	Nanorods
$Ce(NO_3)_3$ $6H_2O$, 3.0	200 mL, 15M	100	10	Nanorods
$Ce(NO_3)_3$ $6H_2O$, 3.0	200 mL, 15M	180	10	Nanocubes

The resulting nanostructured product was filtered from the basic solution and washed with copious distilled water and dried in a vacuum oven overnight at 80 ºC before being ground up with a pestle and mortar to a fine powder.

The titanate nanotubes were additionally washed with a solution of 0.1 M sulphuric acid until reaching a pH of 7, at which point the majority of sodium ions in the titanate surface have been replaced by hydrogen. After this acid wash, the sample was washed again with distilled water and dried in a vacuum oven at 80 ºC overnight.

2.2. Metal Nanoparticle Immobilisation Methods

Platinum and gold nanoparticles were synthesised on the surface of titanate nanotubes through various loading methods described below. To facilitate the comparison, a larger batch of the support was prepared by combining several synthetic batches to ensure consistency through the metal nanoparticle immobilisation work. The metal precursors used were 30 wt.% gold chloride solution in dilute HCl and 8 wt.% chloroplatanic acid aqueous solution (Sigma Aldrich).

2.2.1. Ion Adsorption/Exchange

The ion adsorption, or ion exchange method, consists of the deposition of the metal ions from a solution into the support in suspension. In a typical experiment, the desired theoretical metal loading is diluted in ultrapure water (50 mL) in a stirred glass round bottom flask. The solution is heated at 60 ºC on a magnetic hot plate using a paraffin oil bath. The temperature is controlled by a thermopar inside the solution which controls the temperature of the plate. Once the temperature is reached, the support material (0.5 g) is added rapidly and the mixture is stirred at temperature for 3 hours. The solution was then filtered and washed with a minimal amount of distilled water before being dried under vacuum at 80 ºC overnight. All the filtrate and washing water was collected for metal content analysis.

2.2.2. Incipient Wetness Impregnation

In the incipient wetness impregnation method the metal precursor is diluted in a solvent volume equal to the pore volume of the support. Initially the wetness volume of the various supports was measured by adding known amounts of water to a known amount of solid until full wetting occurs. The titanate nanotubes synthesised in this thesis were found to have a wetness volume of 1.98 mL g^{-1}. The desired amount of metal is then dissolved in the calculated wetness volume before being impregnated into the support drop wise. The resulting material is finely distributed across a clean surface to facilitate homogeneous drying conditions whilst dried under vacuum at 80 ºC overnight.

2.2.3. Pre-synthesised Metal Nanoparticles

Platinum nanoparticles were pre-synthesised in solution and loaded onto the nanostructured material by the addition of the wetness volume of suspended platinum nanoparticle solution. The platinum nanoparticles were synthesised in a glass round bottom flask, stirred and heated by a magnetic stirrer hotplate and the temperature controlled using a thermopar inside the solution. 45 mL of ethylene glycol is heated to 150 ^{o}C at a rate of 5 ^{o}C min^{-1} whilst stirring. To this, 0.476 mL of H_2PtCl_6 in 5 mL of ethylene glycol is added. Next, 100 mg of PVP (MW 10,000 g mol^{-1}) in 25 mL of ethylene glycol is added drop wise over 13 minutes. The reaction is maintained at 150 ^{o}C and stirred for 1 hour to synthesise nanoparticles of ~6 nm diameter[34].

2.2.4. Metal Reduction

All supported metal nanoparticles were reduced at 120 ^{o}C under a continuous 30 mL min^{-1} flow, of hydrogen for one hour in a quartz tube inside a furnace. The temperature was increased at a rate of 2.5 ^{o}C min^{-1} and controlled with a PID controller using a thermopar above the outside of the catalytic bed. All samples were cooled down and blanketed in nitrogen before removal from the system.

2.3. Characterisation of Materials and Catalysts

2.3.1. Transmission Electron Microscopy

Transmission electron microscopy (TEM) images were obtained using a JEOL JEM-2100 LaB6 and images recorded with Gatan digital camera. Samples are prepared by depositing a

drop containing ~0.5 mg mL^{-1} of sample in ethanol onto a Lacey copper mesh grid (Agar Scientific). Initially the grid is dried in air before storage overnight under vacuum before imaging. Determination of the material morphology, particle sizes and crystal lattice spacing were carried out manually using ImageJ software. Manual measurements were chosen over algorithms due to high contrast of the ceramic support making it impossible to employ a correct threshold to identify metal particles. Particle size distributions were typically carried out on upwards of 100 particles to ensure a representative distribution of size.

2.3.2. X-Ray Diffraction

X-ray diffraction spectra were recorded using a D8 Advance' powder X -ray diffractometer with a copper source. A completely dry powder sample of material was loaded into a 0.5 mm capillary, about 20 mm in height. The capillary is supported and aligned in the diffractometer for analysis between a 2θ value of 17^{o} and 90^{o}.

2.3.3. X-Ray Photoelectron Spectroscopy

X-ray photoelectron spectroscopy (XPS) measurements were performed using a Kratos Axis ultra DLD photoelectron spectrometer using a non-monochromatised Mg Kα X-ray source (hν = 1253.6 eV), 50 eV was used for survey scans and 20 eV for detailed scans. The C1s peak from adventitious carbon contamination, assumed to have a binding energy of 284.5 eV was used as a reference. XPS data was analysed using CasaXPS software, all peaks were fitted with a Gaussian-Lorentzian shape function to fit the data. XPS was performed and analysed by our collaborators with Dr Garcia of the University of Zaragoza.

2.3.4. Low Temperature Nitrogen Adsorption Surface Area Analysis

Low temperature nitrogen adsorption measurements were carried out using an ASAP 2020 instrument from Micromeretics. The samples were degased prior analysis under vacuum at 120 ºC to acquire a clean surface and samples were weighed post degas. Nitrogen adsorption/desorption was performed at 77 K using 45 s equilibration intervals and surface area calculated via BET theory. Free space measurements were performed in all cases. The error in the surface area calculation is performed as a propagation of the error in the gradient and intercept of the BET plot.

2.3.5. Temperature Programmed Reduction/Oxidation/Inert Treatment

Temperature programmed reductions (TPR), oxidations (TPO) and inert treatments (TPIT) were carried out using Micromeritics Autochem II Chemisorption equipment. Samples were pre-treated under a 30 mL min^{-1} flow of helium at 120 ºC to ensure a clean surface and dry material. Then samples were heated at a rate of 2.5 ºC min^{-1} to 1000 ºC under 5% H_2 in Ar, 20% O_2 in He and 100% He for the TPR, TPO and TPIT respectively, all at 30 mL min^{-1}. The outlet gas of the reactor was passed through a cold trap to remove any condensable compounds (mainly water) and analysed with a thermal conductivity detector (TCD) to monitor qualitative changes in the gas composition. The inlet gas composition was used as a reference gas for the detector.

2.3.6. Carbon Monoxide Chemisorption Metal Surface Area Analysis

CO chemisorption analyses were carried out using Micromeritics Autochem II Chemisorption equipment equipped with a thermal conductivity detector (TCD). Samples were pre-treated at 200 ºC under a 30 mL min^{-1} flow of helium to remove any compound adsorbed on the material surface prior their reduction at 150 ºC under 30 mL min^{-1} flow of 5% H_2 in Ar. The sample was then cooled down under a 30 mL min^{-1} flow of helium to -90 ºC. CO pulse chemisorption was carried out by injecting a calibrated volume of 5% CO in He into the flow through the sample bed at set intervals of 5 minutes under a continuous 30 mL min^{-1} flow of He. The outlet gas was analysed using a TCD detector to quantify the amount of CO chemisorbed by the sample. Injections were repeated 30 times. Assuming a monolayer adsorption, the volume of CO adsorbed was used to calculate the metal particle size assuming metal nanoparticles were of a perfect hemispherical morphology. The metal to CO stoichiometry was 1:1 for both Pt and Au following literature data[35, 36] and the data given by manufactures. This method is in accordance with information supplied by the manufacturers, Micromeritics BEL-CAT Application note CAT-APP-002.

2.3.7. Atomic Absorption Spectroscopy

Atomic absorption spectroscopy (AAS) was carried out using an air-acetylene flame and a Perkin Elmer 3100 Atomic Absorption Spectrometer. For the Pt analysis a Perkin Elmer P/N3050162, Pt hollow cathode lamp was used. In the case of the Au analysis the following was used; an AS-2 hollow cathode lamp with a 242.8 nm wavelength sensitivity and an emission stability of less than +/- 1% after 2 hours of heating. Filtrate and washings, made up volumetrically, from the ion exchange and deposition-precipitation methods were run against standards to determine the quantity of metal that had loaded onto the nanostructures. Each

sample was repeated three times and gave standard deviations below 1%, with blanks between each run. Calibrations were repeated between each sample to ensure greatest accuracy.

2.3.8. Raman spectroscopy

Raman spectroscopy was performed using a Renishaw inVia Raman Microscope. The dry powder sample was loaded into a sample tube and then measurements were taken at 532 nm wavelength between 100 and 1800 cm^{-1}.

2.4. Catalytic Tests in a Packed Bed Reactor Rig

The catalytic activity of the nanostructures and immobilised metal nanoparticles was investigated using carbon monoxide oxidation as a model reaction, widely used in the literature to assess the oxidation catalytic activity. Catalytic tests were carried out in a continuous flow packed bed reactor. Its process and instrumentation diagram (P&ID) is shown in Figure 2.1.

The rig consisted of a gas inlet manifold, reactor and on-line gas analysis. 4000 ppm CO/N_2 and 4000 ppm O_2/N_2 cylinders (BOC) were connected to mass flow controllers (Bronkhorst) which allows the introduction of different CO/O_2 compositions into the reactor.

A quartz 'u-shaped' tube was used as the reactor. The inlet branch of ~18 cm length and 0.4 cm internal diameter was used to heat up the inlet gas to the reaction temperature prior to its contact with the catalysts. The outlet branch of the reactor, with a 1cm internal diameter was used to support a packed bed. In a typical reaction, the packed catalytic bed contained 15 mg of catalyst diluted in a 1:1 volume ratio of 24 grit and 200-450 mesh silicon carbide to a total volume of 4 cm^3, quartz wool was used to support the bed. The reactor was held inside a high temperature furnace (max temperature 600 ºC) equipped with a PID controller. The temperature was measured by a thermopar inside the furnace (used for the control) and a thermopar directly

above the packed bed inside the reactor to monitor the reaction temperature. In a typical experiment, 50 mL min^{-1} flow of 2000 ppm CO and 2000 ppm O_2 in N_2 was passed through the packed bed, with a GHSV of 750 $hour^{-1}$ and heated at 2.5 ^oC min^{-1}. The outlet gas composition was measured by on-line analysed using a Fuji Electrics model ZRH Infrared Gas Analyser. The reaction temperature and the gas analyser reading were automatically recorded at 5 second intervals using Labview software.

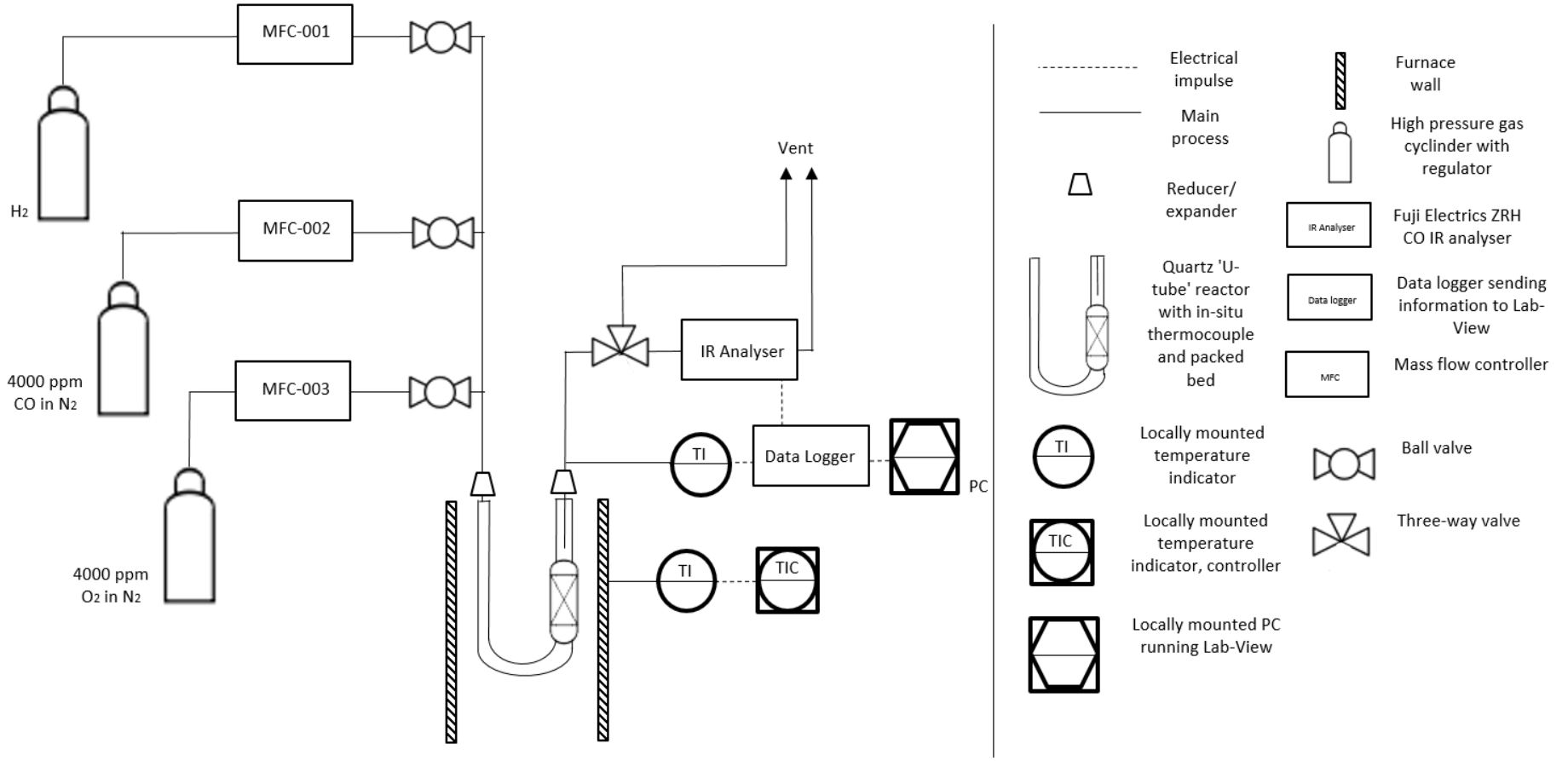

Figure 2.1 – Piping and instrumentation diagram for the continuous gas flow packed bed reactor.

2.4.1 Error Analysis

The error associated to the gas carbon monoxide composition measurements by the Fuji Electrics model ZRH Infrared Gas Analyser was calculated by flowing known concentrations of CO through a blank reactor and monitoring the concentration every 5 seconds for 20 hours. The standard deviation of the IR reading as a function of CO ppm concentrations using a 50 mL min^{-1} flow are shown in Figure 2.2.

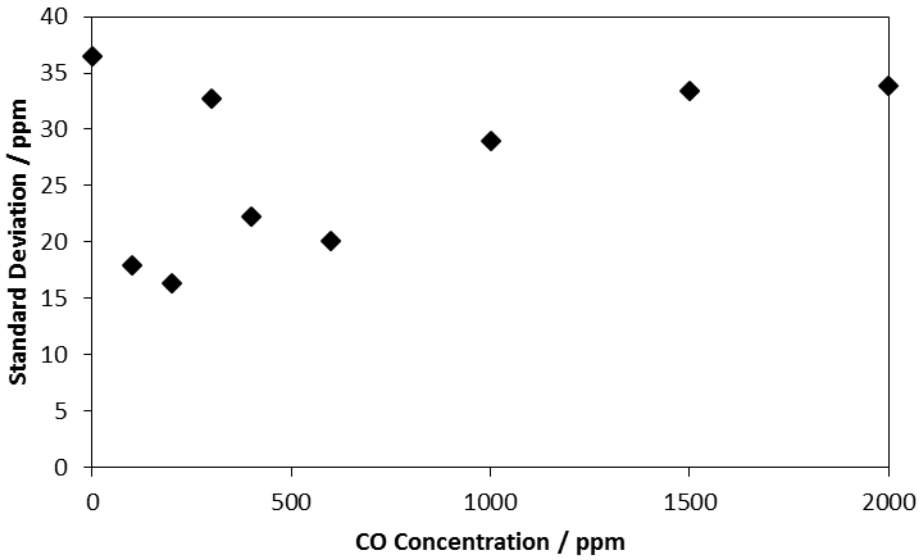

Figure 2.2 – Standard deviation error as a function of CO concentration using a Fuji Electrics ZHR Infrared Gas Analyser. Each standard deviation value is calculated taking data for a 20 hour period at 50 mL min^{-1}.

The error associated to the gas analyser was observed to be independent of the concentration of CO and is likely caused by noise related to the signal between the detector and the PC. As such, a fixed value of 36.4 ppm is used as the error, the highest standard deviation found. To reduce error further, the results are processed as a moving average over a 90 second period, an example of data gathered and handled in this way is shown in Figure 2.3; limits were set for data selection between 0 and 100 % conversion.

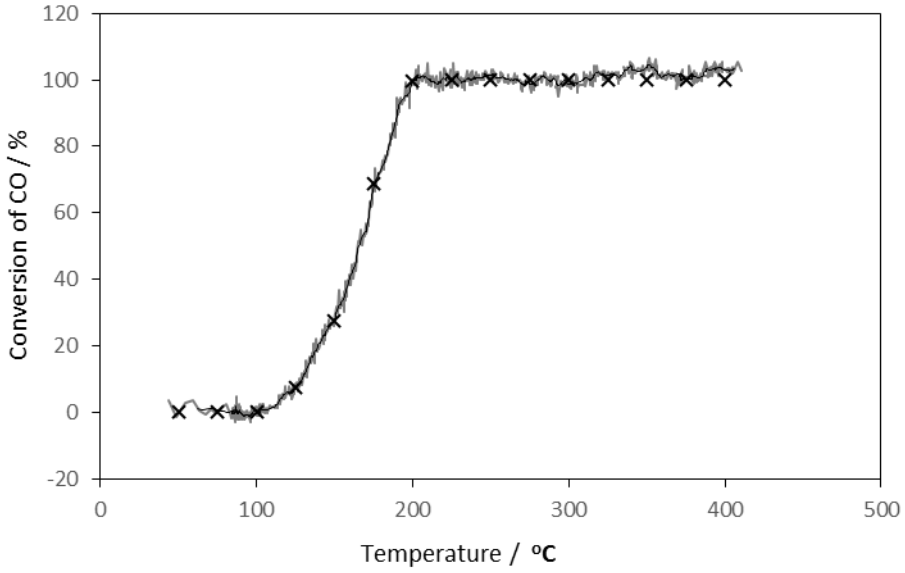

Figure 2.3 – Data handling and selection process. Grey line depicts raw data, black line represents the moving average and black crosses show points selected for data presentation.

During the experimentation, variations of the y-axis intercept of the calibration line were observed without changes to the gradient and therefore, the CO IR detector was calibrated prior to each reaction to ensure the greatest accuracy.

Mass flow controllers (MFC) were calibrated for the 4000 ppm CO/N_2, the 4000 ppm O_2/N_2 and H_2 gases by measuring the actual flow rates with a bubble meter. A five point calibration was carried out across the range of the MFC flow rates using a bubble meter to measure 10 mL. Three independent measurements were taken for each flow rate. The calibration lines are shown in Figure 2.4 for the CO/N_2 mix, Figure 2.5 for the O_2/N_2 mix, and Figure 2.6 for H_2 with error bars of the standard deviation values for the three recordings.

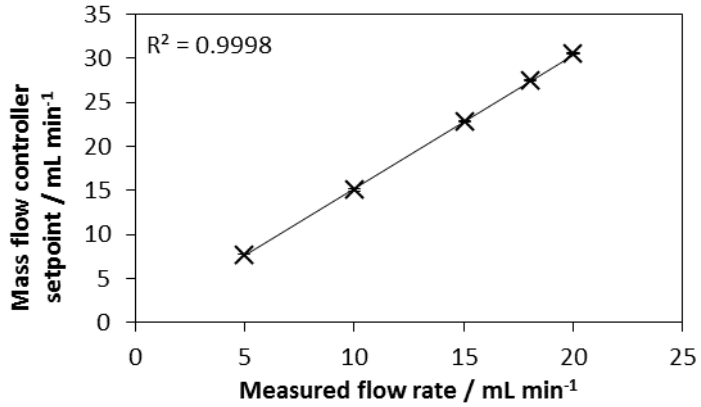

Figure 2.4 – CO mass flow controller calibration line. A bubble meter was used to record an average of three times to obtain 10 mL of 4000 ppm CO in N_2 at different set points at room temperature.

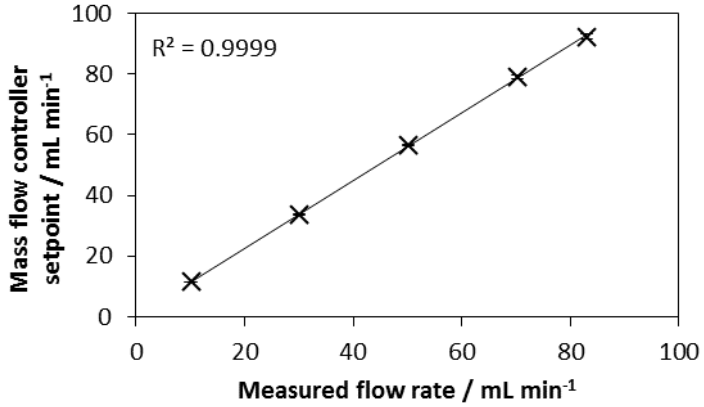

Figure 2.5 – O_2 mass flow controller calibration line. A bubble meter was used to record an average of three times to obtain 10 mL of 4000 ppm O_2 in N_2 at different set points at room temperature.

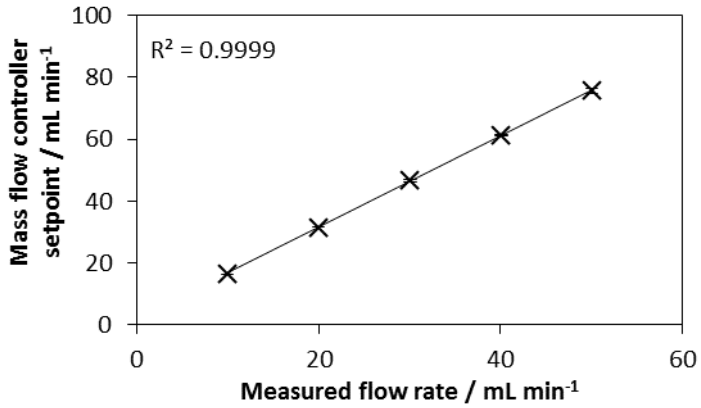

Figure 2.6 - H_2 mass flow controller calibration line. A bubble meter was used to record an average of three times to obtain 10 mL of H_2 at different set points at room temperature.

The background activity of the catalytic rig was determined to be negligible by running a blank reaction using a quartz reactor filled with the quartz wool and silicon carbide (no catalyst) to 600 ºC keeping the rest of the conditions as previously described. This reaction was periodically repeated throughout the body of work to ensure that the reactors did not gain activity between catalyst tests due to contamination.

2.4.2 Data Processing

Selected intervals along the conversion profile are taken for the presentation of results in this work. For the calculation of the activation energy through the use of the Arrhenius plot, an equation that describes the conversion versus temperature is chosen to give best fit in the <20% conversion region, for reasons discussed below. The conversion to the log plot versus reciprocal temperature, outlined below, is performed on this equation.

Arrhenius Data Analysis

The activation energy of each of the catalysts can be calculated for a single continuous run during which the reaction temperature was varied as detailed above. The rate of reaction is shown in Equation 2.1, where $-r_{CO}$ is the rate of reaction, k is the rate constant and p_{CO} and p_{O2} are the partial pressures of CO and O_2 respectively and α and β are the order of reaction with respect to CO and O_2.

$$-r_{CO} = k \cdot p_{CO}^{\alpha} \cdot p_{O2}^{\beta} \qquad (\mathbf{2.1})$$

The relationship of the rate constant and temperature is given by the Arrhenius equation. Linearization of the rate equation through substitution into the Arrhenius equation results in Equation 2.2 where E_a is the activation energy, R is the ideal gas constant and T is the temperature of reaction.

$$\ln(-r_{CO}) = \left(\frac{-E_a}{RT}\right) + \ln(A) + \alpha \cdot \ln(p_{CO}) + \beta \cdot \ln(p_{O2}) \qquad (\mathbf{2.2})$$

To calculate the activation energy from the linearized rate equation the partial pressures of CO and O_2 need to be constant. At low conversion levels (< 20%), it can be considered that the partial pressure of the reactants is constant and equal to the initial pressures. However, at very low conversion (<6%) the error of the reaction is high enough to contribute significantly, especially when converted to a log scale. As such, this allows for the calculation of activation energy only within this region (6-20%).

2.4.3 Validation of Catalytic Studies

Packed Bed Homogeneity

For a packed bed reactor to be suitable for testing the activity of a catalyst it is essential to ensure that there is an even distribution of catalyst and even flow through the reactor. To achieve even dispersion, different particle sizes of silicon carbide dilution material were tested. Using solely 24 grit silicon carbide as a diluent resulted in issues with even catalyst dispersion through the packed bed during the reaction due to migration of the catalyst. A smaller silicon carbide particle size (200-450 mesh) caused a high pressure drop resulting in splitting of the packed bed during the reaction. It was found that a 1:1 volume ratio, 24 grit and 200-450 mesh silicon carbide prevented both of these issues and provided a good dispersion of the catalyst through the packed bed before and after reactions.

Flow homogeneity can be split into two components radial and axial flow. Back mixing or uneven axial flow results in invalid catalytic data. Even axial flow is typical of a reactor that has a high flow velocity to prevent back mixing. The superficial gas hourly space velocity (GHSV) of the reactor is 750 $hour^{-1}$. Assuming a bed of close-packed spherical particles this

would give an interstitial GHSV of 2891 $hour^{-1}$. As temperature increases so does the flow velocity, suggesting higher GHSV during the data used for catalytic studies. The axial mixing profile is studied through the use of residence time distribution data shown below.

Homogeneity occurs radially for a packed bed when there are identical flow conditions throughout all the interstitial spaces from the centre to the edge of the bed. Typically ensuring plug flow is a good way to ensure this. The Reynolds number calculated for this rig was found to be 0.5 for the 24 grit and 0.03 for the 200-450 mesh silicon carbide, this would suggest laminar flow (Reynolds number < 10). Due to the large number of very small channels, this could be expected and the interconnected nature of these pathways results in good mixing.

To ensure that the packed bed flow is homogeneous, reactions were run, changing the axial and radial conditions whilst ensuring there were no changes to the rate of reaction, through changes to the GHSV, demonstrated later in this section in Figure 2.9.

Residence Time Distribution

Although a pulse experiment is more informative than a step for a residence time distribution, due to the design of the reactor only a step experiment is possible. The residence time distribution for a reaction in which the concentration was changed from 0 ppm to 2000ppm of CO is shown in Figure 2.7, raw data is presented with a measurement taken ever second. However, it is important to note that the concentration during this test is switched at the mass flow controllers not the packed bed itself. As such, an estimate is made for the volume between the mass flow controller and packed bed, this volume was calculated to cause a 12 second delay and is taken into account in the F(t) curve below.

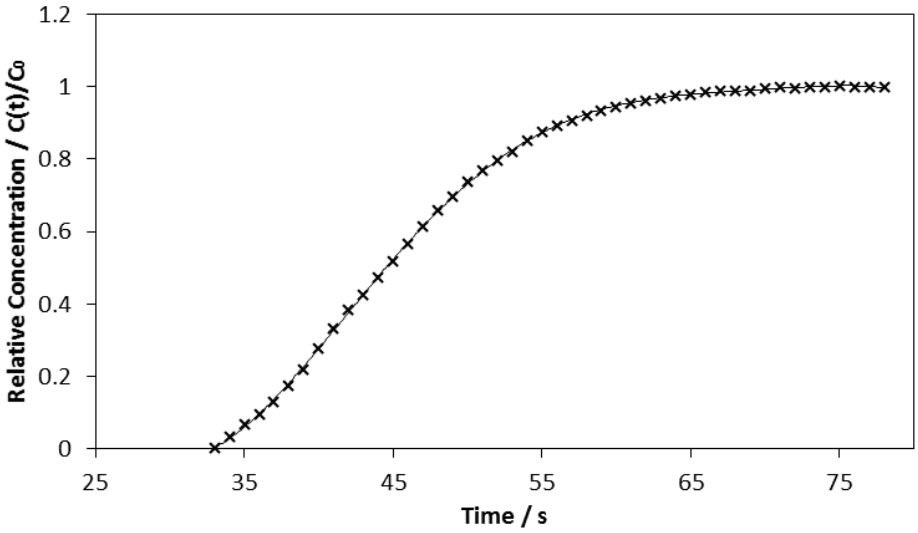

Figure 2.7 – F(t) curve of the step change residence time distribution of the 4 mL packed bed reactor with a 50 mL min^{-1} flow rate. t = 0 when the step change concentration reaches the inlet of the packed bed.

There is a 33 second delay between the introduction of the step change concentration to the reactor and the initial reading by the detector and then a further 23 seconds before 90% change to the CO concentration is observed. The non-dimensional curve, F(t), given by this residence time distribution step experiment can be used to find the exit age distribution E(t). This residence time distribution curve is shown in Figure 2.8.

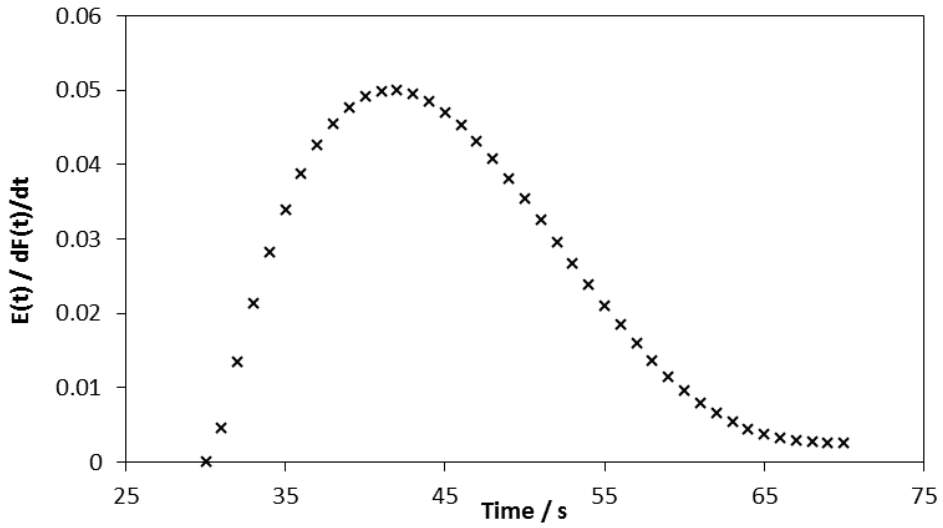

Figure 2.8 – E(t), the exit age distribution of the 4 mL packed bed reactor with a 50 mL min^{-1} flow rate. t = 0 when the step change concentration reaches the inlet of the packed bed.

The residence time distribution curve, E(t), is typical of a well-mixed reactor, suggesting no channelling, parallel paths to the exit or strong internal circulation, i.e. there is little longitudinal dispersion.

Study of Mass Transfer Limitation

To study the kinetics of the reaction, the rate limiting step must be the reaction itself and not the transfer of reactant and product to and from the catalytic site. Reactions to ensure mass transfer limitations were not occurring were run using half and double the packed bed volume, with the same weight of catalyst, i.e. varying the GHSV. This changed the concentration of catalyst in the bed, both axially and radially. If mass transfer was the limiting factor or there was non-homogeneous flow, then there would be an observable change in rate with this change in effective fluid velocity as the mass transfer coefficient increases with fluid velocity (or decreases with particle diameter) until a plateau is reached, where mass transfer is not the limiting step. The plot of rate against GHSV for the catalytic reactor, using 2, 4 and 8 mL of inert diluent to give a GHSV of 1500, 750 and 375 $hour^{-1}$ is shown in Figure 2.9 with the theoretical line showing the relationship between rate of mass transfer and velocity, the dashed line represents the GHSV at which mass transfer in demonstrated to not restrict rate of reaction.

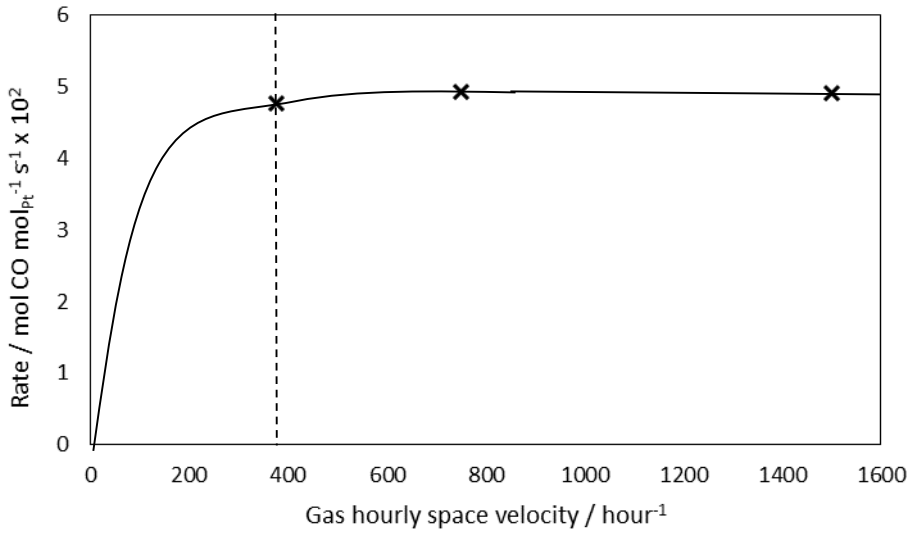

Figure 2.9 – Rate as a function of GHSV. The reaction was run at 50 mL min^{-1} of 2000 ppm CO, 2000 ppm O_2 in N_2 between ambient and400 °C using 15 mg of catalyst in volumes of SiC between 2 and 8 mL to give GHSV of 375, 750 and 1500 hour^{-1}.

The rate as a function of GHSV for the reaction show that within this region the reaction is rate limited and that mass transfer limitations are not in effect and that axial and radial diffusion are not having a significant effect on the catalytic data.

Chapter 3

Literature Review: Nanostructured Materials

The aim of this thesis is to investigate the variations in catalytic activity and thermal stability of nanostructured materials and how these properties can be benefitted through variations in the nanoscale morphology. This first section of the thesis is focused on the effect of the nanostructured morphology on the physical and chemical properties of ceria and what effect this has on the oxidative catalytic activity, while the subsequent section will investigate the effect of the nanostructured morphology on the activity and stabilization of supported metal nanoparticles. This chapter presents a literature review of the methods of synthesising nanostructured materials and their mechanisms of growth, specifically focused on ceria nanomorphologies and titanate nanotubes.

This literature review discusses how different morphologies allow for different crystal surface exposure and how different morphologies can be achieved, focusing on 'bottom-up' techniques. Properties of ceria and methods of synthesising different ceria nanomorphologies

reported in the literature are compared and discussed. The thermal stability of ceria and catalytic activity are also conferred. Finally the properties and mechanism of growth of titanate nanotubes, along with a comparison of synthesis methods and applications are discussed.

The term nanostructure is used to describe a morphology that has at least one dimension in the nanometer range, 1-100 nm. A synthesis method for nanostructured morphologies must be repeatable and capable of producing a well-defined morphology. Growth can be controlled along different dimensions in a variety of ways, either through the favouring of growth along one direction or the suppression of growth along the others.

Ceramic materials have several properties, such as high mechanical[29], thermal[30] and chemical stability[31] that are beneficial to the stability of nanostructured materials. It is well known that surface energy is greater than bulk energy and as such high surface area nanomaterials have a tendency to sinter during thermal treatments. The high stability of ceramics will therefore be useful in helping nanostructured materials retain their morphology during catalytic applications, which can potentially expose them to high temperatures or destructive chemical environments.

This literature review has a strong focus on ceria nanostructures and titanate nanotubes.

3.1 Nanostructure Growth

There are two ways to create nanostructured materials, the 'top-down' and 'the bottom-up' approach. The term 'top-down' is derived from the fact that these processes seek to create nanoscale structures from a larger starting medium[37]. These methods can be a reliable way of reproducing nanostructured designs with a high level of accuracy as they essentially 'draw' the desired design during fabrication, such as the use of lithography in the production of central processing units[38]. However, they are not capable of producing large quantities of nanostructured material as drawing each structure is not practical. Milling like processes can be

used for the ‘top-down’ production of larger quantities of materials, but results in a relatively broad distribution of sizes and does not control the identity of the exposed surfaces[39].

‘Bottom-up’ techniques are the opposite[40], these methods seek to assemble nanostructure morphologies through the building up of smaller starting blocks, such as through crystallisation or the agglomeration of smaller crystallites. Anisotropic growth is one example of a ‘bottom-up’ approach for the synthesis of nanostructured materials with specific morphologies. Anisotropic growth occurs where the favourability to grow in one direction is higher than competing directions, it can also be encouraged by blocking or restricting growth on other surfaces[41]. Some examples of this include the use of capping agents[42], reverse micelles[43] and template structures[44].

The control of growth to favour anisotropic crystallisation using templating techniques are quite common throughout the literature[44, 45]. They are often chosen for their ability to produce consistent nanostructures where control of the morphology can be achieved through subtle changes to the template. Using a porous material is one example, that can allow for the production of nanotubes or fibres inside the pores, after which the template can be removed through calcination to leave the nanotubes or fibres behind[44]. There are various methods of depositing the materials the nanostructures will be comprised of onto solid templates. Some typical examples include chemical vapour deposition, sol-gel and electrochemical deposition.

However, templating techniques require synthesis and destruction of the template increasing the number of steps, costs and complexity of the nanostructure fabrication. Small deviations in the template can result in inconsistent nanostructures, adding more potential for deviation in the nanostructure morphology. Porous templates require a clean surface for the nanostructures to grow and for the nanostructure growth to be controlled, as not to block the pore[44]. Therefore a template free method would provide notable benefits, removing the necessity of producing potentially expensive templates.

The use of template free techniques such as dissolution/recrystallization can remove the necessity of a template[46]. These methods result in the initial formation of smaller nano-crystallites that assemble to form larger nanostructures[47]. Control over the

recrystallization can be obtained through changing the conditions of synthesis that can allow for isotropic or anisotropic growth dependent upon the nature of the crystallites formed[46, 48]. The morphology is also dependent upon the identity of the source of nanostructured material and work looking into the effect of conditions and the precursors identity have been investigated in the literature[46]. The mechanistic study of nano-crystallite growth and agglomeration into larger nanostructures is beyond the scope of this thesis.

3.2 Ceria Nanostructures

Cerium dioxide or ceria (CeO_2) is a ceramic material that, as well as showing good thermal, mechanical and chemical stability, also has a high oxygen storage capacity. Ceria has the fluorite type crystal structure with the $Fm\bar{3}m$ space group consisting of four coordinate O^{2-} and eight coordinate Ce^{4+} ions. Cleaving the crystal unit cell through different planes at the surface changes the nature of the surface and can affect properties such as the oxygen storage capacity of the material. Control of the growth of the nanostructured morphology allows for selective control of the exposed crystal planes.

Ceria is used as an oxidative catalyst. The ability of ceria to catalyse such reaction is related to the oxygen storage capacity. This is due to the mechanism by which such reactions take place. It is generally accepted that such reactions use a Mars-van Krevelen reaction type mechanism, where the reactant adsorbs to the surface at an oxygen site and reacts with the oxygen before desorption to leave an oxygen vacancy that is refilled in a subsequent step. Therefore by changing the nanostructured morphology to change the oxygen storage capacity the catalytic activity can be altered.

3.2.1 Ceria: Properties and Applications

Ceria presents a variety of physical and chemical properties that benefit its application in catalysis, specifically towards oxidising reactions[49]. It has a high oxygen storage capacity (OSC), high ion conductivity, a high dielectric constant and good thermal stability[50]. As such, it applications in various fields of catalysis, such as in electrochemistry[51] and fuel cells[52]. It is used in various catalytic reactions, including volatile organic compound oxidations[49], water gas shift reactions[53], photocatalysis[54] and steam reformation of alcohols[55]. However, it is as a three-way catalyst to control exhaust emissions[56] that ceria is most notably used for. In this reaction ceria is both used as a catalyst and as a support for metals in which it boosts activity by making oxygen readily available, through the Mars-van Krevelen mechanism.

Of the properties that ceria presents the one that plays the largest role in the catalysis of oxidising reactions, and therefore is of the most interest for this thesis, is OSC. The OSC of ceria relates to the materials ability to form and refill oxygen vacancies and therefore the ability to act as an oxidiser in reactions. The reactions occurring in catalytic convertors are a combination of several complex redox reactions occurring upon the surface of the ceria. However, the CO oxidation reaction is a key step and is often chosen as a reaction to test the activity of ceria.

3.2.2 Nanostructured Ceria: Synthesis Methods

This thesis is interested in ‘bottom-up’ type approaches for the synthesis of nanostructured materials. A review of the most relevant reported methods of synthesising nanostructured ceria of different morphologies is reported in Table 3.1.

Table 3.1 – A comparison of template and template-free methods for the synthesis of ceria nanostructures from a 'bottom-up' approach. A brief description of the reagents and conditions required and the resulting morphologies is given.

Method	**Resulting Structure**	**Reagents**	**Synthesis Conditions**	**Ref.**
Reverse Micelles	Square nanoparticles	Cerium nitrate, NH_4OH, octophenyl ether and *n*-hexyl alcohol microemulsion	Cerium nitrate and ammonium hydroxide in microemulsions were mixed, separation of precipitate by centrifuge, washed with methyl alcohol, water and acetone before freeze drying	[57]
Sonochemical	Square nanoparticles	Cerium nitrate, azodicarbonamide	Dissolved in water and sonocated for 3 hours at 80 °C, separated by centrifuge, washed and dried under vacuum	[58]
	Nanorods	Cerium nitrate, NaOH, polyethylene glycol	Aqueous solution sonocated with addition of NaOH, precipitate washed with alcohol and dried	[59]
Solution precipitation	Square nanoparticles	Cerium nitrate, ammonia	Stream O_2/N_2 through at 30 °C, centrifuge and wash with EtOH and water	[60]
	Hexagonal nanoparticles	Cerium nitrate, ammonia	Stream O_2/N_2 through at 90 °C, centrifuge and wash with EtOH and water	[60]
	Ultrathin nanosheets	Cerium nitrate, aminohexanoic acid (AHA), HCl	Heat acidic AHA solution to 95 °C, slowly add cerium nitrate solution by syringe pump and cool	[61]
Solvothermal	Hollow nanocubes	Cerium chloride, peroxyacetic acid (PAA), EtOH	160 °C in autoclave for 9 hours. Wash with water and ethanol, dry in oven.	[62]
Hydrothermal	Square nanoparticles	Cerium nitrate, NH_4OH, pH 10	300 °C in autoclave for 4 hours, washed with water and dried	[63]
	Nanorods	Cerium nitrate, ~ 2M NaOH	100 °C in autoclave for 10 hours, washed with water, dried and calcined at 350 °C for 4 hours	[27]

	Nanotubes	Cerium nitrate, 14M NaOH	100 °C in autoclave for 72 hours, washed with water and dried	[64]
	Nanowires	Cerium nitrate, 14M NaOH	110 °C in autoclave for 24 hours, washed with water and dried	[64]
	Nanocubes	Cerium nitrate, 14M NaOH	160 °C in autoclave for 24 hours, washed with water and dried	[64]

As stated, the use of templates can cause a variety of complications and extra cost as it requires the synthesis and consecutive removal of the templating material. The reverse micelle method, in Table 3.1 is an example of such a templating method. The use of template-free methods, such as the sonochemical, solution precipitation and the solvo/hydro-thermal are also described in Table 3.1. Sonochemical synthesis requires the use of a sonicator. Different reagents were shown to produce different nanostructures[58, 59] and aspect ratios were adapted through changes to the conditions.

The solvo/hydro-thermal and solution precipitation, template-free methods are similar in their approaches. The two main differences are the use of different chemical environments in the solution precipitation which, along with temperature, pH and time adds another variable to the synthesis method. Secondly is the use of a pressurised vessel for the solvo/hydro-thermal methods. The use of non-water solvents in the solvothermal and solution precipitation methods increases environmental impacts, in accordance with the principals of green chemistry[10].

As demonstrated, from the information provided in Table 3.1 the hydrothermal method is capable of producing a wide variety of nanostructured morphologies with relatively small changes to temperature and concentration of base in the alkali solution. This allows for comparable ceria nanostructures of varying morphologies, and thus exposed crystal surfaces, to be synthesised.

Hydrothermal Growth of Nanostructured Ceria

The dissolution/recrystallisation mechanism of hydrothermal synthesis is dependent on the identity of the cerium source, temperature and concentration of hydroxide[65]. The effect of the concentration of OH^- ions and temperature on the selectivity of morphology has been shown previously[49]. For cerium nitrate, there are two proposed mechanisms[66], shown in Figure 3.1.

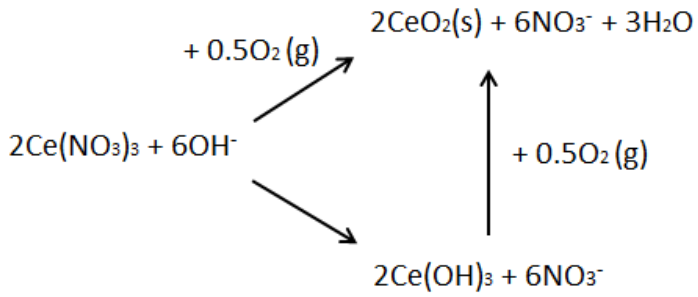

Figure 3.1 – Reaction mechanisms for the hydrothermal synthesis of ceria from cerium nitrate under alkali condition[66].

Though there is an apparent morphological trend with increasing OH^- concentration resulting in the shift from particles to rods to cubes, the effect of the OH^- ions was shown to be independent of the concentration of alkali hydroxide[66]. Therefore it is suggested that the physical factor that effects the reaction mechanism is viscosity; and that the more viscous the medium, the slower the anion exchange[66]. Therefore, for higher concentrations of NaOH, the reaction proceeds through the one-step synthesis directly to CeO_2, whilst for lower NaOH concentrations, the reaction proceeds through the $Ce(OH)_3$ intermediate, Figure 3.1.

The $Ce(OH)_3$ intermediate has been reported to be anisotropic resulting in the growth of rod morphologies, opposed to the isotropic CeO_2 which forms cubic morphologies[46]. The growth of the rod like morphologies from the anisotropic $Ce(OH)_3$ requires sufficient temperature. This is evident by the fact that the production of particles is observed at low NaOH concentrations, that would result in $Ce(OH)_3$ formation, and low temperature[49].

3.2.3 Thermal Stability of Ceria

The energy of surface atoms is higher than those in the bulk. Because of this, there is favourability for nanostructured materials to sinter when heated, to lower their overall energy by reducing the number of surface atoms. There is an energy associated with this mechanism which prevents spontaneous agglomerations. This process is observed at different temperatures under different atmospheres for different materials and structures.

For ceria it has been demonstrated that heating high surface area material under different atmospheres causes sintering to occur at different temperatures[67]. This was theorised to be as a result of the mechanism by which the material was chemically changed by the different atmospheres[67]. As the ceria is changed in different ways under different atmospheres then it is possible that there will be variations in the surface and catalytic activity after these thermal treatments. Knowing how the catalytic activity will change during sintering under different atmospheres can help with predicting when catalyst destruction could occur.

There is no work in the literature covering the effect of catalytic activity of different ceria nanostructured morphologies after thermal treatment under different atmospheres. There is also a limited amount of comparable data for the effects on different morphologies under different environments during thermal treatment. Data from the literature[68], Table 3.2, shows the change in BET surface area of heating ceria at different temperatures under different environments. The ceria had a starting BET surface area of 115 m^2 g^{-1} after 6 hours of calcination at 673 K under air. This data demonstrates the similarity in surface area change between air and vacuum environments and the facilitation of sintering by the presence of hydrogen.

Table 3.2 – Literature data[68]; BET surface area (m^2 g^{-1}) of ceria heated at 8 K min^{-1} to different temperatures under different atmospheres.

	723 K	**773 K**	**823 K**	**873 K**	**973 K**
Vacuum	133	128	120	99	40
Air	-	112	-	108	32
H_2	105	78	48	13	5

3.2.4 Catalytic activity of ceria

Ceria is a good oxidation catalyst as proven by its use commercially in catalytic convertors where its main function is in the oxidation of carbon monoxide. It has already been stated that through the change to the exposed crystal surface the oxygen storage capacity(OSC) and concentration of oxygen defects can be changed as to effect the catalytic activity. This is reported in the literature, with different surfaces having different activity towards CO oxidation[69]. Surfaces which have better CO adsorption are shown to be more active towards CO oxidation[70] and also those which incorporate oxygen atoms with a higher facile nature[25]. This is expected as the Mars van Krevelen reaction mechanism involves the adsorption of CO and the loss of an oxygen atom to the said CO molecule to form CO_2. The exposed surface can be controlled through control of the morphology at the nanoscale.

Computational modelling has shown the trend of surface energy of exposed crystal planes of ceria follows as such, (111) < (110) < (100) < (210) < (310), from lowest to highest energy[46, 71]. The lowest energy surfaces are the most stable and have been reported to have the lowest catalytic activity. Due to their low energy they are more preferentially exposed[71], the use of nanostructured morphologies therefore allow for greater exposure of higher energy surfaces. The (100) surface is demonstrated to be more active than the (111) or (110) surface for CO oxidation[72]. This is a result of the lower energy required to create oxygen vacancies and as a result of this the higher OSC which leads to higher CO oxidation activity[71, 72].

Results of previous literature studies into the effect of crystallite size and surface area of particulate ceria synthesised under different conditions is shown in Table 3.3[68]. These results suggested an increase in the specific rate with an increase in crystallite size and reduction of surface area, which was theorised to be a result of a higher concentration of the more active (100) surfaces compared to (111), which are formed through the calcination at higher temperatures.

Table 3.3 – Literature data[68] comparing the crystallite size and surface area to the specific rate of CO oxidation using 2% CO 1% O_2 in N_2 with a GHSV of ~2 x 10^5 h^{-1}.

Sample	Calcination temperature / °C	BET surface area / m^2 g^{-1}	Mean crystallite size / nm	Specific rate at 270 °C / mol m^{-2} h^{-1} x 10^3
Precipitation of cerium nitrate with a base. Spray dried at 300 °C	300	100	10	5.9
	700	19	21	6.9
	800	4	35	8.7
Commercial "stabilized ceria" calcined at 500 °C	500	57	11	5.0
	700	26	22	8.3
	800	12	41	9.0

3.3 Titanate Nanotubes

Titanium dioxide (TiO_2), can exist naturally in different crystalline forms such as rutile, anatase or brookite, with rutile being the most stable in the bulk phase and the other two converting to rutile under temperature[73]. The chemical inertness, abundance, low cost, photocatalytic effects and nontoxicity of titania[74], along with its well-studied nature[75], make it a useful material for a diverse range of applications, such as in paints[76], solar cells[77] and even bone implants[78].

Titanium dioxides main use in catalysis is as a photocatalyst due to its photo-active band gap. It is also often used as a support for metal nanoparticles, not only for many of the reasons mentioned previously, but also due to the potential tuning of the band gap that allows for different photocatalytic activity. There is a great deal of literature focused on metal nanoparticles immobilised on titania as catalysts and the photocatlytic nature of TiO_2 is outside the scope of this thesis[74, 79-81].

Titanium dioxide can be used as a starting material for the synthesis of titanate nanotubes. The multi-walled tubular morphology is achieved and stabilised through a unique mechanism of stacked unit cells that can potentially afford extra stability to immobilised metal nanoparticles.

3.3.1 Titanate Nanotube Synthesis

Methods of titanate nanotube formation from TiO_2 starting materials are outlined in Table 3.4.

Table 3.4 - A comparison of template and template free methods for the synthesis of titanium dioxide and titanate nanostructures. A brief description of the reagents and conditions required and the resulting morphologies is given.

Method	Structure	Reagents	Conditions	Ref
Hydrothermal	Titanate Tubes	TiO_2, 15M NaOH	150 °C in autoclave for 72 hours, washed with 0.05M HCl, air dried at 400 °C	[82]
	Titanate Rods	TiO_2, 15M NaOH	170 °C and use the above method	[82]
	Titanate Sheets	TiO_2, 10M NaOH	100 °C in oil bath for 12-48 hours, washed with HCl and water, dried at 70 °C	[83]
	Titanate Wires	TiO_2, 10M KOH	130 °C for 72 hours, washed with deionised water	[84]
	Titanate Tubes	TiO_2, 10M KOH	Heat to 56 °C for 298 hours (20-40% yield)	[85]
	Titanate Tubes	TiO_2, 10M NaOH, 10M KOH	Reflux at 100 °C for 48hours, wash with 0.1M HCl and dry at 120 °C	[86]
Anodic oxidation of Ti	TiO_2 Tubes	Pure Ti foil, H_3PO_4, HF	Ti foil was anodised in H_3PO_4 and HF at 20V with a Pt counter electrode.	[87]
	TiO_2 Tubes	Pure Ti foil, ethylene glycol, 1-butyl-3-methylimidazolium tetraflouroborate (BMIM-BF)	Ti foil was anodised in BMIM-BF in ethylene glycol and water at 5-30V with a Pt counter electrode.	[88]

	TiO_2 Tubes	Pure Ti foil, glycerol, NH_4F	Ti foil was anodised in glycerol and NH_4F at 20-100V with a Pt counter electrode.	[89]
Sol-gel templating	TiO_2 Tubes	TiO_2 sol – (t-butyl orthotitanate, EtOH, diethanolamine, H_2O) ZnO nanorod array template.	Dip coating of the sol on the nanorods, was dried, calcined and washed with acid.	[27]

The mechanism of nanotube growth during the hydrothermal method is attributed to the formation of sheets, which stack and roll to form scrolls, this is further discussed in the following section. That the initial step is the formation of nanosheets is further supported through the fact that at lower temperatures and base concentrations (100 °C, 10 M NaOH) they can be isolated[83]. From the data in Table 3.2 it is also shown that upon heating the reaction to higher temperatures (170 °C) the nanotubes will convert into rod or wire like morphologies.

The electrochemical or anodic oxidation method of synthesising titanate nanotubes results in the formation of tubes with less well-defined and consistent structures. The tubes can end up having poorly defined cavities, and are fixed to the Ti surface upon which they were formed and as such are closed at this end. The tubes are also single-walled and have much larger diameters than in the case of the hydrothermally synthesised method.

The usual, previously mentioned issues with template methods, (cost, time and the removal of the template) apply here with the sol-gel templating method for nanotube synthesis. This method grows the titanate nanotubes on zinc oxide nanorod arrays that are destroyed through acid washings.

3.3.2 Titanate Nanotube Morphology

Titanate nanotubes were first reported by Kasuga[90], who initially referred to them as titania nanotubes. However, the chemical composition of the nanotubes has been under debate for some time but recently it has become accepted that they present the titanate crystal structure[91].

Titanate is a salt containing titanium oxide as $[TiO_3]^{-2}$ or $[TiO_4]^{-4}$ balanced by a metal counter ion, which can also include hydrogen[92]. The titanate structure is proposed to exist as layers of edge sharing octahedral stacked on corner sites[93]. However, these crystals are relatively small making the coherence low resulting in peak broadening in the XRD. This effect is further amplified by the wrapping of the layers around a certain crystal axis during nanotube formation to further increase peak broadening[91].

The titanate nanotubes (TiNT) are more accurately described as scrolls, or as layered tubes. These tubes are suggested to form due to the stacking and subsequent curling of stacked titanate sheets[94]. It has been reported that the mechanism responsible for the 'rolling up' of the sheets is an asymmetric chemical environment that causes difference in surface tension on opposite sides of the sheets[91, 95]. Three methods of scrolling have been proposed, a single sheet rolling in a spiral like fashion[96], multi-layered sheets curling and connecting to form concentric circles at the cross section and multi-layered sheet curling and leaving an open end[91, 95]. The cross-sections of the tubes that would be formed by these methods are shown in Figure 3.2.

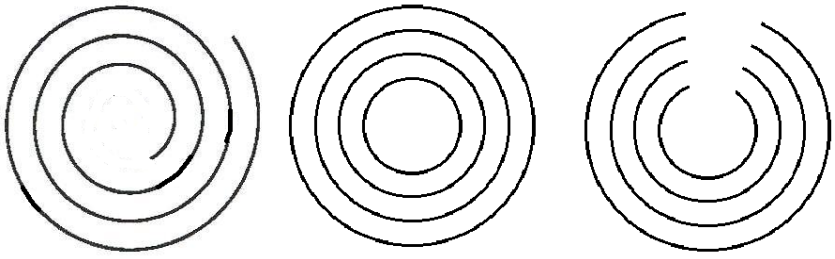

Figure 3.2 – Three proposed mechanisms of titanate nanotube formation. From left to right, the rolling of a single sheet in a spiral fashion, the wrapping and joining of stacked sheets to form full concentric circles and the wrapping of stacked sheets to form an open sided tube.

The curved sheets should be under strain, and in absence of any force maintaining the curved morphology they should theoretically un-scroll to form the stacked layers. The fact that they do not unroll implies that a stabilisation force is in effect. This force has been postulated to be a result of the lining up of titanate unit cells between layers along the radius from the centre of the tube as shown in Figure 3.3[91].

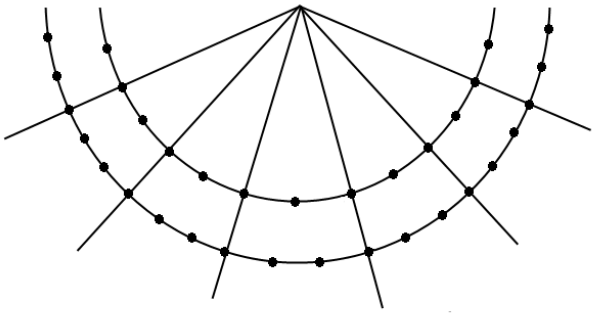

Figure 3.3 – Graphical representation of unit cell alignment in titanate nanotubes stabilising the curvature of the stacked sheets. Unit cells shown as black circles, in the titanate sheets.

3.3.3 Applications of Titanate Nanotubes

Titanate nanotubes possess good electrical conductivity and ion exchange affording them interesting electrochemical potential[91]. By supporting a film of titanate nanotubes or growing them on a surface, this property can be utilised in several applications.

One such application is as a hydrogen sensor, titanate nanotubes have been shown to increase in conductivity by four orders of magnitude when in the presence of 1000 ppm H_2 at 290 °C[41]. Another potential application is as a negative electrode in rechargeable lithium ion batteries due to their ion exchange ratio and good ability to transport lithium ions[82]. Research has also investigated their potential to benefit dye-sensitised solar cells, finding them to afford comparable results to commercial titanium[97].

Alternatively, titanate nanotubes also have the ability to act as a catalyst. Titanate nanotubes role in catalytic studies is often as a support for active metals. It has been suggested that a charge

transfer interaction between the metal and titanate nanotubes can occur which can afford higher catalytic activity[91]. Supported metal nanoparticles can lower the band gap to allow visible light photocatalysis[98] and also to provide different energy levels for redox cascade reactions[11]. Further information regarding the use of titanate nanotubes as a support for metal nanoparticles is discussed and presented in Chapter 6.

Chapter 4

Catalytic Activity of Nanostructured Ceramics

This chapter focuses on ceria nanostructures of particle, rod and cube morphologies and control over the exposed crystal planes and crystallite size through systematic variations in the synthesis conditions. Understanding of the relationship between the different planes and crystallite size and the catalytic activity is undertaken through the use of carbon monoxide oxidation as a model reaction. Full characterisation of titanate nanotubes is also made, though a lack of activity towards carbon monoxide oxidation was observed.

Six nanomorphologies of ceria are synthesised and fully characterised to find a relationship between exposed crystal planes and crystallite size with catalytic activity. One particulate morphology, CeNP, three tubular morphologies, $CeNR_{A/B/C}$ and two cubic morphologies, $CeNC_{A/B,}$ all with different aspect ratios and crystallite size, are synthesised following an alkali hydrothermal method. Systematic variations of the temperature and concentration of NaOH during the synthesis allows for controlled and repeatable growth of the

six nanostructures. A similar hydrothermal route was also used for the growth of titanate nanotubes, TiNT. The nanostructured materials are analysed through TEM, XRD, XPS, TPR, and N_2 adsorption. The oxidation catalytic activity of these nanostructured materials was studied using the CO oxidation reaction. This study provides understanding of the relationship between morphology, crystallite size and exposed crystal planes of the materials with catalytic activity. Comparisons with the literature data is made whenever possible.

4.1 Nanostructured Ceria Synthesis

Ceria nanostructures with particulate, tubular and cubic morphologies are compared catalytically with respect to different aspect ratios and crystallite size. The synthesis of these nanostructures, with distinct and well-defined morphologies, through an alkali hydrothermal method is shown here following methods from the literature[46, 99].

The alkali hydrothermal method is a template free technique that therefore does not require the potentially expensive and complicated step of synthesising a template and uses water as a solvent, a 'green' solvent. It also has potential to be relatively easily scaled up due to the one step process and the convection heating current that would aid with homogeneity in conditions across a large reactor. Furthermore, the hydrothermal method allows for control of the aspect ratio and crystal size of the rods and cubes through controlled changes to the temperature and alkali concentration. The ceria nanostructures synthesised through the alkali hydrothermal method were produced using a 300 mL acid digestion vessel, under the conditions described in Table 4.1, a description of the structures morphology and visual observations are also made. A more detailed synthesis procedure is given in Chapter 2.

Table 4.1 - Conditions of alkali hydrothermal synthesis of nanostructured ceria.

Abbr.	Structure	NaOH conc.	Temperature	Time	Colour
CeNP	Nanoparticles	5 M	70 °C	10 hours	Vibrant yellow
$CeNR_A$	Nanorods	15 M	100 °C	10 hours	Yellow
$CeNR_B$	Nanorods	15 M	70 °C	10 hours	Yellow
$CeNR_C$	Nanorods	10 M	100 °C	10 hours	Yellow
$CeNC_A$	Nanocubes	15 M	180 °C	10 hours	Cream-white
$CeNC_B$	Nanocubes	10 M	180 °C	10 hours	Cream-white

Table 4.1 shows that as the temperature and NaOH concentration is increased there is a shift in morphology from the particles to rods to cubes. The formation of ceria nanostructures through hydrothermal synthesis from cerium nitrate is discussed in the literature.

The lower sodium hydroxide concentrations result in less viscous mediums which are said to facilitate anion exchange from cerium nitrate to the anisotropic cerium(III) hydroxide[66]. Whilst the higher sodium hydroxide concentrations have slower anion exchange and cerium(III) nitrate is oxidised to the isotropic cerium(IV) oxide in one-step. However, 15 M NaOH at 100 °C conditions are shown to result in rods, suggesting the formation of the $Ce(OH)_3$ phase, whilst the 10 M NaOH at 180 °C result in cubes, suggesting a direct conversion of cerium nitrate to CeO_2. This suggests that it is not only viscosity, but also temperature that effects the selection between $Ce(OH)_3$ and CeO_2, with higher temperature facilitating the oxidation directly to CeO_2.

The resulting colour of the nanostructures is typical of a difference in the Ce^{3+} to Ce^{4+} ratio, which are yellow and white respectively. This suggests that the synthesis conditions that cause the metastable $Ce(OH)_3$ phase to form which results in the particle and rod morphologies

still incorporate Ce(III) in their structures after synthesis, to some degree. Whilst the conditions that cause cubic morphologies, which oxidise cerium nitrate directly to ceria, contain a much higher proportion of Ce^{4+} ions. A photograph of ceria nanoparticles, nanorods and nanocubes are shown in Figure 4.1.

Figure 4.1 – Photographs of ceria nanostructures, showing the progression in colour from yellow to white. From left to right the nanostructures are CeNP, $CeNR_A$ and $CeNC_A$.

4.2 Characterisation of Nanostructured Ceria

Various characterisation techniques were employed to analyse the size, morphology and physical and chemical properties of the six ceria nanomorphologies. Techniques employed for these analyses included transmission electron microscopy, X-ray diffraction, low temperature nitrogen adsorption, temperature programmed reduction, X-ray photoelectron-spectroscopy and RAMAN spectroscopy.

The different morphologies were imaged and characterised using transmission electron microscopy (TEM). Images showing a representative sample for the different morphologies, along with a histogram describing distributions of size, measured from all images acquired are shown in Figure 4.2 for the particles, Figure 4.3 for the rods and Figure 4.4 for the cubes.

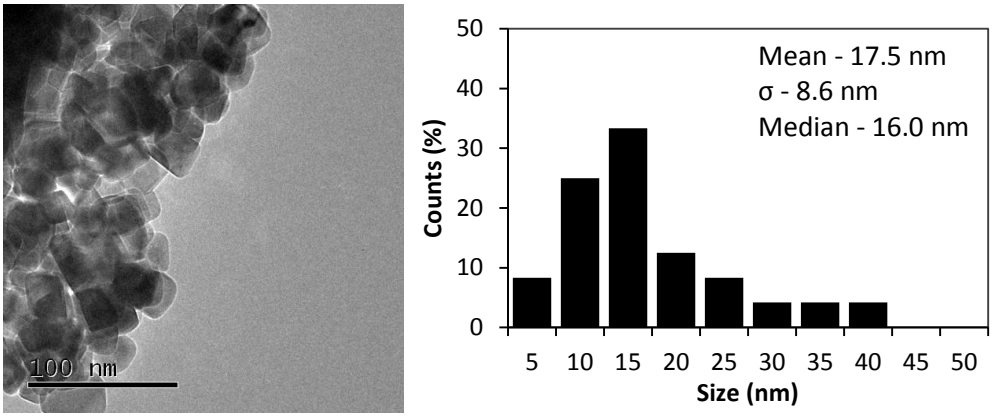

Figure 4.2 - TEM image and histogram of particle diameters of ceria nanoparticles, CeNP. Synthesised at 5 M NaOH and 70 °C with particle diameters measured from several images at different locations.

(a)

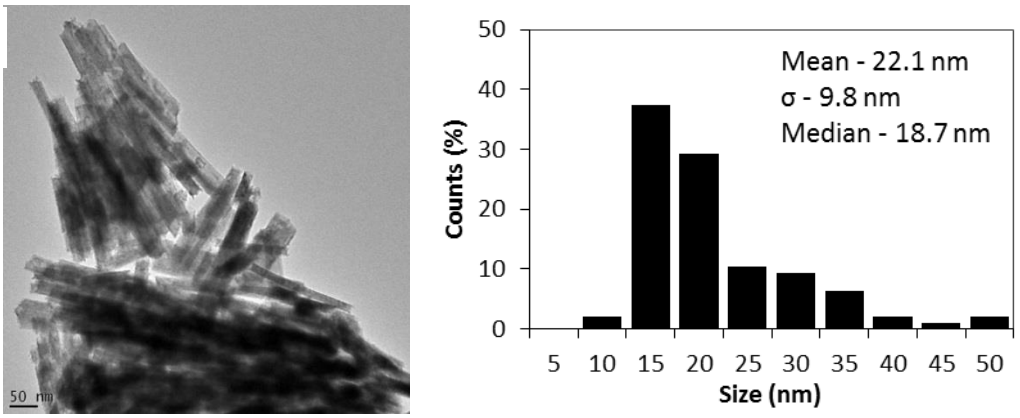

(b)

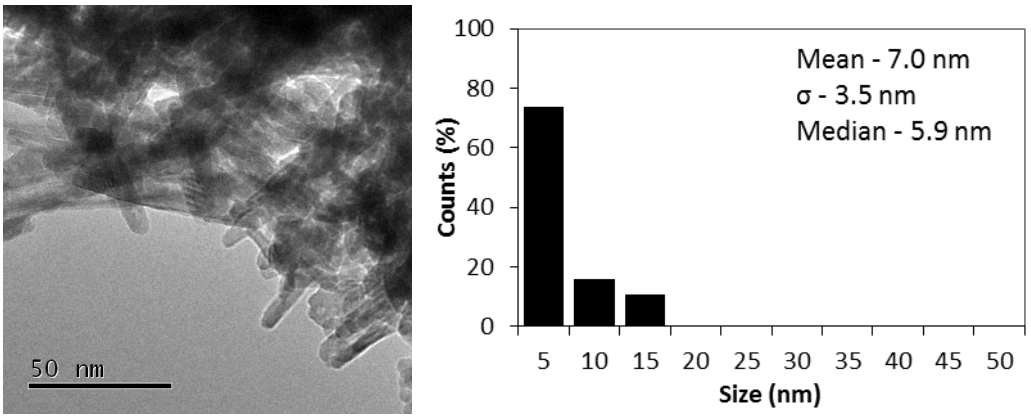

(c)

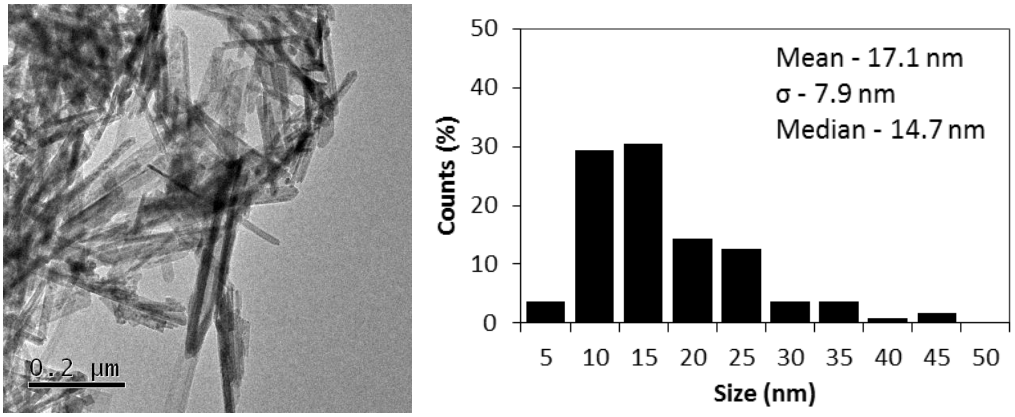

Figure 4.3 – TEM images and histograms of rod diameters for nanorods synthesised under the varying conditions. Rod diameters measured from multiple images at different locations, (a) – $CeNR_A$, 15 M NaOH and 100 °C, (b) – $CeNR_B$, 15 M NaOH and 70 °C, (c) – $CeNR_C$, 10 M NaOH and 100 °C.

Initial observations of the TEM images for the particles and rods show that both structures were synthesised in discreet and well-defined morphologies. The histograms for the size of the rods relate to the diameter; the length cannot be measured in a similar manner due to the overlapping and bundling nature of the rods. This behaviour, along with the restriction on image size at required resolutions results in preferentially making the shorter rods more readily able to view and would give an unreliable representation of length.

The TEM clearly demonstrates that the anisotropic growth leading to rods instead of particles occurs between 5-10 M NaOH and 70-100 °C. There is not a discrete value at which this change occurs and instead it is a gradual change from particles to rods[49].

There is a non-normal distribution of sizes measured from the TEM images. Therefore the median value is used to represent the average size rather than the mean.

The majority of the CeNP sample, displayed in Figure 4.2, consists of particles with a size of 10 to 20 nm, the median diameter being 16 nm. $CeNR_A$, shown in Figure 4.3, have a median diameter value of 18.7 nm and a variety of lengths that range from around 100 nm to over 1 µm in some cases. The $CeNR_B$ sample, Figure 4.3, contains rods of a smaller diameter than $CeNR_A$, with a median value of 5.9 nm and of a shorter length, the majority of sample being made up of rods ~100 nm in length. The $CeNR_C$ sample, Figure 4.3, was observed to share more

similarities with $CeNR_A$ than $CeNR_B$, with a median diameter of 14.7 nm and lengths of 100 nm to around 1 μm.

The $CeNR_A$ and $CeNR_C$ were synthesised under conditions of 15 M NaOH and 100 °C and 10 M NaOH and 100 °C respectively and had more comparable aspect ratios than the $CeNR_B$ synthesised at 15 M NaOH and 70 °C. These observations suggest that temperature plays a more key role in controlling morphology size than NaOH concentration.

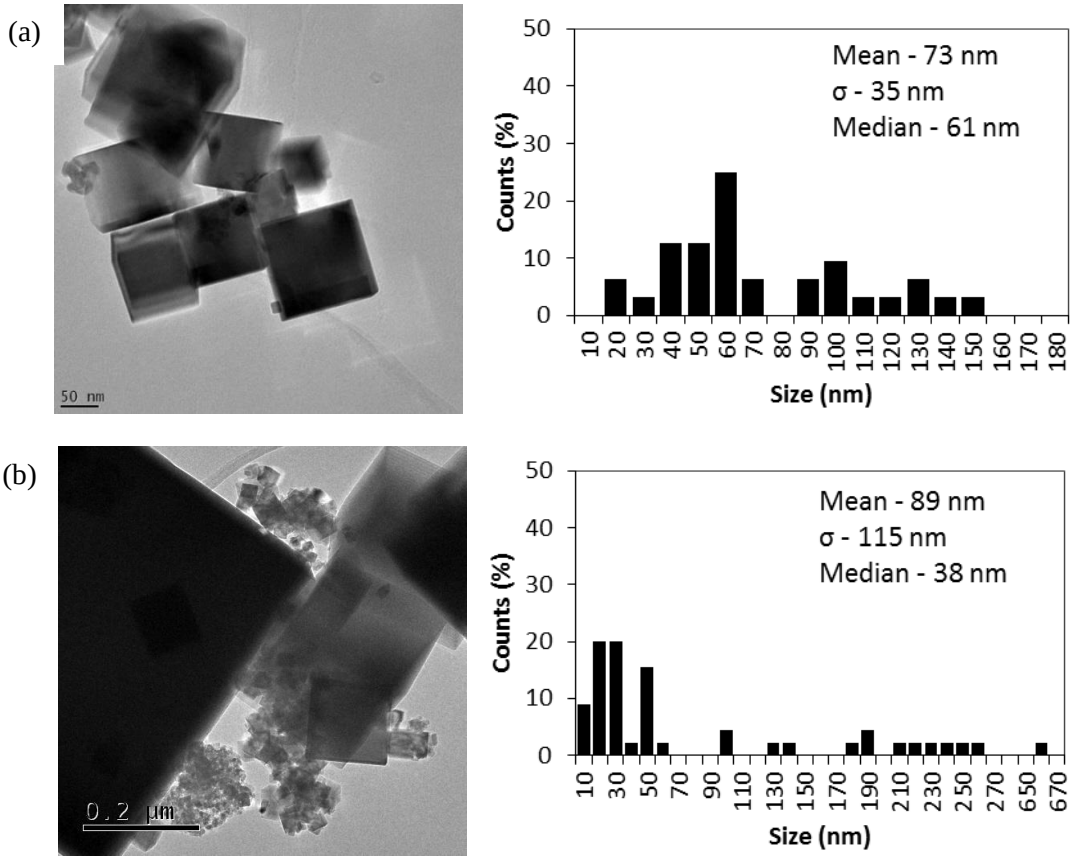

Figure 4.4 - TEM images and histograms of diameters of ceria nanocubes. (a) – $CeNC_A$, 15M NaOH and 180 °C, (b) – $CeNC_B$, 10M NaOH and 180 °C.

The TEM images of the cubes, Figure 4.4, show that the $CeNC_B$ sample has a greater variation in sizes than the $CeNC_A$ material, with the majority of cubes measuring less than 50 nm in diameter, several at around 200 - 250 nm and then the occasional cube at 1 μm or larger. Meanwhile, the variation in sizes of the $CeNC_A$ was much lower, the majority being under 150 nm with a high proportion around 60 nm in diameter.

The ceria is in a cubic morphology at 10 M concentration of NaOH at 180 °C, $CeNC_B$, but a rod like morphology at the same base concentration at 100 °C, $CeNR_C$. This further supports the effect of temperature being more important in forming the CeO_2 phase over $Ce(OH)_3$, from the cerium nitrate and influencing the growth of the cubic structure, than the concentration of base changing the viscosity[66].

The histograms for the cube sizes shown in Figure 4.4 displays these observations more clearly, $CeNC_A$ has a range of sizes from 18 to 150 nm with a median of 61 nm. The $CeNC_B$ sample has a range of diameter varying from 8 to 260 nm with a few cubes found at ~660 nm and a median size of 38 nm.

The XRD of the six ceria nanomorphologies is shown in Figure 4.5 along with the dominant observed crystal planes, labelled on the spectra.

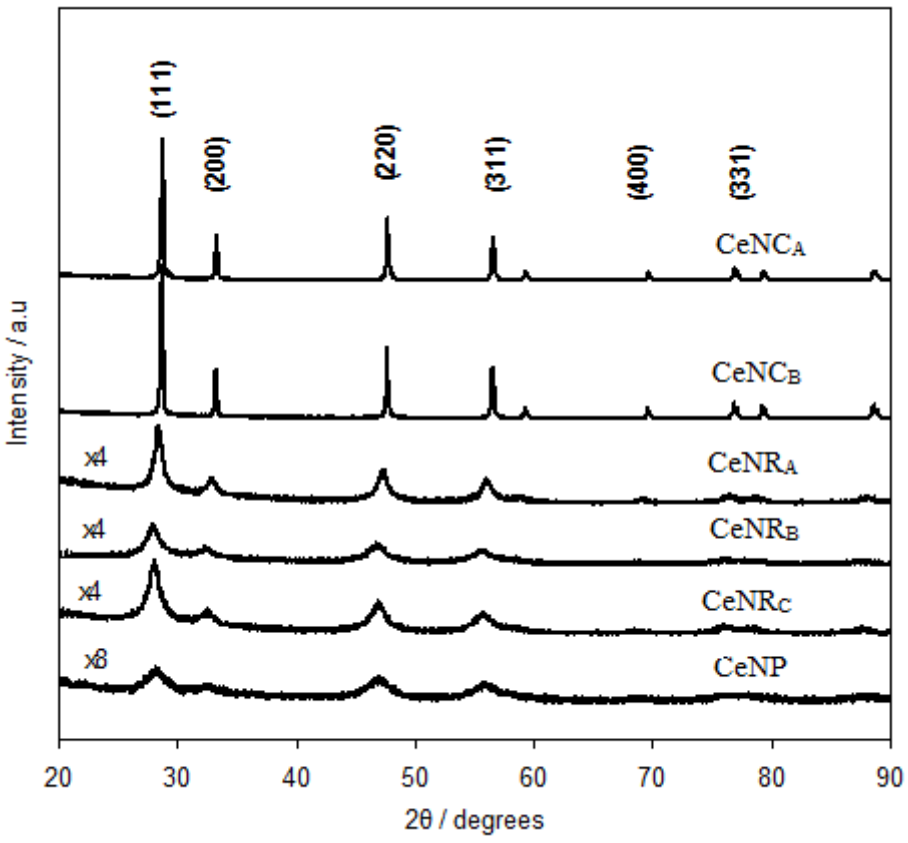

Figure 4.5 - XRD of nanostructured ceria showing the prescence of the (111), (200), (220), (311), (400) and (331) plane in each morphology.

This XRD pattern is typical of cubic fluorite type ceria[100] shown in Figure 4.6. From the XRD spectra, it is possible to determine that all ceria morphologies have the same crystal structure, with the predominant miller indices of (111), (200), (220) and (311) occurring at 2θ angles of 28°, 33°, 47° and 56° respectively. However, the (400) and (331) peaks at 70° and 78° respectively are much smaller and as peak broadening effects become greater it makes them indistinguishable from the base line in the rod and particle morphologies.

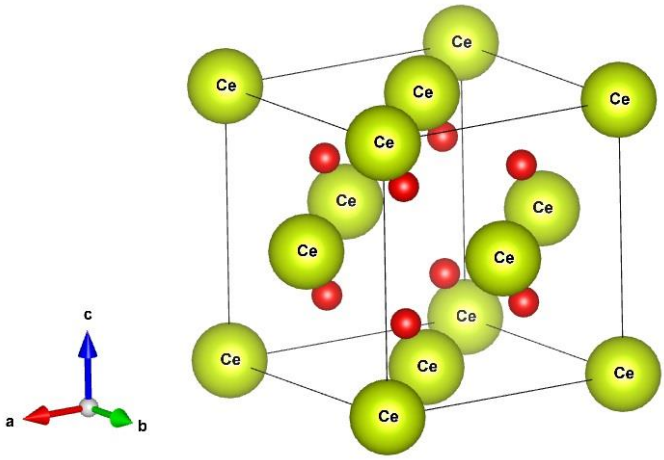

Figure 4.6 – Cubic, fluorite type crystal structure shown for ceria(IV) that is observed by XRD analysis. Yellow atoms correspond to cerium, red atoms correspond to oxygen.

Knowledge of the crystal structure allows for lattice fringe spacings to be measured from the TEM images and a crystalline face assigned. The equation for determining the crystal face of a cubic structure from the measured lattice fringes is shown in Equation 4.1.

$$d_{hkl} = \frac{a}{\sqrt{h^2+k^2+l^2}} \quad \textbf{(4.1)}$$

Where 'd' is the lattice fringe spacing for 'h', 'k' and 'l', the crystal face indices and 'a' is the lattice parameter.

The lattice parameter of cubic fluorite ceria is known in the literature to be 5.40 Å[101]. Although this value is used for lattice space calculations, it is important to note that as crystallite

sizes decreases there is an increase in the content of Ce^{3+}. The ionic radii of Ce^{3+} is significantly larger than Ce^{4+} and as such causes lattice expansion[102]. However, the effect is relatively small and the degree of expansion also varies with the preparation method and environment the ceria is exposed to[101, 103]. Images of the measured lattice spacings for the different morphologies are shown in Figure 4.7 and the assigned the crystal planes from calculations using Equation 4.1 are shown in Table 4.2 along with exposed crystal surfaces denoted in the literature.

Table 4.2 – Lattice spacing measured from TEM images and the assigned Miller indices of the six ceria nano-morphologies.

Nanostructure	**Lattice Spacing / nm**	**Calculated ($h^2 + k^2 + l^2$)**	**Estimated Crystal Planes**	**Dominant Crystal Planes in Literature**	**Ref.**
CeNP	0.32	2.9	(111)	(111) (100)	[25]
$CeNR_A$	0.32	2.9	(111)	(110) (100)	[27]
$CeNR_B$	0.31	3.0	(111)	(110) (100)	[27]
$CeNR_C$	- [a]	-	-	(110) (100)	[27]
$CeNC_A$	0.27	4.0	(200)	(100)	[46]
$CeNC_B$	- [a]	-	-	(100)	[46]

a – No observation of lattice spacing from TEM images was achieved.

Due to the inverse relationship between the spacing, d_{hkl}, and the sum of the reciprocal lattice coordinates squared, ($h^2 + k^2 + l^2$), as the values for h, k and l increase, the spacing becomes smaller and therefore increasingly difficult to measure. In other words, as the sum of the miller index increases, the observed spacing in the TEM images decreases. Therefore it is not possible to make a definitive statement on the identity of all planes purely from lattice fringe measurements. It is only possible to say that the observed planes are present in some of the material. It is also not possible to quantify the degree to which a crystal plane dominates the surface.

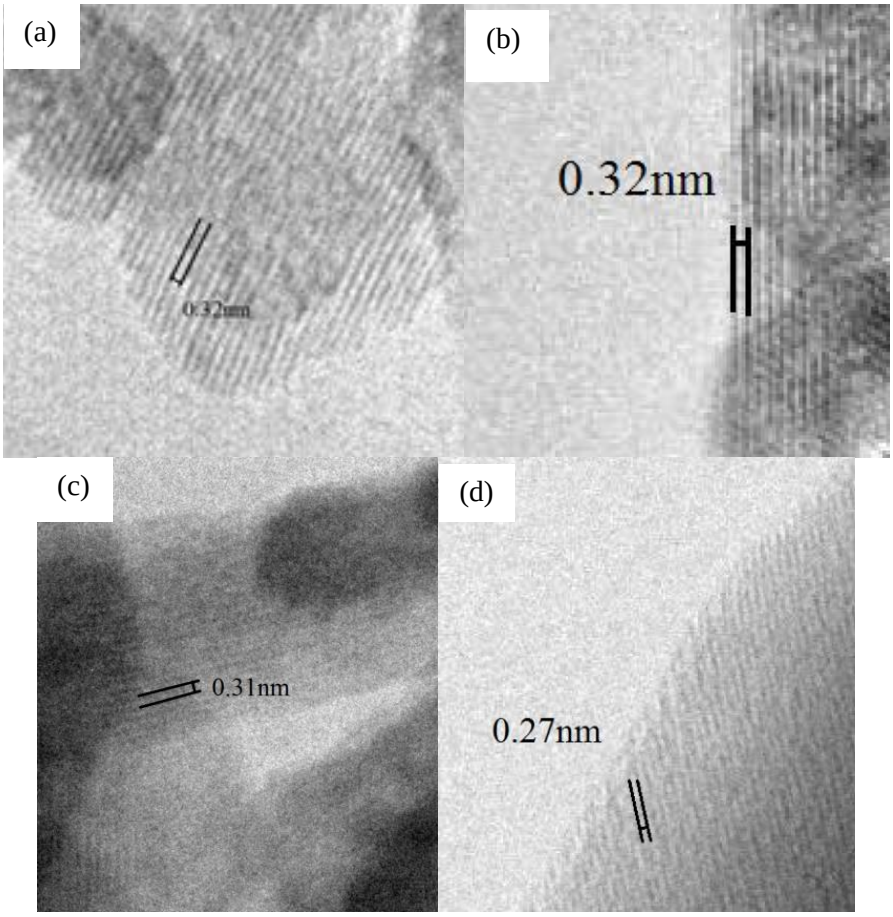

Figure 4.7 – TEM images showing the measured lattice spacings. (a) - CeNP 0.32 nm, (b) - $CeNR_A$ 0.32 nm, (c) - $CeNR_B$ 0.31 nm, (d) - $CeNC_A$ 0.27 nm

The identity of the crystal planes terminating the surface of various ceria nanomorphologies have been measured and calculated in the literature, also reported in Table 4.2. Reported computational simulations for ceria nanoparticles of ~8nm in diameter, calculated that the (111) crystal plane was the dominating surface, with a lower contribution from the (100) crystal plane[25]. The presence of these planes was supported by TEM measurements reported[27] for ceria nanoparticles made through the hydrothermal method and comparable condition to what is reported here. As shown in Table 4.2, the (111) plane is preferential exposed in the ceria nanoparticles in agreement with the literature.

The hydrothermal method and comparable conditions to what is reported here were also used for the synthesis of ceria nanorods, reported in the literature, to possess surfaces dominated by the (110) and (100) planes[27]. Although only the (111) plane was observed here, as discussed, this does not negate the possible presence of any of the (110) plane or (100) planes in any of the

rod morphologies. The (111) plane observed in both the $CeNR_A$ and $CeNR_B$ is not reported in the literature to be a dominating surface. That it was calculated here could suggest a small contribution to the surface or possible error due to the small divergence in lattice spacing required to result in different crystal lattice assignment and the necessity of exact focus which may require a higher resolution TEM.

The literature suggests that the nanocube surfaces are dominated by the (100) plane[46]. Though the cubes synthesised here were only observed to possess the (200) plane, and only in the $CeNC_A$ sample, as with the nanorods samples this does not disqualify the possibility of the (100) presence.

The difference between the literature and measured crystal surfaces can be better understood by comparing the differences in lattice spacing between the various planes. The d-spacing required for the (100), (110), (111) and (200) planes in ceria are shown in Table 4.3.

Table 4.3 – The lattice spacing for cubic fluorite type ceria and the associated miller index.

Miller Crystal Plane	**Lattice spacing / nm**
(100)	0.54
(110)	0.38
(111)	0.31
(200)	0.27

As is demonstrated in Table 4.3, the difference between lattice spacing measurements for different planes is relatively small. As such, a small imperfection in resolution can result in an inaccurately assigned surface. Several sources[25, 27, 46] agree on the identity of the dominating surface terminating crystal planes for the different nanostructures reported here. Many of these literature values agreed with what is calculated from the TEM images, though there were still some surfaces not observed, for reasons discussed above. As such, the reported crystal planes as given in the literature, in Table 4.2, will be used as the dominating crystal surfaces for the different morphologies when discussing the activity with respect to morphology.

XRD peak broadening that was observed in Figure 4.5 is caused by smaller crystallite sizes as a result of non-perfections and random orientation of crystallites resulting in slightly altered Bragg angles. By measuring the width of a peak at half height it is possible to use the Scherrer equation, Equation 4.2, to calculate a good estimate for the average crystallite size.

$$\tau = \frac{K\lambda}{\beta cos\theta} \qquad (\mathbf{4.2})$$

The Scherrer equation, where τ is the mean crystal size, K is a dimensionless shape factor, λ is the X-ray wavelength, β is the full width at half maximum and θ is the Bragg angle.

The calculated crystallite sizes are shown in Table 4.4 along with the median sizes measure from TEM. Assuming that the only source of peak broadening was crystallite size then the Scherrer equation would give an exact value for the average particle size. However, there are other sources of peak broadening, such as inhomogeneity and lattice imperfections that result in a smaller calculated average crystallite size. The difference in measured sizes of nanostructures from TEM and the calculated crystallite sizes from XRD indicate that the morphologies are agglomerations of smaller crystallites.

Low temperature nitrogen adsorption was used to calculate the surface area of the different ceria nanostructures using the BET method. The values are shown in Table 4.4 and the trend between surface area and different morphologies compares well with reported literature values for similar morphologies, surface area increasing with the change from cubes to rods to particles[46, 104]. The adsorption/desorption isotherms of the six morphologies is shown in Figure 4.8. All morphologies appear to have some combination of 'Type IV' and 'Type II' isotherms as denoted by the Brunauer, Deming, Denting, Teller (BDDT) classifications[105], that is typical of the BET adsorption mechanism. The nanocube samples present the most 'Type II' like characteristic, with the steep gradient as the relative pressure approaches 1, typical of macroporous structures. Whilst the hysteresis more notable in the particle and rod morphologies is typical of 'Type IV' suggesting a mesoporosity.

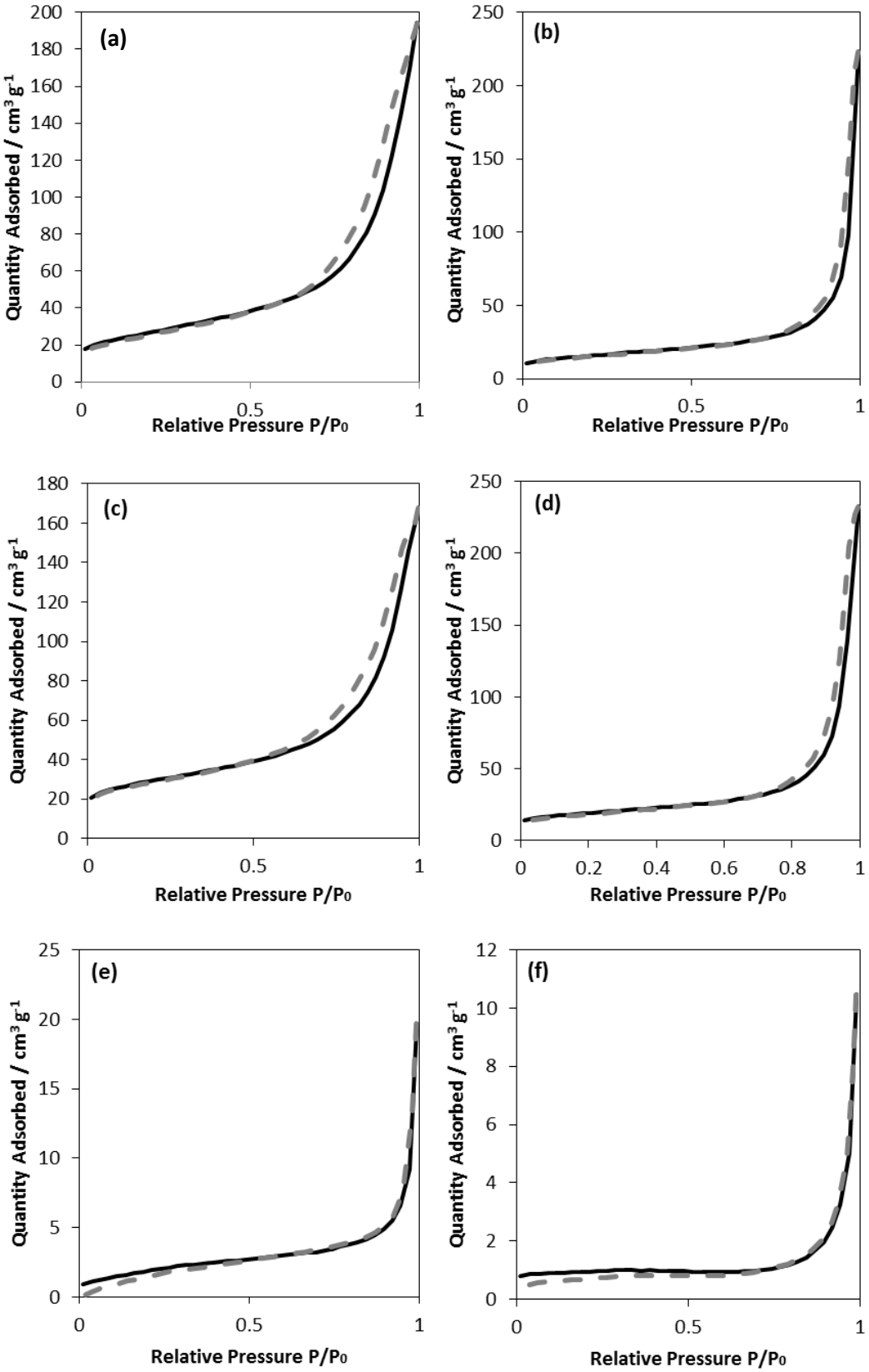

Figure 4.8 – Nitrogen adsorption isotherms of the six nanostructured ceria morphologies showing adsorption denoted by the solid black line and desorption denoted by the dashed grey line. (a) – CeNP (b) – $CeNR_A$ (c) – $CeNR_B$ (d) – $CeNR_C$ (e) – $CeNC_A$ (f) - $CeNC_B$

The surface area of the nanocubes is relatively low resulting in lower accuracy due to limitations of the analytical equipment; as such the values reported in Table 4.4 should be treated as a qualitative description of their lower surface area relative to the rods and particles. The CeNP and $CeNR_B$ which show the highest contribution from a 'Type IV' isotherm, characteristic of mesoporosity, also have the highest surface area and smaller crystallite sizes. This suggests that smaller crystallite sizes allow for a more mesoporous structure and the relationship between crystallite size and surface area supports this observation.

Table 4.4 - Comparison of surface area and particles sizes of the different ceria nanomorphologies.

Nanostructure	**BET Surface area / $m^2\ g^{-1}$**	**XRD crystallite size[a] / nm**	**TEM particle size[b] / nm**
CeNP	89.3 (± 1.4)	4.2	16
$CeNR_A$	53.6 (± 1.1)	9.1	19
$CeNR_B$	98.4 (± 2.1)	5.5	6
$CeNR_C$	63.6 (± 1.4)	6.8	15
$CeNC_A$	6.7 (± 0.2)	35.2	61
$CeNC_B$	2.5 (± 0.1)	37.3	38

a – Mean particles size calculated using Scherrer equation from XRD from (111) peak.
b – Median particle size measured from TEM images.

The difference between TEM and XRD particle and crystallite size is due to the morphologies, particulate, tubular and cubic, being comprised of agglomerates of the smaller crystallites. Comparing the surface areas calculated from the nitrogen adsorption data with the crystallite sizes, there appears to be a trend of increasing surface area with decreasing crystallite size. This is more clearly shown in Figure 4.9.

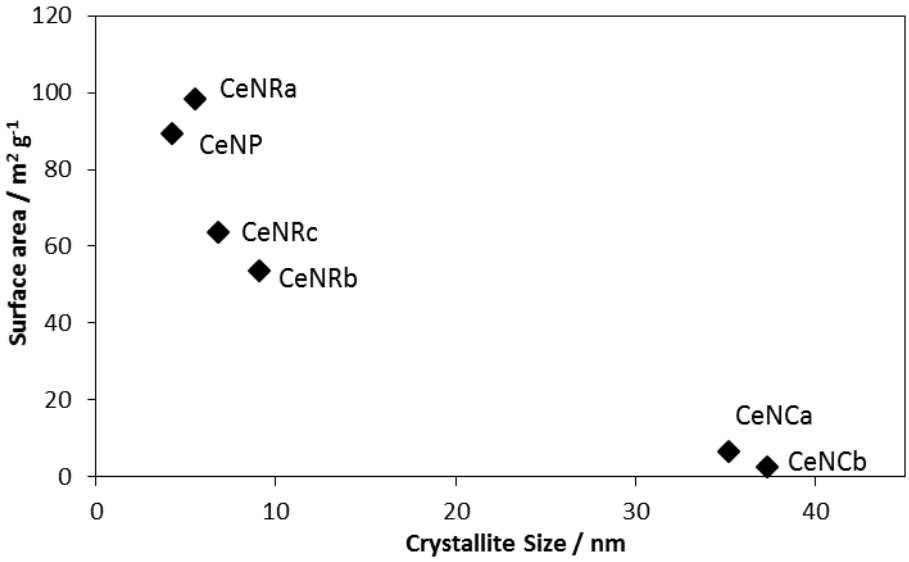

Figure 4.9 – The surface area as a function of crystallite size for ceria nanostructures. Crystallite size calculated using the Scherrer equation from the XRD data, (111) peak.

In general, the surface area increases as the crystallite size decreases. However, the relationship between crystallite size and surface area in Figure 4.9 shows that size of the nanostructure is not the only contribution to surface area. The increase in surface area is known to be mostly related to porosity, suggesting that smaller crystallites allow for more porous structures.

The Raman spectra of ceria nanostructures were obtained at 532 nm wavelength, between 100 and 1300 cm^{-1}. The resulting spectra was dominated by an intense peak at around 400 to 500 cm^{-1} for each structure with a maximum at 462 cm^{-1}. This peak is a characteristic of ceria and due to the strong F_{2g} triple degenerate mode of fluorite type ceria[106]. Figure 4.10 shows the Raman spectra for the three tubular and two cubic morphologies. There was a second, much less intense peak observed at 592 cm^{-1} that is a result of the defect-induced mode[107, 108]. The 532 nm spectra showing the peaks at 462 and 592 cm^{-1} is shown in Figure 4.11.

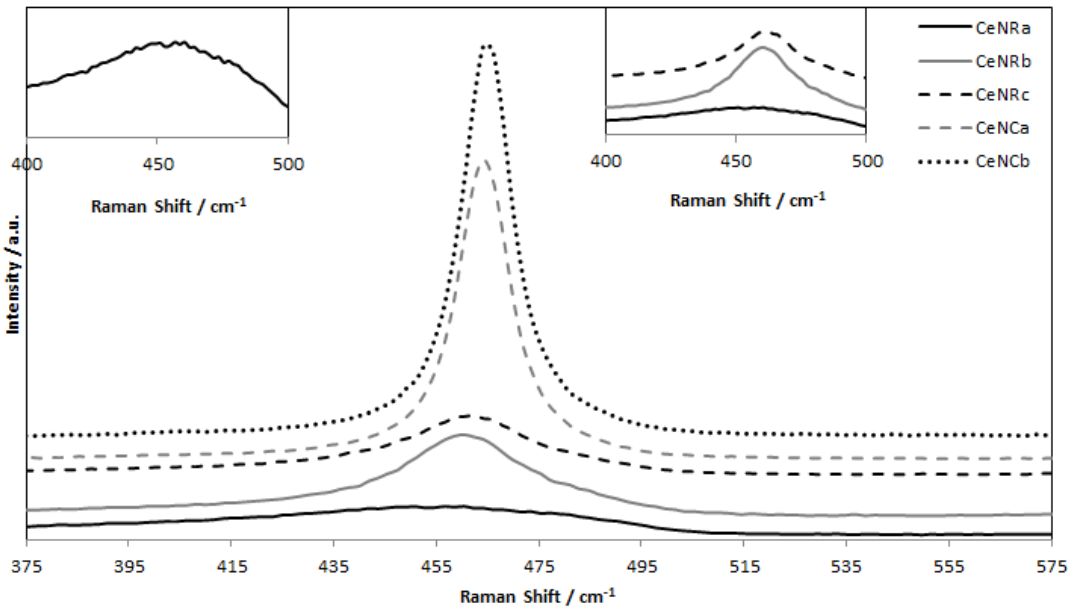

Figure 4.10 – Raman spectra of $CeNR_A$, $CeNR_B$, $CeNR_C$, $CeNC_A$ and $CeNC_B$. Raman shift at 532 nm wavelengths.

The width of the Raman peak is as a result of imperfections to the crystal structure causing small changes in the inelastic scattering energy and has been reported to be inversely proportional to crystallite size due to phonon confinement[109] resulting in the breakdown of selection rules with reducing crystallite size[110] . The full width at half maximum (FWHM) of the peaks in the Raman spectra are shown in Table 4.5.

Table 4.5 - The full width at half maximum (FWHM) of the RAMAN spectra at 532 nm for the ceria nanostructures.

Morphology	**FWHM/ cm^{-1}**
$CeNR_A$	73
$CeNR_B$	30
$CeNR_C$	30
$CeNC_A$	12
$CeNC_B$	12

The FWHM of the Raman spectra shows consistent measurements between the two light sources. It also demonstrates a general inverse relationship between crystallite sizes calculated

using the XRD data and FWHM observed from the Raman spectra. With the rod-like morphologies having smaller crystallites and broader peaks compared to the cubic morphologies. However, the $CeNR_A$ morphology appears to have a broader than expected peak. The additional broadening could suggest a higher concentration of oxygen vacancies, as this has been reported to possibly contribute to peak broadening[111]. This is reported to be a result of a higher contribution of the Ce^{3+}, with increasing oxygen vacancies, changing the Ce-O bond length[111].

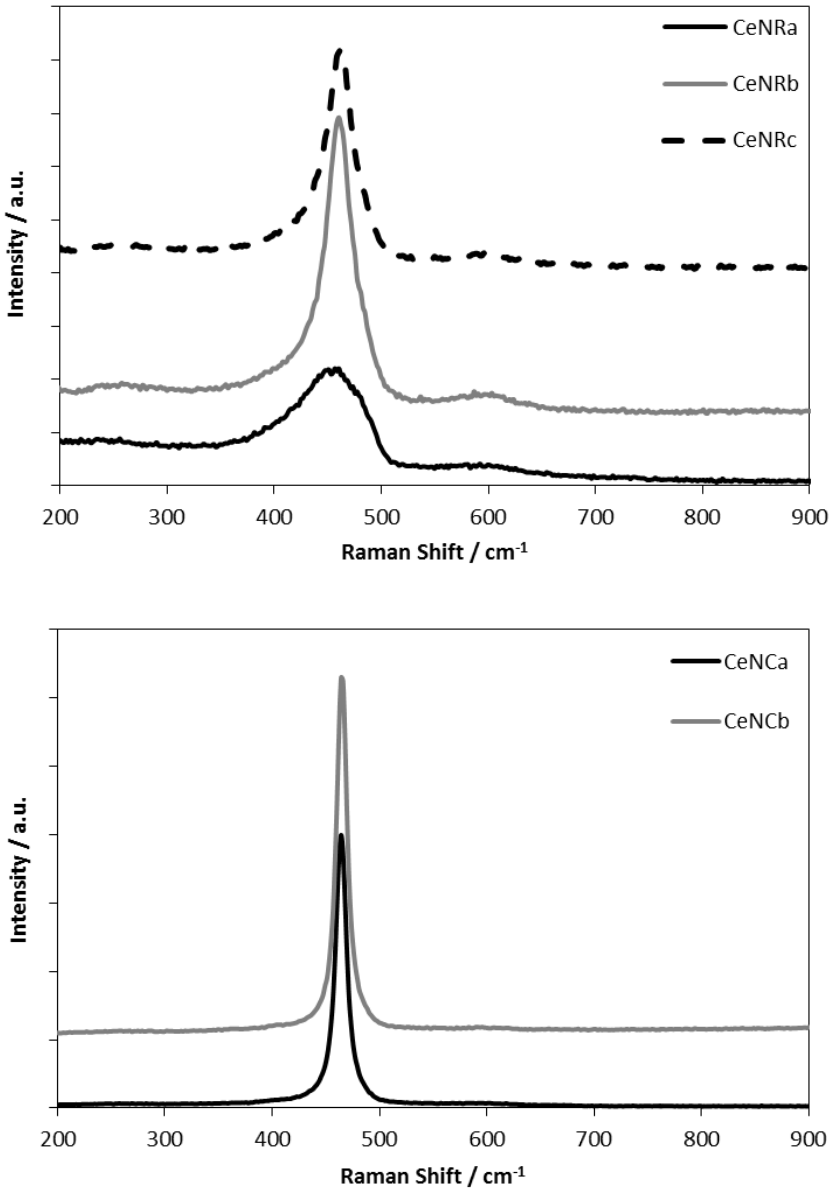

Figure 4.11 - Raman spectra of $CeNR_A$, $CeNR_B$, $CeNR_C$, $CeNC_A$ and $CeNC_B$ with a Raman shift at 532 nm wavelength.

The peak at 592 cm^{-1} is more visible in the rod-like morphologies than the cubic morphologies. A ratio of the intensities of the 592 cm^{-1} and 462 cm^{-1} peak gives an approximation of the relative oxygen vacancy concentration[107]. These values are calculated and shown in Table 4.6. From these values, it is possible to observe that the rod-like morphologies have a greater oxygen vacancy concentration compared to the cubic morphologies. It is also apparent that the $CeNR_A$ morphology has a higher concentration of oxygen vacancies compared to the other rod-like morphologies, supporting the results of the FWHM, which also suggests this to be the case.

Table 4.6 – Relative intensities of the two peaks in the Raman spectra. Observed at 462 and 592 cm^{-1} in the 532 nm wavelength spectra.

Morphology	**I_{592}/I_{462}[a]**
$CeNR_A$	0.045
$CeNR_B$	0.026
$CeNR_C$	0.021
$CeNC_A$	0.009
$CeNC_B$	0.007

a – Relative intensity of 592 cm^{-1} and 462 cm^{-1} peaks

The ceria nanostructure samples were characterised by temperature programmed reduction (TPR) to 1000 °C from ambient under a flow of hydrogen as described in the experimental section. Through monitoring the thermal conductivity of the outlet gases, the hydrogen consumption can be quantified as the material is reduced. It is important to note that the signal can be affected by the presence of any molecules adsorbed to the material or formed during the reduction process that are released during the analysis. The TPR of the ceria particles and rod morphologies are shown in Figure 4.12 and in Figure 4.13 for the cubic morphologies. As hydrogen is consumed the signal increases, so that peaks correspond to hydrogen consumption implying the reduction of ceria at these temperatures.

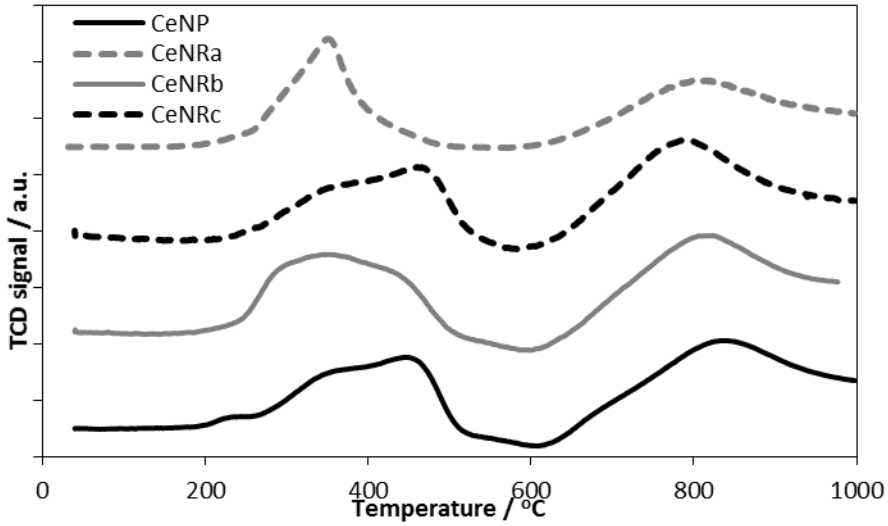

Figure 4.12 – Temperature programmed reduction of the nanoparticle and three nanorods. Run between ambient and 1000 °C under 30 mL min^{-1} 5%H_2 in Ar and normalised for weight.

The TPR profiles of the ceria nanoparticles and nanorods, Figure 4.12, show two well distinguished regions. The first in the 200 to 550 °C temperature range that appears to consist of several overlapped peaks. The second region shows a single broad peak with a maximum at around 800 °C for all rod and particle morphologies.

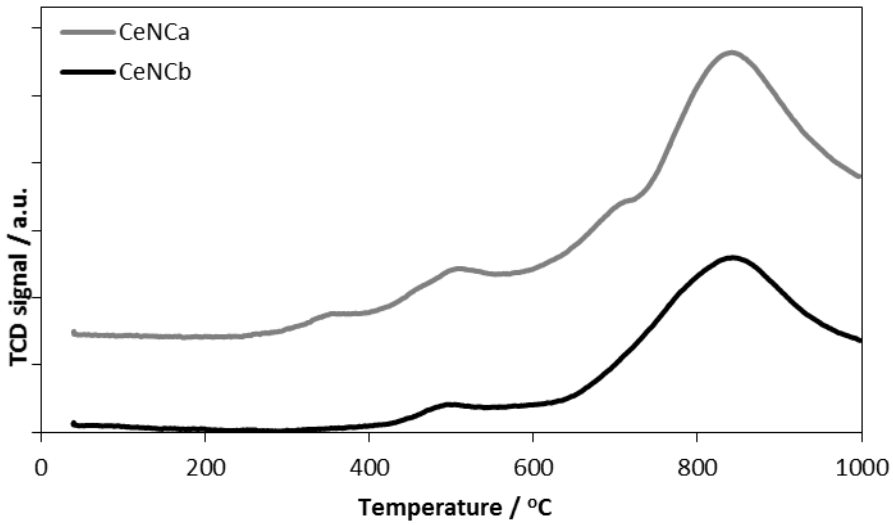

Figure 4.13 – Temperature programmed reduction of the two nanocube samples. Run between ambient and 1000 °C under 30 mL min^{-1} 5%H_2 in Ar and normalised for weight.

The TPR of the ceria nanocube samples is greatly dominated by the peak observed at temperatures over 600 °C with a maximum of around 850 °C. The peaks between 200 and 550 °C observed for the particles and rods are much smaller and appear to overlap with the tail of the higher temperature peak.

The mechanism for the reduction of ceria occurs in two steps[67, 112]. Initially the reduction of the surface occurs with the surface oxygen combining with hydrogen to form water. Then at a higher temperature there is sufficient energy to allow a migration of bulk oxygen to the surface, which undergoes reduction to water resulting in the full reduction of the ceria. This two reduction step process is observed in the TPR as the two regions, between 200 and 550 °C and over 600 °C. The lower temperatures peaks, below 550 °C correspond to the surface oxygen and the larger and broader peak above this temperature, corresponds to the bulk oxygen content.

The non-uniform shapes of the lower temperature peaks could be ascribed to different crystal planes at the surface of ceria reducing at different temperatures. This would be due to the variance in energy levels of forming surface oxygen vacancies on different miller planes. This multi-peak behaviour is observed in all morphologies except for the $CeNR_A$ and $CeNC_B$. This could suggest that these two have a single crystal plane that dominates most of the surface.

As mentioned, the two peaks corresponding to the surface and bulk reductions so that by integrating the peaks it is possible to quantify the ratio between surface and bulk oxygen, Table 4.7.

Table 4.7 - Relative concentration of surface and bulk oxygen for the six ceria nanostructures calculated from hydrogen consumption.

Morphology	**H consumption / µmol g^{-1}**	**Surface [O] %**	**H consumption / µmol g^{-1}**	**Bulk [O] %**
CeNP	8.2	38.6	13.0	61.4
$CeNR_A$	11.2	41.6	15.9	58.4
$CeNR_B$	8.0	40.4	11.9	59.6
$CeNR_C$	7.1	37.2	12.0	62.8
$CeNC_A$	2.6	13.5	16.8	86.5
$CeNC_B$	1.2	7.0	16.6	93.0

The ratios of surface to bulk oxygen for the different ceria morphologies shows the particle and rod morphologies to have significantly more surface oxygen relative to bulk than the cube morphologies. The difference in surface to oxygen content between the particle and three rod morphologies is slight, the $CeNR_A$ having the highest ratio of surface oxygen, followed by $CeNR_B$. The concentration of surface oxygen appears to increase as the surface area increases, as would be expected. However, the $CeNR_B$ material does not follow this trend as it presents the highest surface area and yet does not show a higher concentration of surface oxygen relative to $CeNR_A$ or $CeNR_C$. This could indicate a different proportion of surface dominating crystal planes, with a higher ratio of (110) to (111) present in the case of $CeNR_B$ as suggested by the lower surface oxygen content.

X-ray photoelectron spectroscopy (XPS) spectra were obtained for the nanostructured ceria morphologies, through collaboration with Dr Garcia of the University of Zaragoza. The XPS spectra were obtained for both Ce3d, Figure 4.14, and O1s, Figure 4.15, to determine the average cerium oxidation state and the relative ratio of surface to bulk oxygen content.

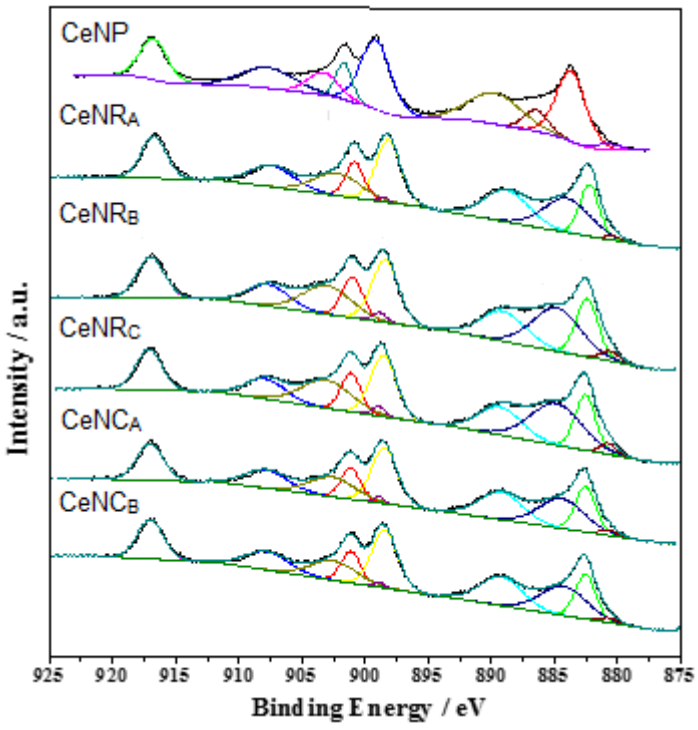

Figure 4.14 – Ce3d XPS spectra of ceria nanomorphologies.

Initial observations of the deconvoluted peaks of the Ce3d XPS spectra, Figure 4.14, show no discernable difference between the peaks across the different structures. All spectra were comprised of two multiplets (V and U) corresponding to the Ce $3d_{5/2}$ and Ce $3d_{3/2}$ core holes respectively[113] observed at binding energies of 882.5 and 901.1 eV. Four satellite peaks of the U multiplet, due to ionisation, were observed at energies of 898.5, 898.5, 907.8 and 917.1 eV and are associated with Ce^{4+}. The remaining peaks in the Ce3d spectra are associated with Ce^{3+} and are observed at around 880.7, 884.4, 898.8 and 902.6 eV. The contribution of Ce^{3+} for the morphologies, calculated from the Ce3d spectra are reported in Table 4.8; however, it is important to note that XPS is a surface technique that extends only to a depth of ~50-70 Angstroms which prevents direct comparisons between the larger cubes and the particles/rods. The interpretation of the XPS data were carried out by researchers at the University of Zaragoza and used in this thesis to further understand the effect of morphology on the physical and chemical properties of nanostructured ceria.

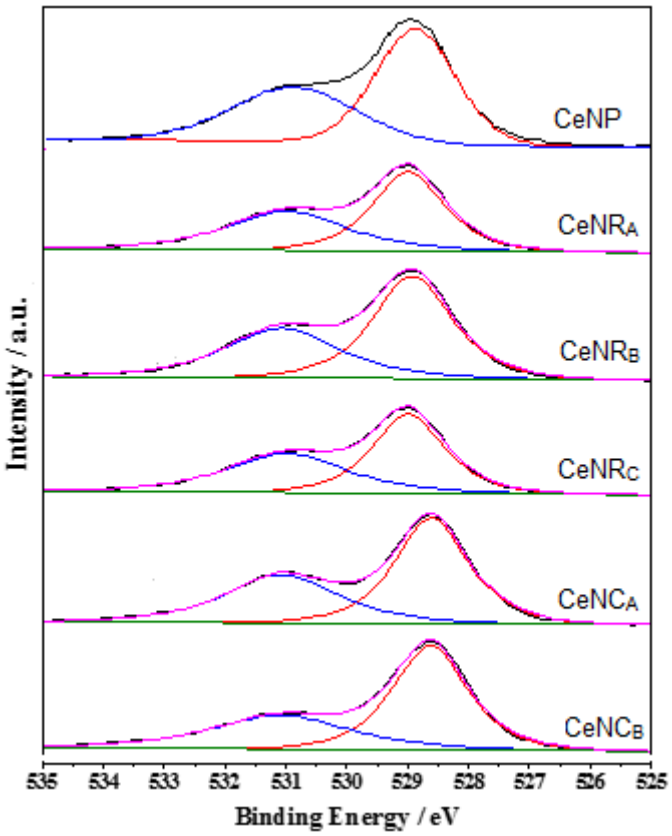

Figure 4.15 – O1s XPS spectra of ceria nanomorphologies.

The O1s XPS spectra for the ceria morphologies is shown in Figure 4.15 and after Gaussian curve fitting, displays two different energy bands. The lower energy peak, 528-529 eV, is ascribed to lattice oxygen, O_α. Whilst the higher energy peak, 530-533 eV, is commonly assigned to oxygen atoms in higher energy environments, O_β, such as surface adsorbed oxygen, hydroxyl groups or water contamination[114]. As there are no hydroxyl groups present and samples were prepared to eliminate the presence of water, then by taking a ratio of O_β/O_α an estimate of the bulk to surface oxygen content ratio can be calculated. The estimated surface oxygen from the O1s XPS is shown, in Table 4.8, alongside the surface oxygen content previously estimated from TPR analysis to give a comparison between the two methods.

Table 4.8 –Ratio of surface to bulk oxygen, calculated from TPR and XPS data, shown alongside the percentage surface content of Ce^{3+} relative to Ce^{4+} calculated from Ce3d.

Morphology	**O1s XPS (O_β/O_α)**	**TPR (O surf/bulk)**	**Ce^{3+} content from Ce3d XPS / %**
CeNP	0.72	0.63	14
$CeNR_A$	0.85	0.71	29
$CeNR_B$	0.69	0.68	35
$CeNR_C$	0.59	0.59	37
$CeNC_A$	0.69	0.16	28
$CeNC_B$	0.61	0.08	29

Comparing the ratio of surface to bulk oxygen content estimated from the XPS and TPR data in Table 4.8 a relatively good agreement is obtained for the particles and rods using both techniques. However, the content of surface oxygen calculated for $CeNC_A$ from the XPS is significantly higher than what was observed for the TPR. The low surface area for $CeNC_A$ suggests that it would indeed have lower surface oxygen content than calculated through XPS, similar to what is calculated from TPR data. An explanation for this is that XPS is only capable of penetrating ~50-70 Angstroms into the surface and as such is not giving an accurate bulk oxygen measurement for the much larger cubic structures. The content of Ce^{3+} of the morphologies is given in Table 4.8, and suggests the content to increase with the morphological trend, particles < cubes < rods, with morphologies possessing higher O_β/O_α ratio having a lower Ce^{3+} content. However, as stated the cubes are not fully penetrated, compared to the rods and particles and as such the conclusion that can be drawn from this is that rods possess a higher content of Ce^{3+} relative to particles and that it decreases with increasing surface to bulk oxygen ratio.

The particles and rods have been shown through TPR studies to have a higher content of surface oxygen to bulk oxygen, relative to cubes. Of the particles and rods, it is the rods that are shown to have a higher surface oxygen contents. It has been reported that the (100) and (110) surfaces more readily form oxygen vacancies[33] and that these surfaces are present in ceria nanorods[27]. Although these surfaces were not observed in the TEM, image resolution was not

high enough to conclude its absence. XPS results supported the trends observed in the TPR between the particles and rods for surface to bulk oxygen content and gave further information regarding the content of reduced Ce^{3+} in the surface of the morphologies and had an inverse trend (for each morphology separately) with the O_β/O_α ratio from the O 1s spectra, demonstrating a relationship between Ce^{3+} content and more facile oxygen ions.

4.3 Catalytic Activity of Nanostructured Ceria

Ceria is widely used in catalytic processes, specifically in oxidative reactions due to its high oxygen storage capacity (OSC). It is used commercially in catalytic convertors; the principal reaction where it plays a key role is the oxidation of CO to CO_2. It is this reaction that has often been used to compare the catalytic activity of different catalysts[115]. Due to the simple stoichiometry and limit on competing pathways, despite its complicated mechanism, it is often treated as a model reaction to assess catalytic activity and so shall be treated as such here.

In this section, the different properties of the six ceria nanostructures, described in the previous section, and how they affect the catalytic activity is investigated. This is performed through the use of continuous reactor equipped with a temperature controlled oven which allows for the study of their oxidative activity in the range of 30 to 600 °C. The CO conversions of ceria particles rods and cubes are shown in Figure 4.16. By monitoring the CO concentration of the outlet of the reactor, the rate of CO conversion can be calculated. A more detailed outline of the experimental procedures, analysis methods, interpretation of data and preliminary tests are outlined in Chapter 2.

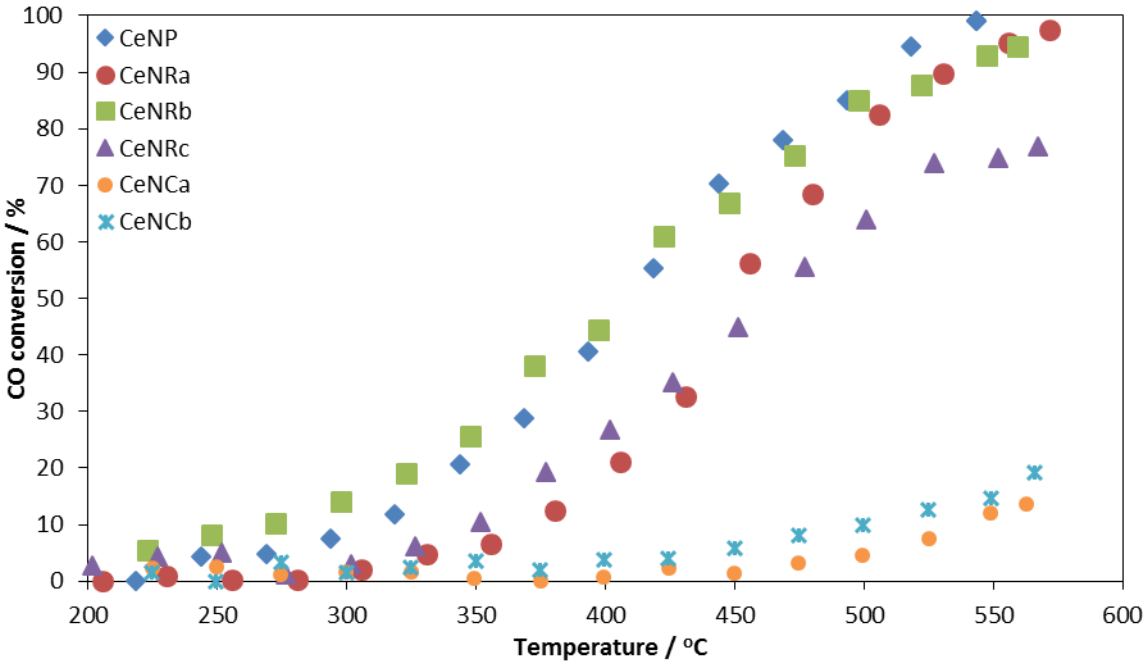

Figure 4.16 - CO conversion of nanostructured ceria particles rods and cubes as a function of temperature. Running at 50 mL min^{-1} of 2000 ppm CO, 2000 ppm O_2 in N_2 using 15mg of catalyst with a GHSV of 750 hour^{-1}.

The catalytic data shows that the particles and three rod ceria morphologies present a similar activity towards CO oxidation per mass of catalyst. Initial activity starts at around 250 °C, 325 °C, 225 °C and 325 °C for the CeNP, $CeNR_A$, $CeNR_B$ and $CeNR_C$ respectively. They all reach ~85% conversion at 500 °C except for the $CeNR_C$ which appear to have the lowest activity by mass of catalyst. However, this data does not consider the differences in surface area, where the reaction takes place.

Both ceria nanocube morphologies have much lower activity compared to the particles and rods, at similar temperatures, no activity being observed until around 350 to 400 °C. The $CeNC_A$ appear to have the lower conversion, but only by a small margin. The lower activity of the cubes relative to particles and rods is likely due to the significantly lower surface area. To further investigate the relative activity of surfaces between the particles, rods and cubes, the catalytic activity adjusted for surface area is compared in Table 4.9.

The temperatures of 10% and 50% conversion, where applicable, along with the turn over frequencies per mass and surface area of catalyst, at 350 °C for particles and rods and 525 °C

for cubes, are shown in Table 4.9. The BET calculated surface area is also shown for comparison.

Table 4.9 – Comparison of activity and surface area for ceria nanostructures. The temperatures of 10% conversion ($T_{10\%}$) and 50% conversion ($T_{50\%}$) and the turn over frequencies (TOF) by weight and surface area at 350 °C for the ceria particles and rods and 525 °C for cubes. The surface areas are also shown for comparison.

Morphology	**$T_{10\%}$ °C**	**$T_{50\%}$ °C**	**Product formation**		**BET Surface area / m^2 g^{-1}**
			g CO_2 kg cat^{-1} h^{-1}	**g CO_2 m^{-2} h^{-1} x10^2**	
			At 350 °C		
CeNP	318	410	15.2	17.0	89.3 (± 1.4)
$CeNR_A$	365	465	4.9	9.1	53.6 (± 1.1)
$CeNR_B$	275	409	17.0	17.3	98.4 (± 2.1)
$CeNR_C$	349	462	8.0	12.3	63.6 (± 1.4)
			At 525 °C		
$CeNC_A$	535	N/A	5,547	82.3	6.7 (± 0.2)
$CeNC_B$	499	N/A	7,681	307	2.5 (± 0.1)

It is possible to observe that there is a trend between $T_{10\%}$ and BET surface area and also between the TOF in terms of mass and surface area for the particles and rods. As conversion is known to increase with increasing quantity of catalyst and the surface is the catalytically active site, this is intuitive. Figure 4.17 demonstrates a trend between the temperature of 10% conversion of CO in the CO oxidation reaction and the temperature at which reduction begins, as shown in the TPR profiles of Figure 4.12 and Figure 4.13. This is due to the formation of oxygen vacancies being the rate determining step in CO oxidation and the mechanism by which reduction of ceria takes place.

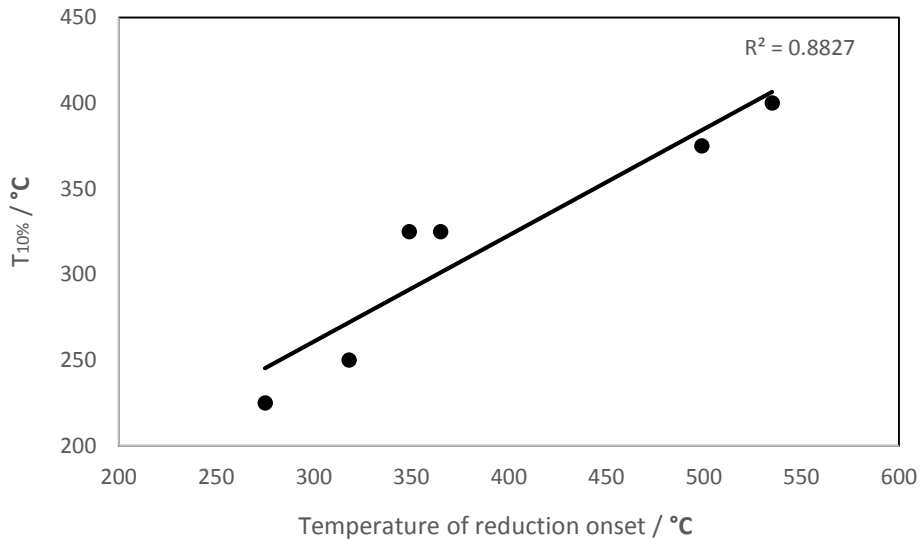

Figure 4.17 – Temperature of 10% conversion of CO in CO oxidation reaction against temperature of initial reduction of the six ceria nanostructures.

Each of the reaction curves was used to calculate the initial rate of reaction, with respect to surface area, for the data below 20% conversion shown in Figure 4.18. Further information regarding the processing of this data is given in Chapter 2.

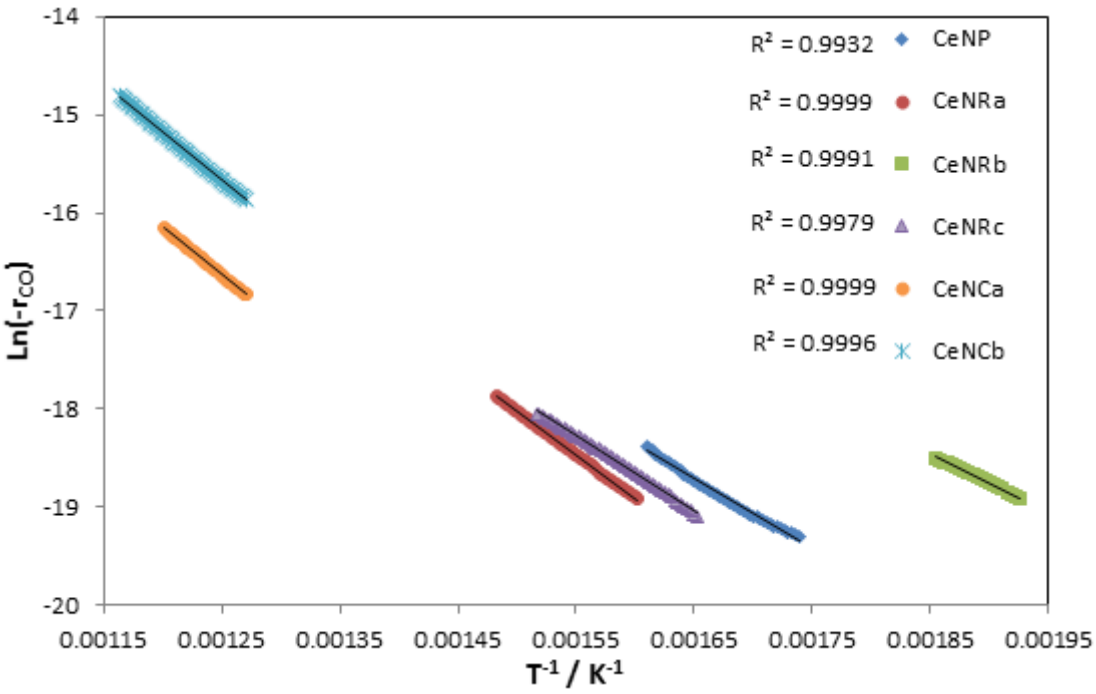

Figure 4.18 – Arrhenius plot of the CO oxidation reaction for the six ceria nanomorphologies using mol(CO) m^2 s^{-1} to calculate the rate.

The Arrhenius plot of the six ceria nanostructures shows that for the region below 20% conversion there is a good linear relationship. Moving up the y-axis signifies an increase in rate and moving right on the x-axis represents a lower temperature. Therefore the $CeNR_B$ can be observed to be the most active catalyst in the sense that they have the fastest rate at the lowest temperature. The activation energies calculated from the gradient of the data in Figure 4.18 for the ceria morphologies are shown versus crystallite size in Figure 4.19.

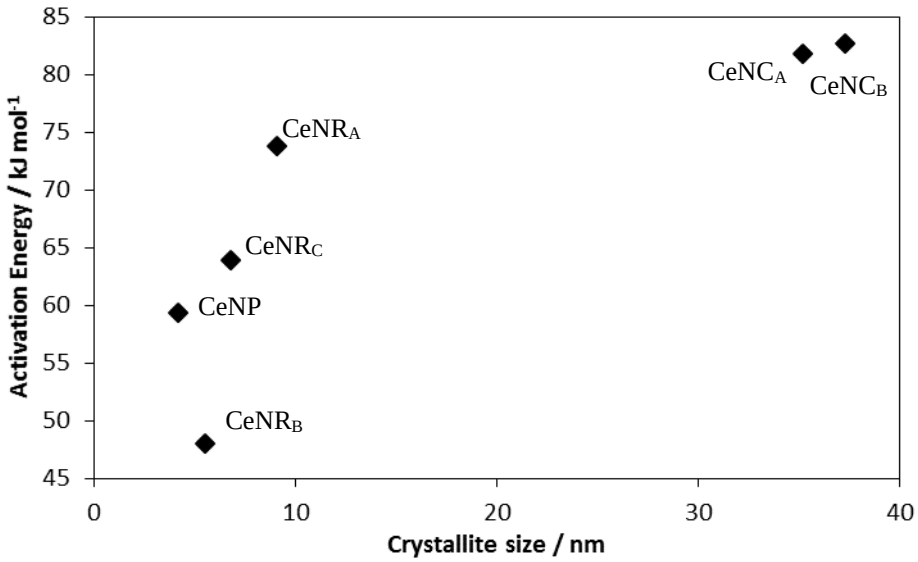

Figure 4.19 – Activation energies for the six ceria nanomorphologies as a function of crystallite size. Measured from the CO oxidation reaction below 20% conversion performed under 2000 ppm CO, 2000ppm O_2 in N_2 with a GHSV of 750 hour^{-1}, crystallite size calculated from XRD peak broadening.

The activation energies calculated from the rate adjusted for surface area fall with decreasing crystallite size and therefore increasing surface area, suggesting, as predicted, that the surfaces present different catalytic activity. During the CO oxidation reaction, the adsorption of CO to the ceria surface and the formation of oxygen vacancies in the oxidation of CO step, are relative to the energy of the ceria surface. A higher surface energy has been reported to be better able to facilitate the creations of oxygen vacancies and as such allow the CO oxidation reaction to proceed more readily[46]. The trend in surface energy of ceria surface terminating

crystal planes has been calculated in the literature to follow (100) > (110) > (111)[33, 116]. This would suggest that the rods with the (110) and (100) and cubes with the (100) dominated surfaces, would be more active towards CO oxidation than the particles with their (111) and (100) dominated surface. That the particles have a higher activity than expected could be attributed to their small crystallite size resulting in a higher concentration of defects, which have a higher facile nature, and as such a potential for higher activity due to being of high energy[46]. This is also true for the rod-like morphologies, where increasing activation energy is observed with increasing crystallite size.

The proportion of cerium terminating atoms in the materials varies depending on the terminating surface plane, increasing from (100) to the (110) and (111). The higher the proportion of cerium atoms, the higher the surface energy[33, 116]. Thus in the presence of the oxygen in the atmosphere they will allow for the adsorption of oxygen atoms to the surface with a relatively low binding potential and high facile nature. The (100), (110) and (111) planes are portrayed more clearly in Figure 4.20, Figure 4.21 and Figure 4.22 respectively.

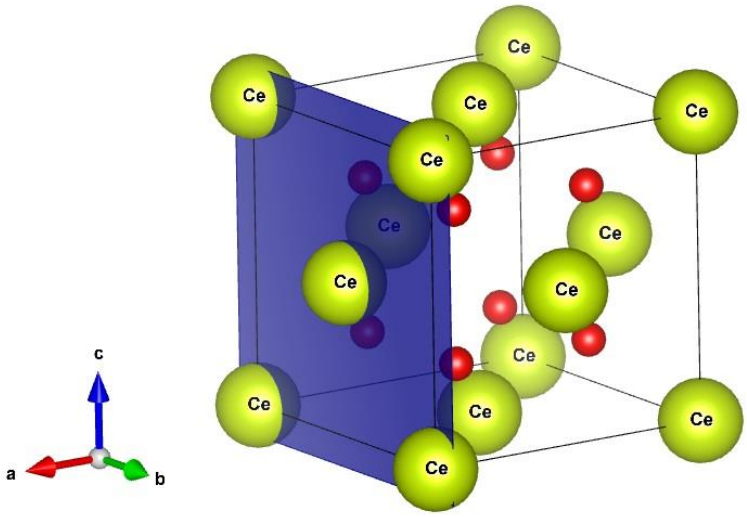

Figure 4.20 - Cubic, fluorite type crystal structure shown for ceria(IV), yellow atoms correspond to cerium, red atoms correspond to oxygen, the blue plane represents the (100) miller index surface.

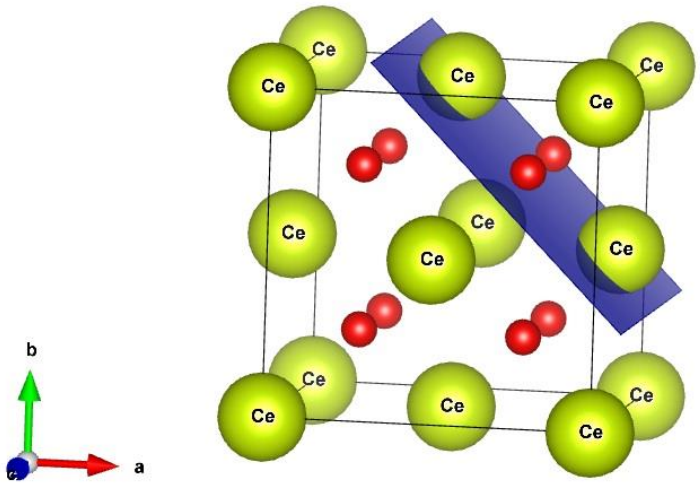

Figure 4.21 - Cubic, fluorite type crystal structure shown for ceria(IV), yellow atoms correspond to cerium, red atoms correspond to oxygen, the blue plane represents the (110) miller index surface.

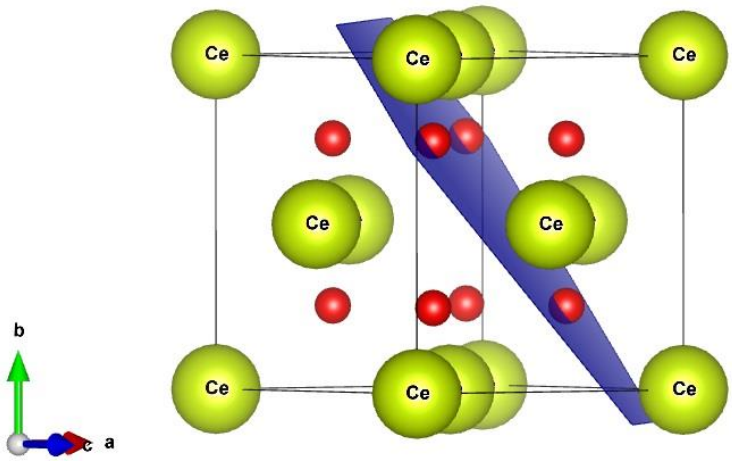

Figure 4.22 - Cubic, fluorite type crystal structure shown for ceria(IV), yellow atoms correspond to cerium, red atoms correspond to oxygen, the blue plane represents the (111) miller index surface.

As stated, the high activity of the (110) and (100) surfaces is associated with their ability to adsorb oxygen with a highly facile nature. Figure 4.23 shows the relationship between the activation energy of the ceria nanostructures as catalysts towards CO oxidation with their $O_{surface}$ to O_{bulk} ratio calculated from TPR experiments and the relative intensity of the peaks in the Raman spectroscopy, I_{592}/I_{462}.

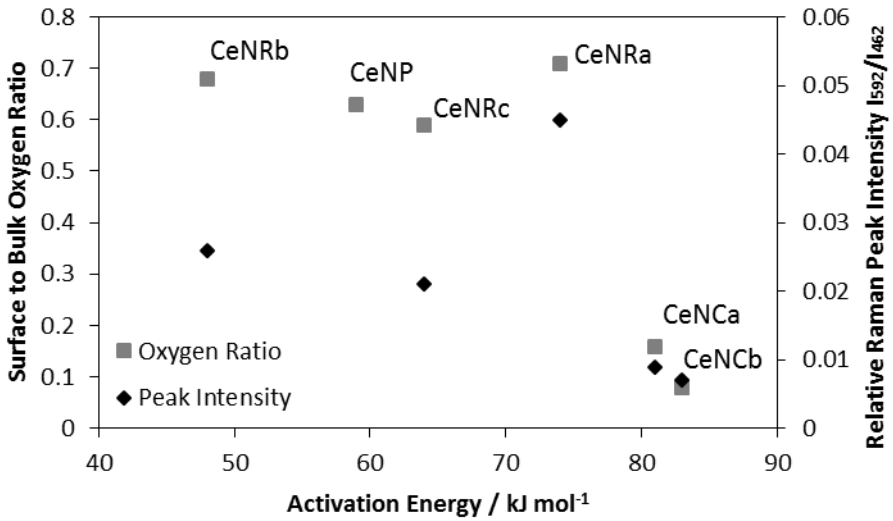

Figure 4.23 – Activation energy towards CO oxidation of the ceria nanostructures against the surface to bulk oxygen content calculated from TPR and the relative Raman peak intensities.

There is a slight trend observed between the surface to bulk oxygen content, suggested by TPR and Raman spectroscopy, and the activation energies of the six ceria nanostructures with the exception of the $CeNR_A$. This exception could be a result of the low Ce^{3+} content, which would suggest a low oxygen vacancy concentration, as oxygen vacancies are known to improve catalytic activity through migration of oxygen ions to the surface[111].

Comparisons between activity and the XPS data showed no apparent trends either with the activation energy or turn over frequency. However, the $CeNR_B$ and $CeNR_C$ morphologies, with the lowest activation energies had the highest Ce^{3+} content, which is known to suggest a higher concentration of oxygen vacancies. However, there was no correlation between Ce^{3+} content and activation energy beyond this.

The literature reports[68] an increase in specific rate with a decrease in surface area and decrease of crystallite size. However, the opposite was observed here. The reason for this discrepancy could be as a result of the crystallite size being increased in the literature post synthesis and theorised to result in the creation of a higher concentration of high energy surfaces due to the method used. It does, however, report an activation energy range of 14-16 kcal mol^{-1} (59-67 kJ mol^{-1}) [68] which agrees well with the values observed in this work.

The CeNP, $CeNR_A$ and $CeNC_A$ materials were also studied in the naphthalene oxidation reaction by Dr Garcia at the University of Zaragoza. A similar trend of activity is observed in the reaction compared to the CO oxidation reactions, which could suggest a similar reaction mechanism in both cases.

The CO oxidation reaction takes place via the Mars-Van Krevelen reaction mechanism[117]. This mechanism involves CO adsorbing to the surface, migrating to an oxygen atom on the surface of the ceria, reacting, leaving and creating an oxygen vacancy that would be filled by in a subsequent step.

From the comparison of catalytic activity with the physical properties of the six ceria nanomorphologies there is an apparent trend between activity and surface area. As surface area increases with crystallite size, the activity could be also be ascribed to a decrease in crystallite size. There was no discernable trend in activity with surface oxygen content measured through XPS. Though, with the exception of $CeNR_A$, a trend is observed between activity and surface to bulk oxygen measured by TPR and Raman. The Ce^{3+} content as measured by XPS suggested that higher Ce^{3+} concentrations at the surface resulted in higher activity, but no actual trend could be drawn. The smaller crystallites appear to be the largest contributor to the higher activity with the best correlation observed between their size and activity. This is likely due to the higher concentration of defects that provide the most facile atoms of highest energy and the reported trends between surface energy and activity due to the formation of the most facile oxygen atoms.

4.4 Titanate Nanotubes Synthesis and Characterisation

Titanate nanotubes (TiNT) were synthesised in acid digestion vessels of 300 mL volume using the alkali hydrothermal method, 10 g of TiO_2 and 200 mL of 10 M NaOH are heated to 130 °C for 24 hours before being, wash and dried, ground up and neutralised with acid to replace Na ions with H in the metal titanate structure. Good consistency in terms of purity and properties

was found between TiNT synthesised in the 50 mL and 300 mL acid digestion vessels suggesting homogeneous temperature distribution across the vessels during synthesis. More detailed synthesis procedures are given in the experimental chapter. The resulting white powder was characterised by TEM, images are shown in Figure 4.24.

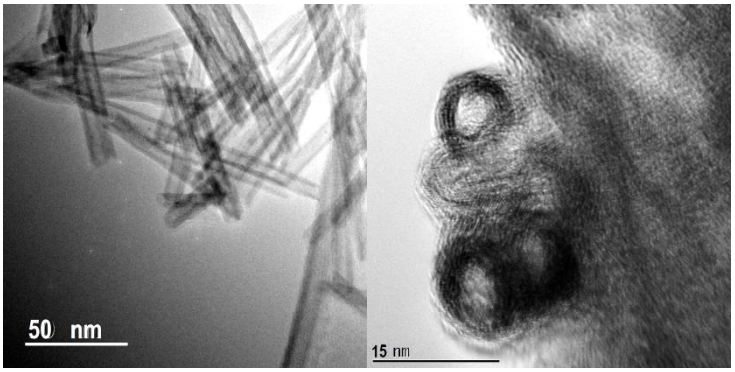

Figure 4.24 - TEM images of the TiNT showing a representation of typical aspect ratios

The TiNT structure presents a multi-layered morphology, typically of three layers, due to the due to the scrolling of multiple layers of sheets during synthesis. The tubes have an outer diameter of around 10 nm, an internal diameter of around 6 nm and a typical length of approximately 100 nm. The material showed very good consistency in morphology throughout the sample, without the presence of amorphous material. These aspect ratios agreed well with the literature which reports TiNT of very similar dimensions[118].

Surface area measured using low temperature nitrogen adsorption and calculated through the use of BET theory gave a surface area of 111.8 (± 2.4) m^2 g^{-1}, which compares well with literature values for TiNT synthesised under similar conditions[12, 118]. The adsorption/desorption isotherm is shown in Figure 4.25 and the differential pore volume distribution is shown in Figure 4.26.

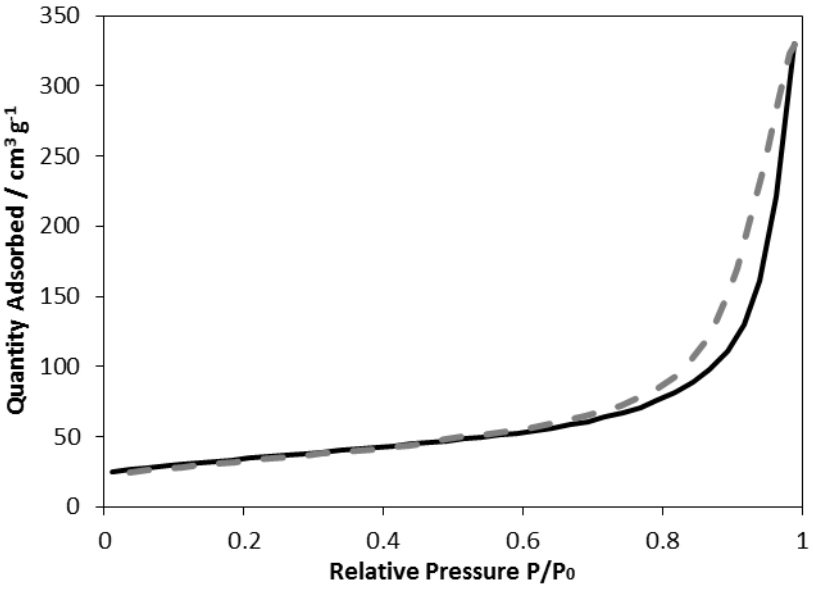

Figure 4.25 – BET isotherm of the TiNT showing adsorption denoted by the solid black line and desorption denoted by the dashed grey line.

The adsorption/desorption isotherm is a combination of 'Type II' and 'Type IV' isotherms, as described by BDDT classification[105] and typical of a BET adsorption mechanism showing macroporosity and mesooporosity.

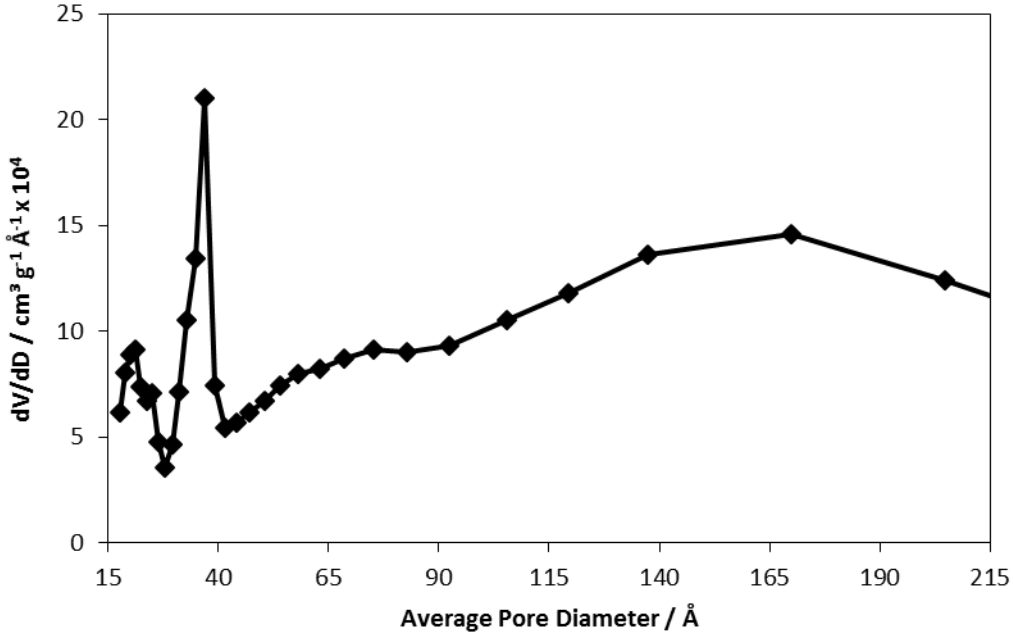

Figure 4.26 - Differential pore volume distribution for the TiNT calculated from low temperature nitrogen adsorption studies.

The differential pore volume for the TiNT, Figure 4.26, shows a high level of mesoporosity (porous between 2-50 nm). A large number of pores are observed between 3.0 and 4.4 nm that corresponds well to the internal diameter of the tubes as observed by TEM. The smaller peak occurring between 1.7 and 2.9 nm could be attributed to the spacing between layers of the TiNT multi-layered structure.

The TPR of the TiNT was carried out as to assess the reducibility of the material and to provide a baseline upon which the TPR of the metal nanoparticles on TiNT in later chapters could be compared and to verify that the support itself was not being reduced and changed under the temperature of the metal reductions. There was negligible hydrogen consumption by the TiNT at temperatures below 500 °C.

TiNT was tested as a catalyst for the CO oxidation reaction displaying no activity below 600 °C. The difference between the TiNT and ceria nanostructures in catalytic activity towards CO oxidation can likely be attributed to the high OSC of ceria, the ability to form and refill oxygen vacancies making it suitable for an oxidation reaction. However, TiNT can be used as a support for metal nanoparticles to study the effect of different methods of metal loading on catalytic activity due to the absence of inherent catalytic activity towards the reaction.

It has been shown through the use of TEM and BET surface area calculations that it is possible to synthesise the TiNT support with good consistency and well-defined morphologies in agreement to similar materials reported in the literature[12, 118].

4.5 Conclusions

Nanostructured ceria has been successfully synthesised using a hydrothermal method with cerium nitrate and sodium hydroxide. In accordance to a dissolution/recrystallization mechanism, systematic variations of the hydrothermal conditions (temperatures and base concentration) allows for the control of the ceria morphology leading to the selective synthesis

of particle, rods and cubes. The formation of cerium hydroxide crystallites as an intermediate has been previously reported to be responsible for the anisotropic growth into rods. The formation of this intermediate over the direct synthesis of ceria crystallites is related to the viscosity of the solution as a result of NaOH concentration. However, it was established that the temperature also plays a key role in the selection of morphology, with higher temperatures at a given NaOH concentration promoting the transition between ceria rods and cubes. Selective synthesise of morphologies is achieved under different conditions, specifically: 5 M NaOH and 70 °C produced nanoparticles, 10-15 M NaOH and 70-100 °C produced nanorods and 10-15M NaOH and 180 °C produced nanocubes.

Characterisation of these nanostructured ceria morphologies have revealed a relationship between morphology and the chemical properties. Crystallite size was found to increase as morphology changes from particles to rods to cubes. Additionally, smaller crystallite sizes result in a higher surface area, both due to the higher surface to bulk ratio and higher mesoporosity, suggested from nitrogen adsorption isotherms. The surface to bulk oxygen contents of the different ceria materials was estimated using TPR, Raman and XPS (O_β/O_α) techniques. As the surface area of ceria increases so does the surface to bulk oxygen content. However, it was observed that the ceria rods present a higher surface to bulk oxygen content than would be predicted, likely as a result of the preferential exposure of (110) and (100) planes. These exposed surfaces in the ceria rods also result in a higher Ce^{3+} content, as measured by XPS. Interestingly, for a given morphology, increasing Ce^{3+} content resulted in a lower surface to bulk oxygen ratio, in spite of rods having the highest surface to bulk oxygen content and highest Ce^{3+} content.

The CO oxidation reaction, used as a model reaction to test the oxidative catalytic activity of the nanostructured ceria revealed that the activity normalised for surface area had a direct correlation with crystallite size. The smaller the crystallite size the higher the degree of constrained geometry, and thus a higher concentration of defects with higher catalytic activity, due to higher surface energy, a property that benefits CO oxidation.

The activation energy of the nanostructured ceria for the CO oxidation reaction decreased as the surface to bulk oxygen content ratio increased. A higher surface to bulk oxygen content results in a higher concentration of facile oxygen atoms at the ceria surface capable of oxidising a CO molecule forming an oxygen vacancy which is then re-oxidised be oxygen in the gas phase. A similar trend between catalytic activity and the morphology of the ceria catalysts was observed for the naphthalene oxidation (carried out on these catalysts by Dr Garcia at the University of Zaragoza). As CO oxidation is known to take place via the Mars-Van Krevelen reaction mechanism, it could suggest a similar reaction mechanism for this oxidative reaction.

Titanate nanotubes were also synthesised via a similar hydrothermal method using TiO_2 and NaOH, where the resulting Na-titanate nanotube product, was protonated by successive washing with a weak acid. Characterisations of the titanate nanotubes demonstrated a discrete and well-defined hollow tubular morphology with an internal diameter of ~6 nm and an external of ~10 nm. The catalytic activity of the titanate nanotubes towards CO oxidation was investigated and negligible conversion was observed at temperature up to 600 °C. Titanate nanotubes are studied for the support and stabilisation of metal nanoparticles in Chapter 7.

Chapter 5

Thermal Stability of Ceria Nanostructures

This chapter focuses on catalytic stability of ceria nanostructures after thermal treatment. The catalytic stability of ceria after the CO oxidation reaction and also after thermal pre-treatment under different atmospheres is investigated.

Ceria samples, CeNP, $CeNR_A$ and $CeNC_A$ are studied as representative samples of ceria nanoparticles, nanorods and nanocubes respectively. The catalytic stability of the materials was studied by measuring their catalytic activity in consecutive runs. In each run the temperature is increased from ambient to 575 °C and reduced back to ambient while CO conversion is monitored downstream throughout. The structures were also pre-treated, prior to catalytic tests, at high temperature under oxidising, reducing and inert atmospheres to study the effect of thermal treatment on the chemical and physical properties. To this end the thermally treated samples were also characterised using low temperature nitrogen adsorption to calculate surface area and TEM imaging to observe morphological changes.

5.1 Thermal Stability of Ceria Nanostructures During Reaction Conditions

The thermal stability of nanostructured materials is inherently lower than their bulk counterpart, due to the higher energy of surface atoms and the high ratio of surface to bulk atoms in nanoscale materials. As such thermal stability studies were done to study not only the stability of the different ceria nanostructures under high temperature, but also the effect of heating in different atmospheres and the activity of the catalysts after thermal treatment. The morphologies studied were the ceria particles, rods and cubes synthesised under NaOH concentrations of 5 M, 15 M and 15 M and temperatures of 70 °C, 100 °C and 180 °C respectively. Full characterisation of these morphologies, CeNP, $CeNR_A$ and $CeNC_A$, is presented in Chapter 4.

The stability of the catalytic activity of different ceria nanostructures under CO oxidation reaction conditions was assessed by carrying out consecutive catalytic runs. In each run, the reaction temperature was increased from room temperature to 575 °C, before being cooled to ambient. This heating and cooling cycle was repeated at least three times while CO conversion was measured downstream. The CO conversion as a function of temperature for consecutive runs for ceria nanorods ($CeNR_A$) is shown in Figure 5.1.

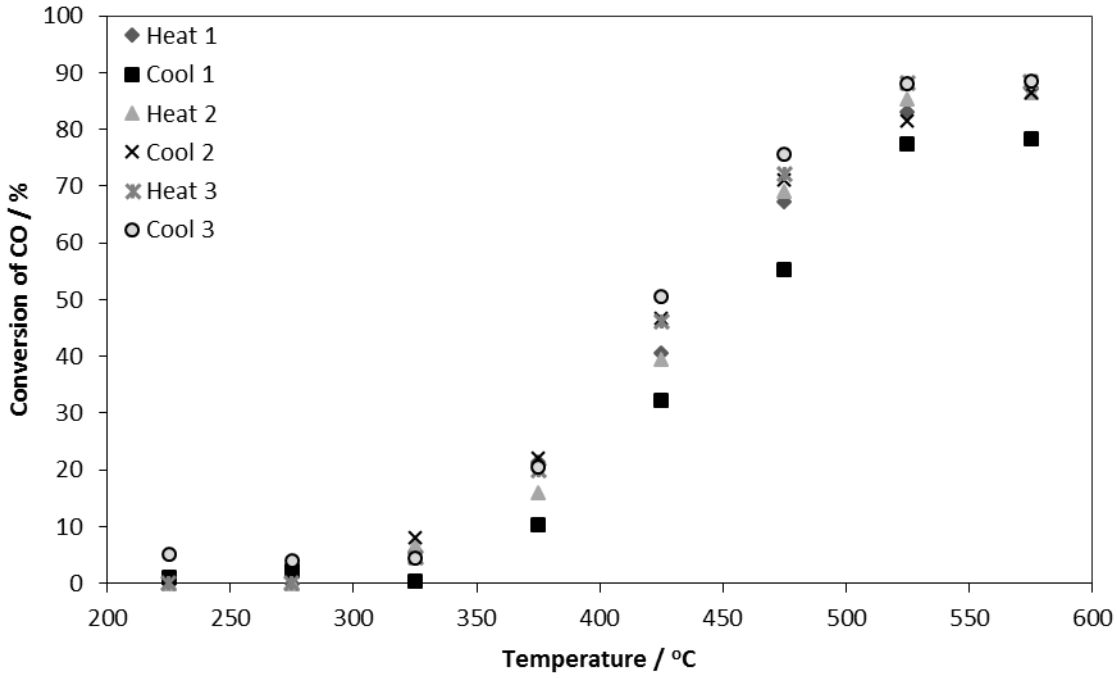

Figure 5.1 - CO oxidation reaction using $CeNR_A$ as a catalyst in consecutive runs. Conditions: 15 mg of catalyst, 50 mL min^{-1} of 2000 ppm CO, 2000 ppm O_2 in N_2, GHSV of 750 $hour^{-1}$.

$CeNR_A$ are thermally stable showing repeatable catalytic activity in three consecutive heating and cooling runs under the reaction conditions. For each heating and cooling cycle the ceria nanorods show catalytic activity at temperatures above 300 °C and a similar rate of conversion with respect to temperature is observed across the studied temperature range. The slight variations between runs are within experimental error boundaries. Similar stability studies using the CO oxidation reaction and CeNP and $CeNC_A$ as catalysts were carried out. Similar to the ceria rods, the particle and cube nanostructures were found to be stable for three heating and cooling cycles. The results of these reactions are shown in Appendix B.

Further studies to study the effect of higher temperatures on the stability of the ceria nanostructures was carried out. Due to the limitations of the furnace in the CO oxidation catalyst rig (of 600 °C) it was not possible to carry out such higher temperature pre-treatments in-situ.

CeNP, $CeNR_A$ and $CeNC_A$ were first pre-treated at different temperatures, 575, 800 and 1000 °C under a mixture of CO and O_2 to simulate reaction conditions. Figure 5.2 shows the

catalytic activity towards CO oxidation respect to temperature of the $CeNR_A$ pre-treated under these conditions.

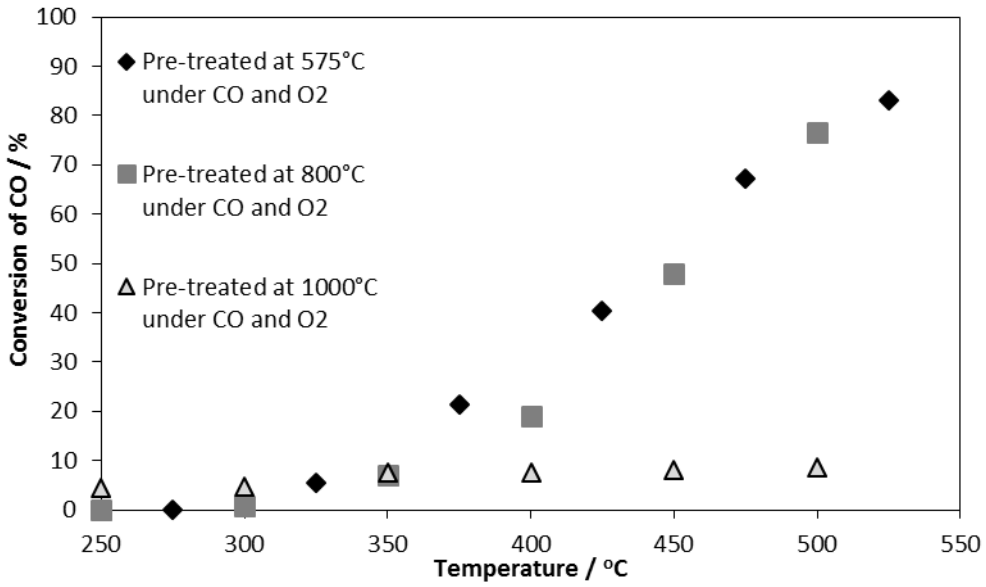

Figure 5.2 – CO oxidation reaction using $CeNR_A$ as a catalyst that had been pre-treated under 2000ppm CO, 2000ppm O_2 in N_2 to 575 °C, 800 °C and 1000 °C prior to its use here. Conditions of reaction: 15 mg of catalyst, 50 mL min^{-1} of 2000 ppm CO, 2000 ppm O_2 in N_2, GHSV of 750 $hour^{-1}$.

The $CeNR_A$ catalyst pre-treated at 575 and 800 °C in 2000 ppm CO and 2000 ppm O_2 in N_2, showed similar activity to the fresh catalyst, demonstrating $CeNR_A$ was catalytically stable to at least 800 °C. Subsequent runs using these two pre-heated materials showed similar conversion versus temperature as is observed for the first catalytic cycle in Figure 5.2, showing that these ceria nanorods are stable up to at least 800 °C.

However, when $CeNR_A$ is pre-heated to 1000 °C under 2000 ppm CO and 2000 ppm O_2 in N_2, its CO oxidation activity greatly decreased as shown in Figure 5.2. The material presents a similar temperature of initial activity to that of the fresh sample, at around 300 °C, but a maximum conversion of only ~10% at 500 °C whilst the fresh catalysts presented a CO conversion of ~70% at this temperature. These trends were identical to what was observed in the case of the CeNP and $CeNC_A$.

To study the deactivation mechanism and the effect of the pre-treatment atmosphere, the three ceria morphologies were heated to 1000 °C under an oxidising, a reducing and an inert atmosphere whilst monitoring the outlet gas conductivity using a TCD. The thermally treated samples were then used as catalysts for CO oxidation to observe relative changes in their catalytic activity.

5.2 Effect of Atmosphere on the Thermal Stability of Ceria Nanostructures

Ceria nanostructures were pre-treated thermally to 1000 °C under an oxidising flow of 20 % O_2 in He to simulate the oxidising effect of air. The relative thermal conductivity of the outlet stream during the pre-treatment was monitored with a TCD as a function of temperature as shown in Figure 5.3.

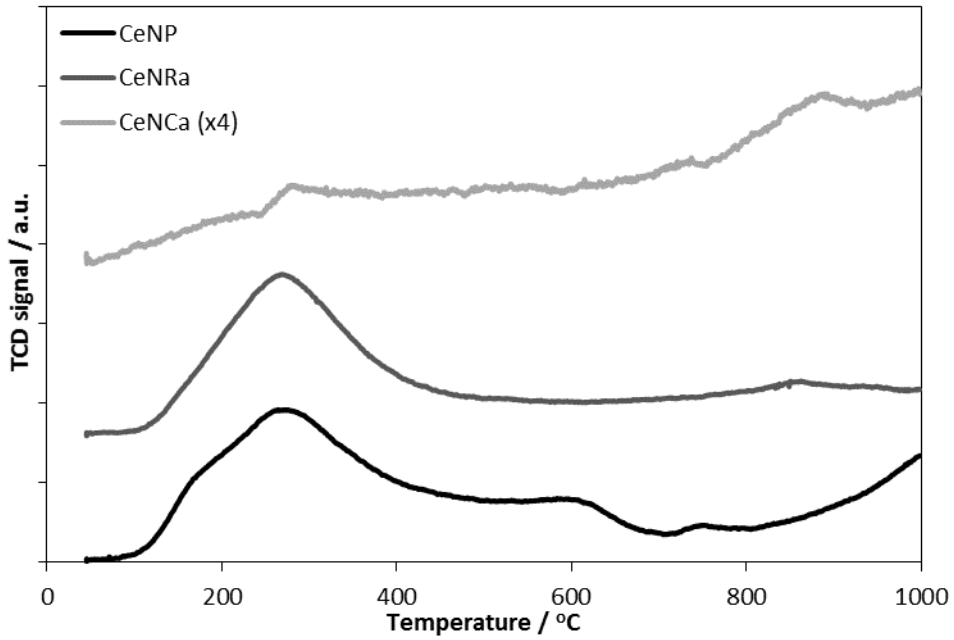

Figure 5.3 - Temperature programmed oxidation of CeNP, $CeNR_A$ and $CeNC_A$. Run between ambient and 1000 °C using 20% O_2 in He at 30 mL min^{-1}, signal adjusted for weight. TCD signal is inverted.

The temperature programmed oxidation (TPO) shows that the $CeNR_A$ and CeNP materials have a more intense signal than that of the $CeNC_A$, displaying one large peak with a maximum of ~275 °C. This peak could be a result of the particle and rods having a higher surface to bulk oxygen ratio as suggested by TPR analysis in Chapter 4 and the peak relating to the release of oxygen at this temperature. As the peaks are inverted and as the conductivity of oxygen is lower than that of helium, the peaks can potentially be ascribed to a higher concentration of oxygen than the baseline. This further supports the peaks being attributed to the release of surface oxygen at this temperature.

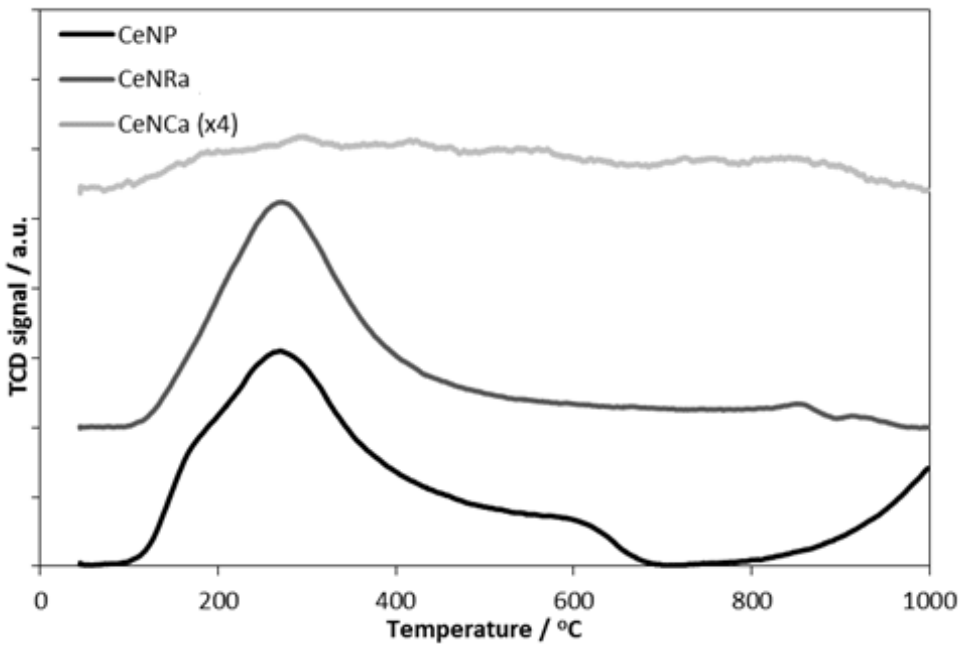

Figure 5.4 - Temperature programmed treatment under inert atmosphere of CeNP, $CeNR_A$ and $CeNC_A$. Run between ambient and 1000 °C under helium at 30 mL min^{-1}, signal adjusted for weight. TCD signal is inverted.

The TCD signal for the CeNP and $CeNR_A$ in the temperature programmed inert treatment (TPIT), shown in Figure 5.4, is almost identical to that of the TPO in Figure 5.3. The same shaped peaks, occurring with a maximum of ~275 °C, for the CeNP and the $CeNR_A$, and the increase in signal after 800 °C for the CeNP are observed in both the TPO and TPIT. The

only difference is observed in the case of $CeNC_A$ above 800 °C, the TCD signal in the TPO increasing, whilst the signal in the TPIT does not. However, it should be noted that both the TPO and TPIT of $CeNC_A$ have a signal close enough to the baseline to be attributed to noise. The $CeNC_A$ have a much smaller surface area and as such it is expected that the material would release a much smaller volume of oxygen.

The TCD signal of the TPIT is inverted and as such the peaks could be attributed to oxygen release. The temperature of this process appears to be independent of the presence of oxygen in the treatment atmosphere as it is identical between the TPO and TPIT. The major limitation of a TCD is that measuring the conductivity of gas stream gives no direct information regarding the exact gas composition.

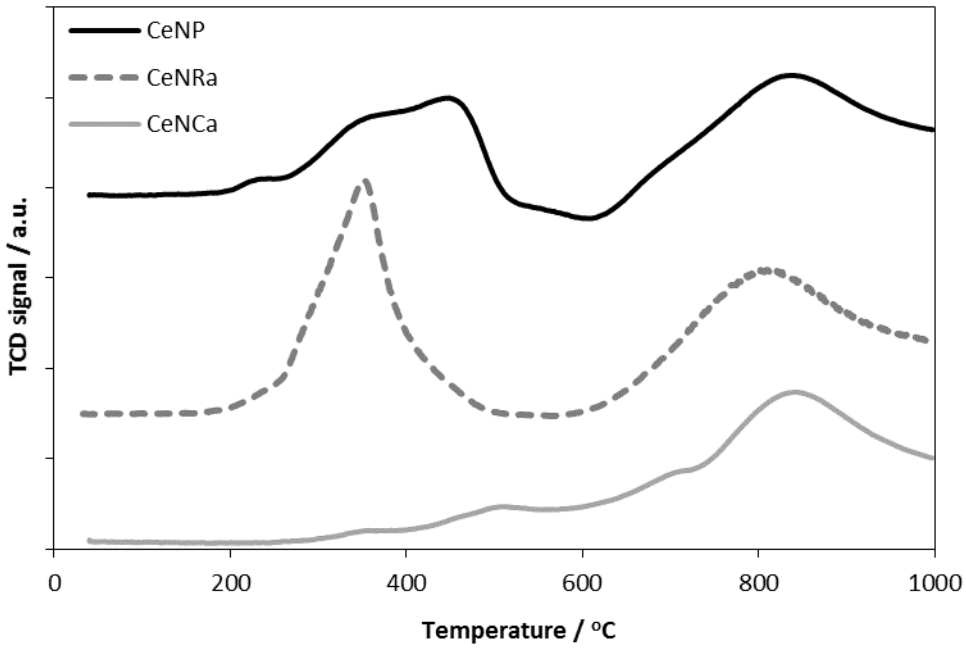

Figure 5.5 - Temperature programmed reduction of CeNP, $CeNR_A$ and $CeNC_A$. Run between ambient and 1000 °C using 5% H_2 in Ar at 30 mL min^{-1}, signal is adjusted for weight.

The temperature programmed reduction of the ceria nanostructures in 5% H_2 in Ar shown in Chapter 4 is replicated here in Figure 5.5 for comparison. The TCD signal in the TPR of the $CeNC_A$ displays a more intense signal than in either the TPO or TPIT. The CeNP and $CeNR_A$ both show peaks at around 375 °C. They then present a broader peak that begins at

around 600 °C and rises to a maximum at around 875 and 825 °C in the CeNP and $CeNR_A$ respectively. The CeNP peak at around 375 °C appears to be the combination of two or more peaks due to different contributions of different crystal planes to the surface[25]. Without further knowledge of the full surface and the reduction temperature of different crystal surfaces, ascribing the different peaks to different surfaces is not possible.

However, $CeNC_A$ still present a much less intense low temperature signal, 200 to 500 °C, than either the CeNP or $CeNR_A$. This could be as a result of lower surface area, the lower temperature peaks corresponding to the reduction of the surface. The higher temperature corresponds to the rearrangement of bulk atoms to the surface as has been previously reported in the literature[67]. It is also reported that the hydrogen facilitates the sintering of nanostructured ceria due to the rearrangement of atoms that starts at around 600 °C with the bulk oxygen reduction[67].

To further investigate the changes to the ceria nanostructures after pre-treatment at 1000 °C several characterisation techniques were used. The BET calculated surface area for the heat treated and fresh nanostructures are shown in Table 5.1.

Table 5.1 - BET surface areas of CeNP, $CeNR_A$ and $CeNC_A$ samples after thermal treatment under different atmospheres.

	BET calculated surface are / $m^2 g^{-1}$			
Pre-treatment	**None**	**TPR**	**TPO**	**TPIT**
CeNP	89.3 (± 1.4)	1.5 (± 0.03)	0.5 (± 0.02)	0.4 (± 0.02)
$CeNR_A$	53.6 (± 1.1)	4.2 (± 0.1)	1.9 (± 0.03)	2.4 (± 0.1)
$CeNC_A$	6.7 (± 0.2)	1.3 (± 0.1)	1.4 (± 0.1)	1.9 (± 0.02)

The surface area of the three ceria morphologies decreases enormously to less than 5 $m^2 g^{-1}$ after thermal treatment for all samples, independently of the atmosphere under which the treatment is carried out. Due to the low surface area value, the associated experimental error is considerably high due to the required mass for accurate measurement being greater than the equipment limitation or available sample material. As such they are reported to demonstrate that

sintering has occurred, but not to what degree and are not used in any calculation of rate by surface area.

TEM imagining was performed to observe morphological changes that occurred during the pre-treatment at 1000 °C to obtain a qualitative measure of the degree of sintering. The TEM of samples heated to 1000 °C under 20 % O_2 in He is shown in Figure 5.6.

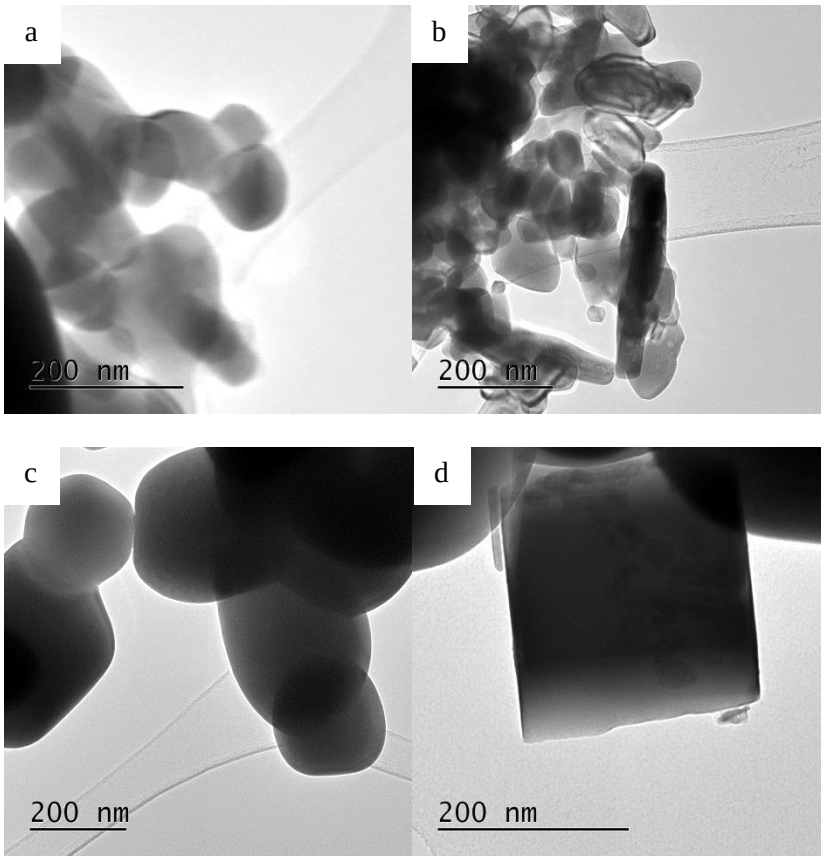

Figure 5.6 - TEM images of ceria samples after heating to 1000 °C in 20 % O_2 in He; (a) - CeNP, (b) - $CeNR_A$, (c) & (d) - $CeNC_A$

From the TEM images in Figure 5.6 it is possible to conclude that sintering has occurred in all materials in agreement with the decrease in surface area previously discussed. The $CeNR_A$ sample appears to conserve its rod-like morphology, although the dimensions of said rods have greatly increased with respect to the original $CeNR_A$ morphology. Similarly it is also noted that larger $CeNC_A$ cubes have retained their cubic morphology after thermal treatment, Figure 5.6 (d). The TEM images of the samples after pre-treatment at 1000 °C under He were virtually

identical to what was observed for those after pre-treatment under oxidising conditions. This suggests that, as previously hypothesised from the TCD measurements, there was a similar mechanism or process occurring when treated under inert or oxidising atmosphere. The TEM images of the samples pre-treated at 1000 °C under 5% H_2 in Ar are shown in Figure 5.7.

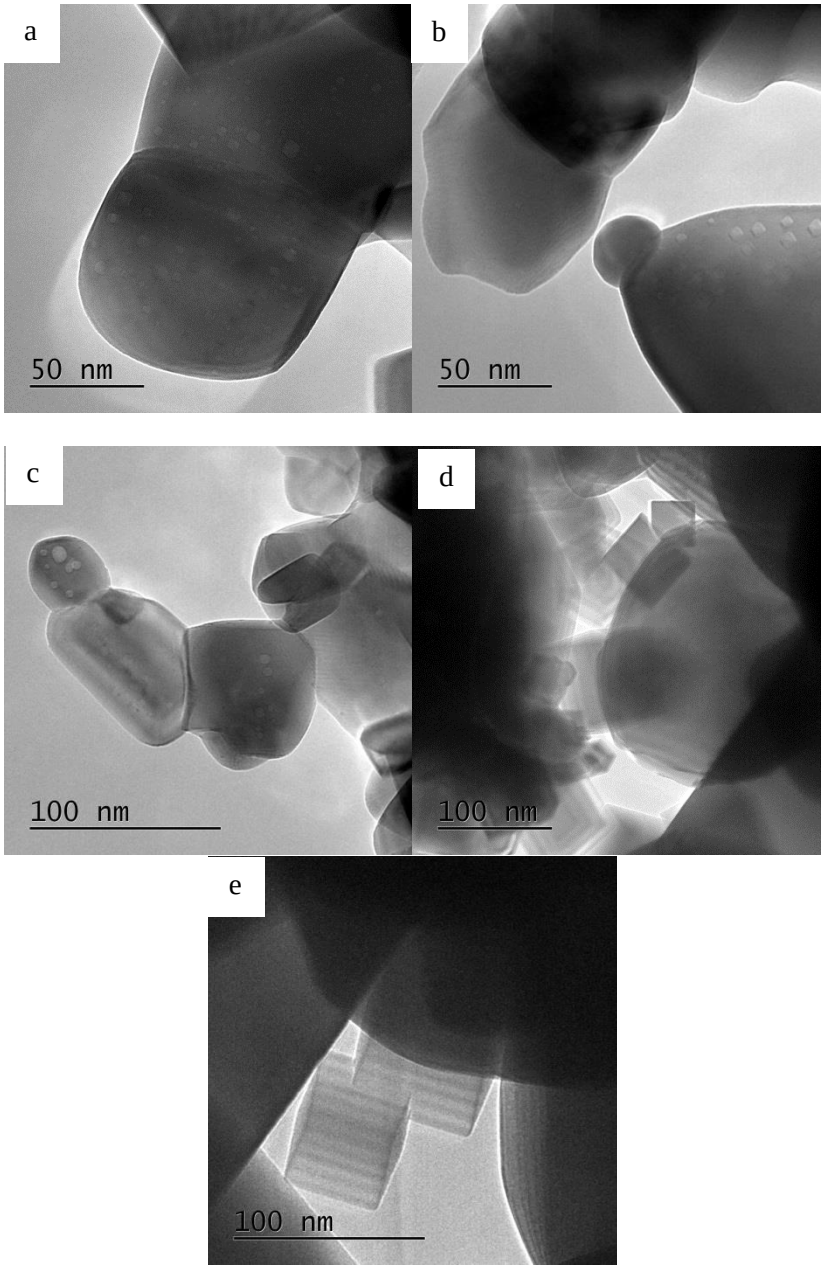

Figure 5.7 - TEM images of ceria nanostructures after heating to 1000 °C in 5 % H_2 in Ar; (a) & (b) - CeNP, (c) - $CeNR_A$, (d) & (e) - $CeNC_A$

The TEM images of the ceria nanostructures thermally treated at 1000 °C under 5% H_2 in Ar show sintering of the materials to a greater degree than observed under oxidising or inert atmospheres. The CeNP and $CeNR_A$ samples appear to be relatively similar to one another and do not retain any similarity to the fresh nanostructures. The CeNP and $CeNR_A$ also appear to have pitting, or defects upon their surfaces that were not observed in the oxidised or inert treatment samples. However, the $CeNC_A$ after heating to 1000 °C under a reducing atmosphere have retained their morphology to a greater degree than what was observed after thermal treatment under oxidising or inert atmospheres, with cubes under 100 nm being imaged. This is counterintuitive to what would be expected based on the literature[67], which suggested that sintering would be facilitated by the presence of hydrogen due to the reduction to form water. However, the imaging of these cubes was sparse and no quantification of their contribution to the material can be made.

Visual observations of the ceria nanostructures after treatment at 1000 °C under reducing, oxidising and inert atmospheres were also made. After high temperature oxidising and inert treatment all structures were white, typical of a high Ce^{4+} content ceria.

The high temperature reduced ceria was observed to be a vibrant royal blue colour for all materials. The literature[119] suggests that the blue colour is due to a "grossly unstoichiometric ceria", causing a large number of Ce(IV)-Ce(III) transitions, suggesting a very high oxygen deficiency. The blue colour was present at room temperature in air, and when heated to at least 120 °C under vacuum, but would rapidly change to white if heated in an oxidising environment. This suggests a relatively stable, highly oxygen deficient ceria.

5.3 Effect of Pre-Thermal Treatment on the Catalytic Activity of Ceria Nanostructures

The effect of the pre-thermal treatment under different atmospheres (reducing under a hydrogen flow, oxidising under an air flow and inert under a helium flow) on the oxidation catalytic activity of the ceria nanostructures was studied using the CO oxidation reaction. The plot for the CO conversion versus temperature using CeNP as a catalyst after different pre-treatment is shown in Figure 5.8. The activity of the fresh material is also shown for comparison.

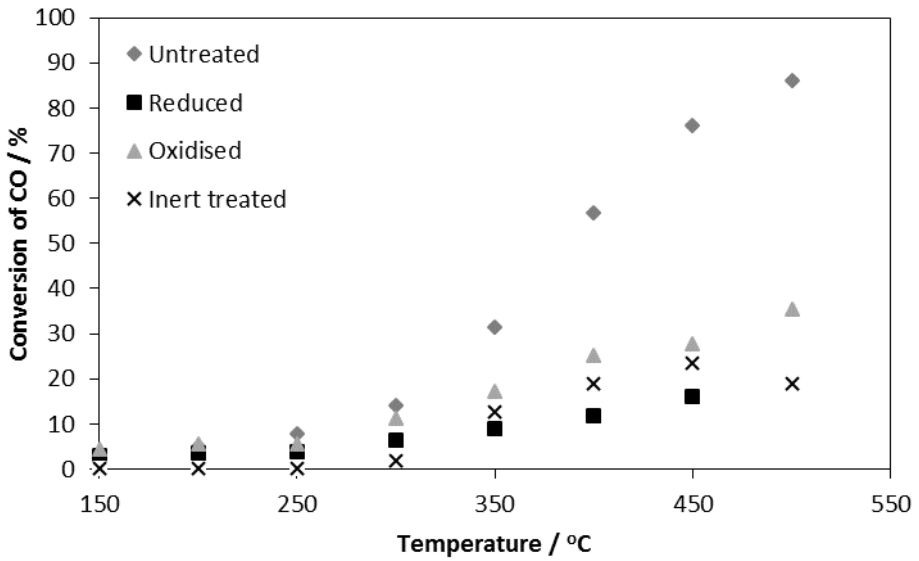

Figure 5.8 – CO oxidation reaction using CeNP as a catalyst, after heating to 1000 °C under reducing, oxidising and inert environments, along with the fresh CeNP. Conditions: 15 mg of catalyst, 50 mL min^{-1} of 2000 ppm CO, 2000 ppm O_2 in N_2, GHSV of 750 $hour^{-1}$.

The catalytic activity of the CeNP samples pre-treated at 1000 °C under all environments, is considerably lower than the fresh CeNP material, irrespective of the environment of pre-thermal treatment. The activity between the three pre-treated samples is comparable below 350 °C, the conversion starting at around 250 to 300 °C and increasing at a similar rate. However, it appears that the samples that underwent an inert or oxidising

pre-treatment present slightly higher conversions as temperature increases beyond 350 °C, relative to the samples that underwent a reducing pre-treatment. The CeNP catalyst pre-treated under helium show a drop in conversion at temperatures above 450 °C. This fall in the conversion is irreversible as the material does not present any considerable activity in a consecutive second catalytic run, shown in Figure 5.9.

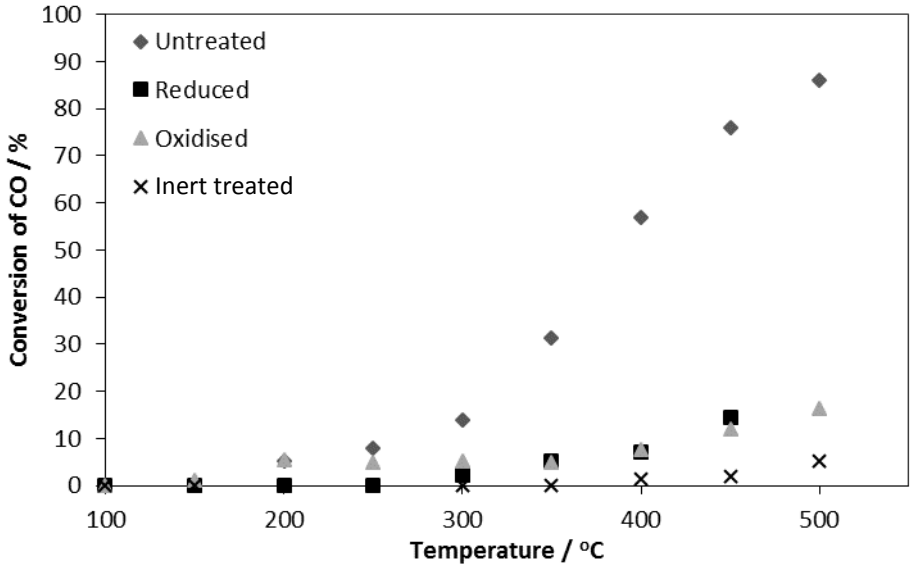

Figure 5.9 - CO oxidation reaction using CeNP as a catalyst that had been treated at 1000 °C under reducing, oxidising and inert environments, along with the fresh CeNP for comparison, second catalytic cycle. The catalysts had previously been used in an identical CO oxidation reaction. Conditions: 15 mg of catalyst, 50 mL min^{-1} of 2000 ppm CO, 2000 ppm O_2 in N_2, GHSV of 750 $hour^{-1}$.

Figure 5.9 shows that the CeNP samples thermally treated under inert and oxidising atmospheres have a drop in activity for consecutive runs compared to the conversion in the first reaction. This suggests that an irreversible process is occurring during the CO oxidation that leaves the surface with lower oxygen availability. As presented in Chapter 4, the surfaces with higher oxygen content in the terminating crystal plane are less active. This could suggest that these surface are left as the (111) oxygen terminating plane that required heating under the presence of oxygen to be fully oxidised. However, interestingly, the sample thermally treated under hydrogen appeared to maintain its activity in consecutive runs, suggesting that the facile nature of the oxygen atoms is retained for repeat reactions.

Similar trends were observed for the $CeNR_A$ and $CeNC_A$ pre-treated samples, shown in Figure 5.10 and Figure 5.11.

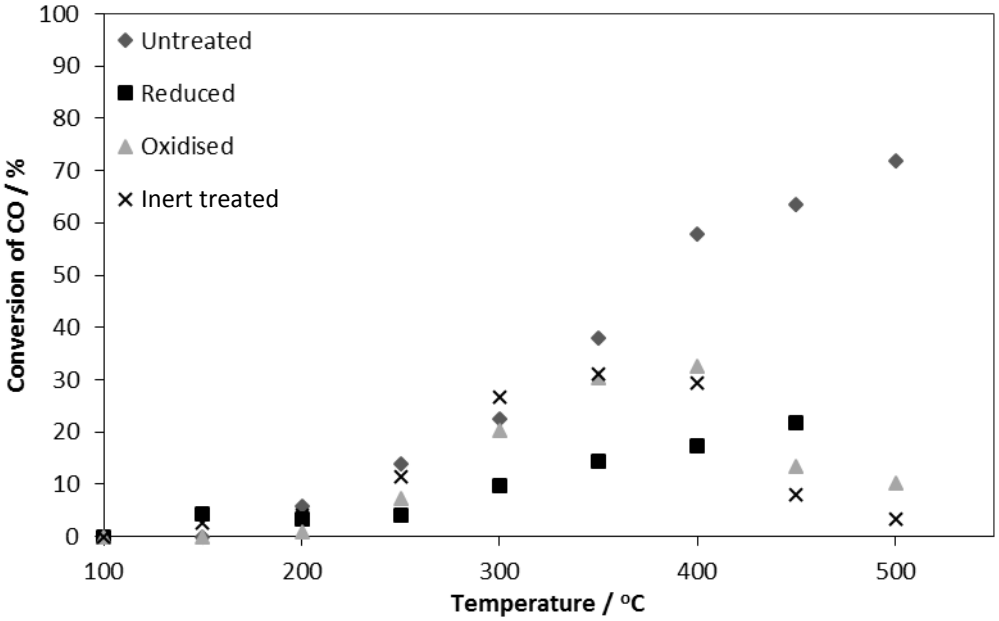

Figure 5.10 - CO oxidation reaction using $CeNR_A$ as a catalyst, after heating to 1000 °C under reducing, oxidising and inert environments, along with the fresh $CeNR_A$. Conditions: 15 mg of catalyst, 50 mL min^{-1} of 2000 ppm CO, 2000 ppm O_2 in N_2, GHSV of 750 $hour^{-1}$.

Overall, there is a similar trend on the effect of pre-thermal treatment of the $CeNR_A$ material when compared to the effect on the CeNP material, Figure 5.8, with a few key differences. All pre-treated samples present an initial temperature of activity at around 200 to 250 °C, similar to the fresh material. The samples pre-treated via inert and oxidising environments show a higher rate of CO conversion when compared to the sample pre-treated under hydrogen, similar to what was presented for the CeNP. The activity of the $CeNR_A$ samples pre-treated under inert and oxidising atmospheres is comparable to the fresh catalysts until ~300 to 350 °C. At higher temperatures their activity drops in an irreversible manner, showing negligible activity for subsequent catalytic runs. Conversely the $CeNR_A$ sample, pre-treated under hydrogen, despite having initial loss of catalytic activity relative to the fresh catalyst maintains this activity in consecutive catalytic runs.

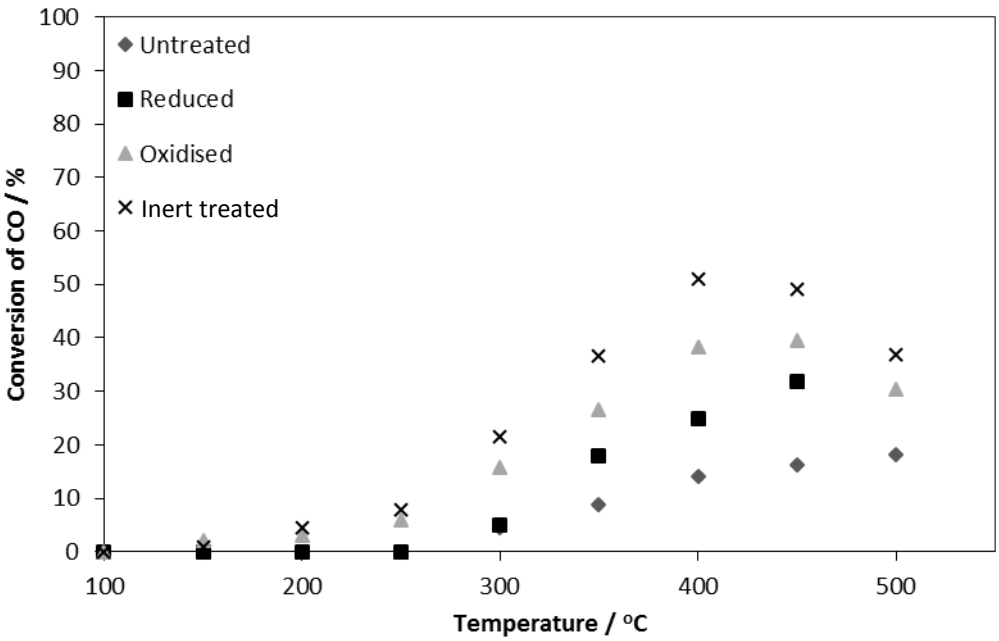

Figure 5.11 - CO oxidation reaction using $CeNC_A$ as a catalyst, after heating to 1000 °C under reducing, oxidising and inert environments, along with the fresh $CeNC_A$. Conditions: 15 mg of catalyst, 50 mL min^{-1} of 2000 ppm CO, 2000 ppm O_2 in N_2, GHSV of 750 $hour^{-1}$.

The catalytic activity of the $CeNC_A$ samples that were thermally treated for CO oxidation is shown in Figure 5.11. The activity of the three pre-treated $CeNC_A$ is, unlike the CeNP and $CeNR_A$, higher than that of the fresh CeNC. The ceria cubes pre-treated under inert and oxidising atmosphere show a fall in activity, at around 400 to 425 °C and limited activity on subsequent runs similar to the particles and rods. However, the $CeNC_A$ pre-treated under reducing atmosphere has a higher conversion with respect to temperature than fresh $CeNC_A$ and maintains similar activity for subsequent reactions.

The similarity in colour and thermal conductivity readings between the ceria treated under inert and oxidising atmospheres and TEM images suggests that a similar transformation during thermal treatment with and without the presence of oxygen. As suggested above, this could be a result of desorption of surface oxygen as thermal energy increases, that is unaffected by the oxygen content in the atmosphere. This observation agrees with the TPR for the quantification of surface and bulk oxygen under a hydrogen flow which facilitates the reduction of oxygen. Additionally the hydrogen atmosphere facilitates the rearrangement of atoms to remove bulk oxygen, not apparent for the TPO or TPIT experiments. The removal of oxygen

from the ceria(IV) structure can be balanced using in Kröger–Vink notation, shown in Equation 5.1.

$$O_O^X + 2Ce_{Ce}^X \rightarrow 2Ce'_{Ce} + V_O^{\bullet\bullet} + \frac{1}{2}O_2(g) \qquad (\mathbf{5.1})$$

Kröger–Vink notation for the removal of oxygen from an oxygen lattice site to form oxygen and an oxygen vacancy.

The ceria nanostructures sintered under air and helium at high temperatures suffer a dramatic decrease in surface area. However, their catalytic activity per surface area for CO oxidation is relatively high with respect to their fresh counterparts, although they become inactive after a single catalytic run. As discussed in Chapter 4, a high energy surface is more active for CO oxidation[46] and a surface incorporating a high concentration of vacancies would suffer from high unsatisfied coordination, increasing the energy. Therefore it is likely that the relatively high catalytic activity, per surface area is an effect of these oxygen vacancies. It also suggests that whilst atmospheric conditions do not fill the vacancies irreversibly, the CO oxidation reaction does and kills this catalytic activity. The exact mechanism of this process is outside the scope of this work.

The thermal pre-treatment of ceria under reducing atmosphere causes a change in activity that was stable for subsequent heating and cooling cycles towards CO oxidation. Due to the low surface area of the pre-treated ceria, this resulted in an extremely active catalyst per surface area. The low initial surface area of $CeNC_A$ and the observation of a lower degree of sintering in the TEM images for $CeNC_A$ relative to CeNP and $CeNR_A$, resulted in a smaller change in surface area after sintering. These facts resulted in the thermally pre-treated $CeNC_A$, under hydrogen, having a higher catalytic activity for CO oxidation than the fresh $CeNC_A$.

Most fascinating was the colour change of pre-treated ceria under hydrogen to a blue colour, caused by the high oxygen vacancy content. If heated in vacuum, to 120 °C this colour remained, though heating in air changed the colour to white, suggesting the oxidation of the sample. The apparent stability of the ‘blue ceria’ and its behaviour suggests a stable low oxygen

content ceria, though it has been reported that $CeO_{1.7}$ is the lowest oxygen content of ceria and requires low partial pressures of oxygen to be present[119].

$CeNC_A$ material that was pre-treated under hydrogen and then heated in air to oxidise ceria, as suggested by the colour shift from blue to white was tested for its catalytic activity towards CO oxidation and behaved identically to pre-treated sample without reoxidation. This suggests that the oxygen vacancies, that are stable under ambient conditions, are filled when heated under an oxidising environment are still relatively facile in nature and capable of being recreated to continue to facilitate the CO oxidation reaction.

Despite the uncertainties of the transformation occurring during the thermal pre-treatments of ceria, the results suggest that after pre-treatment under hydrogen, the samples have higher specific activity than the fresh ceria and that this activity is stable under the conditions of the CO oxidation reaction. Opposed to what is observed for the inert and oxidising pre-treatment samples that lose activity on subsequent runs. A summary of the findings is shown in Table 5.2 that suggest the sustained stability could be a result of the bulk oxygen removal. As the increased activity is stable for multiple runs it is possible that the mechanism that results in the bulk oxygen removal also results in the creation of exposed crystal planes that are of higher activity, similar to what was reported in the literature for increasing crystallite sizes through the use of thermal treatments[68].

Table 5.2 – Comparison of the trends of activity in the initial CO oxidation reaction after thermal treatment and subsequent catalytic cycles, with the removal of surface and bulk oxygen.

Pre-treatment atmosphere	**Surface oxygen removed**	**Bulk oxygen removed**	**Active for initial CO oxidation reaction**	**Active for subsequent CO oxidation reactions**
He	✓	×	✓	×
20% O_2 in He	✓	×	✓	×
5% H_2 in Ar	✓	✓	✓	✓

5.4 Conclusions

The effect of thermal treatment under different atmospheres on the activity of ceria nanostructured catalysts was studied using representative materials with particle, rod and cube morphologies. Three atmospheres were used to study the effect of thermal stability on these morphologies, oxidative (20% O_2 in He), reductive (5% H_2 in Ar) and inert (He).

After thermal treatment materials were observed to sinter resulting in a drastic decrease in surface area, to below 5 $m^2 g^{-1}$ accompanied by a loss of their morphologies irrespective of the atmospheric composition. The catalytic activity as a function of temperature towards CO oxidation for these morphologies after thermal treatment was considerably lower than that of the fresh catalysts in the case of the rods and particles. However, similar catalytic activities were observed between the fresh ceria cubes and those after thermal treatment at 1000 °C. This similarity in activity is due to the much lower relative decrease in surface area after thermal treatment in the case of the cubes. Interestingly, all ceria nanostructures experienced an increase in activity values normalised for surface area.

This enhanced catalytic activity per surface area was not sustained in consecutive cycles when the ceria was thermally treated under oxidising or inert atmospheric compositions. These treated materials had a dramatic decrease in catalytic activity when heated above 450 °C and presented negligible activity for a second catalytic run. However, the samples treated under a reducing atmosphere were stable in consecutive catalytic runs up to 575 °C. Temperature programmed characterisation during the thermal pre-treatments of the ceria nanostructures revealed that under an oxidising or inert atmosphere, surface oxygen was released. However, in the presence of hydrogen additional removal of bulk oxygen was facilitated with the consequent formation of water.

Chapter 6

Literature Review: Metal Nanoparticles

The aim of this thesis is to investigate the variations in catalytic activity and thermal stability of nanostructured materials and how these properties can be benefitted through variations in the nanoscale morphology. The previous section of the thesis is focused on the effect of the nanostructured morphology on the physical and chemical properties of ceria and what effect this has on the oxidative catalytic activity, while this section will investigate the effect of the nanostructured morphology on the activity and stabilization of supported metal nanoparticles. This chapter will present a literature review on metal nanoparticles and their catalytic activity for oxidation reactions, with a specific focus on platinum nanoparticles and CO oxidation.

A variety of metal loading methods will be discussed including, incipient wetness impregnation, ion adsorption, deposition-precipitation and photo-deposition. Catalytic and characterisation data from the literature of Pt supported on different supports will be compared and discussed with a focus on titanate nanotubes. The theories explaining the effect of enhanced catalytic activity of metal nanoparticles are also reviewed. Specific focus will be given to

studying the use of Pt immobilised metal nanoparticles on ceramic supports as catalysts for carbon monoxide oxidation.

6.1 Introduction

Metal nanoparticles are typically defined as metal clusters with a diameter between 1 and 100 nm. Although the IUPAC definition of a nanoparticle is a "particle of any shape with dimensions in the 1×10^{-9} and 1×10^{-7} m range" and includes rods and fibres with two dimensions below 100 nm[120]. For the purpose of this thesis metal nanoparticles will be considered as those that are below ~15nm due to the higher fraction of surface atoms below this size, Figure 6.1.

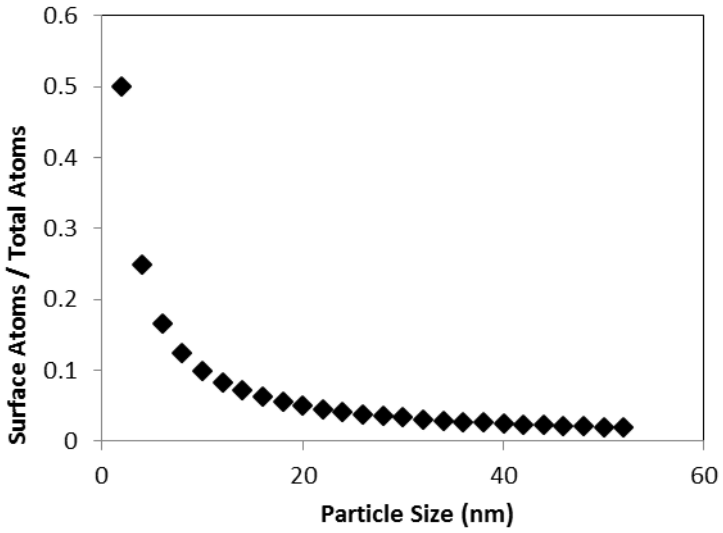

Figure 6.1 - Fraction of atoms at the surface of spherical nanoparticles[13]

The higher fraction of surface atoms is not the only property that makes < 15 nm metal nanoparticles of interest. There are further properties that are only applicable to smaller metal nanoparticles, such as higher concentrations of defects, which have a higher degree of unsatisfied coordination, and a shift to non-metallic like properties[14]. The non-metallic nature

of small metal nanoparticles occurs when particle sizes are similar to the de Broglie wavelength[11]. The metal atoms can be considered as discrete energy levels and the metallic nature no longer applies as there is a discrete gap between the conduction and valence band.

The high surface energy and unsatisfied coordination, also results in another challenge, the prevention of agglomerations. The smaller the nanoparticle, the higher the proportion of higher energy surface atoms, therefore the higher the favourability that the particles will agglomerate to reduce this energy. In solution this can be overcome through the use of capping agents that stabilise the surfaces. However, this blocks the surface and can create diffusion limitations of reactants. A more advantageous method of preventing agglomeration for catalytic purposes, which also aids in the separation of catalyst from the product, is to immobilise the metal nanoparticles on a support, so called heterogenisation.

There is a vast amount of research studying heterogeneous catalysts that comprise of immobilised metal nanoparticles. A high number of metal-support combinations have been studied for their catalytic activity. Supports such as cellulose[20], ceramics[21], zeolites[22] and carbon[23] have all been studied with a variety of metals. Though there are still challenges to be overcome in this field, specifically regarding thermal stability and mass transfer limitations.

As the temperature is increased during reaction conditions there is a tendency for metal nanoparticles to become mobile upon the surface facilitated by the correlation between particle size and melting point[18]. This leads to agglomerations into larger, often less catalytically active nanoparticles. There is also the possibility that in some cases the reaction conditions will denature the support itself, making it clearly unsuitable.

Highly porous structures can often result in a higher surface area, making agglomeration less of an issue due to higher dispersion reducing nanoparticle encounters. Though, the creation of long diffusion pathways to the metal nanoparticle can create mass transfer limitations. The blocking of pores can also result in significant portions of the catalyst becoming unavailable.

To overcome these limitations, nanostructured materials, defined as materials with at least one dimension within the nanometer scale, offer an alternative for the immobilisation of metal nanoparticles on their external surfaces. Their high surface areas, tuneable chemical

compositions and exposed crystal surfaces, facilitate the dispersion of the metal and interaction between the metal and support. Currently, most of the research in this area has been devoted to the use of carbon nanotubes as catalytic support due to their high surface area, unique physical properties, high electrical conductivity and hollow geometry[24]. However, other morphologies and chemical compositions are still to be exploited.

This literature review will focus on Pt nanoparticles and loading on titania and titanate supports.

6.2 Synthesis methods of supported metal nanoparticles

The synthesis of metal nanoparticles on supports is most often achieved through either, the adsorption or deposition of the metal ion or complex, or through the adsorption of pre-formed metal nanoparticles[121]. This thesis focuses on the prior, with an emphasis on ion adsorption, incipient wetness impregnation and deposition-precipitation techniques. These methods synthesise the nanoparticles directly on the support, but pre-synthesised nanoparticles can also be loaded onto supports through the incipient wetness impregnation method. These three methods were selected for their simplicity in both synthesis methods and equipment requirements and also for their prominent use in the literature.

The synthesis of metal nanoparticles prior to their immobilisation upon a support is one option for metal nanoparticle immobilisation. The synthesis of metal nanoparticles will typically require the use of capping agents to prevent agglomerations and control size. This pre-synthesis method can encounter issues with the removal of the capping agents after metal nanoparticle immobilisation. High temperatures are needed to remove these compounds that can facilitate the melting and agglomeration of the nanoparticles. Agglomerations are also facilitated by the low contact angle between the nanoparticles and the support that will be a result of such

loadings. As they are synthesised as spheres, when loaded they have a low contact angle compared to hemispherical particles. Figure 6.2 demonstrates the change in contact angle with changing nanoparticle shape of supported nanoparticles.

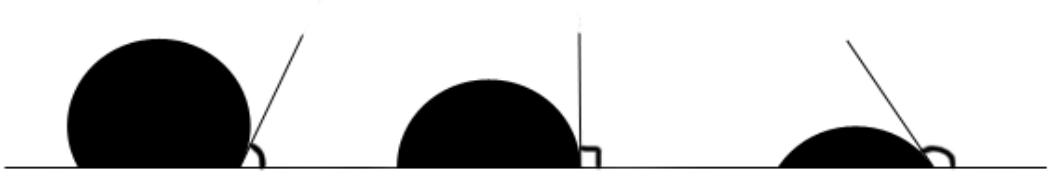

Figure 6.2 – Contact angle variation with changing particle shape.

In-situ synthesis of metal nanoparticles directly on the support can allow for smaller nanoparticles with higher contact angles with the support. Size and shape can be controlled through changes to conditions. A comparison of particle size with changes to methods and conditions is made later in this literature chapter.

Deposition-precipitation is the method by which the solid support is evenly suspended in a solution containing the metal ions, to which precipitation is facilitated to cause the reduction of the metal onto the support, forming nanoparticles. The precipitation can be facilitated through changing the solubility of the metal; this can be achieved, for example, by the addition of a precipitation agent or by the reduction of the solvent volume through heating over time.

During the deposition-precipitation, the surface of the support acts as a nucleating agent for the metal precipitation[88]. It is desired that the precipitation takes place exclusively on the surface of the support. As such, local super-saturation must be as limited as much as possible to prevent precipitation occurring freely in solution[122]. From a catalysis perspective, this method could encounter issues with the precipitation agent adsorbing to the support and potentially blocking catalytic sites requiring the catalyst to be calcined at high temperatures to activate.

Ion adsorption is the method by which metal ions are adsorbed to the surface or are exchanged with ions in the surface of the support. To facilitate the adsorption of ions to the surface the charge of the surface should be adjusted through changing the pH relative to the isoelectric point. The isoelectric point is the pH at which a surface has no charge, by lowering the pH a positively charged surface is created, and by raising the pH a negatively charge surface is created[88]. Ion exchange is typically performed by suspending the support in a solution containing the metal ion; at a low pH for anion adsorption and a high pH for cation adsorption, whilst heating.

The isoelectric point is unique to the support and can vary with the exposed crystal plane at the surface[123]. The ion exchange method could potentially allow for a more even distribution of metal across the surface of the support than the deposition-precipitation. This variation in resulting particle size distribution is mainly due to the deposition of metal during ion exchange occurring as single ions across the support, opposed to nucleation sites at specific points on the surface as in the deposition-precipitation method. Both the deposition-precipitation and the ion exchange method have a similar disadvantage, the inability to ensure the utilisation of 100 % of the metal during synthesis. That is to say, that a certain percentage of metal will remain in solution, rather than on the support after synthesis is complete. Although at low loading weights the percentage of metal left in solution can be relatively low, due to the expense of catalytic active metals this could still be a significant cost and would require addition metal recovery steps.

The incipient wetness impregnation consists of the wetting of the support by a metal solution whose volume is exactly equal to the volume of the pores[88]. In this case, and contrary to the ion exchange and deposition-precipitation method, it utilises 100 % of the metal. However, it also guarantees the full loading of any other ions in the metal solution to the support, which can potentially act as poisons for catalytic applications. It is similar in some ways to the deposition-precipitation, as the drying process forces the metal to precipitate out as the supersaturating point is reached. However, during drying a wicking effect of the solvent can

cause an uneven precipitation of metal at the air-surface interface. Due to this, the process presents a lower level of control in the loading conditions than the other two reported here.

Photo-deposition is a technique for synthesising metal nanoparticles on a photoactive support. The method takes advantage of the semiconductor nature of the support, in which high energy light is used to cause metal ion reduction through the creation of an electron-hole pair[124]. It is therefore similar in some way to the deposition-precipitation, though in this case light is the precipitation agent. The resulting immobilised metal nanoparticles on semi-conductor support have potential to act as photo-catalysts. This can result in the wavelength of light required for the synthesis of the catalyst, catalysing other reactions in the synthesis procedure. This needs consideration as the potential production of radicals, for example, could be of danger of destroying the catalyst support[124].

Post treatment reduction of these immobilised metals on supports is normally required to fully reduce the metal ions to metals. Certain metal nanoparticles, such as iron, can easily re-oxidise in the presence of oxygen which requires their in-situ reduction prior to reaction [125]. The two most common methods of reductions used post metal ion immobilisation is the thermal treatment under a flow of hydrogen[126] and the reduction after metal loading, in solution, through the addition of a reducing agent such as $NaBH_4$[127].

6.3 Platinum nanoparticles

Platinum nanoparticles of varying shapes and sizes have been synthesised both in solution[128] and immobilised on supports[129]. They have been demonstrated to have a high activity for catalysis in many reactions, including water gas shift[130], carbon monoxide oxidation[131], oxidation of organic compounds[132] and hydrogenation[133]. Platinum nanoparticles are also shown to have photocatalytic activity, often when immobilised on titania as a semiconductor support[134, 135].

Platinum nanoparticles have no absorbance in the UV-visible spectra[136] appearing black in colour. Several publications comparing the activity of different Pt crystal surfaces, to investigate nanoparticle shape effects, both experimentally and through computational simulations, have focused on the (111), (110) and (100) surface[133, 137]. These studies found the stepped (111) surface to be more active due to the defect sites[133]. Also it was discussed that CO diffusion to and from the surface was significantly faster than the rate of CO oxidation[138] but that CO adsorption becomes restricted as particle sizes fall below a certain size between 2 and 3 nm[133]. However, the specific crystal surfaces and shape effects are outside the scope of this thesis, which mainly focuses on the effect of the metal loading method on the particle size distribution and catalytic activity.

6.3.1 Platinum nanoparticle immobilisation on ceramic supports

The previously mentioned methods of synthesis for metal nanoparticles directly onto a support are not standardised or fully understood in the literature. There has been some work that study the effect of changes to the loading conditions[88]; but often different papers report variations in concentrations, pH, temperature, time, metal precursors and washing methods that make different papers incomparable. Take the deposition-precipitation method as an example, variables include, pH, precipitation agent, concentrations, temperature, atmosphere, reduction method, metal precursor and time. The full contribution to controlling metal particle size and interaction with the support of each variable is not fully understood. Table 6.1 gives brief information on a few techniques of synthesising Pt nanoparticles on different supports and the resulting metal particle sizes and loading efficiency where possible.

Table 6.1 - Data on synthesis methods of Pt nanoparticles immobilised on carbon and ceramic supports by deposition-precipitation. Loading weights and particles sizes are shown along with a brief description of conditions.

Support	**Conditions**	**Total potential metal loading wt.%[a]**	**Actual metal loading wt.%[b]**	**Average particle size (TEM) / nm**	**Ref.**
Graphene	H_2PtCl_6, ethylene glycol, pH 13, reflux 130 °C under Ar	5.28	5.28[c]	<10	[139]
Multiwalled Carbon Nanotubes	H_2PtCl_6, ethylene glycol, pH 13, reflux 140 °C under Ar	11.1	11.1[c]	2.6	[140]
	Aqueous H_2PtCl_6, pH 11, reflux 85 °C, under Ar	11.1	11.1[c]	3.4	[140]
SBA-15 Mesoporous Silica	Aqueous $[Pt(NH_3)_4](OH)_2$, pH 3.5, urea, 90 °C, under N_2	0.5	0.25	3.4	[141]
CeO_2	Aqueous H_2PtCl_6, pH 7, 70 °C	n/a[d]	5	1.6	[142]
TiO_2 particles	Aqueous H_2PtCl_6, ethylene glycol, 130 °C, under inert	0.5	0.2	n/a	[143]
Commercial TiO_2 P25	Aqueous H_2PtCl_6, evaporated at 40 °C under vacuum to a paste	1	1	1.4	[144]
	Aqueous H_2PtCl_6, pH 7-10, six repeat loadings	n/a[d]	1	1.3	[144]

a - Weight of metal if 100% loading was achieved, given as a weight % of Pt-support / wt.%

b - Actual weight of metal, given as a weight % of Pt-support / wt.%

c – The final weight is implied to be 100% of loaded Pt

d – The initial weight is not given in the paper

Table 6.1 demonstrates the variations reported in the literature for the methods of loading Pt by deposition-precipitation. The lack of data to determine what the real final metal loading efficiency is and whether it has been assumed to be 100% or not, makes comparisons less meaningful, especially considering literature reports that 100% loading through deposition-precipitation with Pt is not possible[88]. The most notable issue however, is with the

methods that appear to diverge from that of deposition-precipitation. The loading method on ceria, for example, is quite possibly proceeding, to at least some extent, through ion adsorption, whilst that of the TiO_2 P25, appear to be somewhat similar to incipient wetness impregnation methods. These hybrid techniques, which cross the line between different loading methods make literature comparisons complicated and in some cases impossible.

The incipient wetness impregnation method, which appears to be the most consistent method through the literature[88, 145, 146], still presents possible variations through the use of different reduction conditions, supports and metal sources, resulting in a huge array of possible variation in immobilised metal nanoparticles.

The data in Table 6.1 demonstrates that ceramic materials are capable of stabilising metal nanoparticles synthesised by deposition-precipitation, of similar or smaller sizes, to those reported for the more intensively studied carbon supports. Several further methods of platinum nanoparticle synthesise directly on the surface of titania are compared in Table 6.2.

Table 6.2 - Data on deposition-precipitation, incipient wetness impregnation and photo-deposition methods of synthesis for Pt nanoparticles on titania. Loading weights and particles sizes are shown along with a brief description of conditions.

Support	**Method of loading Pt**	**Conditions**	**Total potential metal loading wt.%[a]**	**Actual metal loading wt.%[b]**	**Average particle size (TEM) / nm**	**Ref.**
Commercial TiO_2 (53 m^2 g^{-1})	Incipient Wetness Impregnation	$Pt(acac)_2$ in DMSO, reduced/dried at 420 °C	2	2	1.9	[146]
Commercial TiO_2 (340 m^2 g^{-1})			2	2	2.0	[146]
TiO_2 (57 m^2 g^{-1})			2	2	2.5	[146]
TiO_2 (98 m^2 g^{-1})			2	2	2.3	[146]
TiO_2 (58 m^2 g^{-1})	Photo-Deposition	H_2PtCl_6, isopropyl alcohol, 240min 300W lamp under N_2	0.5	0.33	5.9	[147]
			2	1.00	>10	[147]
		H_2PtCl_6, isopropyl alcohol, 15 min 300W lamp under N_2	0.5	0.23	2.9	[147]
Commercial TiO_2 P25 (50 m^2 g^{-1})	Deposition-Precipitation	Aqueous H_2PtCl_6, evaporated at 40 °C under vacuum to a paste	1	1	1.4	[144]
		Aqueous H_2PtCl_6, pH 7-10, six repeat loadings	n/a[c]	1	1.3	[144]

a - Weight of metal if 100% loading was achieved, given as a weight % of Pt-TiO_2 / wt.%

b - Actual weight of metal, given as a weight % of Pt-TiO_2 / wt.%

c – The initial weight is not given in the paper

The methods displayed in Table 6.2 show that relatively small platinum nanoparticles immobilised on titania can be synthesised through a variety of methods. Several papers report the use of photo-deposition; however, these methods appear to give a poor loading efficiency of

platinum. There does not appear to be a relationship between TiO_2 surface area and metal particle size, suggesting that dispersion is not an issue during synthesis for the metal to surface ratios reported.

The literature appears to be in some disagreement about the methods of metal loading and the conditions which distinguish between them. Often papers following previous methods will make adaptations that appear somewhat arbitrary, furthering comparison complications.

Comparing the resulting metal nanoparticles sizes of the Pt on titania, Table 6.2, with the Pt on other supports, Table 6.1, it can be observed that typically titania allows for the stabilisation of nanoparticles similar in size to those supported on carbon or other ceramics.

Table 6.3 - Data on synthesis methods of Pt nanoparticles immobilised on titania and titanate nanotubes. Loading weights and particles sizes are shown along with a brief description of conditions.

Support	**Method of loading Pt**	**Conditions**	**Total potential metal loading wt.%[a]**	**Actual metal loading wt.%[b]**	**Average particle size (TEM) / nm**	**Ref.**
TiO_2 nanotubes[c]	Incipient Wetness Impregnation	Aqueous H_2PtCl_6, reduced at 500 °C	0.4	0.4	~10	[148]
Titanate nanotubes[d]		Aqueous H_2PtCl_6, sonicated, reduced by $NaBH_4$	10	10	3 to 9	[127]
Titanate nanotubes[d]	Ion Exchange	Aqueous H_2PtCl_6, reduced at 400 °C	1.2	1.2[e]	2 to 5	[149]
Titanate nanotubes[d]	Vapour phase impregnation decomposition	Platinum acetylacetonate at 400 °C	16.5	14.5	2.1	[150]
TiO_2 nanotubes[c]	Photo-Deposition	H_2PtCl_6, water and ethanol, 4hours 300W lamp	2	2[e]	2 to 4	[124]
Titanate nanotubes[d]			2	2[e]	n/a[f]	[124]
TiO_2 nanotubes[d]	Deposition-Precipitation	H_2PtCl_6, water and formaldehyde, 80 °C under UV (254 nm)	1.5	1.5[e]	3	[12]

a - Weight of metal if 100% loading was achieved, given as a weight % of Pt-Support / wt.%

b - Actual weight of metal, given as a weight % of Pt-Support / wt.%

c – TiO_2 nanotubes are prepared through the anodization of Ti foil

d – Titanate nanotubes are prepared through the alkali hydrothermal synthesis method of TiO_2

e - The final weight is not analysed and is implied to be 100% of added Pt

f – Not given, nanotube morphology destroyed

As discussed, there are numerous variables that play a role in varying metal loading; however, often procedures are not vigorous enough to allow for total replication of works. Additionally the assumptions of total loadings that are sometimes made have been suggested to be untrue elsewhere in the literature[88] preventing comparisons with different papers.

Several methods of immobilisation of Pt nanoparticles on titania[148] and titanate[127] nanotubes are reported in Table 6.3. The incipient wetness impregnation method appears to produce smaller Pt nanoparticles on titanate nanotubes synthesised through the hydrothermal method than titania nanotubes synthesised through Ti foil annodization despite the Pt loading being an order of magnitude higher in the first case. It is also worth noting that the TEM images of the Pt immobilised on titanate nanotubes appeared to show some denaturing of the nanotube morphology, that could have been a result of the ultrasonic treatment step[127].

It is known the titanate nanotubes have a good cation exchange[91] and the method of platinum loading during ion adsorption is a likely result of ion exchange with the hydrogen ions[91]. Studies[149] found that loading of greater than 1% Pt caused the nanotube morphology to be lost although the same result was not observed in similar studies[91].

The photo-deposition method was employed for the anodized titania and hydrothermally produced titanate nanotubes[124]. Although it has been demonstrated elsewhere[147] that full loading does not necessarily occur, the work implies that it does here. It also notes that the titanate nanotube structure is denatured, possibly due to the photo-decomposition of H_2O to form $H^{\bullet}$ radicals which in turn combine with OH or unsaturated O on the surface of the nanotubes and break the Ti-O bonds[124]. This suggests that photo-deposition is not a suitable method for loading Pt nanoparticles on titanate nanotubes and also that when suspended in an aqueous phase the exposure to light can be detrimental.

The use of the deposition-precipitation method for the synthesis of Pt nanoparticle, on what are reported as titania nanotubes[12] similarly to the photo-depostion method, assumed 100 % loading efficiency. It also performed the synthesis in the presence of UV light and formaldehyde, the latter of which was reported to be employed as a reducer. Although synthesis

was performed in the presence of light, albeit UV, the TiNT structure was maintained contrary to the observations of the photo-deposition work[124].

From the state of the art, on TiNT supported Pt nanoparticles it is possible to ascertain that similar particle sizes to those observed for titania and other ceramic supported Pt are achievable. However, the synthetic procedure must be carefully controlled as not to destroy the TiNT morphology as both light and sonication have been indicated to do so[124, 127]. It is also important that for methods where metal ions are capable of remaining in solution, that actual metal loading is analysed[88]. With these considerations in mind, the ion exchange and incipient wetness impregnation methods appear to be the most suitable 'wet chemical' methods for loading Pt nanoparticles on TiNT supports.

6.4 Catalytic activity of supported metal nanoparticles

The activity of transition metal nanoparticles for catalysis is well known for a wide range of catalytic applications. Their numerous oxidation states allow for them to accept or donate electrons, depending on the nature of the reaction to provide the catalytic activity. As the size of a metal nanoparticles is reduced to the point where the diameter is of a similar order of magnitude to the de Broglie wavelength[11] the physical properties of the metal change as predicted by quantum mechanics[151]. This size is between that of small molecules and the bulk material and the physical properties are highly dependent on the particle size and environment of the particle[11]. The metallic nature of the material observed in the bulk no longer applies; the number of atoms is small enough for the particle to be considered as discrete energy levels with a gap between the valence and conduction band, not present in the bulk metal, Figure 6.3[14].

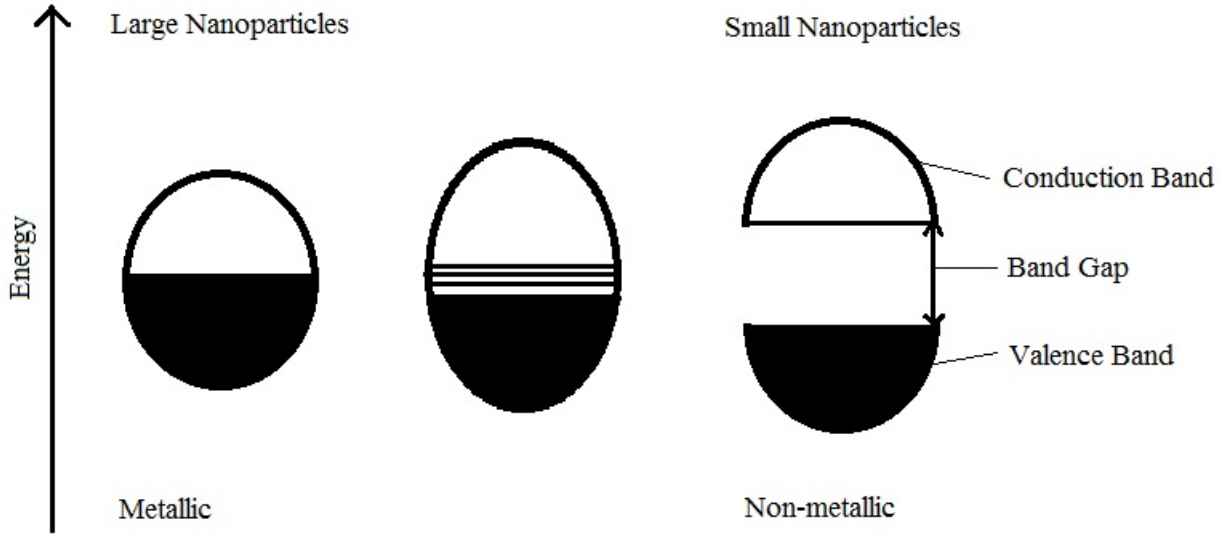

Figure 6.3 – Metallic to non-metallic nature of nanoparticles with decreasing particle size

When a metal nanoparticle is supported on a semiconducting support there is the possibility for the metal to lower the Fermi level potential by accepting excited electrons at a lower energy than the higher energy state in the semiconductor[152]. This is shown in Figure 6.4.

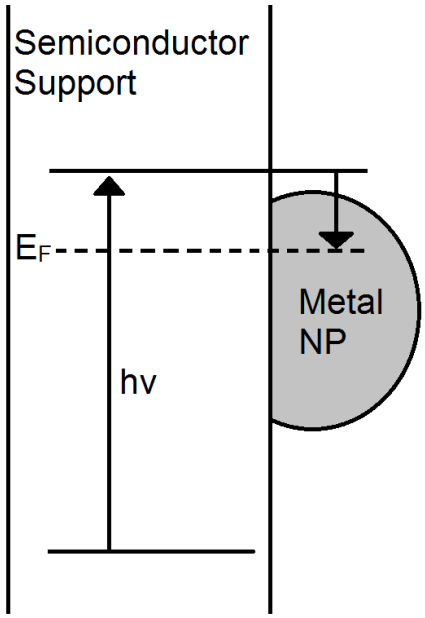

Figure 6.4 – Representation of how a metal nanoparticle (NP) can accept an excited electron to reduce the Fermi energy (E_F) level.

As the size of the nanoparticle is reduced to the point where the metal nanoparticle moves away from metallic like bonding[153] discrete energy levels occur. Small metal nanoparticles have been shown to have a high number of redox states that can allow for redox cascades, creating lower energy pathways for reactions to occur[11, 14]. The degree to which this occurs can be described by the Kubo gap equation, Equation 6.1, which gives an average energy for the spacing between energy levels.

$$\delta = \frac{4E_F}{3n} \quad \textbf{(6.1)}$$

Where δ is the Kubo gap, E_F is the Fermi level of the bulk and n is the number of valence electrons in the particle.

As the Kubo gap becomes higher than the thermal energy (kT), either through a reduction in the size of the metal nanoparticle to increase the Kubo gap or a reduction in the temperature to decrease the thermal energy, there is less metallic bonding[153, 154]. This means that as temperature increases the metallic nature of a nanoparticle will reduce, and so will the potential to offer a higher catalytic activity. This causes a pseudo 'race' for the activation energy with increasing metallic nature as temperature is increased.

The effect of the non-metallic nature of small metal nanoparticles and the ability of supported metal nanoparticles to lower the Fermi level can combine to afford extra catalytic activity. DFT studies in the literature have suggested evidence to support this; where higher catalytic activity is observed for active metal particles with catalytic sites blocked by less active semi-conductors, than the corresponding 'clean' metal particle[155]. This demonstrates a clear effect of the support playing a major role on the activity of small metal nanoparticles. These effects, along with the higher concentration of defects across the surface as the nanoparticle size reduces and the unsatisfied coordination of said defects result in catalysts of exceptional activity.

6.4.1 Catalytic Oxidation

Immobilised metal nanoparticles have been demonstrated to catalyse a vast array of reactions; decomposition of ammonia[156], water splitting[157] and Fischer–Tropsch processes[158] to name a few. However, this literature review is more concerned with the applications for oxidation reactions. The oxidation of hydrocarbons [159] primary alcohols[160], formic acid and formaldehyde[161] and other volatile organic compounds[162] have all been reported in the literature. However, the oxidation of carbon monoxide is still one of the most reported reactions to assess the relative activity of different metal nanoparticles, allowing a clearer comparison between studies.

Carbon monoxide oxidation is one of the main reactions taking place in the catalytic convertors of motor vehicles. Though CO is not a greenhouse gas itself and has a low lifetime relative to CO_2, it increases the residence time of methane and is eventually oxidised to CO_2 in the atmosphere[163]. Additionally it is a highly poisonous gas to humans at relatively low concentrations, responsible for air pollution in major cities and formation of smog.

The oxidation of carbon monoxide is often treated as a model reaction and shall be for the purpose of this thesis. CO often poisons metals due to its high chemisorption potential to many metals; however, in this reaction, that property is beneficial to the activity. The reaction mechanism of CO oxidation is assumed to be a Langmuir–Hinshelwood mechanism, the CO and O_2 both adsorbing to the surface of the catalyst, the O_2 bond breaking, O combining with CO and finally desorbing as CO_2, shown in Figure 6.5.

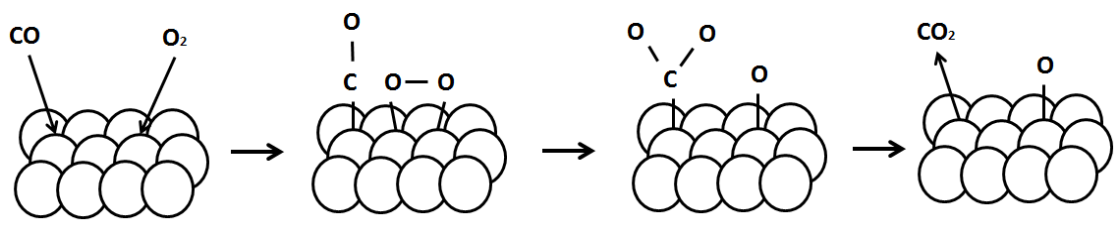

Figure 6.5 –Langmuir-Hinshelwood mechanism for CO oxidation on a heterogeneous catalyst.

However, for reactions on a surface with a high oxygen storage capacity the reaction can proceed through a Mars-van Krevelen mechanism, where the CO is absorbed to the surface and reacts with an O adatom in the crystal lattice, desorbing as CO_2. Finally, the oxygen vacancy is healed by O_2 closing the catalytic cycle, depicted in Figure 6.6.

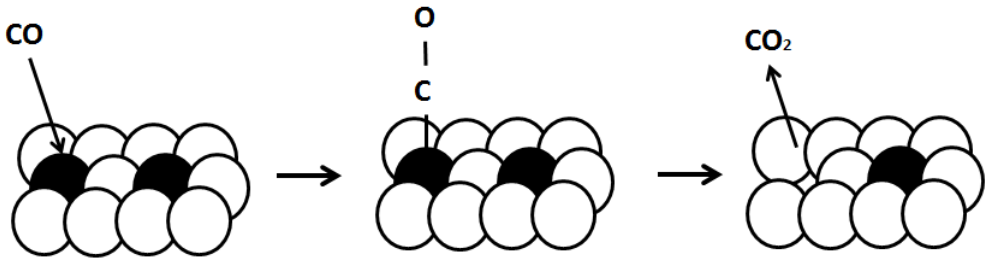

Figure 6.6 - Mars-van Krevelen mechanism for CO oxidation on a heterogeneous catalyst, black circles represent oxygen atoms in the crystal lattice, re-oxidation of surface is not shown.

6.4.2 Carbon Monoxide Oxidation of Supported Pt Nanoparticles

The use of supported Pt nanoparticles to oxidise carbon monoxide is extensively reported in the literature[21, 123, 131, 142, 164, 165].It is accepted that variations in the catalytic support have an important effect on the catalytic activity of identical nanoparticles[123]. Here, the activity of Pt supported nanoparticles are reviewed and compared to get a relative comparison of their activity. Table 6.7 compares the activity Pt supported on a variety of materials for CO oxidation.

Table 6.7 – Comparison of activity of Pt nanoparticles immobilised on different supports for the oxidation of carbon monoxide. Temperatures where conversion was first reported to occur and turn over frequencies (TOF) are reported where possible along with particle size and method of Pt immobilisation.

Catalyst	**Loading Method**	**Particle Size / nm**	**T_0 / °C**	**TOF[b] (at T / °C) / s^{-1}**	**Ref.**
Al_2O_3 / 5 wt.% Pt	Aqueous mixture with Pt precursor, evaporated to dry	3 to 10	< 20	3.08 x 10^{-3} (125)	[131]
SiO_2 / 5 wt.% Pt		3 to 7	< 20	2.39 x 10^{-3} (125)	[131]
Al_2O_3 / 2 wt.% Pt	Incipient Wetness Impregnation	0.9	204[c]	4.82 x 10^{-2} (175)	[21]
SiO_2 / 2 wt.% Pt		1.9	299[c]	4.92 x 10^{-2} (275)	[21]
TiO_2 / 3 wt.% Pt		1.3	188[c]	5.22 x 10^{-2} (125)	[21]
TiO_2 / 1 wt.% Pt	Deposition-Precipitation	1.3 ± 0.3	n/a	2.7 x 10^{-3} (27)	[144]
TiO_2 / 1 wt.% Pt	Incipient Wetness Impregnation	1.4 ± 0.3	n/a	3.8 x 10^{-3} (27)	[144]
TiO_2 / 0.9 wt.% Pt	Photo-Deposition	2.4 ± 0.6	n/a	9.2 x 10^{-3} (27)	[144]
NiO / 1 wt.% Pt	Colloid-Deposition	1.5 to 2.5	60	3.12 x 10^{-2} (100)	[166]
Al_2O_3 / 1 wt.% Pt		1.5 to 2.5	< 30	1.01 x 10^{-2} (100)	[166]
ZnO / 1 wt.% Pt		1.5 to 2.5	75	8.46 x 10^{-3} (130)	[166]
Titanate nanotubes / 1.5 wt.% Pt	Deposition-Precipitation	1 to 5	25 ± 5	n/a	[12]

a – Temperature at which activity is first observed

b - Turnover frequency (TOF) is given in terms of moles of CO per moles of Pt

c - Temperature is ignition temperature, where a switch to substantially higher activity is observed, rather than initial temperature of activity

The pre-synthesised Pt nanoparticles that are then immobilised on titanate nanotubes in Table 6.7[12] could result in poor surface-metal interaction. Though a low initial temperature of activity is observed, this can be misleading, as it has been shown that at higher CO concentrations and lower temperature there is low conversion region of CO by Pt nanoparticles, and at lower CO concentration and higher temperature there is a higher conversion region[167]. As temperature is increased there is an 'ignition' point, where activity suddenly increases, which was shown by EXFAS data to be due to a change of the metal to a metal oxide with higher activity[21].

The incipient wetness impregnation synthesised Pt nanoparticles on titania, silica and alumina, reported in Table 6.7[21], have a much higher initial temperature of activity than the others reported here. However, this is likely due to the fact that these temperatures are reported as the point of 'ignition', with negligible conversion occurring at lower temperatures that is not observed but present below baseline noise. This is supported by the fact that it was observed that using larger weights of catalyst lowered the apparent temperature of initial activity, implying that conversion was occurring below the reported temperature of initial activity, but below detectable levels. This demonstrates an obvious limitation in comparisons of activity versus temperature between different reports in the literature.

The turn over frequency (TOF) values of the Pt immobilised nanoparticles, Table 6.7, cannot be calculated where conversion has already reached 100% and as such is necessary to report at different temperatures. It appears that the titania supported Pt, by incipient wetness impregnation, has a much higher TOF at 125 °C than platinum on alumina or silica synthesised by the aqueous evaporation method. The TOF of titania supported Pt at 125 °C is similar to the values of the Pt on alumina and silica at 200 and 275 °C respectively. The TOF values of Pt on titania reported at 27 °C show low values, relative to those reported at higher temperatures (as would likely be expected). The TOF values in Table 6.7 appear to suggest that for Pt nanoparticle catalysts supported on ceramics, titania is a more active support than either silica or alumina[21].

The TOF values are strongly dependent on the catalyst preparation and treatment, as both affect the activity of the metal nanoparticles. To have a real comparison, TOF should be expressed in terms of the number of active sites instead of in terms of moles of metal as some metal atoms do not partake in the reaction. Ideally, it should also be adjusted to the particle size and consider factors such as contact angle and the interaction between the metal and support. Despite these limitations TOF provides a useful way to compare activity between different catalysts.

The Pt nanoparticles on titanate nanotubes synthesised through ion exchange[149], specifically the 0.5 mol% sample, was reported to be seven times more photoactive than commercially available P25 TiO_2. Whether this translates to non-photoactive reactions is unknown, as CO oxidation reactions using Pt on titanate nanotubes that are reported do not give enough information to calculate TOF values. However, the photo-activity and the fact that Pt on titanate nanotubes, Table 6.7, were active around room temperature, does suggest promise for Pt supported on titanate nanotube for CO oxidation catalysis.

Whilst this review has demonstrated that a large range of work has been produced that studies the loading and activity of metal nanoparticles on a variety of supports through different methods, it has also outlined the limitations with comparisons across the literature. The vast number of variables and the use of considerably different methods and conditions between different papers present a significant issue. Single studies comparing a wider range of conditions and methods using an identical procedure allow for a better understanding of these effects on the resulting metal loading and particle size, such as the study by Zanella *et. al.* focused on the loading of Au on TiO_2[88]. This thesis attempts to further the understanding of the effect of variable metal loading via different loading techniques on titanate nanotube support, and how these changes affect the loading efficiency and metal particle size. These metal nanoparticle supported materials are then tested for their oxidative catalytic activity using CO oxidation as a model reaction, to compare their variations in particle size and loading methods with catalytic activity.

Chapter 7

The Effect of Metal Loading Method of Titanate Nanotube Supported Metal Nanoparticles

This chapter focuses on the immobilisation of metal nanoparticles, specifically platinum, on titanate nanotubes and their characterisation. The relationship between the loading techniques and the metal loading on the resulting particle size are discussed. Relationships between the loading methods and catalytic activity and thermal stability are also investigated.

Titanate nanotubes are synthesised via a hydrothermal method. The support characterisation can be found in Chapter 4. Titanate nanotubes are used as a support for Pt nanoparticles with variable metal loadings made through different techniques, namely, ion exchange and incipient wetness impregnation. Average metal particles sizes were estimated by complimentary TEM measurements and CO chemisorption techniques. The reducibility of the supported metal nanoparticles was studied through temperature programmed reductions. These samples after being reduced thermally under hydrogen are tested for their catalytic activity using

CO oxidation as a model reaction to 400 °C. Multiple heating and cooling cycles on the same catalytic bed are used to investigate the stability of the catalysts.

7.1 Synthesis of Platinum Nanoparticles on Titanate Nanotubes

Platinum nanoparticles supported on titanate nanotubes (TiPt) have been prepared through several methods. The three methods of synthesis studied were ion exchange (IE), incipient wetness impregnation (IWI) and pre-synthesised nanoparticles (Pre-NP) loaded through the IWI method. The different methods were compared to study their effect on the resulting particle size, one of the main parameters determining their catalytic activity. A variety of metal loadings were also selected to study the effect of metal dispersion on particle sizes.

Platinum nanoparticles were synthesised via the IE methods using a range of initial platinum precursor (H_2PtCl_6) concentrations corresponding to 1.0, 2.9, 4.8, 6.5 and 9.1 metal weight%. However, the adsorption and exchange of the metal ions onto the support is an equilibrium, where the concentration of metal in the solution and the adsorption capacity of the support will determine the actual metal loading[88]. As such, temperature, time, metal, the nature of the support and concentration can all affect the loading efficiency. Atomic absorption spectroscopy (AAS) was used to measure the remaining Pt in the filtrate solution after synthesis to determine the actual platinum metal loading, as shown in Figure 7.1.

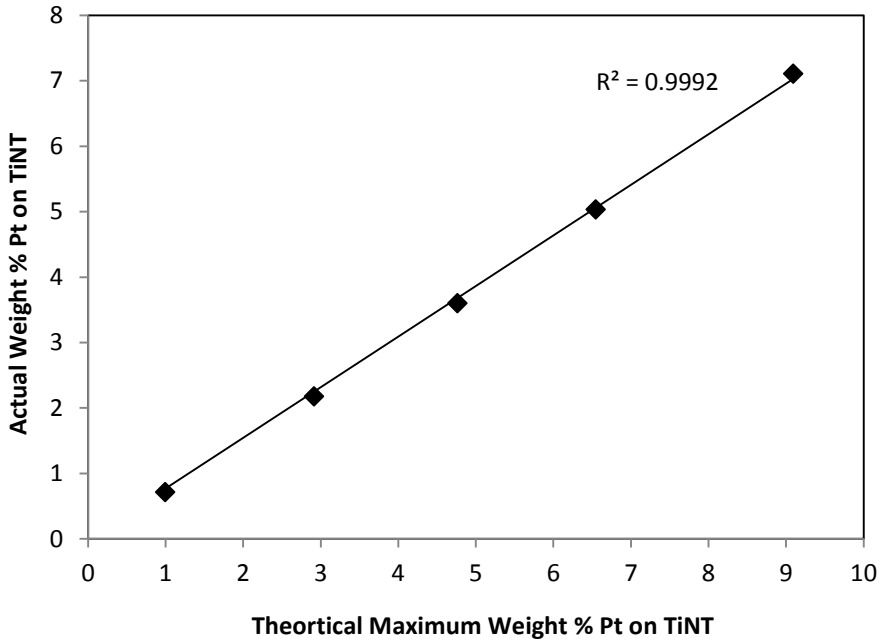

Figure 7.1- Relationship between metal concentration and metal loading for the synthesis of platinum nanoparticles on titanate nanotubes via ion exchange.

The AAS results show that there was a linear relationship between actual loading of Pt on TiNT and the concentration of Pt in solution for the IE method in the range of 1.0 and 9.1 wt.% under the experimental conditions. The 'actual metal loading' calculations were carried out using triple analysis of the metal content in the filtrate solutions, with blanks used between each reading and calibrations checked between each sample to ensure accuracy in the readings. The error bars were negligible, comparable to the size of the points on the graph. This demonstrates that the ratio of Pt on the support to the Pt in solution is constant throughout the concentrations used and under the conditions. The loading weights inferred from the results of the AAS for the IE synthesis and the notation used for TiPt prepared by this method is shown in Table 7.1.

Table 7.1 - Pt loadings and notation after ion exchange synthesis.

Pt during synthesis / wt.%	Total Pt Loading after synthesis / wt.%	Abbreviation
1.0	0.7	TiPt0.7%IE
2.9	2.2	TiPt2.2%IE
4.8	3.6	TiPt3.6%IE
6.5	5.0	TiPt5.0%IE
9.1	7.1	TiPt7.1%IE

Platinum nanoparticles were also synthesised on titanate nanotubes via incipient wetness impregnation (IWI). In this case, quantities of H_2PtCl_6 were diluted in the wetness volume of water to obtain loadings of 1.0, 2.9 and 4.8 weight%. Pre-synthesised nanoparticles were also prepared using a method from the literature[34], outlined in the experimental section, Chapter 2, and then loaded onto TiNT through the same IWI method. Due to the low concentration of Pt nanoparticles in solution during the pre-synthesis and the low wetness volume of ethylene glycol the maximum loading of these pre-synthesised nanoparticles with a single wetness impregnation was 0.6 wt.%. The use of ethylene glycol as a solvent for the nanoparticles was an integral part of the pre-synthesis method. The loadings and notations of TiPt made through IWI of H_2PtCl_6 and pre-synthesised Pt nanoparticles are shown in Table 7.2.

Table 7.2 – Platinum loading of the different TiNT catalysts prepared by incipient wetness impregnation and pre-synthesised Pt nanoparticles.

Pt added via IWI / wt.%	Source of Pt	Abbreviation
1.0	H_2PtCl_6	TiPt1.0%IWI
2.9	H_2PtCl_6	TiPt2.9%IWI
4.8	H_2PtCl_6	TiPt4.8%IWI
0.6	Pre-synthesised nanoparticles	TiPt0.6%Pre-NP

The platinum loadings were chosen to provide a good comparison between the two methods. Although a higher loading of Pt could be achieved by repeating the IWI process of the

pre-synthesised Pt nanoparticles successive times, a single impregnations was employed to minimise the number of variables, e.g. pre-established anchoring points. In any case, there will be some variations inherent to the different methods. For example, in the pre-synthesised nanoparticles case, they are reduced prior to the loading step while in the other two methods, loading is followed by reduction. There is also the potential for IWI synthesised TiPt samples to show less homogeneity of particles across the support due to the wicking effect during drying. The wicking effect occurs as the sample dries when the platinum containing solution is drawn to the surface during evaporation, potentially leading to a higher concentration of platinum on the surface of the support. To lessen this effect, the sample was well distributed across a clean surface during drying.

After metal loading, all samples were reduced under a 30 mL min^{-1} flow of hydrogen at 120 °C for 1 hour. This temperature was chosen to reduce any thermal destabilisation of the nanoparticles immobilised on the support so that all effects could be monitored through the catalytic studies investigated below. The already reduced Pt nanoparticles made through the Pre-NP IWI method were also treated to this reduction to maintain consistency in comparisons regarding thermal stability.

7.2 Characterisation of Platinum Nanoparticles Supported on Titanate Nanotubes

Temperature programmed reduction (TPR) experiments were performed on the TiPt samples to study how the temperature of Pt reduction and the shape of the reduction profile would be affected by the loading method and the metal content. The TPR profiles for the ion exchange synthesised TiPt samples is shown in Figure 7.2.

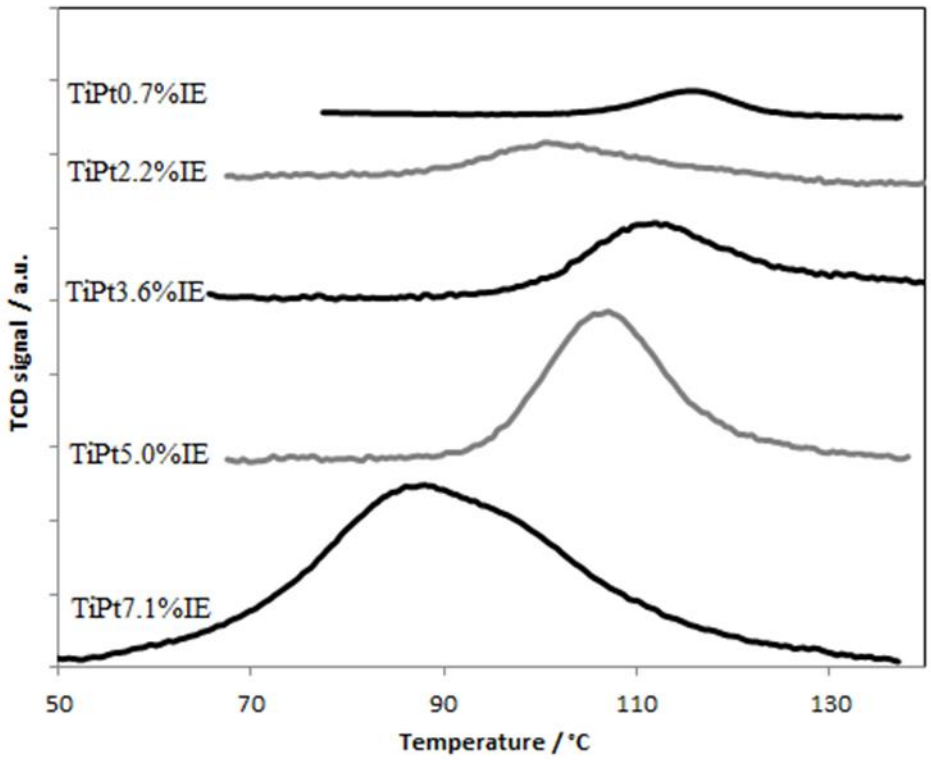

Figure 7.2 – Mass normalised TPR of platinum supported titanate nanotubes catalysts prepared by ion exchange. Conditions: 30 mL min^{-1} flow of 5% H_2 in Ar, heating rate of 10 °C min^{-1}.

The most notable observation of the TPR profiles shown in Figure 7.2, is the increased hydrogen consumption as Pt loading increases. Quantification of hydrogen consumption can theoretically be used to estimate the metal loading in the sample, however, this estimate was found to be highly inaccurate. The error is likely due to the partial pre reduction of the metal during the drying of the catalyst.

It is also observed that as the metal loading increases the reduction temperature decreases and the width of the peaks become broader. As metal particles with different sizes reduce at different temperatures, then this would suggest a larger distribution of particle sizes as loading increases. There is a general relationship between metal loading and the temperature of the maximum of the reduction profile, values shown in Table 7.3.

Table 7.3 –Temperature of maximum reduction during TPR of platinum supported on titanate nanotubes prepared by ion exchange.

Sample	Temperature of Maximum Reduction / °C
TiPt0.7%IE	116
TiPt2.2%IE	101
TiPt3.6%IE	112
TiPt5.0%IE	107
TiPt7.1%IE	88

The temperature maximum reduction decreases as the Pt loading increases, a relationship between this temperature and particle size is made later is this chapter, Figure 7.8. The TPR profiles of the IWI synthesised TiPt samples are shown in Figure 7.3 for the 1.0, 2.9 and 4.8 wt.% samples.

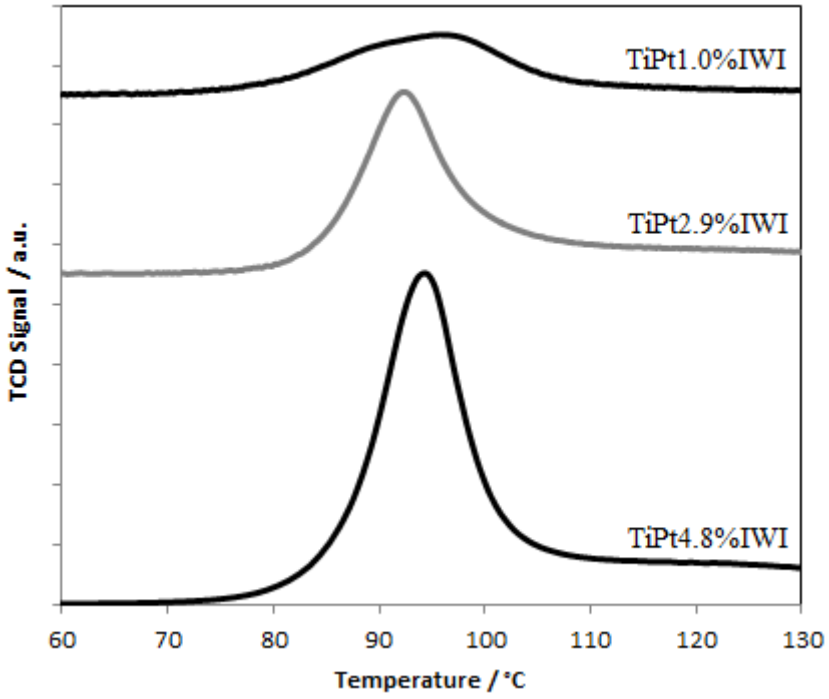

Figure 7.3 - Mass normalised TPR of platinum supported titanate nanotubes catalysts prepared by incipient wetness impregnation. Conditions: 30 mL min^{-1} flow of 5% H_2 in Ar, heating rate of 10 °C min^{-1}.

The TPR profiles of the IWI synthesised TiPt, Figure 7.3, show a similar relationship between hydrogen consumption and platinum loading to the ones synthesised by IE in Figure 7.2. Noticeably, the width of the reduction peaks is similar to, or slightly smaller than the peaks of similar Pt loadings synthesised through IE which suggests a similar dispersion of particle size. An important difference between the TPR profiles of IE and IWI synthesised catalysts is the relationship between maximum temperature and metal loading. Where, in the case of the IWI synthesised catalysts a similar temperature of maximum reduction is observed independently of the metal loading, Table 7.4, possibly suggesting a similar average particle size.

Table 7.4 - Temperature of maximum reduction during TPR of platinum supported on titanate nanotubes prepared by incipient wetness impregnation.

Sample	**Maximum Temperature of Reduction Profile / °C**
TiPt1.0%IWI	96
TiPt2.9%IWI	92
TiPt4.8%IWI	95

Considering that the maximum temperature of reduction is a function of particle size, catalysts with Pt loadings of 1.0, 2.9 and 4.8 wt.% are expected to have a similar average particle size to TiPt5.0%IE and TiPt7.1%IE. In order to confirm such a hypothesis and to further investigate the relationship between TPR profiles and particle size distribution, particle sizing was performed by complementary TEM imaging and CO chemisorption studies.

TEM images were taken of TiPt synthesised by IE and IWI after reduction at 120 °C. Multiple images were taken at different locations across the sample to get a good representation of the material. Representative images of TiPt samples are shown in Figure 7.4, further images can be found in Appendix A.

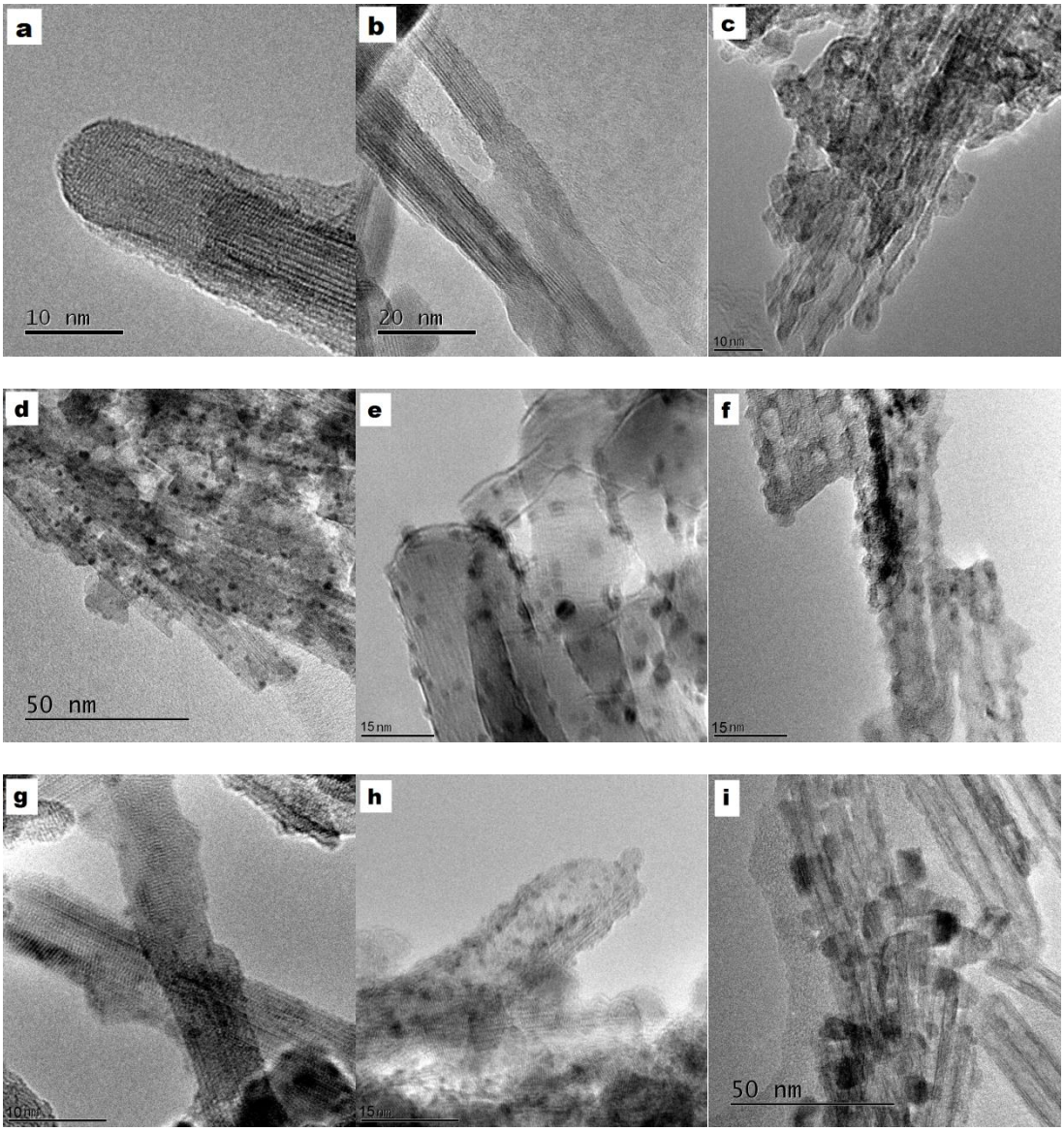

Figure 7.4- TEM images of platinum nanoparticles supported on titanate nanotubes synthesised through different methods. (a) – TiPt0.7%IE, (b) - TiPt2.2%IE, (c) - TiPt3.6%IE, (d) – TiPt5.0%IE, (e) – TiPt7.1%IE, (f) - TiPt1.0%IWI, (g) - TiPt2.9%IWI, (h) – TiPt4.8%IWI, (i) - TiPt0.6%Pre-NP

Visual observations and size measurements of the TiNT morphologies from the TEM images showed that TiNT retained their morphology during metal loading and reduction. This is contrary to what was reported in the literature[149] where the total destruction of the nanotube morphology was observed when using the ion exchange method at Pt loadings over 2.4 wt.%., possibly as a result of the layers of the tubular structure being separated.

It was also apparent that there was an increase in the concentration of larger metal particles as the metal loading increased. TEM images of TiPt synthesised through IE with

loadings of 2.2 weight% or below resulted in particles sizes below the resolution limit of the TEM, with no metal particles being observed at multiple locations across the material. This could be due to the resolution limit of the TEM which appears to be at around 1 nm.

In TiPt with platinum loadings above 2.2 wt.% metal particles were observed with an even dispersion across the surface of the TiNT support. However, there were a few areas where no platinum particles were observed as well as the occasional significantly larger Pt particles scattered across the material. These sample heterogeneities are associated with the limitations of TEM for particle sizing. It is possible that those areas where no particles were observed may actually contain nanoparticles of sizes below the detectable resolution limit. In a similar way, the observation of larger particles is likely due to the lower resolution required to detect them, increasing the frequency of such measurements.

Particle size distribution of the Pt nanoparticles from the TEM images was attempted through manually measuring. This method was chosen over algorithms due to the issues encountered with false particle detection due to the contrast of the TiNT support being high enough that no threshold could be selected for particle detection that did not falsely identify the support as metal particles. Even through a reported method[168] of breaking the image up into smaller subdivisions to attempt to discern between metal and support in more localised sections of the image was not sufficient in differentiating nanoparticles. A representation of how the metal particles were manually selected and sized is shown in Figure 7.5 to give a typical example of the selection process.

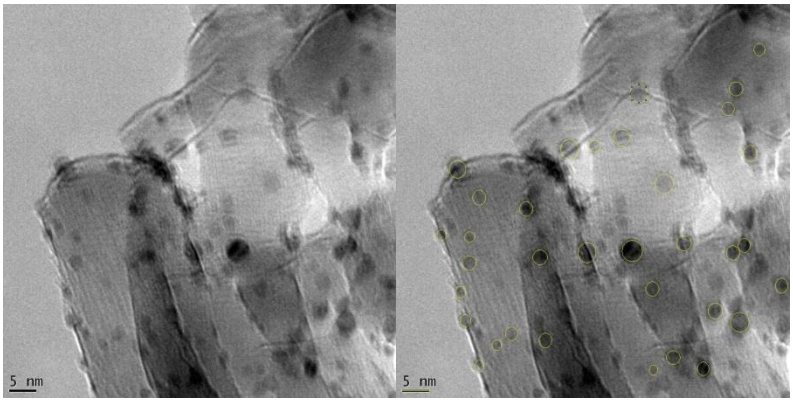

Figure 7.5 - TEM image of TiPt7.1%IE showing a representation of particles that are selected for sizing. The diameter of the yellow circle is used as the value for the particle size.

Nanoparticles that were chosen for imagining were particles that had a well-defined edge and had a circular morphology. The particles were treated as spheres with the diameter being taken as the particle size. Besides the issues regarding inconsistencies in measuring smaller and larger particles already mentioned, there is also a slight error based on the fact that the scale bar is set to a plane of focus in the image. As the image is 3-dimensional, certain particles will be above or below this plane and will give slightly larger or smaller particle sizes. However, this is an error of any measuring method using TEM. Consistency was also improved by measuring particle sizes of all images within a short time frame to maintain consistency in particle selection methods.

The distribution of particle sizes for the TiPt samples measured from TEM images are shown in Figure 7.6 as a box and whisker diagram. This method of representation was preferred to the typical size histogram as it allows for a direct comparison of the different particle size distributions in a clearer and more concise manner. The upper and lower bars represents the largest and smallest particles respectively and the box represents the data between the first and third quartiles of the distribution with the intersect line being the median value. In this way, narrower particle size distributions would show a small box and small bars.

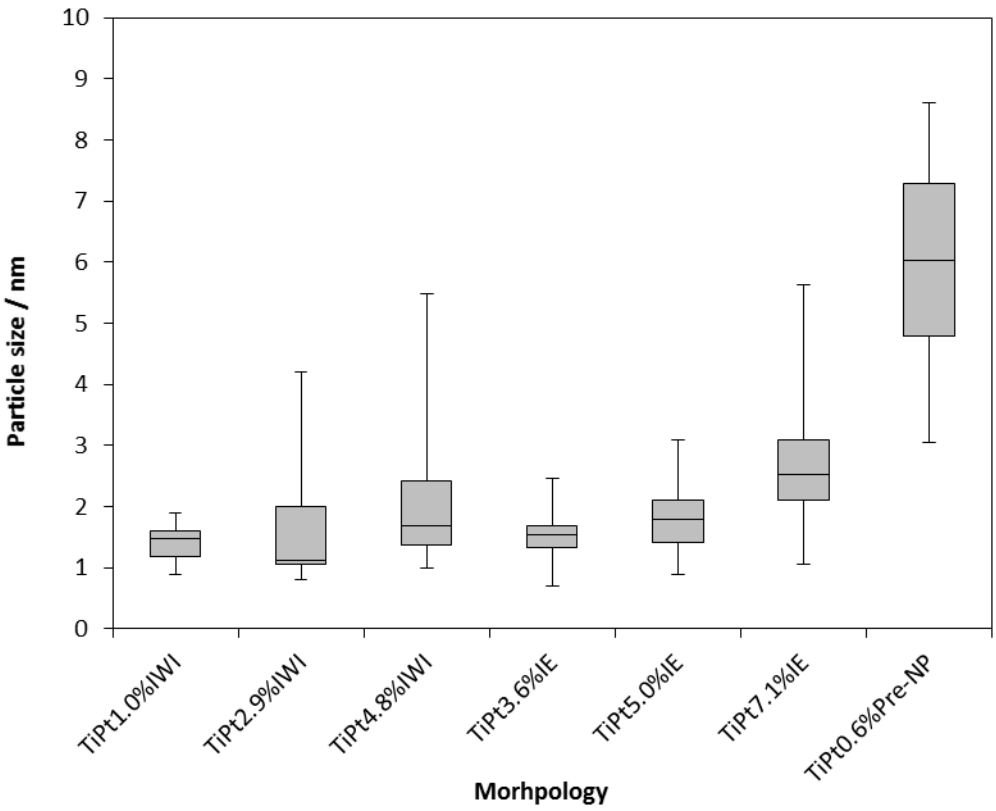

Figure 7.6 – Box and whisker particle size distributions measured from TEM imaging of TiPt catalysts reduced at 120 °C.

The IWI method provides larger particle sizes with a wider distribution of size than IE prepared TiPt. The large distribution in sizes could potentially be in part due to the wicking effect discussed before. This effect leads to less homogeneity and as such a large particle size distribution. The pre-synthesised nanoparticles result in significantly larger particles than either of the other methods, similar to what was predicted from the literature, ~7nm[34]. However, the average size was slightly lower than predicted, this could be an effect of supporting the particles, allowing for a more direct measurement, or as a result of the limitations discussed for sizing through the use of TEM. From the median particle size it is observed that, as metal loading increases so does the average particle size. This observation applies to all the samples except for the TiPt2.9%IWI which appeared to have a lower average particle size. However, considering the third quartile and the upper range of the 1.0, 2.9 and 4.8 wt.% IWI samples, there is a clear direct relationship between particle size and metal loading.

It is observed that for cases where the range of the 1st quartile is significantly smaller than the range of the 4th quartile, that the median is closer to the 1st quartile than the 3rd, as in cases of TiPt2.9%IWI, TiPt4.8%IWI and TiPt7.1%IE. To simplify, the distribution is weighted towards the smaller particle sizes. This is due to the reasons limiting the smallest particle observations as discussed and also the physical limit on particle size.

The average Pt nanoparticles sizes measured via TEM and CO chemisorption are shown in Table 7.5.

Table 7.5 - Particle sizes of Pt on TiNT synthesised through IE and IWI after reduction at 120 °C.

Sample	Median particle size measured by TEM[a] / nm	Mean particle size measured by TEM (1 σ) / nm	Mean particle size measured by CO chemisorption / nm
TiPt0.7%IE	N/A	N/A	0.9
TiPt2.2%IE	N/A	N/A	2.8
TiPt3.6%IE	1.5	1.5 (0.4)	3.8
TiPt5.0%IE	2.0	1.8 (0.4)	4.4
TiPt7.1%IE	2.5	2.7 (0.8)	3.6
TiPt1.0%IWI	1.5	1.4 (0.3)	2.6
TiPt2.9%IWI	1.0	1.6 (1.0)	3.1
TiPt4.8%IWI	1.5	2.0 (0.8)	6.4
TiPt0.6%Pre-NP	6.0	6.0 (1.4)	N/A

a – To nearest 0.5 nm

For the samples where the particle distribution measured by TEM, appeared to fit to a normal distribution, the median and mean were, as would be expected, identical. Whilst the median particle size for the IWI prepared TiPt shows TiPt2.9%IWI to be smaller than TiPt1.0%IWI, the mean size follows the trend noted for the IE samples, where there is a direct relationship between metal loading and size. The CO chemisorption calculated average particle sizes were consistently larger than the TEM measure particle sizes, but displayed the same relationships as observed from TEM imaging.

Comparisons between the Pt particle sizes, measured by TEM for the samples prepared by IWI, with the literature, show that they had similar particle sizes to those loaded on TiO_2 of different surface areas (1.9 to 2.5 nm)[146]. The particle size of Pt loaded by IWI, on silica supports[145] and titanate nanotube supports[148] in the literature (7.8 nm and ~10 nm respectively) is larger than those produced here (<6.4 nm).

As mentioned in the literature review, Chapter 6, the non-standardisation of experimental procedures resulted in very few publications where a comparable IE method is used for the synthesis of platinum nanoparticles on titania or titanate nanotubes. From the limited data available in the literature, it appears that previous methods of loading Pt on TiNT by IE have resulted in larger nanoparticles than measured in these studies at ~2-5nm for ~1 wt.% Pt[149].

Variations in particle sizes observed in Table 7.5 between the TEM and CO chemisorption methods are not unexpected. There are several assumptions and limitations to each technique that make them suitable for comparison, rather than for actual particle sizing. As previously mentioned, the particle size of 0.7% and 2.2% Pt on TiNT loaded by IE were not observable via TEM due to being below detectable limits. The TiPt0.6%Pre-NP particle size was not detectable by CO chemisorption due to the low metal surface area per weight of sample and thus the sample required to acquire accurate measurement was larger than could be accommodated into the sample bed.

The CO chemisorption technique presents some limitations associated to the assumptions made during the particle size calculations. It assumes the metal particles are perfectly hemispherical in shape. In reality the contact angle of the particle varies based on the metal interaction with the surface and the shape of the particle can change due to several factors, including the environment it is exposed to[169]. The full extent of this assumption and the potential error is shown in Figure 7.7, where the points represent the average particle size of the platinum nanoparticles assuming hemispherical morphology (contact angle 90°). The top bar is the size assuming a full sphere (contact angle 0°) and the bottom bar the particle size assuming full wetting (contact angle 180°), these two scenarios are practically unfeasible but demonstrate the full limits of the assumption.

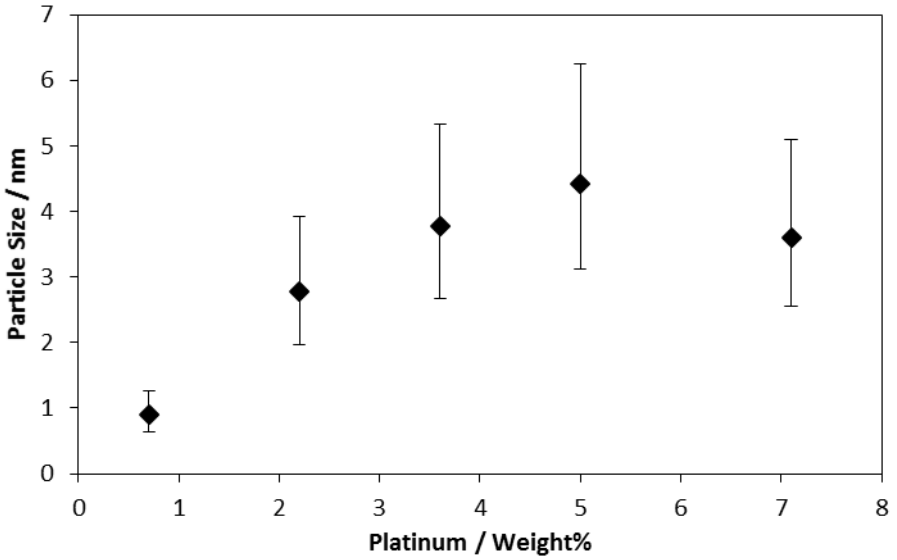

Figure 7.7 – Particle size calculated from CO chemisorption analysis of TiPt synthesised through the IE method as a function of metal loading. The error bars correspond to the sizes assuming perfect spheres (lower) and full wetting (upper).

Additionally, the CO chemisorption technique for particle sizing assumes a certain metal atom to CO molecule stoichiometry. However, this ratio strongly depends on the location of the metal atom, those atoms at corner and edge sites for example can potentially adsorb a higher number of CO molecules. Accurate fitting is extremely complex as it would require full knowledge of the stoichiometry for each site and the concentration of edge, step and face metal atoms for each particle size and shape. In this study, it was assumed that a CO:Pt stoichiometry value of 1:1 existed, following the literature[35, 36] and data given by the manufacturers, Micromeritics, in BEL-CAT application note, CAT-APP-002, 6th June 2003.

The CO chemisorption data for the TiPt samples, shown in Table 7.5, estimates larger values for the average particle size than what was observed via TEM. The CO chemisorption values for the particle sizes for the IWI synthesised TiPt was similar to the maximum value of the particle sizes measured through TEM. This observation could suggest that metal particles have a higher contact angle that 90°, which would, as shown in Figure 7.7, result in a smaller average diameter than those assuming hemispherical morphology.

The reducibility of the particles as a function of their size was studied in Figure 7.8 showing a slight the relationship between temperature of maximum reduction and Pt particle size.

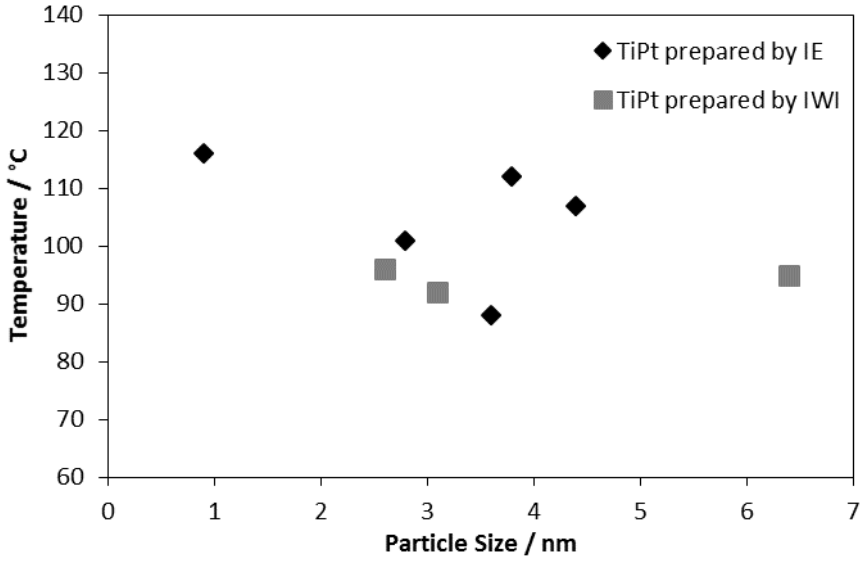

Figure 7.8 – Average particle size measured by CO chemisorption as a function of the temperature of the maximum peak in TPR experiments.

For this study, CO chemisorption was chosen as a sizing technique as it provides average platinum size values for all the catalysts. There appears to be a relationship between smaller particles and a higher temperature of reduction. However, the particle sizes are averages and, as mentioned, Pt was partially reduced by heating under air, both of which can lead to obfuscation of this trend. That the temperature required to reduce the Pt increases with decreasing particle size, is intuitive, when considering that smaller particles have higher surface to bulk ratio, increasing their energy per atom.

To conclude, in the platinum nanoparticles supported on titanate nanotubes, by ion exchange and incipient wetness impregnation, using chloroplatanic acid metal source, there was a general relationship between particle size and metal loading, with smaller particles as metal loading decreases. Both TEM and CO chemisorption are suitable techniques for particle sizing, however, both present limitations and assumptions which make the direct comparison of the

estimated particle sizes between the techniques unsuitable. The difference between the CO chemisorption and TEM particle sizes, with CO chemisorption suggesting larger sizes, is likely a result of uneven particle distributions but could suggest platinum particles with contact angles above 90°. There was an inverse relationship between platinum particle size and reduction temperature for the catalysts synthesised by IE; however, no relationship is observed for those catalysts synthesised by IWI. Pt nanoparticles loaded by IWI of similar metal loadings had similar median particle sizes to those synthesised by IE, measured via TEM. However, they had a larger size distribution compared to IE synthesised catalysts that resulted in a larger average particle size measurement by CO chemisorption, due to it measuring an average of all particle sizes.

Identical synthesis methods employing chloroauric acid in the place of chloroplatanic acid resulted in the synthesis of gold nanoparticles supported on titanate nanotubes. These supported nanoparticles synthesised by IE and IWI presented very similar trends to those observed for Pt, where larger particles and larger particle size distribution were observed for IWI synthesised catalysts compared to IE. This supports the conclusion that these larger particle distributions, compared to IE, are an effect of the IWI method using chloro-metallic acid as a metal source within the reaction parameters studied.

Metal loading efficiencies of Au by IE were lower than Pt (~50% compared to ~75%) and are shown in Appendix D, similar notation to that of Pt is used and identical synthesis methods as outlined in Chapter 2. Figure 7.9 shows the particle distribution of Au nanoparticles on titanate nanotubes synthesised by IE and IWI.

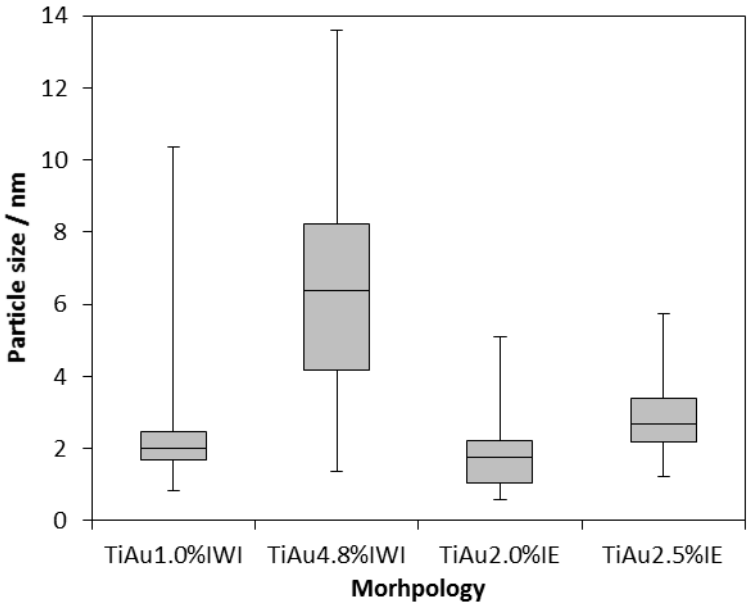

Figure 7.9 - Box and whisker particle size distributions measured from TEM imaging of TiAu catalysts reduced at 120 °C.

Table 7.6 shows the median particle size measured by TEM and the mean size measured by TEM and CO chemisorption for the TiNT supported Au nanoparticles. Similarly to the cases of the Pt, larger nanoparticles were observed through CO chemisorption analysis compared to TEM. Images used for TEM particle sizing are shown in Appendix A.

Table 7.6 – Particle sizes of Au on TiNT synthesised through IE and IWI after reduction at 120 °C.

Sample	**Median particle size measured by TEM[a] / nm**	**Mean particle size measured by TEM (1 σ) / nm**	**Mean particle size measured by CO chemisorption / nm**
TiAu0.5%IE	n/a	n/a	1.6
TiAu2.0%IE	2.0	1.8 (0.8)	2.9
TiAu2.5%IE	2.5	2.8 (1.0)	5.1
TiAu1.0%IWI	2.0	2.1 (0.7)	4.8
TiAu2.9%IWI	n/a	n/a	7.5
TiAu4.8%IWI	6.5	6.2 (2.5)	9.1

a – To nearest 0.5nm

7.3 Activity and Stability of Platinum Nanoparticles on Titanate Nanotubes as Catalysts for CO Oxidation

The oxidative catalytic activity of the platinum nanoparticles supported on titanate nanotubes (TiPt) synthesised through two different loading methods, ion exchange (IE) and incipient wetness impregnation (IWI) were studied using CO oxidation as a model reaction. The stability of the catalysts under reaction conditions were also studied by carrying out consecutive heating and cooling cycles. Turn over frequency and activation energy values were calculated for the different catalysts to compare their activity and reveal the effect of metal loading methods and particle sizes determined earlier in this chapter.

7.3.1 Platinum Nanoparticles Supported on Titanate Nanotubes via Ion Exchange Synthesis

Platinum nanoparticles were supported on titanate nanotubes via ion exchange of protons on the support surface by platinum cations followed by reduction as described in the experimental chapter. The conversion of CO oxidation versus temperature between ambient temperature and 400 °C in the first catalytic cycle, using TiPt catalysts with different metal loading between 0.7 and 7.1 weight% are shown in Figure 7.10.

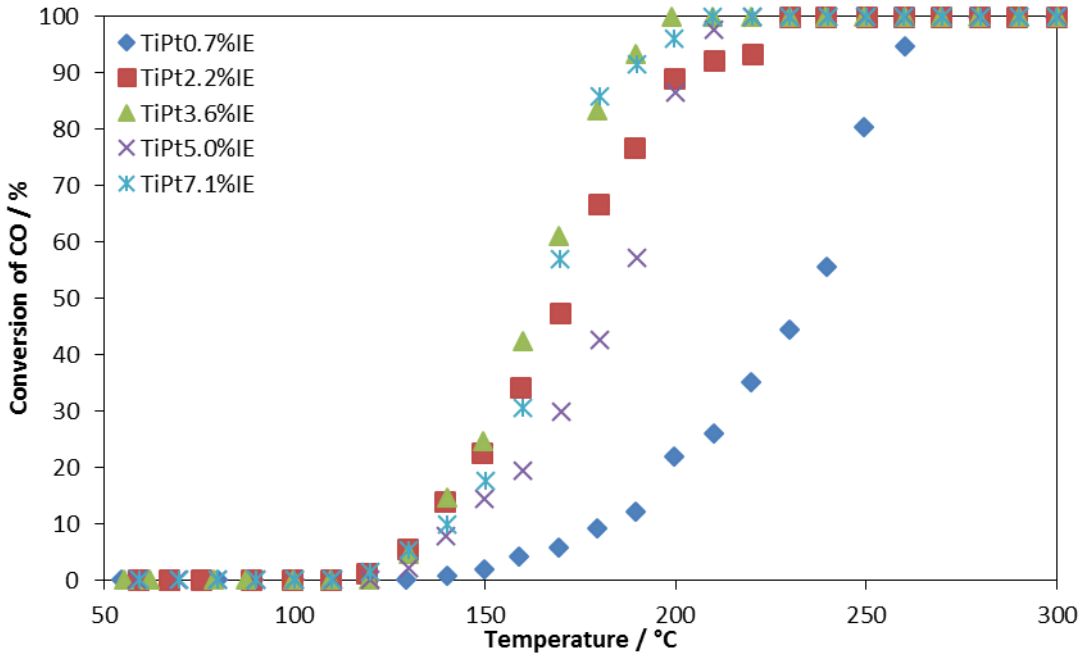

Figure 7.10- CO conversion of ion exchange synthesised titanate nanotube supported Pt nanoparticle catalysts as a function of temperature. Running at 50 mL min^{-1} of 2000 ppm CO, 2000 ppm O_2 in N_2 using 15mg of catalyst with a GHSV of 750 hour^{-1}.

It is observed that TiPt catalysts with Pt loadings of 2.2 wt.% and higher have a temperature of initial CO conversion at around 125 °C independent of the platinum loading within the studied range. However, the TiPt0.7%IE catalyst has significantly lower activity and an initial conversion starting at around 150 °C. The TiPt5.0%IE presents a slightly lower conversion relative to the catalysts with 3.6 and 5.0 wt% metal loadings.

The concept of an ignition temperature was discussed in the literature[21], Chapter 6. It is defined as the temperature below which, negligible conversion is observed and above which, significant increase in rates occur with further heating. This was reported to be due to a transition of Pt from a metal to a metal oxide[21]. It could be that what are thought to be the temperatures of initial activity in Figure 7.10 are in actuality the ignition temperatures and that negligible conversions are taking place below this temperature, low enough to be hidden by baseline noise. This is consistent with what was reported in the literature for similar catalysts, Pt on TiO_2, where the ignition temperatures were observed to be around 188 °C[21].

After the first heating catalytic cycle, the reactor was cooled in a controlled manner, at a rate of 2.5 °C min^{-1} to ambient temperature followed by a second consecutive run under the same conditions, increasing the temperature to 400 °C. The results of the second run are shown in Figure 7.11.

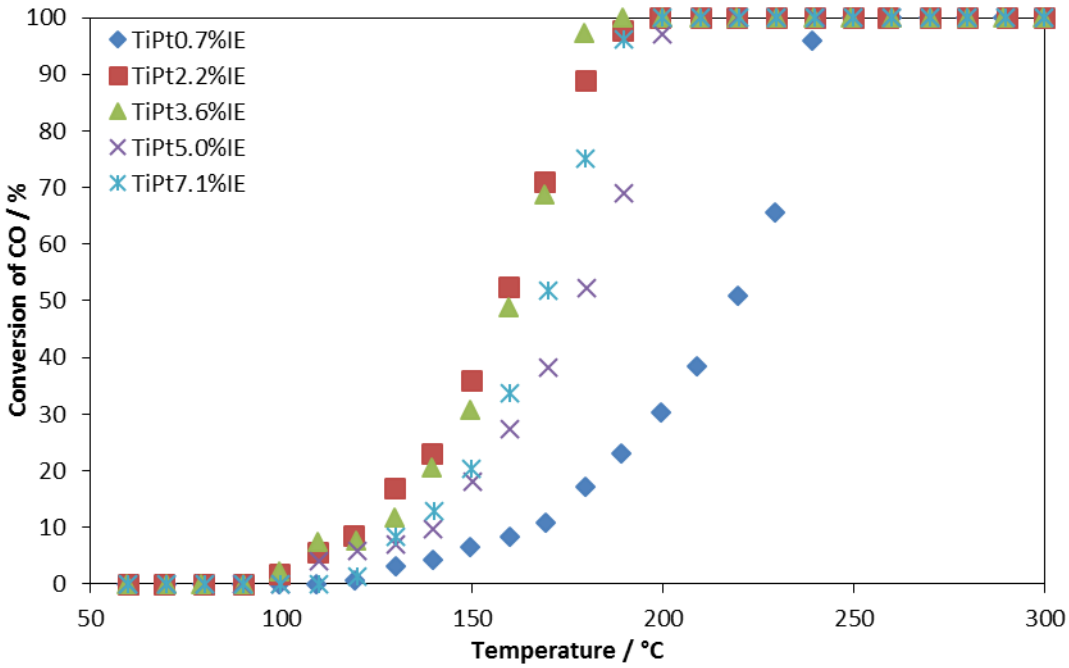

Figure 7.11 - CO conversion of ion exchange synthesised titanate nanotube supported platinum catalysts as a function of temperature in the second reaction run. Running at 50 mL min^{-1} of 2000 ppm CO, 2000 ppm O_2 in N_2 using 15mg of catalyst with a GHSV of 750 $hour^{-1}$.

Comparison of the CO oxidation reaction using IE synthesised TiPt catalysts during the second heating, Figure 7.11, and the initial heating, Figure 7.10, showed that the general trend in activity by Pt loading stays the same. However, the temperature where initial CO conversion is observed decreases in the second run from 125 °C to around 100 °C for Pt weight % of 2.2 to 5.0, whilst the 0.7 Pt weight % catalyst decreases from 150 °C to around 120 °C and the 7.1 Pt weight % catalyst only decreases very little. This demonstrates that the catalysts become more active after heating to 400 °C under the conditions of the CO oxidation reaction and that as such; their temperatures of initial activity are lower. This effect is less pronounced as the metal loading increases, with the greatest increase observed for the lowest metal loadings and little difference

in activity observed for the TiPt7.1%IE sample after the first run. As particle size has been shown to increase with metal loading, this could suggest that the increase in activity of low metal loading samples is as of a result of a change to the smaller nanoparticles.

There are two potential causes that can be responsible for this increase in activity. The first, is that active sites of the nanoparticles are partially blocked by molecules remaining after their preparation (e.g. chloride). These adsorbed compounds can be released during the first catalytic cycle under reaction conditions, especially as temperature is increased. However, CO chemisorption would be seriously hindered by these molecules and the results of such experiments did not suggest this.

Alternatively, the increase in activity in the second catalytic run can be associated with an agglomeration of the Pt nanoparticles that increases the activity. Although intuitively it may appear that particle agglomeration would result in reduced activity due to the reduction of surface area to mass, there have been reports in the literature that agglomerations can increase activity[170]. This could be as a result of increased metal-surface interaction due to shape changes or increased concentrations of certain more active surface sites that are more prevalent in the larger particle size. The literature has also demonstrated that Pt nanoparticles of less than 2 nm can be substantially hindered in their catalytic activity by a much slower CO adsorption below this size[133]. This would also explain why the activity increase was more pronounced for the lower metal loading samples, with the smaller nanoparticle sizes, as it would be the agglomeration of these sub 2 nm particles that increased activity.

This increase in activity after the initial heating and cooling cycle was then stable for subsequent catalytic cycles. The same catalytic bed that had been pre-reduced at 120 °C and used for CO oxidation to 400 °C in two subsequent runs, was again used for a third reaction to 400 °C. The catalytic activity during the third heating was observed to be identical to that of the second heating. An example of this stability for subsequent reactions after the first heating and cooling cycle is shown in Figure 7.12, where TiPt0.7%IE was used as a catalyst, due to it presenting the largest variation after the first catalytic heating cycle to 400 °C.

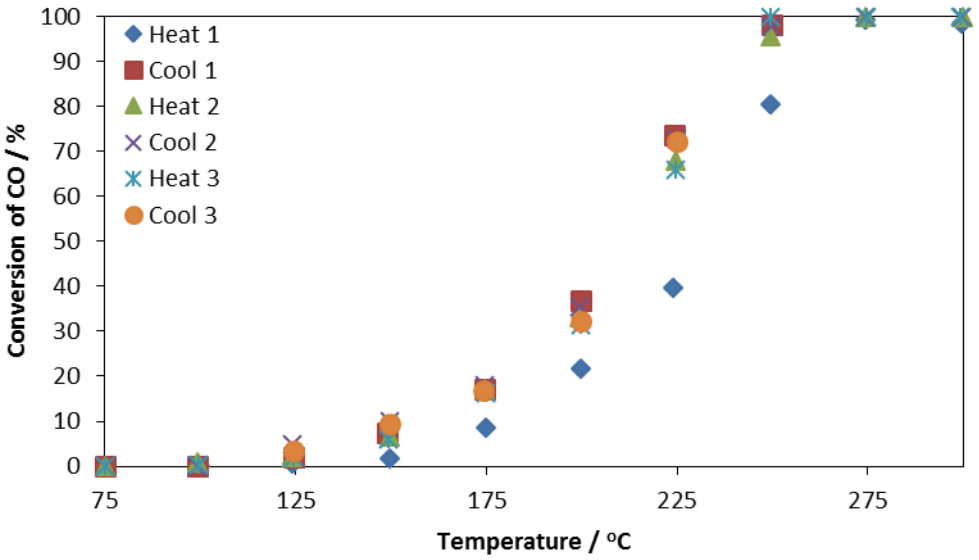

Figure 7.12 - CO conversion of TiPt0.7%IE catalyst as a function of temperature through multiple heating and cooling cycles. Running at 50 mL min^{-1} of 2000 ppm CO, 2000 ppm O_2 in N_2 using 15mg of catalyst with a GHSV of 750 $hour^{-1}$.

From consecutive heating and cooling catalytic cycles using the TiPt0.7%IE catalyst, it can be concluded that after the initial increase in activity after the first cycle, the catalyst is stable for the second and subsequent runs under the conditions used. This observation is also applicable to the TiPt catalysts synthesised through IE of other metal loadings up to at least 7.1 Pt weight % and is demonstrated in Appendix B.

The comparison of the reaction profiles of the different catalysts provides information of their relative activities and stability in activity in consecutive runs, however, it is difficult to understand the intrinsic differences due to the different platinum loading in each system. Thus the normalisation of the catalytic data per mole of platinum using turn over frequency values is shown in Figure 7.13.

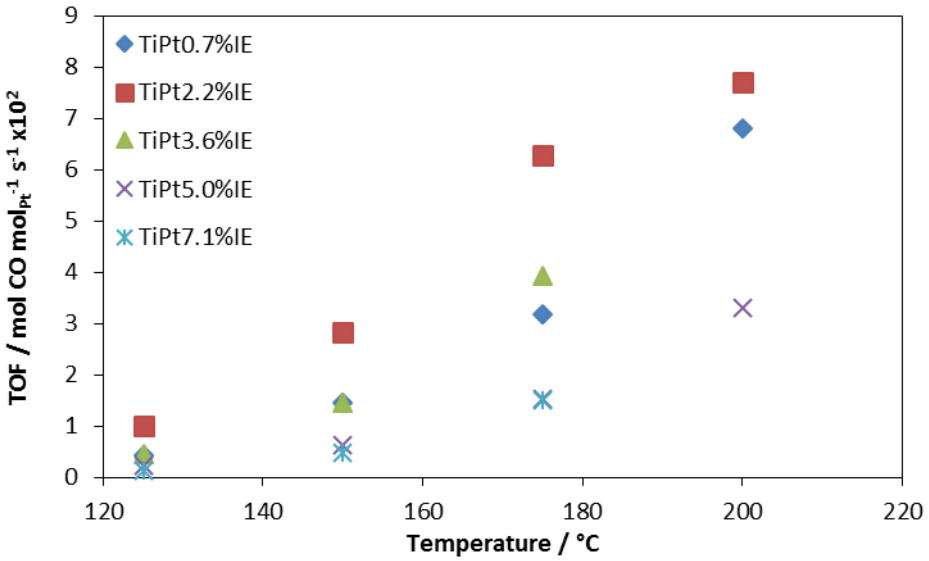

Figure 7.13 – TOF (mol CO mol_{Pt}^{-1} s^{-1}) values for the CO oxidation reaction using TiPt catalyst, synthesised by ion exchange used in the second heating catalytic cycle.

No data is given at 200 °C for the TiPt3.6%IE catalyst due to 100 % conversion being obtained by 190°C. There is an increase in the TOF values with respect to temperature for all catalysts after the initial reaction, the trend in activity remaining the same in both cases; 2.2 > 3.6 > 0.7 > 5.0 = 7.1.

The Arrhenius equation, Equation 7.1, is used to calculate the activation energy of the catalysts, to this end, the logarithm of the rate is plotted against the reciprocal temperature to produce a straight line that has a gradient proportional to the activation energy. The experimental chapter, Chapter 2, demonstrates the validity of the catalytic reactor in determining this and discusses the limitations and theory behind such calculations.

$$k = A\, e^{-\left(\frac{E_a}{RT}\right)} \qquad (\mathbf{7.1})$$

A typical example of the data that was calculated and used to determine the activation energies is shown in Figure 7.14, shown here to demonstrate the linear nature and consistency of results after the first heating cycle.

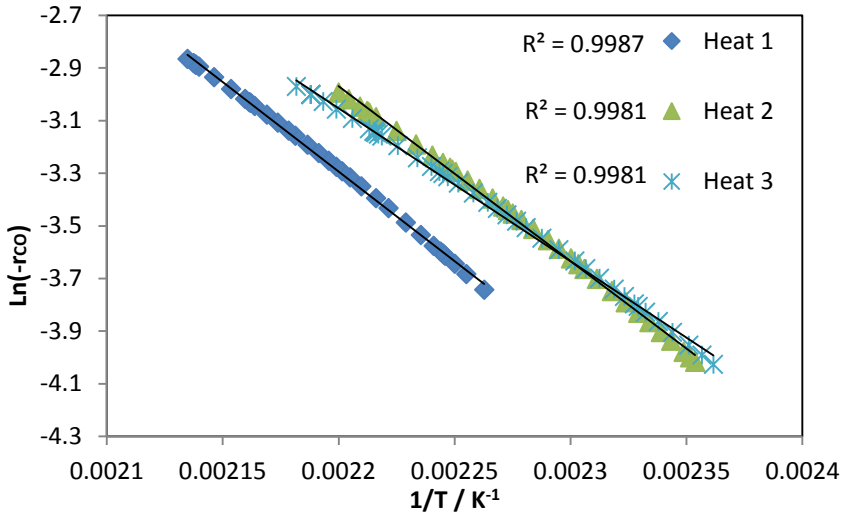

Figure 7.14 - The Arrhenius plot for the catalytic cycles between ambient and 400 °C using TiPt0.7%IE as a catalyst for CO oxidation reaction. Rate is calculated in terms of mol(CO) mol(Pt)$^{-1}$ s^{-1}.

From the Arrhenius plots it is important to note that the data shows a good linear nature. It is also observed that other than the initial heating, subsequent catalytic cycles displayed good consistency. The Arrhenius plots for the other TiPt samples synthesised via IE follow an identical trend and are shown in Appendix C. The activation energies for the different metal loadings of the first heating cycle and an average of the subsequent heating cycles are shown in Figure 7.15.

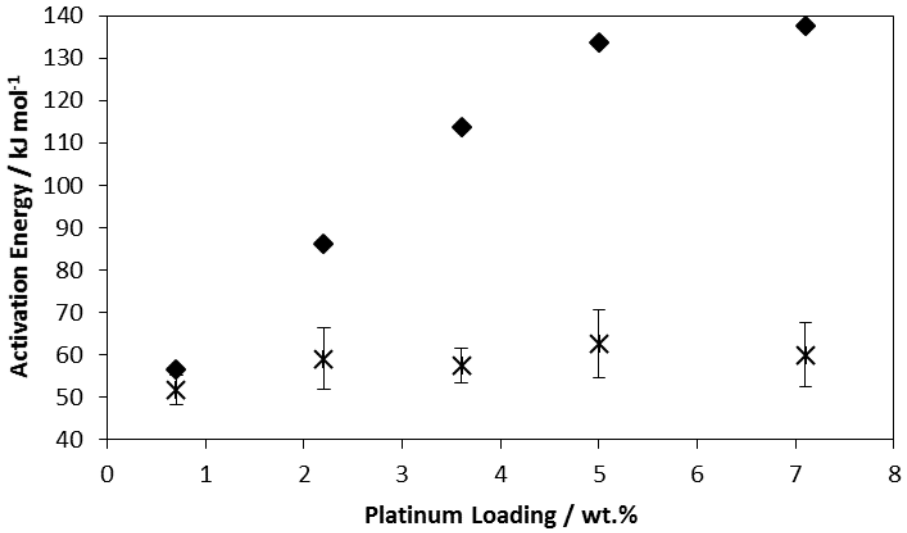

Figure 7.15 – The activation energy of CO oxidation using titanate nanotube supported platinum nanoparticles synthesised by ion exchange as a function of platinum loading. ♦ - *First catalytic cycle.* X *– Average of the subsequent catalytic cycles with standard deviation error bars.*

For the initial heating cycle using TiPt synthesised by IE there is a direct relationship between increased metal loading and activation energy. After the first cycle, all catalysts experience a decrease in activation energy which suggests a modification of the active sites. The catalysts after the initial heating cycle display a similar activation energy independent of metal loading. The activation energy after first cycle of the IE synthesised TiPt varies between 51 to 62 kJ mol^{-1}, lower values than any of the catalysts in the initial cycle.

The similar activation energies after the initial catalytic cycle suggest that after the first catalytic cycle the active sites responsible for conversion below 20 % are identical for all ion exchange synthesised TiPt catalysts. Interestingly, the catalysts that had the lowest Pt weight %, which were observed to have the largest change in conversion versus temperature had the smallest change in activation energy. The activation energy, taken from the gradient of the Arrhenius plot, is independent of the metal loading. The implication of this is that it suggests the low Pt weight % samples, which had the same active sites before and after the first catalytic cycle, had an increase in the number of active sites resulting in the lower initial conversion temperature. Whilst the higher Pt weight % samples, had a change in the type of active sites and

potentially number, that resulted in similar initial temperature of conversion. To better understand these observations a comparison of the TOF values and particle sizes can be made.

The average particle size for IE synthesised TiPt catalysts, was calculated using CO chemisorption and measured via TEM imaging. The particle size was compared to the TOF values at 150 °C for the catalysts after the first catalytic cycle to 400 °C in the CO oxidation reaction, shown in Figure 7.16.

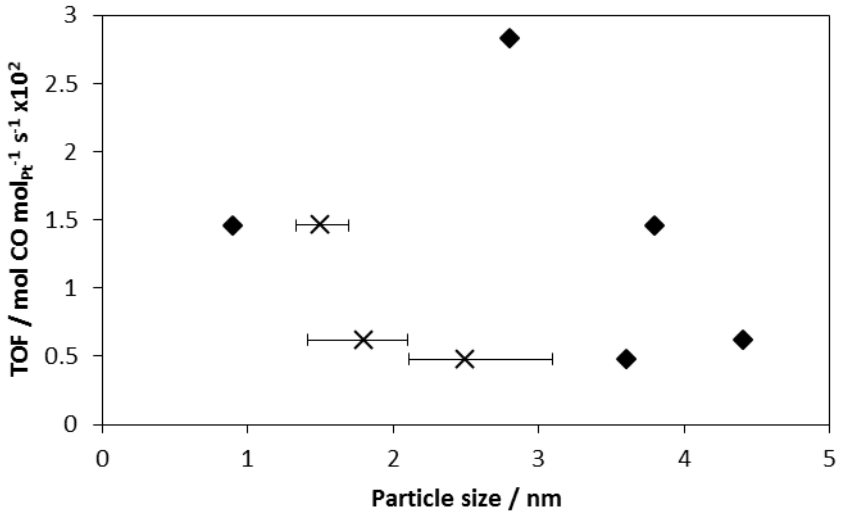

Figure 7.16 – Relationship between TOF values at 150 °C and average Pt particle size for the ion exchange synthesised titanate nanotube supported platinum nanoparticle catalysts. TOF values are calculated from the second catalytic cycles. ♦ *- Mean particle sizes measured by CO chemisorption.* X *– Median particle sizes measured by TEM imaging, showing first and third quartile error bars.*

The relationship between TOF values and platinum particle sizes measured from CO chemisorption results indicates an increase in oxidation activity with decreasing particle size, with an optimum size between 0.9 and 2.8 nm, below which activity decreases. The TEM measure particle sizes were only attainable for those catalysts with a metal loading of 3.6 Pt weight % and higher. It is also important to note the aforementioned observation regarding the consistency of CO chemisorption to report larger particle sizes. For the TEM measure particle sizes there is an inverse relationship between TOF values and particle size.

It was reported in the literature[133] that the CO adsorption-desorption was significantly faster than the oxidation reaction on platinum surfaces. However, it was also calculated that for particle sizes that were below 2 nm, the CO adsorption was significantly hindered. The fall in activity occurring below 2.8 nm, could therefore be as of a result of the CO adsorption limiting the rate of reaction below this particle size.

A major limitation of comparisons between particle size and catalytic activity is the inability to produce a catalyst with a homogeneous particle size evenly distributed across the support using wet chemistry methods reported herein. This experimental limitation should be taken into consideration in the above discussion as particle distributions are not always evenly distributed and catalytic activity is not linearly associated with particle diameter. Additionally, whilst the use of CO chemisorption technique for particle sizing provide an average metal particle size, it is not possible to provide information on the particle size distribution. This information can be obtained through the use of TEM imaging, however, it was found that there was a limit on the lowest observable particle size of ~1 nm, which infringes on many of the particle size distributions of those reported here. In this work both techniques have been used to complement one another considering their limitations to understand the relationship between activity and particle size of TiPt catalysts, however, absolute conclusions related to the optimum size is not feasible.

Platinum nanoparticles supported on TiNT catalysts using ion exchange have not been previously reported in the literature for CO oxidation. In any case, their activity will be compared to similar catalysts supported via incipient wetness impregnation as well as other literature reported platinum based catalysts using ceramic supports in Table 7.8.

7.3.2 Platinum Nanoparticles Supported on Titanate Nanotubes via Incipient Wetness Impregnation Synthesis

A similar set of TiPt catalysts were prepared using titanate nanotube supports with varying platinum loadings by incipient wetness impregnation, TiPtX%IWI, where X represents the platinum weight % loading. All catalysts were reduced at 120 °C under hydrogen flow to form platinum nanoparticles on the support surface. The catalysts were tested for oxidative catalytic activity using CO oxidation as a model reaction in consecutive catalytic cycles. Similarly to those TiPt catalysts synthesised through ion exchange, the incipient wetness impregnation synthesised catalysts presented an increase in catalytic activity after the first catalytic run, which were then stable for consecutive catalytic cycles. However, contrary to the IE synthesised catalysts, in the case of the IWI synthesised catalysts the variation in conversion versus temperature was more pronounced in the catalysts with a higher Pt loading weight %. A similar explanation related to the modification of the platinum particle size and platinum-support interaction applies here.

The reaction profiles for the catalysts with varying platinum loading weights for the second catalytic cycle is shown in Figure 7.17. The TiPt catalysts with platinum loadings of 1.0, 2.9 and 4.8 wt.% presented conversion at temperatures of around 150, 150 and 170 °C respectively and as expected, the conversion increased with temperature reaching full conversion at around 240 °C for all metal loadings.

Additionally, a TiPt catalyst was prepared by pre-synthesising platinum nanoparticles using and ethylene glycol method from the literature[34], fully explained in Chapter 2, followed by the deposition on the TiNT support using wetness impregnation, TiPt0.6%Pre-NP. The catalysts was also tested for the CO oxidation reaction and its reaction profile is shown alongside the other IWI synthesised catalysts in Figure 7.17 for comparison. In this case, the initial conversion temperature is ~220 °C, reaching full conversion at ~300 °C.

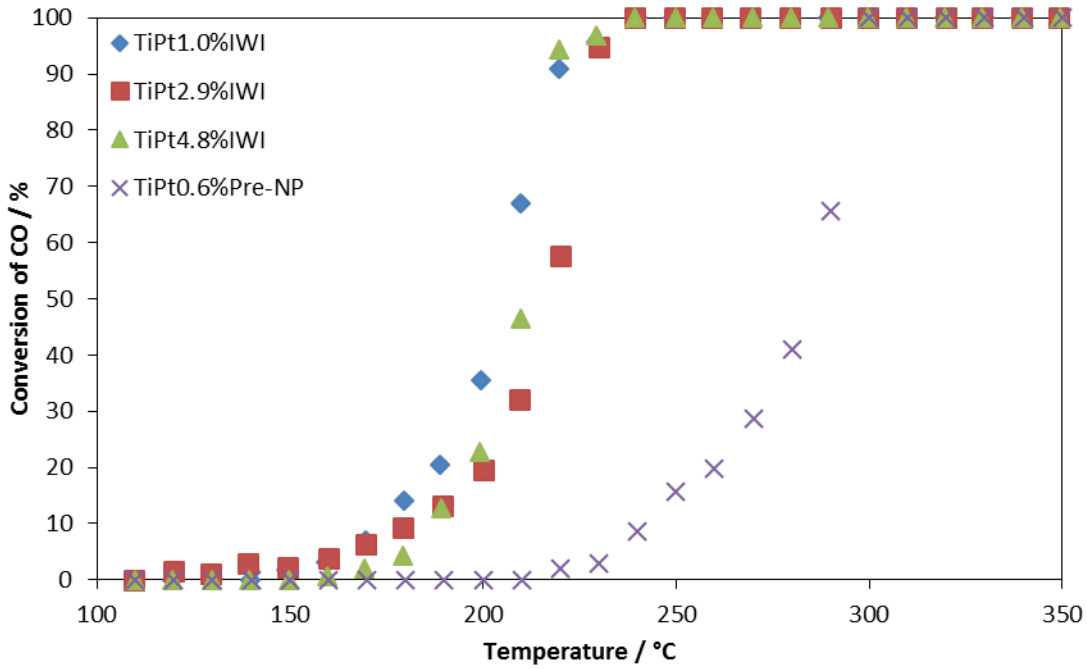

Figure 7.17 - CO conversion of incipient wetness impregnation synthesised titanate nanotube supported Pt nanoparticle catalysts as a function of temperature of the second catalytic cycle. Running at 50 mL min^{-1} of 2000 ppm CO, 2000 ppm O_2 in N_2 using 15mg of catalyst with a GHSV of 750 hour^{-1}.

The IWI synthesised catalysts were cooled a second time and used in a third catalytic cycle for the CO oxidation reaction. The subsequent reactions showed identical conversion versus temperature to those shown in Figure 7.17, demonstrating the stability of the IWI synthesised catalysts for multiple heating cycles up to 400 °C under the CO oxidation reaction conditions after the initial heating. Further results demonstrating the change in activity after the first heating and the subsequent stability through multiple catalytic cycles, are attached in Appendix B.

Although the reaction profile plots provide relative comparisons between the catalysts they fail to allow direct comparisons with literature data or to take into account the difference in metal loadings. Instead, normalisation of the activity data by metal loading, the turn over frequency (TOF) values, for the different catalysts can be employed to get a more representative comparison, as was done with the IE synthesised TiPt catalysts. The TOF values, expressed as mol CO mol_{Pt}^{-1} s^{-1} for the TiPt catalysts synthesised by the IWI method for the second catalytic run are shown in Table 7.7.

Table 7.7 – TOF values for the second catalytic cycle of the CO oxidation reaction for TiPt catalysts synthesised by incipient wetness impregnation.

Catalyst	**TOF / mol CO mol_{Pt}^{-1} s^{-1} $x10^2$**		
	150 °C	**175** °C	**200** °C
TiPt1.0%IWI	0.24	1.89	6.40
TiPt2.9%IWI	0.14	0.47	1.18
TiPt4.8%IWI	N/A	0.11	0.82
	225 °C	**250 °C**	**275 °C**
TiPt0.6%Pre-NP	0.71	4.51	10.03

The IWI synthesised TiPt catalysts have decreasing TOF values with increasing metal loadings. The TOF values in Table 7.7 along with the data already presented in Figure 7.11 and Figure 7.17 allow for an observation of the difference between the catalysts synthesised via IE and those synthesised via IWI. The IE synthesised catalysts are more active at lower temperatures with higher TOF values.

The TiPt0.6%Pre-NP catalyst was synthesised by IWI loading of pre-synthesised Pt nanoparticles onto TiNT. This catalyst shows significantly lower catalytic activity that the other TiPt catalyst. TOF values can only be calculated at temperatures above 220 °C, due to its negligible activity at lower temperatures. Therefore, TOF values at temperatures of 225, 250 and 275 °C are presented instead, although direct comparison is not possible with catalysts synthesised via IE and IWI.

The activation energies for the IWI synthesised TiPt catalysts are calculated using the linearized form of the Arrhenius equation as discussed in Chapter 2. The Arrhenius plots of each of the different catalysts are shown in Appendix C. As expected based on the reaction temperature profiles, the value of the activation energy decreases after the first catalytic cycle and then remains constant in consecutive reactions. The relationship between the activation energy and the metal loading for the first catalytic cycle and average of the consecutive ones is shown in Figure 7.18, where error bars represent one standard deviation.

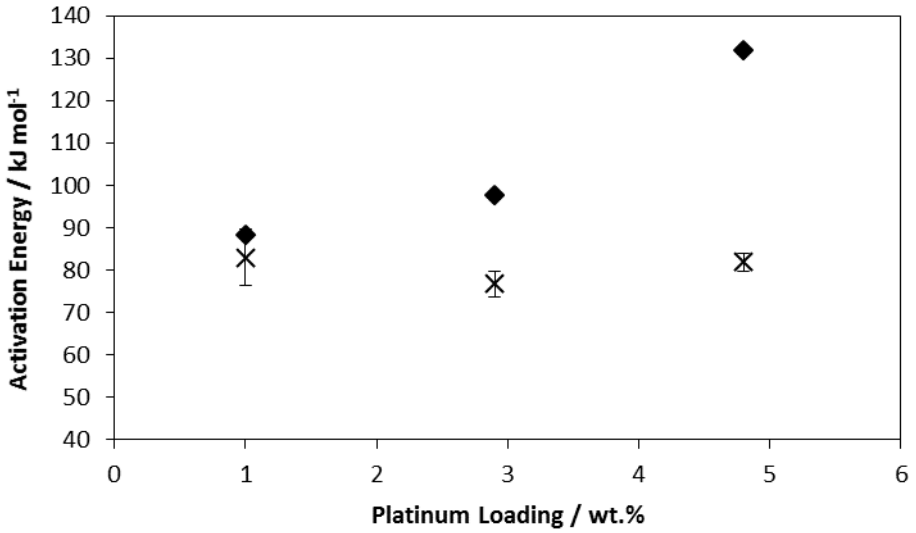

Figure 7.18 – The activation energy of CO oxidation using titanate nanotube supported platinum nanoparticles synthesised by incipient wetness impregnation as a function of metal loading. ♦ - First catalytic cycle. X – Average of the subsequent catalytic cycles with standard deviation error bars.

Similarly to the IE synthesised TiPt catalyst, the activation energy appears to increase for the TiPt catalysts synthesised by IWI with increasing loading weight for the first catalytic run. After this catalytic cycle, consistent activation energies are observed suggesting that similar active sites are present in all IWI synthesised TiPt catalysts, independent of metal loading (within the studied range) with values between 76 to 82 kJ mol^{-1}. These values are higher than what was observed for those synthesised by IE, 51 to 62 kJ mol^{-1}, suggesting that the different loading methods produce catalysts with different active sites, independent of metal loading after the first catalytic cycle, with IE synthesised catalysts having the lower activation energy.

The relationship between activity and particle size measured by CO chemisorption for the IWI synthesised TiPt catalysts, showed an exponential increase in TOF values for the second catalytic cycle with decreasing particle size. The same trend is observed with respect to the mean particle size estimated by TEM imaging measurements. However, is not observed for the median particle size estimates by TEM, due to the heavy weighting of the TiPt2.9%IWI towards smaller particle sizes that resulted in a smaller median value than observed for the TiPt1.0%IWI

catalyst. The relationship between the TOF values of the second catalytic cycle and particle size are depicted in Figure 7.19.

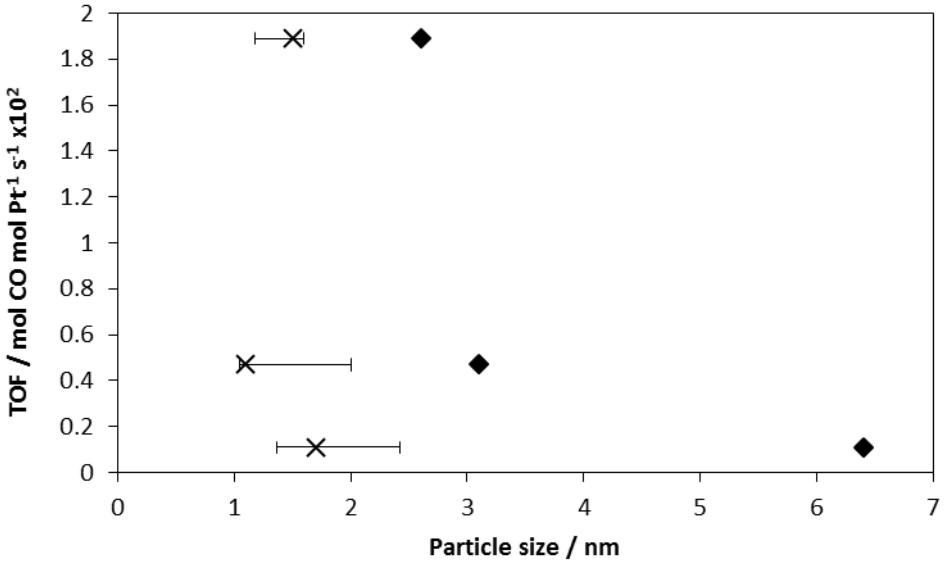

Figure 7.19 - Relationship between TOF values at 175 °C and average Pt particle size for the incipient wetness impregnation synthesised titanate nanotube supported platinum nanoparticle catalysts. TOF values are calculated from the second catalytic cycles. ♦ *- Mean particle sizes measured by CO chemisorption.* X *– Median particle sizes measured by TEM imaging, showing first and third quartile error bars.*

Though an identical activation energy was observed regardless of metal loading after the first heating cycle, there is a difference in TOF values, this suggests that though the active sites are the same, there must be a higher quantity on those with the smaller particle sizes.

Comparisons between IE and IWI synthesised TiPt catalysts reveal a common characteristic; the TOF value increases with decreasing particle size, observed to at least 2.6 nm (CO chemisorption particle size). However, in the case of the IE synthesised catalysts a decrease in activity was observed at Pt sizes of 0.9 nm. This decrease in activity could not be studied in the IWI synthesised TiPt catalysts as particle sizes well above 1 nm were present in all cases. Additionally, it can be concluded that the IE method produced smaller nanoparticles with a narrower particle distribution than the IWI method for a given metal loading.

Incipient wetness impregnation is one of the most common methods of loading Pt onto ceramics supports in the literature as well as being a standard technique used for catalyst

production in industry[171]. Relevant data of the activity, in terms of TOF values of ceramic supported Pt nanoparticles towards CO oxidation from the literature is shown in Table 7.8 where activity values in the kinetic regime could be obtained at identical temperatures to those studied in this work. TiPt catalysts synthesised by IE and IWI in this thesis, are also included for a comparison of catalytic efficiency in terms of conversion per mass of Pt. It is important to note that although there is a great deal of work regarding supported platinum catalysts, that due to variations in catalytic testing methods, data lacking for TOF value calculations and the limitations of comparing TOF values at different temperatures, few values are comparable.

Table 7.8 – Comparison of TOF values of Pt nanoparticle supported catalysts synthesised in this work, with those in the literature, for CO oxidation.

Catalyst	**Loading Method**	**Particle Size / nm**	**TOF (at T / °C) / mol CO mol_{Pt}^{-1} s^{-1}**	**Ref.**
Al_2O_3 / 5 wt.% Pt	Aqueous mixture with Pt precursor, evaporated to dry	3 to 10[a]	3.08×10^{-3} (125)	[131]
SiO_2 / 5 wt.% Pt		3 to 7[a]	2.39×10^{-3} (125)	[131]
TiO_2 / 3 wt.% Pt	Incipient Wetness Impregnation	1.3[a]	1.46×10^{-1} (175) 5.22×10^{-2} (125)	[21]
Al_2O_3 / 2wt.% Pt		0.9[a]	4.82×10^{-2} (175)	[21]
TiPt0.7%IE	Ion Exchange,	0.9[b]	3.17×10^{-2} (175) 4.3×10^{-3} (125)	This thesis
TiPt2.2%IE		2.8[b]	6.28×10^{-2} (175) 1.0×10^{-2} (125)	
TiPt3.6%IE		1.5[c] / 3.8[b]	3.94×10^{-2} (175) 4.6×10^{-3} (125)	
TiPt5.0%IE		2.0[c] / 4.4[b]	1.54×10^{-2} (175) 2.2×10^{-3} (125)	
TiPt7.1%IE		2.5[c] / 3.6[b]	1.52×10^{-2} (175) 1.2×10^{-3} (125)	
TiPt1.0%IWI	Incipient Wetness Impregnation	1.5[c] / 1.9[b]	1.89×10^{-2} (175)	
TiPt2.9%IWI		1.0[c] / 3.1[b]	4.7×10^{-3} (175)	
TiPt4.8%IWI		1.5[c] / 6.4[b]	1.1×10^{-3} (175)	

a – Mean particle size measured by TEM

b – CO chemisorption calculated particle size

c – Median particle size measured by TEM to nearest 0.5 nm

Comparing the 5 wt.% platinum nanoparticles supported on silica and alumina[131] to the TiPt5.0%IE and TiPt4.8%IWI catalysts, higher TOF values were reported for the former case. Interestingly, the silica and alumina supported samples were also reported to possess larger platinum particle sizes (3 to 10) than what was observed for titanate supported catalysts synthesised by IE and IWI within the range of conditions studied. In principle, this would

suggest that the optimum platinum size for the CO oxidation reaction might be within the 3-10 nm range. However, other aspects such as dispersion and metal-support interaction needs to be considered and from the data presented in this thesis and previous reports[133] it would appear that the optimum particle size is lower (0.9 to 2.6 nm).

IWI was reported in the literature as a method of loading Pt nanoparticles on titania and alumina with loadings of 3 and 2 wt.% Pt respectively[21]. The 2 wt.% Pt on alumina catalysts had lower TOF values than TiPt2.2%IE. Although TEM was not capable of imaging particle sizes for TiPt2.2%IE due to resolution limitations. As previously discussed there is a trend between metal loading and particle sizes for the IE catalysts between TEM imaging and CO chemisorption, with CO chemisorption reporting larger sizes, this suggests similar particle sizes between the 2 wt.% Pt on alumina catalyst and TiPt2.2%IE. Comparing the 2 wt.% Pt on alumina synthesised by IWI to TiPt1.0%IWI and TiPt2.9%IWI catalysts, the alumina supported catalysts had a much higher TOF value and a lower particle size measured by TEM than either of the TiNT supported catalysts. This could suggest the dependence on the support in stabilising metal particles of a certain size and also follows with the observations reported here of smaller nanoparticles achieving higher activity. However, the particles sizes of the alumina supported catalyst were 0.9 nm, the size at which activity was reported to fall in the case of ion exchange synthesised TiNT supported Pt catalysts. This could suggest a variation in ideal particle sizes with either loading method or support identity.

The 3 wt.% Pt on titania synthesised by IWI methods reported in the literature[21], had a higher TOF value than either the IE or IWI synthesised TiNT supported catalysts of similar metal loadings reported here. The particle size, whilst smaller than the IWI synthesised TiNT supported catalysts, was comparable to those produced by IE.

These comparisons allow for two important conclusions to be drawn. Firstly, the support strongly affects the resulting metal particle size achieved with the same loading method. This is observed when comparing IWI synthesised Pt nanoparticles on TiNT with alumina and titania. Secondly, catalysts of similar particle sizes and metal loadings synthesised with the same loading methods have different activity, suggesting the importance of the support in determining

active sites. It was demonstrated earlier in this work that although the TOF value provides information regarding the average reaction rate per mol of metal, it does not reveal the nature of the active sites. The activation energy of the catalysts can instead be used as a means of comparing the active sites responsible for catalytic activity and a comparison of those studied in this thesis with Pt supported nanoparticles in the literature is made in Table 7.9.

Table 7.9 – Comparisons of activation energies of Pt nanoparticle supported catalysts synthesised in this work, with those in the literature, for the CO oxidation reaction.

Support and Pt loading weight	**Loading Method**	**Activation Energy / kJ mol^{-1}**	**Ref.**
TiNT 0.7 to 7.1 wt.%	IE	51 to 62	Chapter 7
TiNT 1.0 to 4.8 wt.%	IWI	76 to 82	
Al_2O_3 1.5 wt.%	IWI	115.5	[172]
Al_2O_3 1.0 wt.%	IWI	120	[173]
FeO_x 0.23 wt.%	Co-Precipitation	33	[172]
TiO_2 1.0 wt.%	Deposition-Precipitation	49	[144]
TiO_2 1.0 wt.%	IWI	60	[144]
TiO_2 0.5 wt.%	Photo-depostion	51	[144]
TiO_2 3.0 wt.%	Photo-depostion	49	[144]
TiO_2[a] film	IWI	106.7	[165]
TiO_2 – (1.50×10^{15} atoms cm^{-2})	Chemical Vapour Depostion	68.6	[174]

a – Metal loading weight is not reported

As was previously shown, the activation energy and therefore the active sites for Pt nanoparticles supported on titanate nanotubes was independent of metal loading, and was instead inherent of the loading method. Comparisons with the literature reveal that the active sites of Pt on TiNT catalysts have a lower activation energy than those supported on alumina by IWI (~120 kJ mol^{-1})[173]. Additionally, and in agreement with this work, the activation energy of Pt supported catalysts synthesised through the same technique have an activation energy

independent of metal loading[172]. TiNT supported catalysts by IE and IWI both had activation energies higher than those synthesised on FeO_x by co-precipitation (33 kJ mol^{-1})[172].

Titania film supported Pt nanoparticles were reported to be synthesised by an IWI method and have an activation energy (106.7 kJ mol^{-1})[165] higher than that of the TiNT supported Pt, synthesised by IWI. However, the use of titania as a support instead of a titania film, resulted in the synthesis by IWI of Pt nanoparticles with a lower activation energy (60 kJ mol^{-1})[144] than those on TiNT, similar to those synthesised by IE on TiNT supports. This trend demonstrates that changes in the support morphology have an effect on the resulting catalyst active sites, highlighting the importance of being able to synthesise a well-defined and discreet morphology, such as was achieved through the use of the hydrothermal method to synthesise TiNT supports.

The use of chemical vapour deposition was employed to produce a monolayer of (111) platinum on (100) titania[174]. This catalysts was treated as a model catalysts and reported to have an activation energy (68.6 kJ mol^{-1}) between that of the IE and IWI synthesised catalysts using TiNT supports. This could suggest a similarity between the IE and IWI synthesised platinum on titanate nanotubes to a (111) Pt surface on (100) titania, however, TEM resolution did not allow for high enough resolution to characterise the crystal surfaces of Pt nanoparticles synthesised in this work.

Titania supported platinum synthesised by deposition-precipitation was also reported, and produced catalysts with an activation energy (49 kJ mol^{-1})[144] similar to catalysts synthesised by photo-deposition on titania (49 to 51 kJ mol^{-1})[144], both lower than that of the TiNT supported catalysts within the parameters of this study. This could suggest that these methods would produce catalysts with a lower activation energy on TiNT than IE or IWI, as Pt on titania reported in the same work, loaded by IWI had a higher activation energy (60 kJ mol^{-1})[144].

The literature further validates the observation and conclusion of activation energy being a property of the metal loading method, independent of metal loading. It also demonstrates the importance of the support and the role it plays, with similar synthesise methods producing widely different activation energies dependent on the nature of the support.

The TOF values of Pt nanoparticles supported on TiNT synthesised by IE and IWI were lower than Pt on titania supported by IWI, when comparing both metal loading and particle size. However, the activation energies of the Pt on TiNT catalysts were of similar values to that of Pt on titania catalysts in the literature. The IWI method appeared produce platinum nanoparticles with a lower activation energy when supported on TiNT (76 to 82 kJ mol^{-1}) with respect to titania films (106.7 kJ mol^{-1}), though slightly higher than those on titania (60 kJ mol^{-1}). This suggests that IWI synthesised Pt nanoparticles on TiNT could have active sites that are of similar activity to titania analogies, however, the lower TOF values suggest they are less efficient, with a lower concentration of active sites per mass of Pt. This could potentially be due to the larger particle sizes on TiNT, with 1.6 (±1.0) nm mean particle size measured by TEM observed for TiPt2.9%IWI compared to 1.3 nm reported for 3wt.% Pt on titania[21] resulting in lower surface to bulk metal ratios. However, as discussed, there is a minimum ideal particle size for Pt CO oxidation catalysts in terms of TOF values and particle sizes are an average of a distribution and it is more likely an effect of the support identity which has been demonstrated to effect both activation energies and concentration of active sites.

As previously mentioned in the literature review, Chapter 6, previous work has been reported studying the use of TiNT supported Pt nanoparticles by deposition-precipitation as catalysts for CO oxidation[12]. Although the work presented lacked data required to calculate TOF values or activation energies, a comparison of the findings can be made with the results for the catalytic activity of IE and IWI prepared TiNT supported Pt nanoparticles.

It was reported that a typical reaction consisted of 50 to 60 mg of catalyst under a 60 mL min^{-1} flow of 1 to 20 % CO and 10 to 40 % O_2[12]. The reported catalyst displayed initial conversion at room temperature in the first catalytic heating. After heating to 400 °C, the catalytic activity was reported to be substantially lower in a subsequent catalytic cycle, initial conversion not appearing until ~225 °C. This fall in catalytic activity after the initial catalytic cycle is contrary to what was observed for both the IE and IWI synthesised catalysts reported here. It appears to be extreme in the loss of activity with the catalyst having an initial temperature of conversion (225 °C) that is significantly higher than any of the IE or IWI prepared catalysts

reported here (120 and 170 °C respectively) after the first catalytic cycle. This fall in activity was attributed to particle agglomerations of 3 to 7 nm, that were caused by local overheating due to a strong exothermic effect resulting in temperatures in the reactor reaching up to 800 °C[12].

7.4 Conclusions

The use of ion exchange and incipient wetness impregnation to synthesise Pt nanoparticles have been demonstrated as effective means of producing small particles (0.9 to 6.4 nm) with high dispersion across titanate nanotube supports. The ion exchange method presented a metal loading efficiency of ~75% that, for the parameters of this study, was independent of the metal loading. It was observed through the use of CO chemisorption that the ion exchange method produced smaller average particle sizes than incipient wetness impregnation for a given metal loading. It was also observed, through TEM imaging that the ion exchange method produced a narrower particle size distribution than incipient wetness impregnation. Similar observations were obtained when gold is supported through identical procedures, suggesting these conclusions to be applicable to other noble metals supported on titanate nanotubes.

The study of the catalytic activity of platinum nanoparticles supported on titanate nanotubes for the CO oxidation reaction demonstrates an inverse relationship between the activation energy and metal loading for the first catalytic cycle, for both ion exchange and incipient wetness impregnations synthesised catalysts. However, the second catalytic cycle had a fall in activation energy that was stable for subsequent catalytic cycles and was independent of the metal loading and instead inherent of the loading method; 51 to 62 kJ mol^{-1} for ion exchange and 76 to 82 kJ mol^{-1} for incipient wetness impregnation. This fall in activation energy was as a result of the fall in temperatures of initial conversion and increased rates with respect

for temperatures. This increased activity after the initial catalytic cycle is ascribed to either a change in particle shape, a cleaning of the active sites or agglomeration of small nanoparticles.

The ion exchange method of metal loading result in an increased activity, normalised for metal weight compared to incipient wetness impregnation. Ion exchange synthesised catalysts displayed CO conversion at lower temperatures than incipient wetness impregnation, with lower activation energies, which indicated the presence of different active sites. An inverse relationship was observed between particle size and catalytic activity in the case of both loading methods. However, there appeared to be an ideal particle size between 0.9 and 2.8 nm, with activity falling below this size, likely as a result of CO adsorption rate being significantly lower for particles below 2 nm[133].

These results demonstrate titanate nanotubes to produce catalysts similar in activity to those reported in the literature. It has also been shown that the activation energy is independent of metal loading and is instead an inherent property of the loading method. Ion exchange and incipient wetness impregnation methods of loading Pt on titanate nanotubes also appear to produce catalysts more stable for subsequent catalytic cycles than deposition-precipitation methods reported in the literature.

As nanoparticle size is a distribution of sizes and as activity does not have a direct relationship with particle size, being dependant on the metal identity and particle shape, it becomes difficult to accurately ascribe activity to a certain loading technique or metal loading without knowing the exact contribution from each discreet particle size or the exact particle size distribution. Due to this and the vast number of variables that can affect nanoparticle loading methods, a body of work that compares different metal loadings, different loading methods and different metals on an identical support and the resulting particle sizes and catalytic activity, is a particularly useful and novel catalogue of information, not available through comparisons in the literature.

Chapter 8

Conclusions and Future Work

The overall aim of this thesis is to investigate the effect of the morphology at the nanoscale on the physical and surface properties of different ceramic nanostructured materials, specifically in their use as a catalysts and as metal nanoparticle supports. The conclusion of the four objectives identified are presented in the following text.

Investigate the relationship between ceria nanostructured morphology and its catalytic activity.

Different nanostructured ceria morphologies were produced by varying the conditions of hydrothermal synthesis, specifically temperature and base concentration. Ceria nanoparticles were synthesised at 70 °C and a base concentration of 5 M. Increasing the temperature to 70-100 °C and base concentration to 10-15 M resulted in rod morphologies. Increasing temperature and further, to 180 °C with the same base concentration as in the case of the rods, 10-15 M, resulted in the formation of cube morphologies. The difference in morphology at

different conditions is a result of the dissolution/recrystallization process with the formation of cerium hydroxide crystallites as an intermediate responsible for the anisotropic growth in rods. The effect of the base concentration was previously reported in the literature, and in this work it has also been demonstrated that the temperature plays a key role in morphological control, with high temperatures of the same base concentration affecting morphology.

Characterisation of the different nanostructured ceria morphologies reveal that crystallite size increases with a change from particles to rods to cubes and that smaller crystallites would result in a higher surface area, both due to the higher surface to bulk ratio and higher mesoporosity, suggested by BET isotherms. Higher surface to bulk oxygen contents were observed by XPS, TPR and Raman spectroscopy, for materials with a higher surface area, with the rod like morphologies presenting slightly higher surface oxygen content than would be predicted from this trend. The (110) and (100) crystal planes that both dominate the surfaces of rod morphologies are reported to more readily form oxygen vacancies than other crystal planes. This ability to form oxygen vacancies could have been responsible for the increased surface oxygen content.

It was also observed that the Ce^{3+} content, measured by XPS, was highest for the rods and lowest for particles and that for the same morphology, a higher Ce^{3+} content resulted in a lower surface to bulk oxygen ratio. Higher Ce^{3+} content results in higher oxygen vacancy concentration and thus less oxygen ions present in the surface, resulting in the lower surface to bulk oxygen ratio. However, in spite of this, it was the rod morphologies with the highest Ce^{3+} that had the highest surface to bulk oxygen content ratios.

The CO oxidation reaction, used as a model reaction to test the oxidative catalytic activity of the nanostructured ceria revealed that the rates normalised for surface area had a direct correlation with surface area. As surface area was observed to increase with decreasing crystallite size, there is an inverse relationship between crystallite size and surface normalised rate. It is known that the activity of ceria surfaces increase with higher surface energy. As defects have a higher energy due to higher unsatisfied coordination and as lower crystallite size results

in higher constrained geometry and thus a higher concentration of defects, this higher defect concentration explains the relationship between crystallite size and reaction rate.

A trend between activation energies and surface to bulk oxygen content was observed. The surface to bulk oxygen content was shown to be a related to more readily formed oxygen vacancies, suggesting that it is the higher concentration of facile oxygen ions that are responsible for the lower activation energies. A similar trend between activity and morphology was observed for the naphthalene oxidation, carried out on these catalysts by Dr Garcia at the University of Zaragoza. As CO oxidation is known to take place via the Mars-Van Krevelen reaction mechanism, it could suggest a similar reaction mechanism for this oxidative reaction.

Investigate the relationship between atmosphere and thermal stability of ceria nanostructured catalysts.

Representative morphologies of three distinct nanostructured ceria, particles, rods and cubes were thermally treated under oxidative (20% O_2 in He), reductive (5% H_2 in Ar) and inert (He) atmospheres prior to characterisation and catalytic tests.

After thermal treatment to 1000 °C, under all atmospheres the materials were observed to sinter, resulting in a drastic drop in surface area, all to below 4.2 $m^2 g^{-1}$, and a significant loss of their morphologies. The catalytic activity of these morphologies after thermal treatment, using CO oxidation as a model reaction, was lower than fresh catalysts for the rods and particles, but higher in the case of the cubes. This is due to the much lower relative drop in surface area for the cubes compared to the particles and rods, as all present an increased activity normalised for surface area. That the catalytic activity increases after this thermal treatment, is likely due to the exposure of higher energy surfaces.

The enhanced (surface area normalised) activity was, however, not sustained for the oxidised or inert treated morphologies. These thermally treated materials lost their catalytic activity during the CO oxidation reaction, when heated above 450 °C and presented negligible activity after this point. However, the samples treated under a reducing atmosphere were stable

for CO oxidation up to at least 575 °C and continued to present the enhanced activity (normalised for surface area). Monitoring the outlet gas during the thermal treatments revealed that whilst those heated under oxidising and inert atmospheres appeared similar, those treated under a reducing atmosphere were appreciable different. From the outlet gas it was determined that whilst all thermal treatments resulted in the loss of surface oxygen, it was only under the presence of hydrogen, that the removal of bulk oxygen was facilitated. This was as a result of H_2 reacting with oxygen at the surface to form H_2O. The stability of the catalytic activity for the thermally treated morphologies under hydrogen was therefore likely due to this difference, which resulted in revealing a higher energy, yet more stable surface.

Investigate the effect of different methods of supporting metal nanoparticles on nanostructured materials.

Titanate nanotubes synthesised through a hydrothermal method and characterised through different analytical techniques, demonstrated that they had a well define and discreet morphology. Different metal loadings were synthesised through both ion exchange and incipient wetness impregnation techniques. The use of gold in the place of platinum was also studied to establish that observations were an effect of the loading method.

It was found that the ion exchange method for loading Pt using H_2PtCl_6 as a metal source afforded a ~75% loading efficiency up to 7.1 wt.% metal loading, whilst Au, using $HAuCl_4$ only provided a ~50% loading efficiency that fell with increased metal loading up to 2.5 wt.% metal loading. This suggests Pt to be more efficient at exchanging ions with protons in the titanate nanotube structure compared to Au when using chloro-metallic acid metal sources. The use of incipient wetness impregnation for the synthesis of supported metal nanoparticles has the intrinsic benefit of affording 100% loading efficiency.

Using CO chemisorption and TEM imaging to measure particle size and particle size distribution, it was discovered than the ion exchange method produced smaller average particle sizes in comparison to similar metal loadings by incipient wetness impregnation. It was also

observed through TEM imaging that the ion exchange synthesis method resulted in a narrower particle size distribution. The use of Au in the place of Pt allowed for these same conclusions to be drawn regarding the particle size and size distribution for the ion exchange and incipient wetness impregnation methods utilising different chloro-metallic acids.

Investigate the catalytic activity of different metal nanoparticles supported on ceramics.

The Pt nanoparticles supported on titanate nanotubes were tested for their oxidative catalytic activity using CO oxidation as a model reaction. The ion exchange method produced catalysts that were more active by metal weight and gave higher rates at similar temperatures and lower activation energies than the incipient wetness impregnation counterparts.

The trend in activity, the TOF values, appeared to mostly be dictated by the metal particle size, with an inverse relationship observed between the two. This was observed in both the case of the ion exchange and incipient wetness synthesised catalyst, with the exception of nanoparticles below 2.8 nm (measured by CO chemisorption), where a fall in activity was observed, that was ascribed to the hindrance to CO adsorption on Pt nanoparticles below ~2 nm. The activation energy of the catalysts during the initial catalytic cycle was found to increase with metal loading, with lower activation energies observed for ion exchange synthesised catalysts relative to incipient wetness impregnations. These activation energies then fell in the case of all catalysts for the second catalytic cycle, where they were stable for subsequent catalytic cycles. The activation energy for catalytic cycles after the initial cycle was found to be independent of metal loading and instead an inherent property of the loading method, with 51 to 62 kJ mol^{-1} for the ion exchange and 76 to 82 kJ mol^{-1} for the incipient wetness impregnation.

8.1. Future Work

Hydrothermal synthesis has been demonstrated as an efficient method of synthesising both titanate nanotubes and ceria nanostructures of varying morphology and aspect ratio, with well-defined and discrete morphologies. Hydrothermal synthesis can also be used to produce other ceramic materials, such as nanostructured MgO. In this area, preliminary results have shown that different morphologies, e.g. hexagonal plates and rod, can be selectively synthesised through similar systematic changes to temperature and NaOH concentration as used here for the synthesis of ceria. These materials can not only be studied for their catalytic activity towards CO oxidation, but also other reactions that may be able to take advantage of some unique properties of other ceramic materials (e.g. acidity in alumina and basicity in MgO).

Doped ceria via the substitution of cerium by dopants such as Zr and La have been shown in the literature to affect crystallite size and surface oxygen content resulting in enhanced catalytic activities. Further progress in this area would involve the simultaneous doping and the morphological control demonstrated here, to achieve a combined effect with the crystal size and potentially reveal new activities and applications. Advance characterisation techniques can further our understanding of nanostructured materials and their evolution under specific conditions. High resolution TEM imaging, of nanostructure materials (e.g. ceria reported in this thesis) could determine the crystal planes exposed in each case.

Thermal treatment of ceria nanostructures under reducing environments has been demonstrated to expose surfaces of higher catalytic activity. A study of the reduction process, by in-situ XPS, can reveal the temperature at which this change in catalytic activity is observed and how exactly the cerium oxidation state is affected throughout. However, it was the sustained activity that was of most interest and proceeding work should focus on this aspect. With that in mind, long-term studies could be performed on these thermally treated, reduced ceria catalysts, under different atmospheres and temperatures to study their stability.

From the titanate nanotube supported platinum nanoparticle catalysts research, there is the intuitive step to studying other metal nanoparticles, synthesised by the same methods reported here. Such methods have been shown to produce similar results both in the case of Pt and Au in the work above and preliminary work has also allowed for the synthesise of Pd analogies. There is also the opportunity to use these same methods, or others with different support-metal combinations building on conclusions of this work. However, it was highlighted here that there is a great importance on the ability to produce nanoparticles with a discrete size distribution and future work should be focused on this aspect.

To obtain a narrower distribution of active sites a well-defined and discrete support morphology is necessary. From this point, a single loading method may be chosen and variations to the numerous variables, such as temperature, time, pH, metal source, washings, solvent, reduction temperature, reduction method and solvent volume to support weight ratio, can be studied to observe how each affect particle size and distribution. Tuning the synthetic method to produce a mono-sized metal nanoparticle being the ultimate goal.

To understand the exact effect the catalytic reaction has on the catalyst, a study to investigate the changes to a single nanoparticle can be undertaken. To do so, the use of high resolution TEM to image a specific nanoparticle on a support can be undertaken and the location of the particle on the TEM grid can be recorded. The grid may then be exposed to reaction conditions before a second high resolution TEM imaging is performed on the same location to observe the same particle. Through such a study, using a single catalyst, observing many particles over the support and the effect of different temperatures a full story regarding changes to the metal nanoparticles during the reaction can be obtained.

References

1. Sá, J., *et al.*, *Magnetic Manipulation of Molecules on a Non-Magnetic Catalytic Surface.* Nanoscale, **2013**, 5(18), p. 8462-8465.
2. Busacca, C.A., *et al.*, *Transition Metal Catalysis in the Pharmaceutical Industry.* Applications of Transition Metal Catalysis in Drug Discovery and Development: An Industrial Perspective, **2012,** p. 1.
3. Hawkins, J.M., *et al., Asymmetric Catalysis in the Pharmaceutical Industry.* Angewandte Chemie International Edition, **2004,** 43(25), p. 3224-3228.
4. Minussi, R.C., *et al.*, *Potential Applications of Laccase in the Food Industry.* Trends in Food Science & Technology, **2002,** 13(6–7), p. 205-216.
5. Rostrup-Nielsen, J.R., *Conversion of Hydrocarbons and Alcohols for Fuel Cells.* Physical Chemistry Chemical Physics, **2001,** 3(3), p. 283-288.
6. Bahnemann, D., *Photocatalytic Water Treatment: Solar Energy Applications.* Solar Energy, **2004,** 77(5), p. 445-459.
7. Erisman, J.W., *et al.*, *How a Century of Ammonia Synthesis Changed the World.* Nature Geoscience, **2008,** 1(10), p. 636-639.
8. Mol, J.C., *Industrial Applications of Olefin Metathesis.* Journal of Molecular Catalysis A: Chemical, **2004,** 213(1), p. 39-45.
9. Schlesinger, W.H., *et al.*, *Global Change: The Nitrogen Cycle and Rivers.* Water Resources Research, **2006,** 42(W03S06), p.1-2.
10. Anastas, P.T., *et al.*, *Life Cycle Assessment and Green Chemistry: The Yin and Yang of Industrial Ecology.* Green Chemistry, **2000,** 2(6), p. 289-295.
11. Daniel, M.C., *et al.*, *Gold Nanoparticles: Assembly, Supramolecular Chemistry, Quantum-Size-Related Properties, and Applications Toward Biology, Catalysis, and Nanotechnology.* Chemical Reviews, **2003,** 104(1), p. 293-346.
12. Grigorieva, A.V., *et al., Titania Nanotubes Supported Platinum Catalyst in CO Oxidation Process.* Applied Catalysis A: General, **2009,** 362(1–2), p. 20-25.
13. Bréchignac, C., *et al.*, *Nanomaterials and Nanochemistry*. **2008,** New York, Springer.
14. Chen, S., *et al., Gold Nanoelectrodes of Varied Size: Transition to Molecule-Like Charging.* Science, **1998,** 280(5372), p. 2098-2101.
15. Rai, M., *et al.*, *Silver Nanoparticles as a New Generation of Antimicrobials.* Biotechnology Advances, **2009,** 27(1), p. 76-83.
16. Minelli, C., *et al.*, *Engineering Nanocomposite Materials for Cancer Therapy.* Small, **2010,** 6(21), p. 2336-2357.
17. Tee, B.C.K., *et al., An Electrically and Mechanically Self-Healing Composite with Pressure and Flexion-Sensitive Properties for Electronic Skin Applications.* Nature Nanotechnology, **2012,** 7(12), p. 825-832.
18. Palik, E., *Handbook of Optical Constants of Solids.* **1985,** New York, Academic Press.
19. Raveendran, P., *et al.*, *Completely "Green" Synthesis and Stabilization of Metal Nanoparticles.* Journal of the American Chemical Society, **2003,** 125(46), p. 13940-13941.

20. Cai, J., *et al., Nanoporous Cellulose as Metal Nanoparticles Support.* Biomacromolecules, **2008,** 10(1), p. 87-94.

21. Alayon, E.M.C., *et al., On Highly Active Partially Oxidized Platinum in Carbon Monoxide Oxidation Over Supported Platinum Catalysts.* Journal of Catalysis, **2009,** 263(2), p. 228-238.

22. Mandal, S., *et al.*, *Pt and Pd Nanoparticles Immobilized on Amine-Functionalized Zeolite: Excellent Catalysts for Hydrogenation and Heck Reactions.* Chemistry of Materials, **2004,** 16(19), p. 3714-3724.

23. Jiang, K., *et al., Selective Attachment of Gold Nanoparticles to Nitrogen-Doped Carbon Nanotubes.* Nano Letters, **2003,** 3(3), p. 275-277.

24. Wildgoose, G.G., *et al.*, *Metal Nanoparticles and Related Materials Supported on Carbon Nanotubes: Methods and Applications.* Small, **2006,** 2(2), p. 182-193.

25. Sayle, T.X.T., *et al.*, *Oxidising CO to CO_2 Using Ceria Nanoparticles.* Physical Chemistry Chemical Physics, **2005,** 7(15), p. 2936-2941.

26. Sayle, T.X.T., *et al.*, *Strain and Architecture-Tuned Reactivity in Ceria Nanostructures; Enhanced Catalytic Oxidation of CO to CO_2.* Chemistry of Materials, **2012,** 24(10), p. 1811-1821.

27. Zhou, K., *et al., Enhanced Catalytic Activity of Ceria Nanorods from Well-Defined Reactive Crystal Planes.* Journal of Catalysis, **2005,** 229(1), p. 206-212.

28. Yang, S., *et al.*, *Controlled Synthesis and Self-Assembly of CeO_2 Nanocubes.* Journal of the American Chemical Society, **2006,** 128(29), p. 9330-9331.

29. Jang, D., *et al., Fabrication and Deformation of Three-Dimensional Hollow Ceramic Nanostructures.* Nature materials, **2013,** 12(10), p. 893-898.

30. Lin, Y.S., *et al.*, *Improvement of Thermal Stability of Porous Nanostructured Ceramic Membranes.* Industrial & Engineering Chemistry Research, **1994,** 33(4), p. 860-870.

31. Anderson, M.A., *et al.*, *Titania and Alumina Ceramic Membranes.* Journal of Membrane Science, **1988,** 39(3), p. 243-258.

32. Yao, H.C., *et al.*, *Ceria in Automotive Exhaust Catalysts: Oxygen Storage.* Journal of Catalysis, **1984,** 86(2), p. 254-265.

33. Sayle, T.X.T., *et al.*, *The Role of Oxygen Vacancies on Ceria Surfaces in the Oxidation of Carbon Monoxide.* Surface Science, **1994,** 316(3), p. 329-336.

34. Wang, Y., *et al.*, *Preparation of Tractable Platinum, Rhodium, and Ruthenium Nanoclusters with Small Particle Size in Organic Media.* Chemistry of Materials, **2000,** 12(6), p. 1622-1627.

35. Perrichon, V., *et al.*, *Metal Dispersion of CeO_2–ZrO_2 Supported Platinum Catalysts Measured by H_2 or CO Chemisorption.* Applied Catalysis A: General, **2004,** 260(1), p. 1-8.

36. Regalbuto, J.R., *et al.*, *An Integrated Study of $Pt/WO_3/SiO_2$ Catalysts for The NO・CO Reaction: Catalyst Characterization by XRD, Chemisorption, and XPS.* Journal of Catalysis, **1987,** 107(1), p. 114-128.

37. Chi, L., *Nanotechnology: Volume 8: Nanostructured Surfaces*. **2010,** John Wiley & Sons.

38. Claasen, T.A.C.M., *An Industry Perspective on Current and Future State of the Art in System-on-Chip (SoC) Technology.* Proceedings of the IEEE, **2006,** 94(6), p. 1121-1137.

39. Jo, B.W., *et al.*, *Effectiveness of the Top-Down Nanotechnology in the Production of Ultrafine Cement (~220 nm).* Journal of Nanomaterials, **2014,** vol. 2014, Article ID 131627.

40. Klok, H.A., *et al., Self-Assembly of Rodlike Hydrogen-Bonded Nanostructures.* Journal of the American Chemical Society, **1999,** 121(30), p. 7154-7155.

41. Xia, Y., *et al., One-Dimensional Nanostructures: Synthesis, Characterization, and Applications.* Advanced Materials, **2003,** 15(5), p. 353-389.

42. Zeng, J., *et al., Controlling the Shapes of Silver Nanocrystals with Different Capping Agents.* Journal of the American Chemical Society, **2010,** 132(25), p. 8552-8553.

43. Uskokovic, V, *et al.*, *Synthesis of Materials Within Reverse Micelles.* Surface Review and Letters, **2005,** 12(2), p. 239-277.

44. C. Hulteen, J., *et al.*, *A General Template-Based Method for the Preparation of Nanomaterials.* Journal of Materials Chemistry, **1997,** 7(7), p. 1075-1087.

45. Gasparac, R., *et al., Template Synthesis of Nano Test Tubes.* Nano Letters, **2004,** 4(3), p. 513-516.

46. Mai, H.X., *et al., Shape-Selective Synthesis and Oxygen Storage Behavior of Ceria Nanopolyhedra, Nanorods, and Nanocubes.* The Journal of Physical Chemistry B, **2005,** 109(51), p. 24380-24385.

47. Deshpande, A.S., *et al., Controlled Assembly of Preformed Ceria Nanocrystals into Highly Ordered 3D Nanostructures.* Small, **2005,** 1(3), p. 313-316.

48. Chen, G., *et al., Interface Reaction Route to Two Different Kinds of CeO_2 Nanotubes.* Inorganic Chemistry, **2007,** 47(2), p. 723-728.

49. Torrente-Murciano, L., *et al., Shape-Dependency Activity of Nanostructured CeO_2 in the Total Oxidation of Polycyclic Aromatic Hydrocarbons.* Applied Catalysis B: Environmental, **2013,** 132–133(0), p. 116-122.

50. Mogensen, M., *et al.*, *Physical, Chemical and Electrochemical Properties of Pure and Doped Ceria.* Solid State Ionics, **2000,** 129(1–4), p. 63-94.

51. Lai, W., *et al.*, *Impedance Spectroscopy as a Tool for Chemical and Electrochemical Analysis of Mixed Conductors: A Case Study of Ceria.* Journal of the American Ceramic Society, **2005,** 88(11), p. 2979-2997.

52. Murray, E.P., *et al.*, *A Direct-Methane Fuel Cell with a Ceria-Based Anode.* Nature, **1999,** 400(6745), p. 649-651.

53. Bunluesin, T., *et al., Studies of the Water-Gas-Shift Reaction on Ceria-Supported Pt, Pd, and Rh: Implications for Oxygen-Storage Properties.* Applied Catalysis B: Environmental, **1998,** 15(1–2), p. 107-114.

54. Yue, L., *et al.*, *Structural Characterization and Photocatalytic Behaviors of Doped CeO_2 Nanoparticles.* Journal of Alloys and Compounds, **2009,** 475(1–2), p. 702-705.

55. Jacobs, G., *et al.*, *Steam Reforming of Ethanol Over Pt/Ceria with Co-Fed Hydrogen.* Journal of Catalysis, **2007,** 245(2), p. 326-337.

56. Kim, G., *Ceria-Promoted Three-Way Catalysts for Auto Exhaust Emission Control.* Industrial & Engineering Chemistry Product Research and Development, **1982,** 21(2), p. 267-274.

57. Masui, T., *et al.*, *Characterization of Cerium(IV) Oxide Ultrafine Particles Prepared Using Reversed Micelles.* Chemistry of Materials, **1997,** 9(10), p. 2197-2204.

58. Yin, L., *et al.*, *Sonochemical Synthesis of Cerium Oxide Nanoparticles: Effect of Additives and Quantum Size Effect.* Journal of Colloid and Interface Science, **2002,** 246(1), p. 78-84.

59. Zhang, D., *et al.*, *Synthesis of CeO_2 Nanorods via Ultrasonication Assisted by Polyethylene Glycol.* Inorganic Chemistry, **2007,** 46(7), p. 2446-2451.

60. Chen, H.I., *et al.*, *Synthesis of Nanocrystalline Cerium Oxide Particles by the Precipitation Method.* Ceramics International, **2005,** 31(6), p. 795-802.

61. Yu, T., *et al.*, *Aqueous-Phase Synthesis of Single-Crystal Ceria Nanosheets.* Angewandte Chemie International Edition, **2010,** 49(26), p. 4484-4487.

62. Chen, G., *et al.*, *Template-Free Synthesis of Single-Crystalline-like CeO_2 Hollow Nanocubes.* Crystal Growth & Design, **2008,** 8(12), p. 4449-4453.

63. Zhou, Y.C, *et al.*, *Hydrothermal Synthesis and Sintering of Ultrafine CeO_2 Powders.* Journal of Materials Research, **1993,** 8(7), p. 1680-1686.

64. Pan, C., *et al., Template-Free Synthesis, Controlled Conversion, and CO Oxidation Properties of CeO_2 Nanorods, Nanotubes, Nanowires, and Nanocubes.* European Journal of Inorganic Chemistry, **2008,** 2008(15), p. 2429-2436.

65. Li, G., *et al.*, *Structural Stability and Valence Characteristics in Cerium Hydrothermal Systems.* Journal of Solid State Chemistry, **1996,** 126(1), p. 74-79.

66. Chouaib, F., *et al., Characterization of Cerium Oxides Prepared in Water and Sodium Hydroxide Mixtures.* Journal of Alloys and Compounds, **1992,** 185(2), p. 279-293.

67. Perrichon, V., *et al.*, *Thermal Stability of a High Surface Area Ceria Under Reducing Atmosphere.* Applied Catalysis A: General, **1995,** 129(1), p. 69-82.

68. Aneggi, E., *et al.*, *Surface-Structure Sensitivity of CO Oxidation Over Polycrystalline Ceria Powders.* Journal of Catalysis, **2005,** 234(1), p. 88-95.

69. Huang, M., *et al., CO Adsorption and Oxidation on Ceria Surfaces from DFT+U Calculations.* The Journal of Physical Chemistry C, **2008,** 112(23), p. 8643-8648.

70. Nolan, M., *et al.*, *The Surface Dependence of CO Adsorption on Ceria.* The Journal of Physical Chemistry B, **2006,** 110(33), p. 16600-16606.

71. Sayle, D.C., *et al., Atomistic Models for CeO_2(111), (110), and (100) Nanoparticles, Supported on Yttrium-Stabilized Zirconia.* Journal of the American Chemical Society, **2002,** 124(38), p. 11429-11439.

72. Wang, D., *et al.*, *Synthesis and Oxygen Storage Capacity of Two-Dimensional Ceria Nanocrystals.* Angewandte Chemie International Edition, **2011,** 50(19), p. 4378-4381.

73. Grant, F.A., *Properties of Rutile (Titanium Dioxide).* Reviews of Modern Physics, **1959,** 31(3), p. 646-674.

74. Zhang, F., *et al.*, *Synthesis of Titania-Supported Platinum Catalyst: The Effect of pH on Morphology Control and Valence State during Photodeposition.* Langmuir, **2004,** 20(21), p. 9329-9334.

75. Diebold, U., *The Surface Science of Titanium Dioxide.* Surface Science Reports, **2003,** 48(5-8), p. 53-229.

76. Cao, W.B., *et al.*, *Visible-Light Activity of N-doped TiO_2 Powders and their Applications.* Materials Science Forum, **2007,** 544-545, p. 167-170.

77. Park, N.G., *et al.*, *Comparison of Dye-Sensitized Rutile and Anatase-Based TiO_2 Solar Cells.* The Journal of Physical Chemistry B, **2000,** 104(38), p. 8989-8994.

78. Gotfredson, K., *et al.*, *Anchorage of TiO_2-Blasted, HA-Coated, and Machined Implants: An Experimental Study with Rabbits.* Journal of Biomedical Materials Research, **1995,** 29(10), p. 1223-1231.

79. Bavykin, D., *et al.*, *Deposition of Pt, Pd, Ru and Au on the Surfaces of Titanate Nanotubes.* Topics in Catalysis, **2006,** 39(3), p. 151-160.

80. Haruta, M., *et al.*, *Low-Temperature Oxidation of CO over Gold Supported on TiO_2, α-Fe_2O_3, and Co_3O_4.* Journal of Catalysis, **1993,** 144(1), p. 175-192.

81. Zhu, B., *et al.*, *Synthesis and Catalytic Performance of TiO_2 Nanotubes-Supported Copper Oxide for Low-Temperature CO Oxidation.* Microporous and Mesoporous Materials, **2007,** 102(1–3), p. 333-336.

82. Armstrong, G., *et al.*, *Nanotubes with the TiO_2-B Structure.* Chemical Communications, **2005**, 19, p. 2454-2456.

83. Wei, M., *et al.*, *Synthesis and Characterization of Nanosheet-Shaped Titanium Dioxide.* Journal of Materials Science, **2007,** 42(2), p. 529-533.

84. Du, G.H., *et al.*, *Potassium Titanate Nanowires: Structure, Growth, and Optical Properties.* Physical Review B, **2003,** 67(3), p. 035323.

85. Bavykin, D.V., *et al.*, *Low-Temperature Synthesis of Titanate Nanotubes in Aqueous KOH.* Australian Journal of Chemistry, **2007,** 60(2), p. 95-98.

86. Cressey, B., *et al.*, *An Aqueous, Alkaline Route to Titanate Nanotubes Under Atmospheric Pressure Conditions.* Nanotechnology, **2008,** 19(27), p. 275604.

87. Raja, K.S., *et al.*, *Formation of Self-Ordered Nano-Tubular Structure of Anodic Oxide Layer on Titanium.* Electrochimica Acta, **2005,** 51(1), p. 154-165.

88. Zanella, R., *et al.*, *Alternative Methods for the Preparation of Gold Nanoparticles Supported on TiO_2.* The Journal of Physical Chemistry B, **2002,** 106(31), p. 7634-7642.

89. Morgan, D.L., *et al.*, *Determination of a Morphological Phase Diagram of Titania/Titanate Nanostructures from Alkaline Hydrothermal Treatment of Degussa P25.* Chemistry of Materials, **2008,** 20(12), p. 3800-3802.

90. Kasuga, T., *et al.*, *Titania Nanotubes Prepared by Chemical Processing.* Advanced Materials, **1999,** 11(15), p. 1307-1311.

91. Bavykin, D.V., *et al.*, *Protonated Titanates and TiO_2 Nanostructured Materials: Synthesis, Properties, and Applications.* Advanced Materials, **2006,** 18(21), p. 2807-2824.

92. Armstrong, A.R., *et al.*, *TiO_2-B Nanowires as Negative Electrodes for Rechargeable Lithium Batteries.* Journal of Power Sources, **2005,** 146(1-2), p. 501-506.

93. Yu, J., *et al.*, *Preparation and Photocatalytic Activity of Mesoporous Anatase TiO_2 Nanofibers by a Hydrothermal Method.* Journal of Photochemistry and Photobiology A: Chemistry, **2006,** 182(2), p. 121-127.

94. Bavykin, D.V., *et al.*, *The Effect of Hydrothermal Conditions on the Mesoporous Structure of TiO_2 Nanotubes.* Journal of Materials Chemistry, **2004,** 14(22), p. 3370-3377.

95. Zhang, S., *et al.*, *Formation Mechanism of $H_2Ti_3O_7$ Nanotubes.* Physical Review Letters, **2003,** 91(25), p. 256103.

96. Yao, B.D., *et al.*, *Formation Mechanism of TiO_2 Nanotubes.* Applied Physics Letters, **2003,** 82(2), p. 281-283.

97. Ohsaki, Y., *et al.*, *Dye-sensitized TiO_2 nanotube Solar Cells: Fabrication and Electronic Characterization.* Physical Chemistry Chemical Physics, **2005,** 7(24), p. 4157-4163.

98. Yu, J., *et al., Preparation, Characterization and Visible-Light-Driven Photocatalytic Activity of Fe-Doped Titania Nanorods and First-Principles Study for Electronic Structures.* Applied Catalysis B: Environmental, **2009,** 90(3–4), p. 595-602.

99. Spalla, O., *et al.*, *Adhesion Between Oxide Nanoparticles: Influence of Surface Complexation.* Journal of Colloid and Interface Science, **1997,** 192(1), p. 43-65.

100. Donnay, J.D.H., *et al.*, *Crystal Data: Determinative Tables*. Vol. 547. **1963,** Buffalo, NY, American crystallographic association.

101. Frevel, L., *Tabulated Diffraction Data for Cubic Isomorphs.* Industrial & Engineering Chemistry Analytical Edition, **1942,** 14(9), p. 687-693.

102. Chen, L., *et al.*, *Size-Related Lattice Parameter Changes and Surface Defects in Ceria Nanocrystals.* The Journal of Physical Chemistry C, **2010,** 114(30), p. 12909-12919.

103. Tok, A.I.Y., *et al.*, *Hydrothermal Synthesis of CeO_2 Nano-Particles.* Journal of Materials Processing Technology, **2007,** 190(1–3), p. 217-222.

104. Araujo, V.D., *et al.*, *CeO_2 Nanoparticles Synthesized by a Microwave-Assisted Hydrothermal Method: Evolution from Nanospheres to Nanorods.* CrystEngComm, **2012,** 14(3), p. 1150-1154.

105. Brunauer, S., *et al.*, *On a Theory of the van der Waals Adsorption of Gases.* Journal of the American Chemical Society, **1940,** 62(7), p. 1723-1732.

106. Martínez-Arias, A., *et al.*, *Structural and Redox Properties of Ceria in Alumina-Supported Ceria Catalyst Supports.* The Journal of Physical Chemistry B, **2000,** 104(17), p. 4038-4046.

107. Wu, Z., *et al., Probing Defect Sites on CeO_2 Nanocrystals with Well-Defined Surface Planes by Raman Spectroscopy and O_2 Adsorption.* Langmuir, **2010,** 26(21), p. 16595-16606.

108. Taniguchi, T., *et al.*, *Identifying Defects in Ceria-Based Nanocrystals by UV Resonance Raman Spectroscopy.* The Journal of Physical Chemistry C, **2009,** 113(46), p. 19789-19793.

109. Spanier, J.E., *et al.*, *Size-Dependent Properties of CeO_{2-y} Nanoparticles as Studied by Raman Scattering.* Physical Review B, **2001,** 64(24), p. 245407.

110. Tuinstra, F., *et al.*, *Raman Spectrum of Graphite.* The Journal of Chemical Physics, **1970,** 53(3), p. 1126-1130.

111. Tok, A.I.Y., *et al.*, *Hydrothermal Synthesis and Characterization of Rare Earth Doped Ceria Nanoparticles.* Materials Science and Engineering: A, **2007,** 466(1–2), p. 223-229.

112. Xu, J., *et al., Size Dependent Oxygen Buffering Capacity of Ceria Nanocrystals.* Chemical Communications, **2010,** 46(11), p. 1887-1889.

113. Bêche, E., *et al.*, *Ce3d XPS Investigation of Cerium Oxides and Mixed Cerium Oxide (CexTiyOz).* Surface and Interface Analysis, **2008,** 40(3-4), p. 264-267.

114. Galtayries, A., *et al., XPS Comparative Study of Ceria/Zirconia Mixed Oxides: Powders and Thin Film Characterisation.* Journal of Electron Spectroscopy and Related Phenomena, **1998,** 88–91(0), p. 951-956.

115. Breysse, M., *et al*., *Catalysis of Carbon Monoxide Oxidation by Cerium Dioxide: Correlations Between Catalytic Activity and Electrical Conductivity.* Journal of Catalysis, **1972,** 27(2), p. 275-280.

116. Conesa, J., *Computer Modeling of Surfaces and Defects on Cerium Dioxide.* Surface Science, **1995,** 339(3), p. 337-352.

117. Kozlov, S.M., *et al*., *O Vacancies on Steps on the CeO_2(111) Surface.* Physical Chemistry Chemical Physics, **2014,** 16, p. 7823-7829.

118. Lan, Y., *et al., Titanate Nanotubes and Nanorods Prepared from Rutile Powder.* Advanced Functional Materials, **2005,** 15(8), p. 1310-1318.

119. Kilbourn, B.T., *A Lanthanide Lanthology: A Collection of Notes Concerning the Lanthanides and Related Elements.* **1993,** White Plains, NY, Molycorp.

120. Vert, M., *et al.*, *Terminology for Biorelated Polymers and Applications (IUPAC Recommendations 2012)*. Pure and Applied Chemistry, **2012,** 84(2), p. 377-410.

121. Corma, A., *et al.*, *Supported Gold Nanoparticles as Catalysts for Organic Reactions.* Chemical Society Reviews, **2008,** 37(9), p. 2096-2126.

122. Hermans, L.A.M., *et al., Interaction of Nickel Ions with Silica Supports During Deposition-Precipitation*. Studies in Surface Science and Catalysis, **1979**, 3, p. 113-130.

123. Haruta, M., *Nanoparticulate Gold Catalysts for Low-Temperature CO Oxidation.* Journal of New Materials for Electrochemical Systems, **2004,** 7(3), p. 163-172.

124. An, H., *et al.*, *Deposition of Pt on the Stable Nanotubular TiO_2 and its Photocatalytic Performance.* Catalysis Communications, **2009,** 11(3), p. 175-179.

125. Huber, D.L., *Synthesis, Properties, and Applications of Iron Nanoparticles.* Small, **2005,** 1(5), p. 482-501.

126. Jiang, J., *et al.*, *Gold Nanocatalysts Supported on Protonic Titanate Nanotubes and Titania Nanocrystals.* Journal of Molecular Catalysis A: Chemical, **2008,** 280(1–2), p. 233-239.

127. Abida, B., *et al.*, *Preparation and Characterization of Pt/TiO_2 Nanotubes Catalyst for Methanol Electro-Oxidation.* Applied Catalysis B: Environmental, **2011**. 106(3–4), p. 609-615.

128. Ahmadi, T.S., *et al.*, *Shape-Controlled Synthesis of Colloidal Platinum Nanoparticles.* Science, **1996,** 272(5270), p. 1924-1926.

129. Joo, S.H., et al., *Ordered nanoporous arrays of carbon supporting high dispersions of platinum nanoparticles.* Nature, 2001. 412(6843): p. 169-172.

130. Park, J.B., *et al., Gold, Copper, and Platinum Nanoparticles Dispersed on CeOx/TiO2(110) Surfaces: High Water-Gas Shift Activity and the Nature of the Mixed-Metal Oxide at the Nanometer Level.* Journal of the American Chemical Society, **2009,** 132(1), p. 356-363.

131. Fukuoka, A., *et al.*, *Preferential Oxidation of Carbon Monoxide Catalyzed by Platinum Nanoparticles in Mesoporous Silica.* Journal of the American Chemical Society, **2007,** 129(33), p. 10120-10125.

132. Hikosaka, K., *et al.*, *Platinum Nanoparticles have an Activity Similar to Mitochondrial NADH: Ubiquinone Oxidoreductase.* Colloids and Surfaces B-Biointerfaces, **2008,** 66(2), p. 195-200.

133. Bratlie, K.M., *et al.*, *Platinum Nanoparticle Shape Effects on Benzene Hydrogenation Selectivity.* Nano Letters, **2007,** 7(10), p. 3097-3101.

134. Teoh, W.Y., *et al., Direct (One-Step) Synthesis of TiO_2 and Pt/TiO_2 Nanoparticles for Photocatalytic Mineralisation of Sucrose.* Chemical Engineering Science, **2005,** 60(21), p. 5852-5861.

135. Hwang, S., *et al.*, *Highly Enhanced Photocatalytic Oxidation of CO on Titania Deposited with Pt Nanoparticles: Kinetics and Mechanism.* Applied Catalysis B: Environmental, **2003,** 46(1), p. 49-63.

136. Li, C., *et al.*, *Facile Solution Synthesis of Ag@Pt Core-Shell Nanoparticles with Dendritic Pt Shells.* Physical Chemistry Chemical Physics, **2013,** 15(10), p. 3490-3496.

137. Maillard, F., *et al., Size Effects on Reactivity of Pt Nanoparticles in CO Monolayer Oxidation: The role of Surface Mobility.* Faraday Discussions, **2004,** 125(0), p. 357-377.

138. Lebedeva, N.P., *et al., Mechanism and Kinetics of the Electrochemical CO Adlayer Oxidation on Pt(111).* Journal of Electroanalytical Chemistry, **2002,** 524–525(0), p. 242-251.

139. Dong, L., *et al., Graphene-Supported Platinum and Platinum–Ruthenium Nanoparticles with High Electrocatalytic Activity for Methanol and Ethanol Oxidation.* Carbon, **2010,** 48(3), p. 781-787.

140. Li, W., *et al., Preparation and Characterization of Multiwalled Carbon Nanotube-Supported Platinum for Cathode Catalysts of Direct Methanol Fuel Cells.* The Journal of Physical Chemistry B, **2003,** 107(26), p. 6292-6299.

141. Chytil, S., *et al., Platinum Incorporated into the SBA-15 Mesostructure via Deposition-Precipitation Method: Pt Nanoparticle Size Estimation and Catalytic Testing.* Topics in Catalysis, **2007,** 45(1-4), p. 93-99.

142. Shimada, S., *et al.*, *Influence of the Preparation Methods for Pt/CeO_2 and Au/CeO_2 Catalysts in CO Oxidation*. Studies in Surface Science and Catalysis, **2010,** 175, p. 843-847.

143. Navarro, R.M., *et al.*, *The Effect of Pt Characteristics on the Photoactivity of Pt/TiO_2 for Hydrogen Production from Ethanol.* Catalysis Today, **2013,** 210(0), p. 33-38.

144. Bamwenda, G.R., *et al., The Influence of the Preparation Methods on the Catalytic Activity of Platinum and Gold Supported on TiO_2 for CO Oxidation.* Catalysis Letters, **1997,** 44(1-2), p. 83-87.

145. Wang, Z.J., *et al.*, *Synthesis and Characterization of Noble Metal (Pd, Pt, Au, Ag) Nanostructured Materials Confined in the Channels of Mesoporous SBA-15.* The Journal of Physical Chemistry C, **2008,** 112(50), p. 19818-19824.

146. Koutsopoulos, S., *et al., Titania-Supported Pt and Pt–Pd Nanoparticle Catalysts for the Oxidation of Sulfur Dioxide.* Journal of Catalysis, **2006,** 238(1), p. 206-213.

147. Murcia, J.J., *et al., Correlation Study Between Photo-Degradation and Surface Adsorption Properties of Phenol and Methyl Orange on TiO_2 vs. Platinum-Supported TiO_2.* Applied Catalysis B: Environmental, **2014,** 150–151(0), p. 107-115.

148. Mohapatra, S.K., *et al., Design of a Highly Efficient Photoelectrolytic Cell for Hydrogen Generation by Water Splitting: Application of TiO_2-xCx Nanotubes as a Photoanode and Pt/TiO_2 Nanotubes as a Cathode.* The Journal of Physical Chemistry C, **2007,** 111(24), p. 8677-8685.

149. Vijayan, B.K., *et al.*, *The Effects of Pt Doping on the Structure and Visible Light Photoactivity of Titania Nanotubes.* The Journal of Physical Chemistry C, **2010,** 114(49), p. 21262-21269.

150. Encarnación Gómez, C., *et al.*, *Pt Nanoparticles on Titania Nanotubes Prepared by Vapor-Phase Impregnation–Decomposition Method.* Journal of Alloys and Compounds, **2010,** 495(2), p. 458-461.

151. Alivisatos, A.P., *Semiconductor Clusters, Nanocrystals, and Quantum Dots.* Science, **1996,** 271(5251), p. 933-937.

152. Jakob, M., *et al.*, *Charge Distribution Between UV-Irradiated TiO_2 and Gold Nanoparticles: Determination of Shift in the Fermi Level.* Nano Letters, **2003,** 3(3), p. 353-358.

153. Nicolais, L., *et al.*, *Nanocomposites: In Situ Synthesis of Polymer-Embedded Nanostructures*. **2013,** John Wiley & Sons.

154. Roduner, E., *Size Matters: Why Nanomaterials are Different.* Chemical Society Reviews, **2006,** 35(7), p. 583-592.

155. Suchorski, Y., *et al., Ceria Nanoformations in CO Oxidation on Pt(111): Promotional Effects and Reversible Redox Behaviour.* Surface Science, **2007,** 601(21), p. 4843-4848.

156. Yin, S.F., *et al.*, *Nano Ru/CNTs: A Highly Active and Stable Catalyst for the Generation of COx-Free Hydrogen in Ammonia Decomposition.* Applied Catalysis B: Environmental, **2004,** 48(4), p. 237-241.

157. Primo, A., *et al., Efficient Visible-Light Photocatalytic Water Splitting by Minute Amounts of Gold Supported on Nanoparticulate CeO_2 Obtained by a Biopolymer Templating Method.* Journal of the American Chemical Society, **2011,** 133(18), p. 6930-6933.

158. Bezemer, G.L., *et al., Cobalt Particle Size Effects in the Fischer–Tropsch Reaction Studied with Carbon Nanofiber Supported Catalysts.* Journal of the American Chemical Society, **2006,** 128(12), p. 3956-3964.

159. Hughes, M.D., *et al., Tunable Gold Catalysts for Selective Hydrocarbon Oxidation Under Mild Conditions.* Nature, **2005,** 437(7062), p. 1132-1135.

160. Enache, D.I., *et al.*, *Solvent-Free Oxidation of Primary Alcohols to Aldehydes Using Au-Pd/TiO_2 Catalysts.* Science, **2006,** 311(5759), p. 362-365.

161. Selvaraj, V., *et al.*, *Synthesis and Characterization of Metal Nanoparticles-Decorated PPY–CNT Composite and their Electrocatalytic Oxidation of Formic Acid and Formaldehyde for Fuel Cell Applications.* Applied Catalysis B: Environmental, **2007,** 75(1–2), p. 129-138.

162. Haruta, M., *et al., Low-Temperature Catalytic Combustion of Methanol and its Decomposed Derivatives Over Supported Gold Catalysts.* Catalysis Today, **1996,** 29(1–4), p. 443-447.

163. Lashof, D.A., *et al., Relative Contributions of Greenhouse Gas Emissions to Global Warming.* Nature, **1990,** 344(6266), p. 529-531.

164. Ribeiro, N.F.P., *et al.*, *Investigation of Activity Losses of Gold Nanoparticles in the CO Selective Oxidation.* Journal of Power Sources, **2010,** 195(21), p. 7386-7390.

165. Qadir, K., *et al., Support Effect of Arc Plasma Deposited Pt Nanoparticles/TiO_2 Substrate on Catalytic Activity of CO Oxidation.* The Journal of Physical Chemistry C, **2012,** 116(45), p. 24054-24059.

166. Li, S., *et al., Low-Temperature CO Oxidation Over Supported Pt Catalysts Prepared by Colloid-Deposition Method.* Catalysis Communications, **2008,** 9(6), p. 1045-1049.

167. Somorjai, G.A., *New Model Catalysts (Platinum Nanoparticles) and New Techniques (SFG and STM) for Studies of Reaction Intermediates and Surface Restructuring at High Pressures During Catalytic Reactions.* Applied Surface Science, **1997,** 121–122(0), p. 1-19.

168. Cervera Gontard, *et al.*, *A Simple Algorithm for Measuring Particle Size Distributions on an Uneven Background from TEM Images.* Ultramicroscopy, **2011,** 111(2), p. 101-106.

169. Uchiyama, T., *et al.*, *Systematic Morphology Changes of Gold Nanoparticles Supported on CeO_2 during CO Oxidation.* Angewandte Chemie, **2011,** 123(43), p. 10339-10342.

170. Haruta, M., *Catalysis of Gold Nanoparticles Deposited on Metal Oxides.* CATTECH, **2002,** 6(3), p. 102-115.

171. Padin, J., *et al.*, *New Sorbents for Olefin/Paraffin Separations by Adsorption via π-Complexation: Synthesis and Effects of Substrates.* Chemical Engineering Science, **2000,** 55(14), p. 2607-2616.

172. Liu, L., *et al., Low-Temperature CO Oxidation Over Supported Pt, Pd Satalysts: Particular Role of FeO_x Support for Oxygen Supply During Reactions.* Journal of Catalysis, **2010,** 274(1), p. 1-10.

173. Oran, U., *et al.*, *Mechanisms of CO Oxidation Reaction and Effect of Chlorine Ions on the CO Oxidation Reaction Over Pt/CeO_2 and Pt/CeO_2/γ-Al_2O_3 Catalysts.* Applied Catalysis B: Environmental, **2004,** 54(3), p. 183-191.

174. Tenney, S.A., *et al.*, *Novel Recirculating Loop Reactor for Studies on Model Catalysts: CO Oxidation on Pt/TiO_2(110).* Review of Scientific Instruments, **2013,** 84(10), p. 104101

Appendix A – Transmission Electron Microscopy Images

All samples reduced at 120 °C prior to imaging.

3.6 weight% Pt loaded onto titanate nanotubes via ion exchange

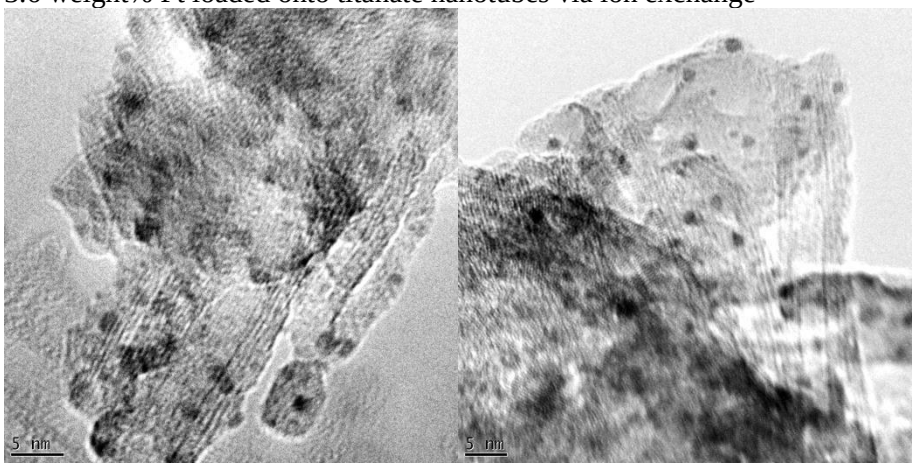

5.0 weight% Pt loaded onto titanate nanotubes via ion exchange

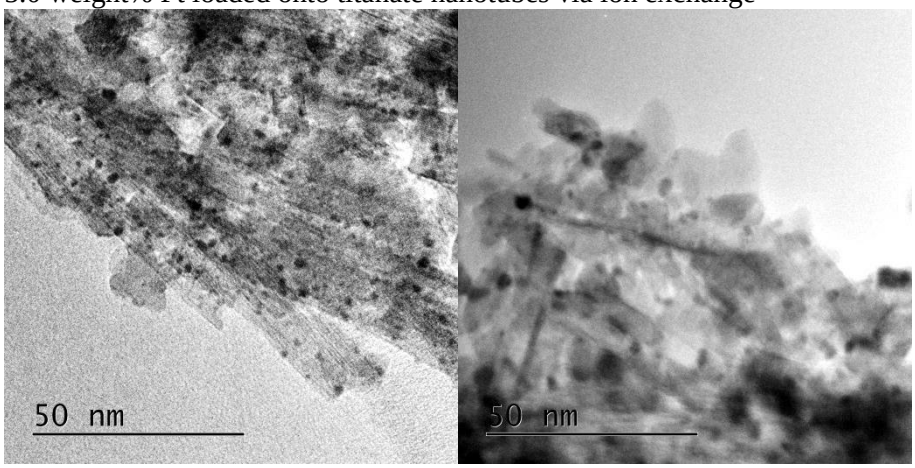

7.1 weight% Pt loaded onto titanate nanotubes via ion exchange

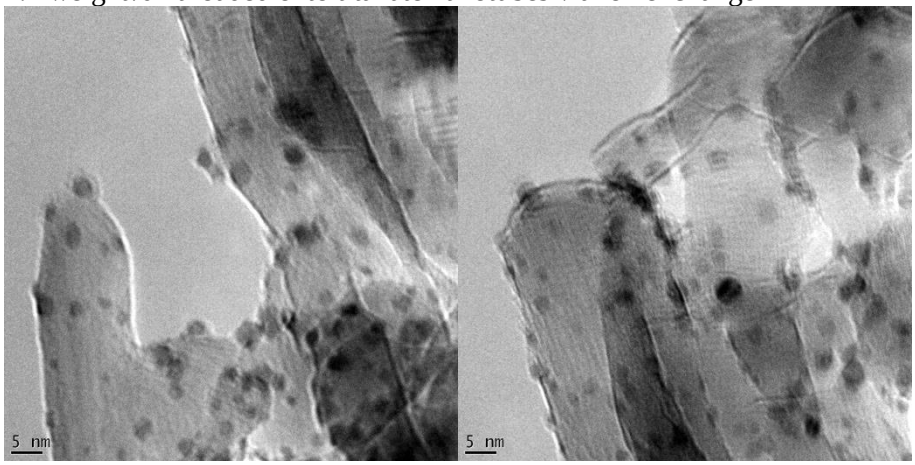

1.0 weight% Pt loaded onto titanate nanotubes via incipient wetness impregnation

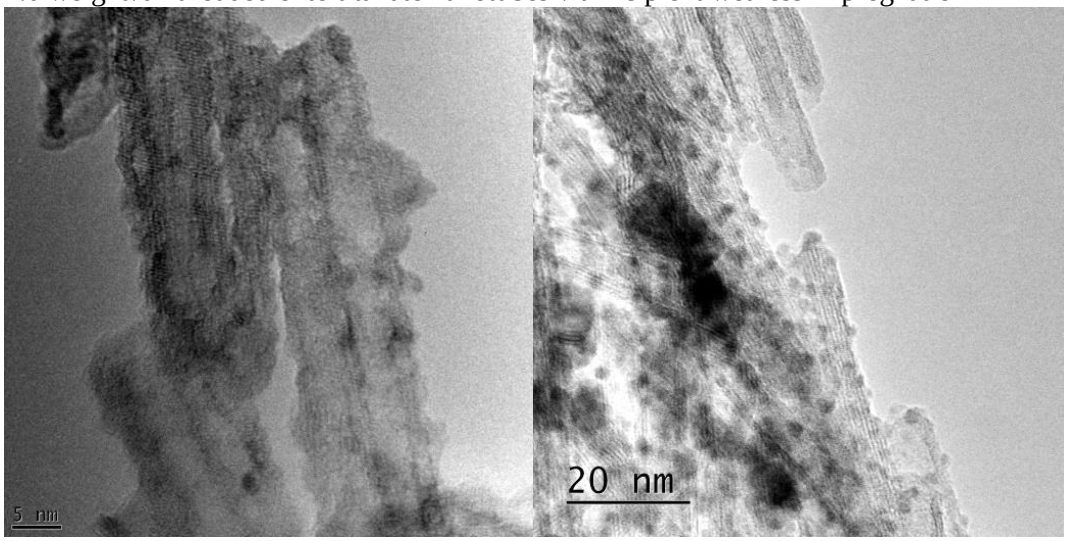

2.9 weight% Pt loaded onto titanate nanotubes via incipient wetness impregnation

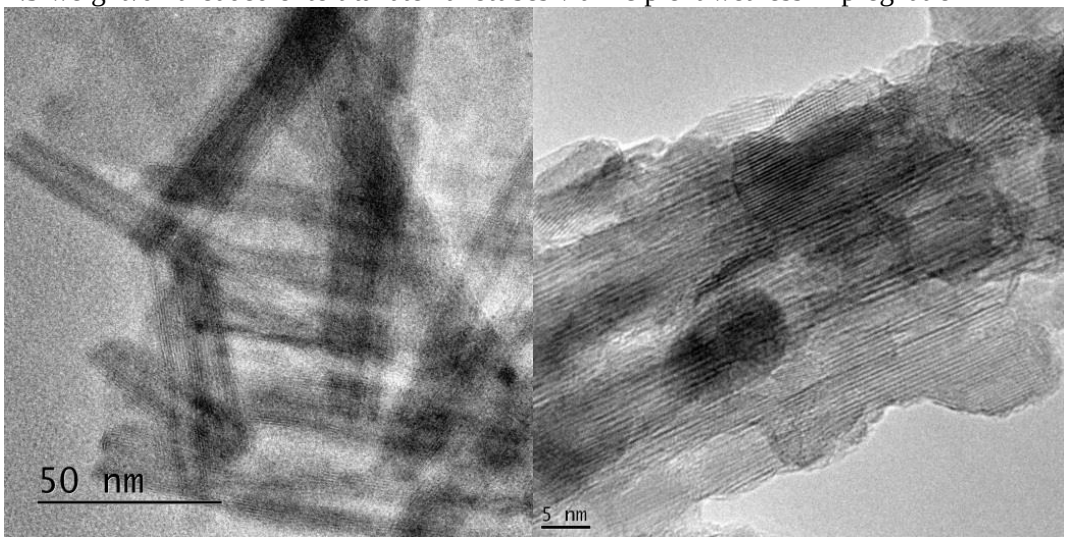

4.8 weight% Pt loaded onto titanate nanotubes via incipient wetness impregnation

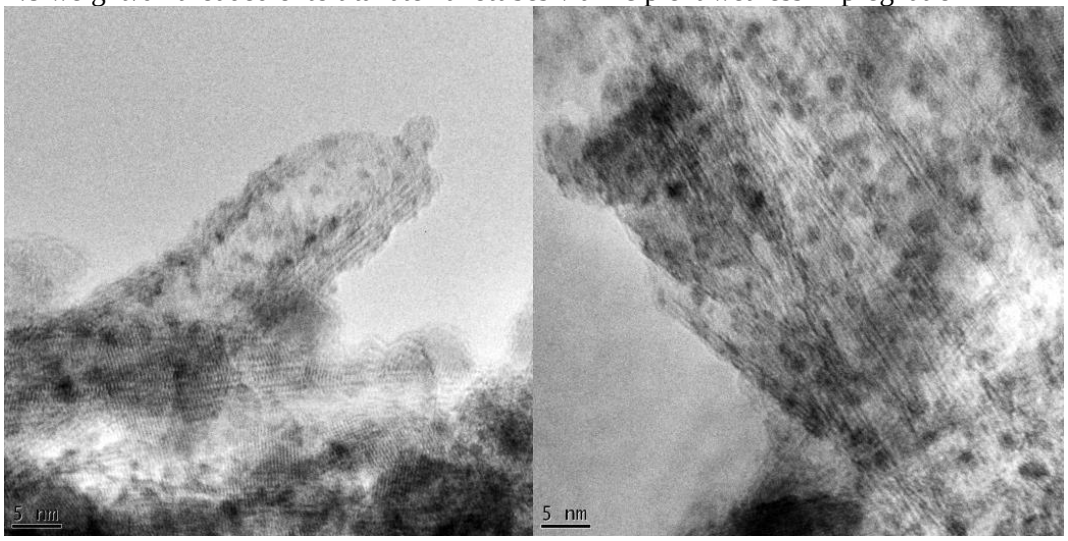

0.63 weight% Pt nanoparticles synthesised in ethylene glycol before loading onto titanate nanotubes via incipient wetness impregnation

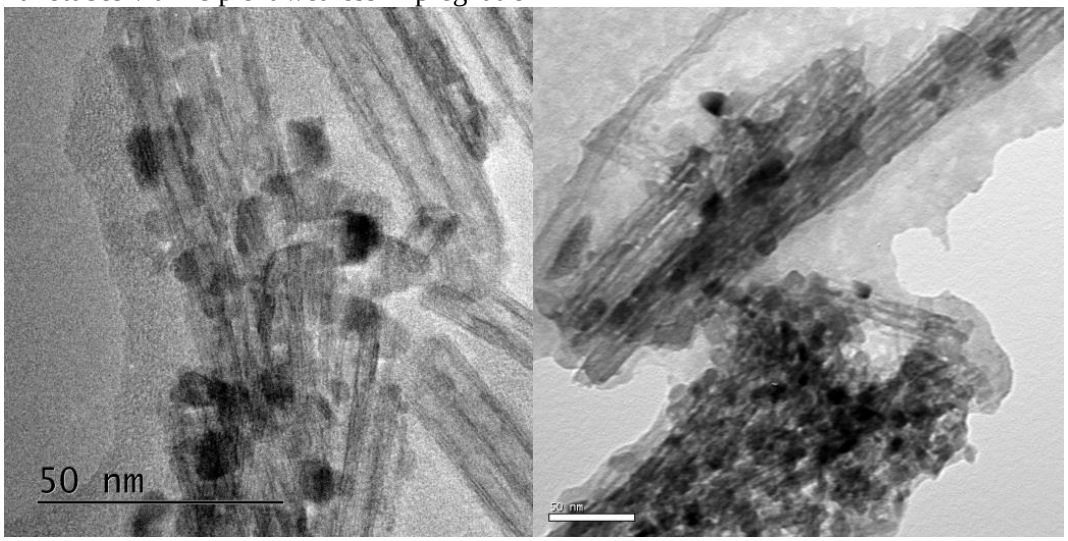

0.5 weight% Au loaded onto titanate nanotubes via ion exchange

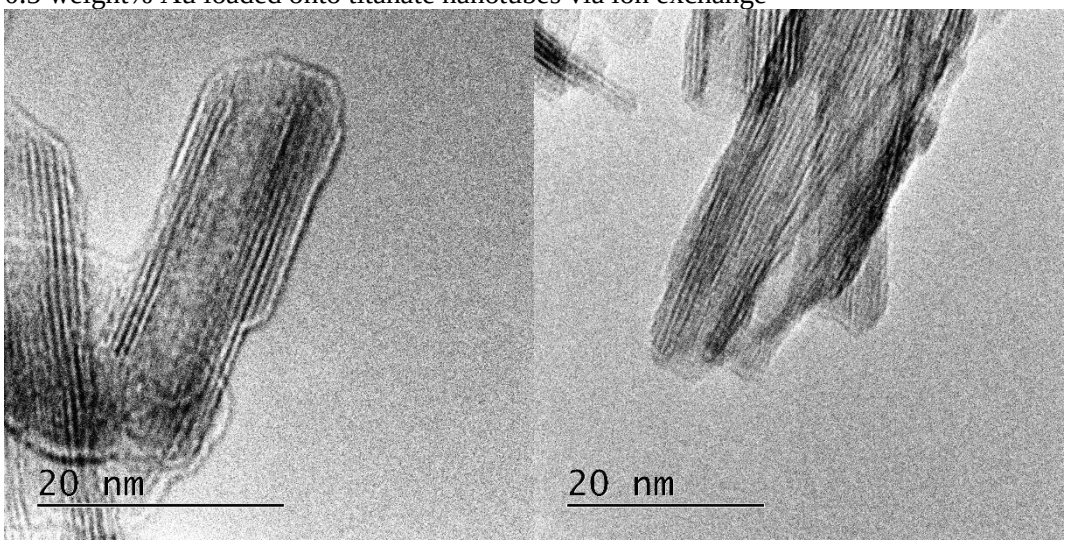

2.0 weight% Au loaded onto titanate nanotubes via ion exchange

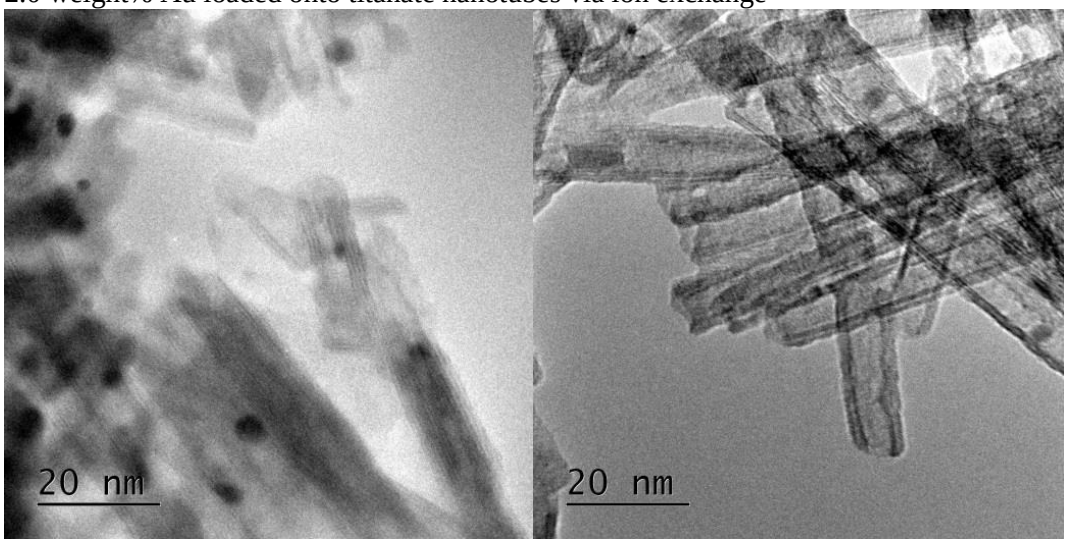

2.5 weight% Au loaded onto titanate nanotubes via ion exchange

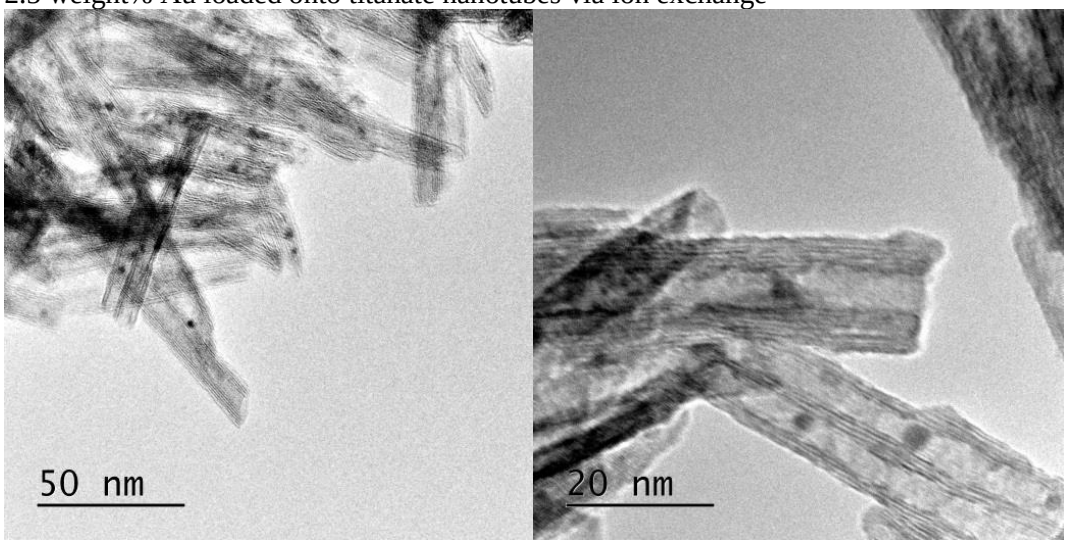

1.0 weight% Au loaded onto titanate nanotubes via incipient wetness impregnation

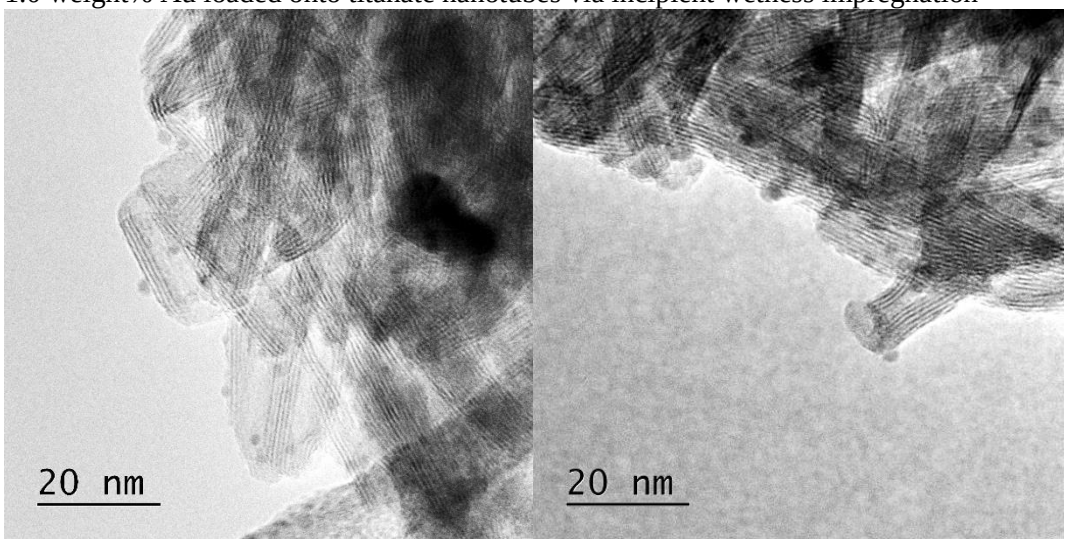

4.8 weight% Au loaded onto titanate nanotubes via incipient wetness impregnation

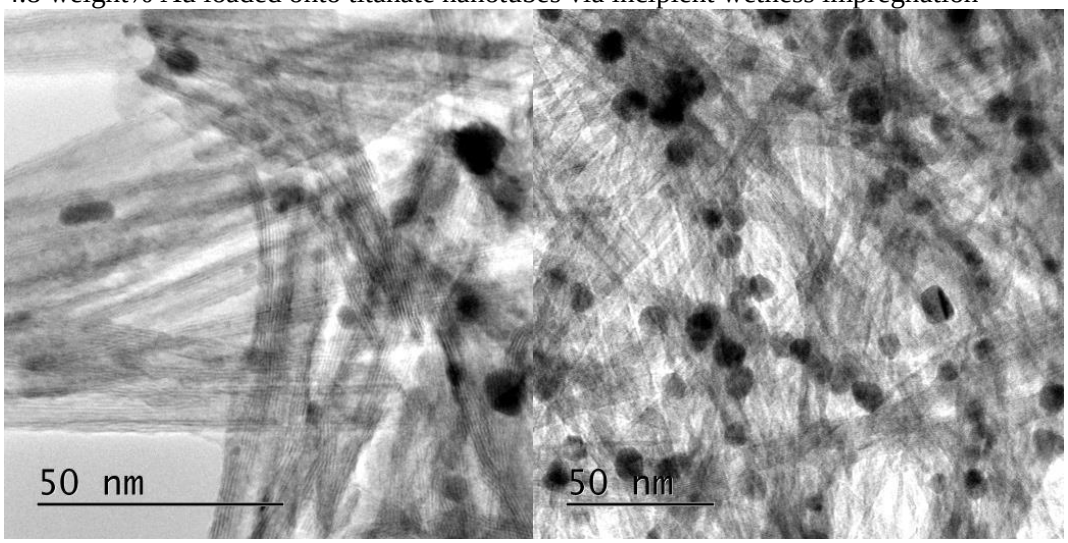

Appendix B – CO Oxidation Conversion versus Temperature Profiles

Conditions: 15mg of catalyst, 50 mL min^{-1} 2000ppm CO, 2000ppm O_2 in N_2, GHSV 750 $hour^{-1}$, heating and cooling at 2.5 $^oC\ min^{-1}$.

CeNP

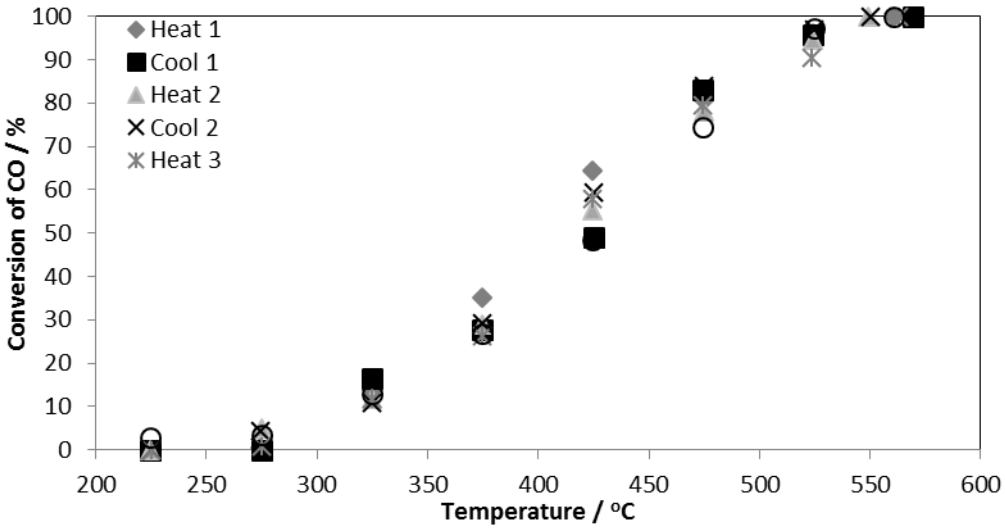

$CeNC_A$

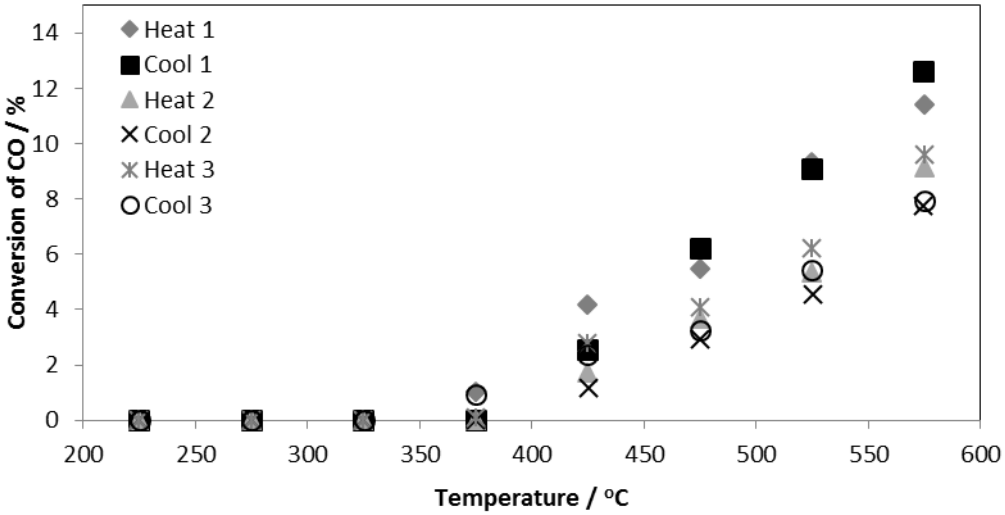

TiPt2.2%IE

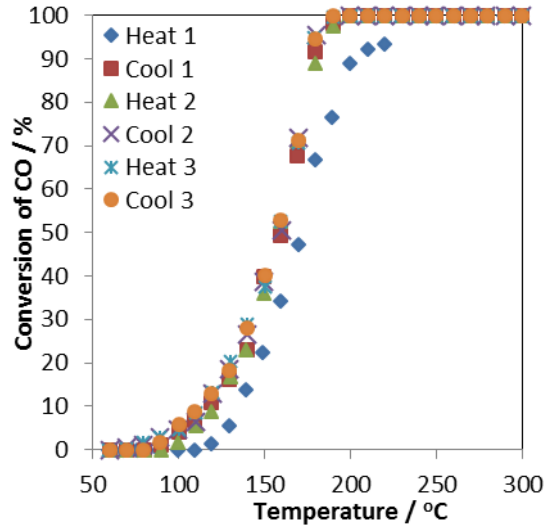

TiPt3.6%IE

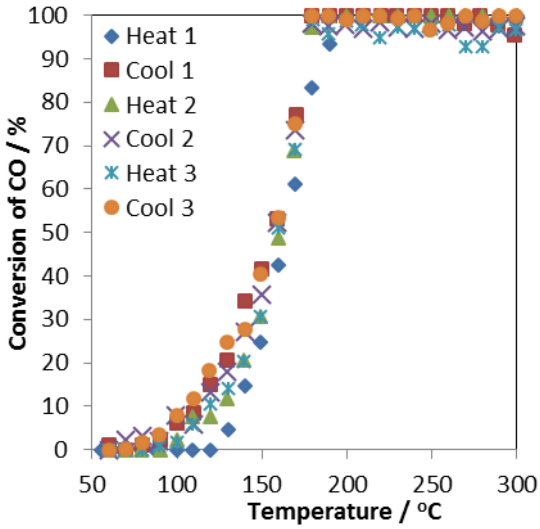

TiPt5.0%IE

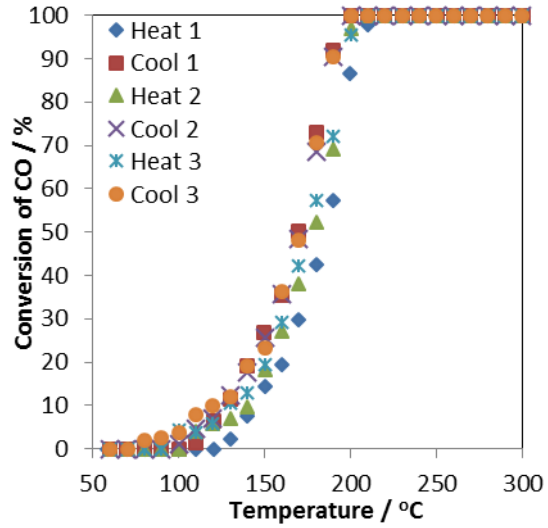

TiPt7.1%IE

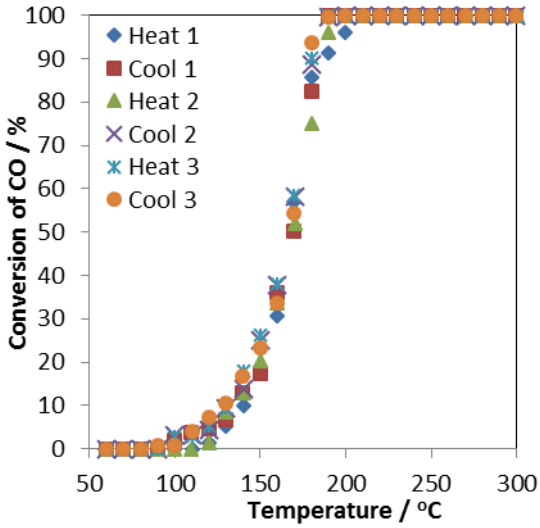

TiPt1.0%IWI

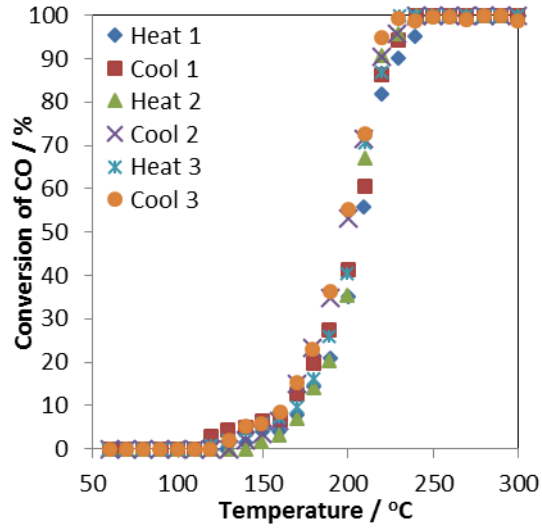

TiPt2.9%IWI

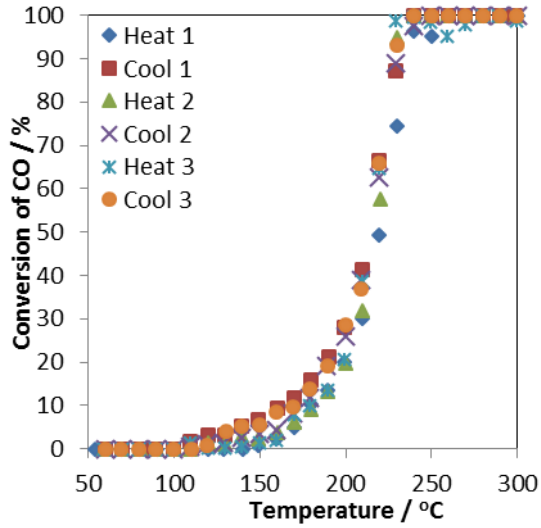

TiPt4.8%IWI

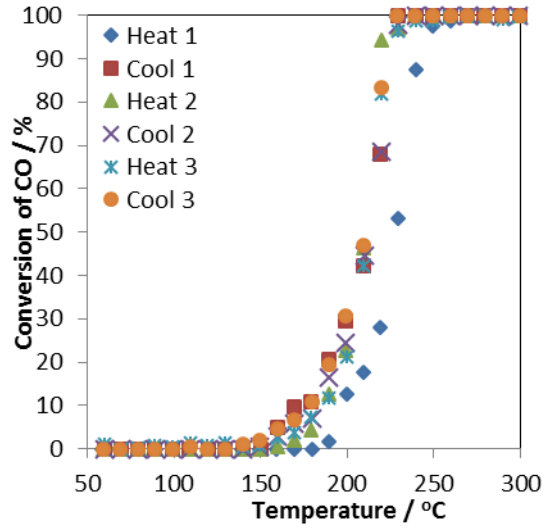

TiPt0.6%Pre-NP

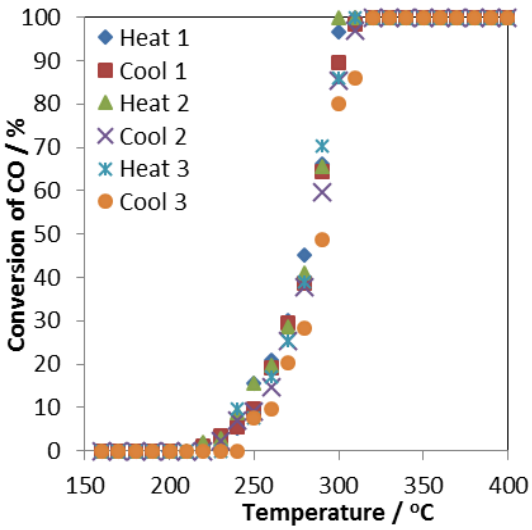

Appendix C – Linearised Arrhenius Data for CO Oxidation Reactions

Conditions: 15mg of catalyst, 50 mL min^{-1} 2000ppm CO, 2000ppm O_2 in N_2, GHSV 750 $hour^{-1}$, heating at 2.5 ^oC min^{-1}. Data shown is between 7 and 20 % conversion.

TiPt2.2%IE

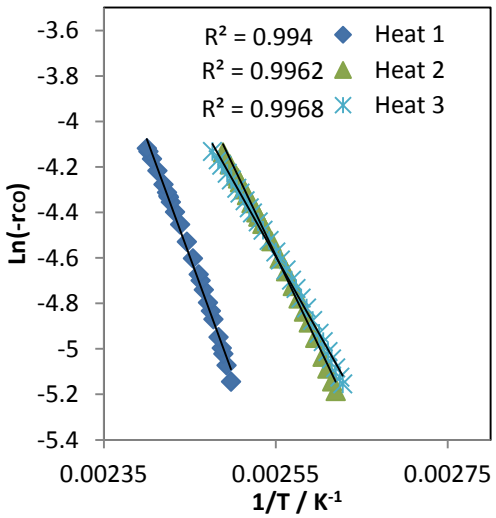

TiPt3.6%IE

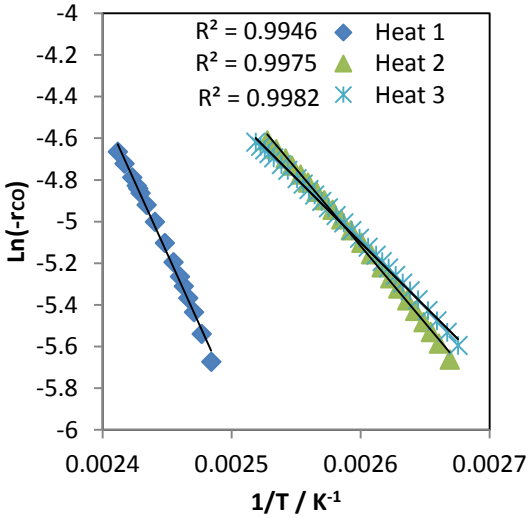

TiPt5.0%IE

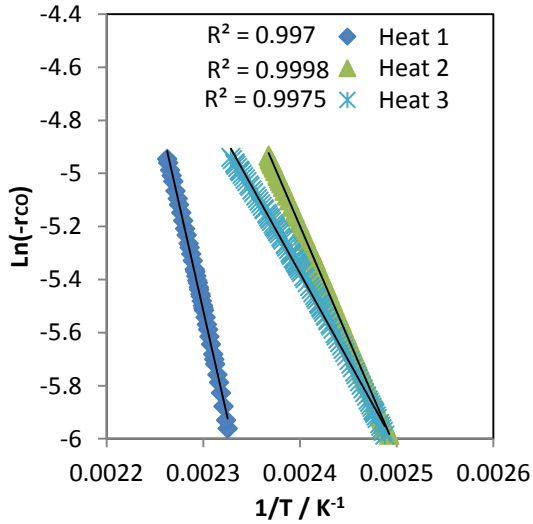

TiPt7.1%IE

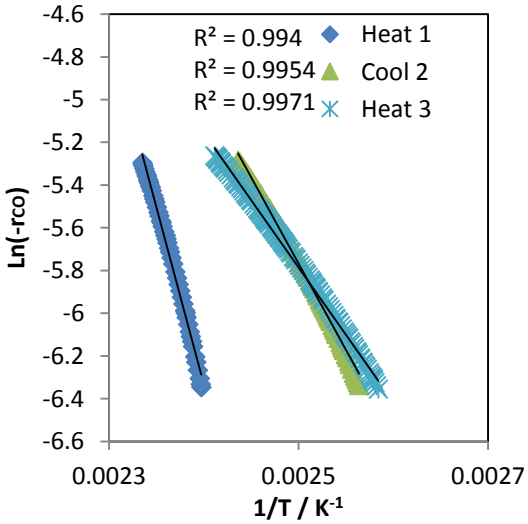

TiPt1.0%IWI

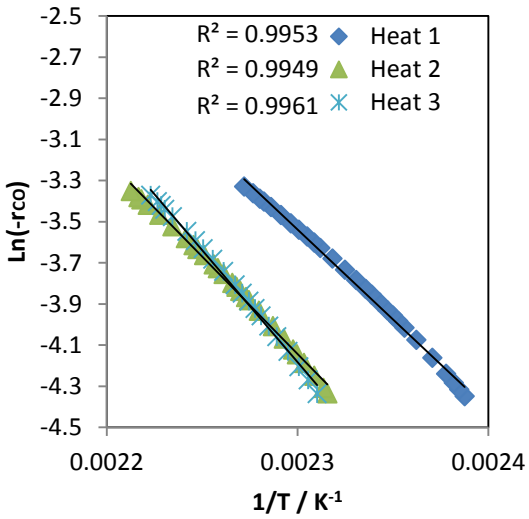

TiPt2.9%IWI

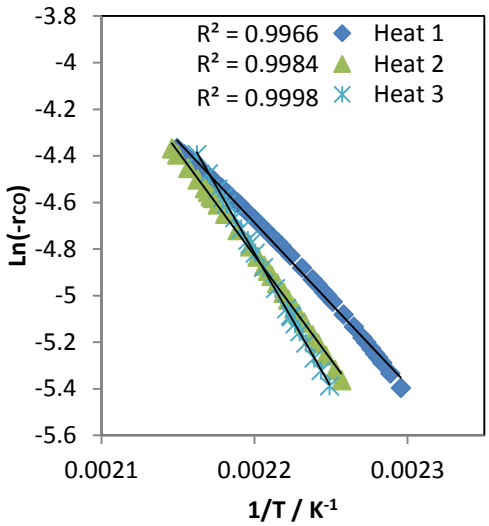

TiPt4.8%IWI

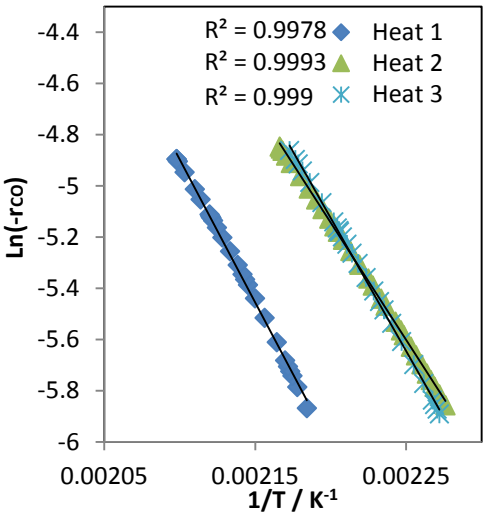

Appendix D – Platinum and Gold Nanoparticles Supported on Titanate Nanotubes Data

Au loadings after synthesis by ion exchange and incipient wetness impregnation, the weight% used to obtain said loading and notation used.

Au added during synthesis / weight%	Au loaded onto TiNT / weight%	Loading efficiency / %	Method of synthesis	Notation
1.0	0.5	50	IE	TiAu0.5%IE
2.9	2.0	69	IE	TiAu2.0%IE
4.8	2.5	52	IE	TiAu2.5%IE
1.0	1.0	100	IWI	TiAu1.0%IWI
2.9	2.9	100	IWI	TiAu2.9%IWI
4.8	4.8	100	IWI	TiAu4.8%IWI

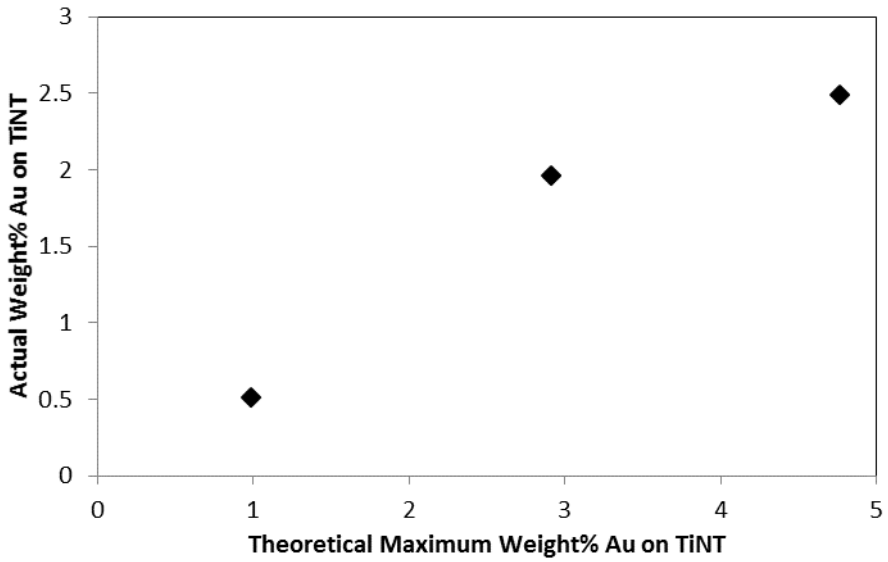

Relationship between maximum and actual gold loading on titanate nanotubes using ion exchange, measured by AAS.

TiPt1.0%IWI

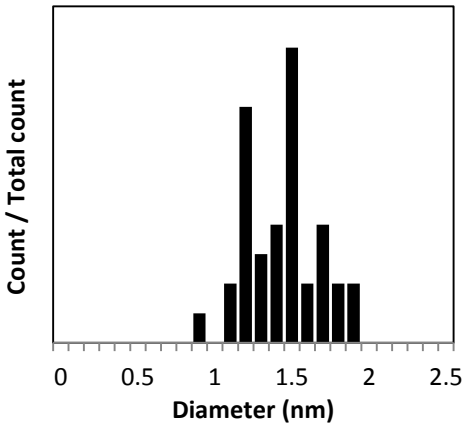

TiPt2.9%IWI

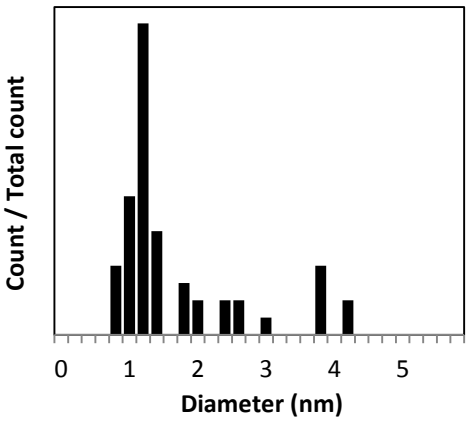

TiPt4.8%IWI

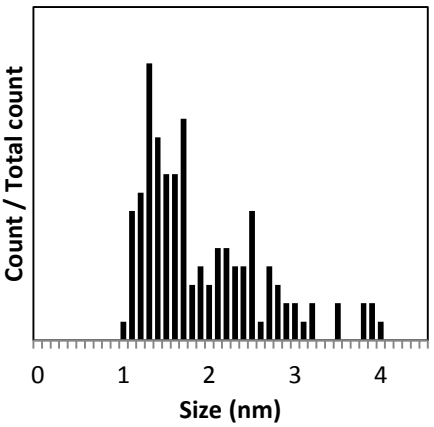

TiPt3.6%IE

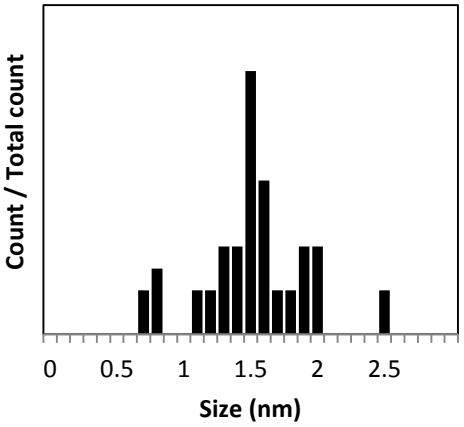

TiPt5.0%IE

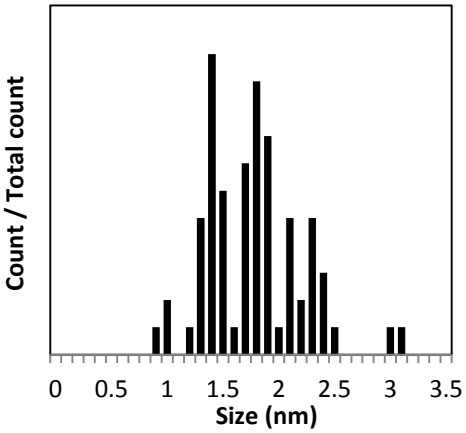

TiPt7.1%IE

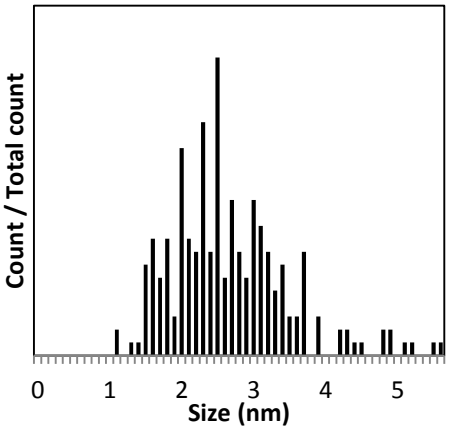

TiPt0.6%Pre-NP

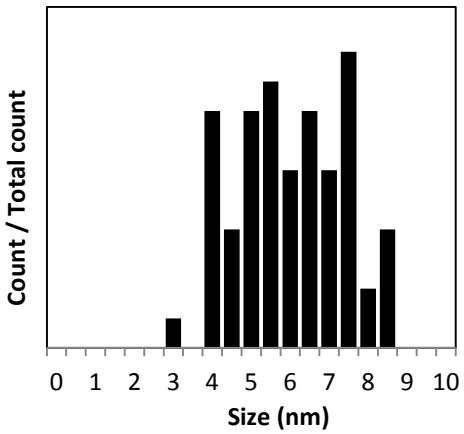

TiAu1.0%IWI

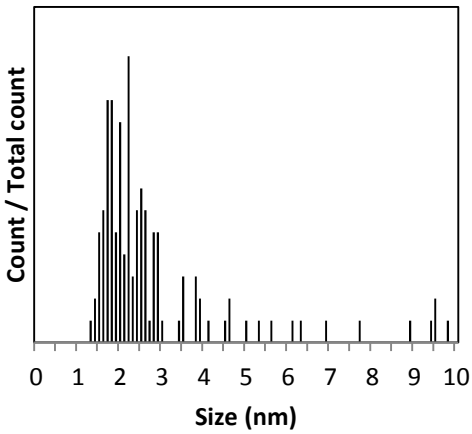

TiAu4.8%IWI

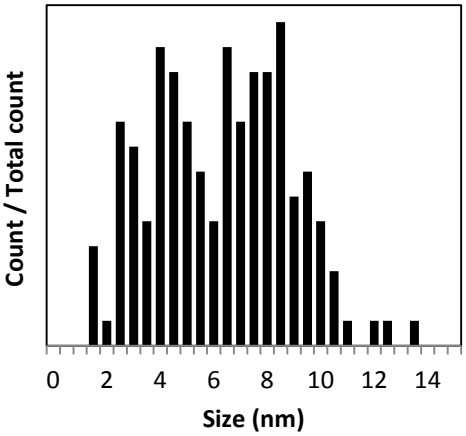

TiAu2.0%IE

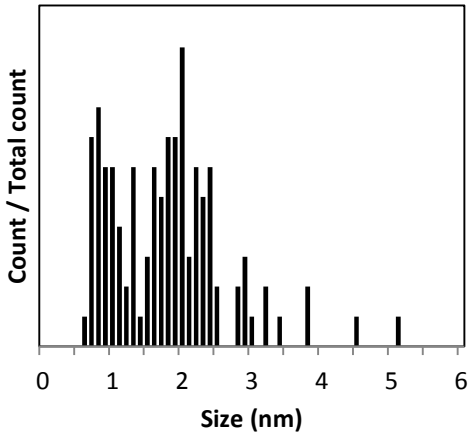

TiAu2.5%IE